
Electronic Thesis and Dissertation Repository

9-6-2017 10:00 AM

Scanning Electrochemical Microscopy of Human Bladder Cancer (T24) Cells

Michelle S. M. Li
The University of Western Ontario

Supervisor
Dr. Zhifeng Ding
The University of Western Ontario

Graduate Program in Chemistry
A thesis submitted in partial fulfillment of the requirements for the degree in Doctor of Philosophy
© Michelle S. M. Li 2017

Follow this and additional works at: <https://ir.lib.uwo.ca/etd>

 Part of the [Physical Chemistry Commons](#)

Recommended Citation

Li, Michelle S. M., "Scanning Electrochemical Microscopy of Human Bladder Cancer (T24) Cells" (2017). *Electronic Thesis and Dissertation Repository*. 4906.
<https://ir.lib.uwo.ca/etd/4906>

This Dissertation/Thesis is brought to you for free and open access by Scholarship@Western. It has been accepted for inclusion in Electronic Thesis and Dissertation Repository by an authorized administrator of Scholarship@Western. For more information, please contact wlsadmin@uwo.ca.

Abstract

Scanning electrochemical microscopy (SECM) employs a biased ultramicroelectrode (few nm to 25 μm diameter) as a probe that is scanned over a sample to electrochemically characterize its physical properties and chemical reactivity with high temporal and spatial resolutions. In this dissertation, SECM was used to investigate the membrane responses of single live human bladder cancer (T24) cells to obtain insights into their topography, physiology and pathology.

First, the membrane-impermeable ferrocene carboxylate was used as the SECM redox mediator to investigate the geometry and topography of these cells along with 3D finite elemental analysis (FEA) simulations generated in COMSOL Multiphysics. The success of these 3D simulation models now allows characterization of asymmetric samples, previously restricted to a 2D axially symmetric geometry (Chapter 2).

Upon exposure to toxic and non-essential Cd^{2+} (mM range), the membrane permeability to the hydrophobic mediator, ferrocenemethanol, in T24 cells increased within minutes. Time-lapsed SECM was able to measure and quantify these changes in membrane permeability (Chapter 3). Expanding on this work, T24 cells were exposed to low exposure (25 μM , up to 6 hours) or 1 hour of acute Cd^{2+} concentrations (Chapter 4). Specifically, the permeation of hydrophilic redox mediators: ferrocene carboxylate, ferrocene dicarboxylate, and hexaamineruthenium(III), into Cd^{2+} -treated T24 cells confirmed membrane integrity loss. In conjunction with FEA, the membrane permeability coefficients were quantified. A correlation between cellular loss and membrane integrity was confirmed using MTT cell proliferation assays.

Exposure to the trace essential Zn^{2+} (0-75 μM , 24 hours) did not significantly affect the cell membranes of T24 cells. Higher Zn^{2+} -treatment led to cytotoxicity, where membrane integrity loss (increased permeation) and cellular death were observed (100-400 μM). The above discoveries suggested the Zn^{2+} -induced apoptosis in these cells. This was confirmed

by several apoptotic indicators, such as the externalization of phosphatidylserine and activation of caspases 3 and 7 (Chapter 5).

Finally, to improve the spatial resolution of SECM, a fabrication method of nanometer-sized probes was successfully developed. This led to the reduction of Pt electrode disk diameters from 25 μm to 25 nm. Visualization of reactivity features of nanometer-sized samples using SECM is anticipated with this advancement (Chapter 6).

Keywords

• scanning electrochemical microscopy • single live cells • human bladder cancer cells • redox mediators • depth scan • probe approach curves • cellular topography • membrane permeability • heavy metal stimulation • toxic heavy metal • trace essential heavy metal • cadmium • zinc • cytotoxicity • cellular death • apoptosis •

Co-Authorship Statement

This thesis includes material from four previously published manuscripts that are presented in Chapters 2, 3, 4 and 6. Also included in this thesis is material from two manuscripts prepared for submission, which are presented in Chapter 5 and portions of Chapter 6.

The manuscript presented in Chapter 2 was published and co-authored by M.S.M. Li, F.P. Filice and Z. Ding (*J. Electroanal. Chem.* **2016**, 779, 176-186). All of the experiments were completed by MSML and COMSOL simulations were completed by FPF. MSML was responsible for writing and revision of the manuscript, which was edited by FPF and ZD.

The manuscript presented in Chapter 3 was published and co-authored by M.S.M. Li, F.P. Filice and Z. Ding (*J. Inorg. Biochem.* **2014**, 136, 177-183). All of the experiments were completed by MSML and COMSOL simulations were completed by FPF. MSML was responsible for writing and revision of the manuscript, which was edited by FPF and ZD.

The manuscript presented in Chapter 4 was published and co-authored by M.S.M. Li, F.P. Filice, J.D. Henderson and Z. Ding (*J. Phys. Chem. C.* **2016**, 120, 6094-6103). All of the experiments were completed by MSML. COMSOL simulations were completed by FPF. MSML was responsible for writing and revision of the manuscript, which was edited by FPF, JDH and ZD.

The manuscript, Zn²⁺-Induced Apoptosis in Single Human Bladder Cancer Cells Interrogated by Scanning Electrochemical Microscopy, presented in Chapter 5 has been prepared for submission and is co-authored by M.S.M. Li, F.P. Filice and Z. Ding. All of the experiments were completed by MSML and COMSOL simulations were completed by FPF. MSML was responsible for writing and revision of the manuscript, which was edited by FPF and ZD.

There are two manuscripts presented in Chapter 6: one has been prepared for submission and one that was previously published. The manuscript, Electrochemical Functionality of Microband Electrodes Imaged by Scanning Electrochemical Microscopy

with Submicron Probes (Sections 6.4.1.2 and 6.4.2) has been prepared for submission and was co-authored by M.S.M. Li, F.P. Filice and Z. Ding. The published manuscript was also co-authored by M.S.M. Li, F.P. Filice and Z. Ding J. (*Electroanal. Chem.* **2016**, 781, 126-135.) MSML was responsible for completing all the experiments presented in both papers and the COMSOL simulations of the SECM depth scans were completed by FPF. MSML was responsible for writing and revision of both manuscripts, which was edited by FPF and ZD.

Acknowledgments

First and foremost, I must acknowledge and thank my supervisor, Dr. Zhifeng Ding, for his generosity, patience and expert guidance throughout my four years in the Ph.D. program at Western University, as well as my B.Sc. thesis project many years ago. Through his mentorship, I have been given the opportunity to work on several research projects within his lab. His generosity and guidance has allowed me to attend and present at well-respected conferences, both national and internationally. His patience and understanding has been truly tested with my injured ankle/leg, which required a medical leave of absence for surgery and too many physiotherapy sessions and medical appointments to count. The complications from my injury, which occurred 5 days prior to my official start date, will now officially surpass the length of my Ph.D. program. Through my Ph.D., I have been fortunate enough to be financially supported by my supervisor, Department of Chemistry, Western University, and the Ontario Government, through the Queen Elizabeth II Graduate Scholarship in Science and Technology.

I must also acknowledge and thank my former M.Sc. supervisor, Dr. Ian J. Burgess, at the University of Saskatchewan. Without my experience and time in the Burgess' lab, I would not have begun my Ph.D. research project with many of the fundamentals required. It was from Ian's encouragement and approval to present my first poster at a CSC conference back in 2011 that offered me this Ph.D. opportunity with Dr. Ding.

I would also like to thank the Chemistry faculty, especially my committee members, Drs. François Lagugné-Labarhet and Tsun-Kong Sham for their mentoring throughout the 4 years. I must thank Aneta Borecki (Chemistry Department) for her knowledge on cellular viability assays, Dr. Todd Simpson for his assistance at Western's Nanofabrication Facility, and Dr. Kristin Chadwick (The London Regional Flow Cytometry Facility) for her knowledge and guidance for the flow cytometry experiments. In addition, I must thank Drs. Janine Mauzeroll and Laurence Danis at McGill University for their mentoring in the fabrication of laser-pulled nanoelectrodes. I greatly appreciate all of the work the staff of the

Chemistry Department, especially the Electronic Shop, who have spent many hours fixing and modifying our instruments, have done throughout the duration of my studies.

I would also like to take the time and thank Dr. Martin J. Stillman for giving me the opportunity to help organize, run, and present at two conferences in Parry Sound, the 5th and 6th Georgian Bay International Conference on Bioinorganic Chemistry (CanBIC). This unique opportunity of being a local conference organizing committee member and meeting so many exciting and new people from the Bioinorganic Chemistry community was greatly appreciated.

I would like to thank all Ding group members, past and present, for being great friends, listening to countless presentations and for creating a good working environment. For the SECM projects, I must thank Fraser P. Filice and Jeffrey D. Henderson, both of whom I worked closely with. We have spent countless hours discussing our projects and finding solutions when things go awry. For the ECL projects, I must thank Drs. Kalen N. Swanick and Mahdi Hesari for their knowledge and expertise in ECL, as well as Dr. Jacquelyn T. Price from Dr. Nathan D. Jones' Group for synthesizing the thiophene luminophores we studied in ECL.

I must also acknowledge the MSA ground office area graduate students from Drs. Yining Huang and François Lagugné-Labarthe's Research Groups, especially Gregory Q. Wallace, Danielle McRae and Ali Tabatabaei. This communal office area has given me the opportunity to meet and become friends with the graduate students I might not have known otherwise.

Thank you to my friends, who had to listen to all of my graduate school experiences. Terri, Louis, Glenn and Gabby especially, for spending countless hours helping me through this Ph.D. and frustrations regarding my never ending leg issues. Whether it was research, school or life related, your friendship and support has always been greatly appreciated.

Last, but not least, I must give special thanks to my parents, Terry and Jennifer Li, for being great parents and always supporting me, as well as my brother, Justin. My ankle injury alone has required so much from you, whether it was helping me with my physical

limitations or taking days off of work to help me around my surgery, attending or taking me to my medical appointments at any time of the day or just helping me stay sane dealing with all of the frustrations of this injury, it was greatly appreciated, more than you'll ever know. I know I could not have done this without your support.

Table of Contents

Abstract.....	ii
Co-Authorship Statement.....	v
Acknowledgments.....	vii
Table of Contents.....	x
List of Tables.....	xvi
List of Figures.....	xvii
List of Appendices.....	xxvi
List of Abbreviations.....	xxvii
Chapter 1.....	1
1 Introduction.....	1
1.1 Background of SECM.....	1
1.2 SECM Principles.....	1
1.3 Simulations.....	4
1.4 Modes of Operation for SECM.....	4
1.5 Conventional Imaging Modes of SECM.....	6
1.6 SECM Instrumental Setup.....	7
1.7 Ultramicroelectrodes.....	9
1.8 Application of SECM.....	9
1.9 SECM Study on Single Live Cells.....	12
1.10SECM Membrane Permeability.....	12
1.11Exposure to Heavy Metals.....	13
1.12Human Bladder Cancer (T24) Cells.....	13
1.13Scope of Dissertation.....	14

1.14References.....	16
Chapter 2.....	24
2 Determining Live Cell Topography by Scanning Electrochemical Microscopy.....	24
2.1 Introduction.....	24
2.2 Experimental Section.....	26
2.2.1 Materials.....	26
2.2.2 Cell Culture.....	26
2.2.3 Cellular Viability.....	27
2.2.4 Electrode Fabrication.....	27
2.2.5 SECM Instrumentation.....	28
2.2.6 SECM Experiments.....	28
2.2.7 SECM Data Analysis.....	29
2.2.8 The Simulation Workstation Computer.....	29
2.3 Theory and Simulations.....	29
2.3.1 2D Axially Symmetric Simulation Model Geometry.....	29
2.3.2 3D Simulation Model Geometry.....	30
2.3.3 Simulation Methodology.....	32
2.3.4 Validation of the 3D Model.....	34
2.4 Results and Discussion.....	36
2.4.1 Determining Cell Diameter through Optical Micrographs.....	36
2.4.2 Extraction of Cell Heights by Traditional Methods.....	37
2.4.3 Determining Cell Heights by Parameterizing Heights.....	40
2.4.4 3D Mapping of Cell Topography.....	42
2.4.5 Horizontal Sweeps across the Cell.....	45
2.4.6 Horizontal Imaging of the Cell.....	48

2.5	Conclusions.....	50
2.6	References.....	51
Chapter 3.....		55
3	A Time Course Study of the Cadmium Effects on Membrane Permeability in Single Human Bladder Cancer Cells Using Scanning Electrochemical Microscopy	55
3.1	Introduction.....	55
3.2	Experimental.....	57
3.2.1	Materials	57
3.2.2	Electrochemical Measurements	57
3.2.3	SECM Measurements	58
3.3	Simulations	58
3.4	Results and Discussion	62
3.4.1	Cadmium concentration addition.....	62
3.4.2	SECM for time course measurements of membrane permeability	63
3.4.3	Time course study of Cd ²⁺ effect on membrane permeability	65
3.5	Conclusion	70
3.6	References.....	71
Chapter 4.....		76
4	Probing Cd ²⁺ -Stressed Live Cell Membrane Permeability with Various Redox Mediators in Scanning Electrochemical Microscopy	76
4.1	Introduction.....	76
4.2	Experimental Section	78
4.2.1	Materials	78
4.2.2	Electrode Fabrication	79
4.2.3	Cell Culture.....	79
4.2.4	Cell Viability.....	79

4.2.5	SECM Instrumentation	80
4.2.6	SECM Experiments	80
4.2.7	SECM Data Analysis	81
4.2.8	Simulations of PACs.....	81
4.3	Results and Discussion	82
4.3.1	Quantification of the Membrane Permeability to the Three Hydrophilic Redox Mediators.....	82
4.3.2	Time-Dependent Effects of Cadmium Treatment on Membrane Permeability	84
4.3.3	Compromised Structure of the Cell Membrane	87
4.3.4	Time-Dependent Effects of Cd ²⁺ on Cellular Viability	89
4.3.5	Cd ²⁺ Concentration-Dependence of Membrane Permeability	90
4.3.6	Concentration-Dependent Effects of Cd ²⁺ on Cellular Viability.....	92
4.3.7	Comparison of the Time-Dependent vs. Concentration-Dependent Studies	93
4.3.8	Effects on Flux/Membrane Permeability	94
4.4	Conclusions.....	95
4.5	References.....	96
Chapter 5	102
5	Zn ²⁺ -Induced Apoptosis in Single Human Bladder Cancer Cells Interrogated by Scanning Electrochemical Microscopy.....	102
5.1	Introduction.....	102
5.2	Experimental.....	104
5.2.1	Materials	104
5.2.2	Electrode Fabrication	104
5.2.3	Cell Culture.....	104

5.2.4	SECM Instrumentation and Experimentation	105
5.2.5	SECM Data Analysis	105
5.2.6	Optical Imaging	106
5.2.7	Immunofluorescence.....	106
5.2.8	MTT Cell Proliferation Assay	106
5.2.9	Flow Cytometry	107
5.3	Results and Discussion	108
5.3.1	Zn ²⁺ Effects on Cell Membrane Permeability	108
5.3.2	Zn ²⁺ Effects on Cellular Viability.....	112
5.3.3	Confirmation of Apoptosis	114
5.4	Conclusions.....	119
5.5	References.....	120
Chapter 6.....		125
6	Scanning Electrochemical Microscopy with Laser-Pulled Submicron Pt Probes	125
6.1	Introduction.....	125
6.2	Experimental Section	127
6.2.1	Materials	127
6.2.2	Electrode Fabrication	128
6.2.3	Electrochemical Measurements	129
6.2.4	SECM Experiments	129
6.3	Theory and Simulation.....	130
6.3.1	Simulation geometry.....	130
6.3.2	Simulation Methodology	132
6.4	Results and Discussion	133
6.4.1	Laser-pulled Pt Nanoelectrodes	133

6.4.2	SECM Imaging of an IAME by a 250 nm Diameter Pt NE (RG30)	136
6.4.3	SECM Imaging of an IAME by a 4.4 μ m Pt UME (RG3)	142
6.4.4	Redox Cycling Effect.....	147
6.4.5	Determining the sample tilt.....	151
6.5	Conclusions.....	155
6.6	References.....	157
Chapter 7	162
7	Concluding Remarks and Future Work	162
7.1	Concluding Remarks.....	162
7.2	Future Works	165
Appendices	168
Curriculum Vitae	241

List of Tables

Table 2.1. Comparison of the cell heights quantified by the PAC extraction method (2D vs. 3D models) and parameterizing the cell heights method.....	42
Table 3.1. The initial and final membrane permeability of T24 cells exposed to various concentrations of Cd ²⁺	67
Table 4.1. Experimental Parameters of the SECM Redox Mediators Studied	81

List of Figures

- Figure 1.1. Principles of SECM illustrating (A) top: hemispherical diffusion of a reduced redox mediator from the bulk solution to the electrode tip, bottom: a CV of 0.90 mM FcCH₂OH with 0.100 M KCl in deionized water, (B) top: positive feedback between the electrode tip and conductive sample (redox cycling), bottom: the corresponding experimental and simulated PACs approaching a conductive sample and (C) top: illustration of negative feedback principle between the electrode tip and insulating sample, bottom: the corresponding experimental and simulated PACs approaching a non-conductive (insulating) sample. All data shown were collected with a 25 μm Pt UME (RG3). 3
- Figure 1.2. Schematic illustrations of the (A) tip generation/substrate collection (TG/SC) and (B) substrate generation/tip collection (SG/TC) modes of SECM. In (A) the tip acts as the generator, where it is biased at a positive potential to drive the one electron oxidation reaction of FcCH₂OH to Fc⁺CH₂OH forward. The oxidized product Fc⁺CH₂OH can diffuse to the substrate, where it gets reduced back to FcCH₂OH. In (B) the substrate acts as the generator, oxidizing FcCH₂OH at its surface. The oxidized species can diffuse to the tip, where it becomes reduced. The consumption of FcCH₂OH at the (A) electrode tip and (B) substrate are replenished by the diffusion of the species from the bulk solution. 5
- Figure 1.3. The schematic illustrations of the SECM operating in the (A) constant height and (B) constant distance modes. In constant height mode, the probe is scanned at a fixed height relative to the z-axis of the positioning system, while the probe in constant distance mode will be scanned to maintain a constant normalized current and therefore tip-to-sample distance. The dotted line represents the probe's scan path. 6
- Figure 1.4. SECM current map images of T24 cells collected using the (A) constant height and (B) depth scan imaging modes. 7
- Figure 1.5. A schematic illustration of the SECM setup used throughout this dissertation with the 3 components identified: (1) the electrochemical system, (2) a precise positioning system and (3) the data acquisition system. 8

Figure 1.6. Schematic illustration of increased membrane permeability to hydrophilic redox mediators, FcCOO^- , $\text{Fc}(\text{COO})_2^{2-}$ and $\text{Ru}(\text{NH}_3)_6^{3+}$ after treatment with Cd^{2+} 13

Figure 2.1. (A) An illustration of the 2D axially symmetric model of a T24 cell in COMSOL Multiphysics v5.1. c_s and c_c are the bulk concentrations outside and inside the cell, respectively. At the cell membrane, the membrane flux, f , is defined as a no flux boundary, where f is 0 mol·m/L·s. (B) A typical meshed 2D SECM model, with finer meshing located in the areas of interest (Pt tip and cell membrane)..... 30

Figure 2.2. (A) The labelled 3D model geometry of an SECM electrode's approach to a single live cell. (B) Mesh of the full 3D model. (C) Zoomed-in view of the 3D model geometry focusing on the electrode tip and cell membrane (D) Mesh of the zoomed in 3D model..... 31

Figure 2.3. (A) Graphical representation of the 4 vertical cross-section locations over a T24 cell of height $8\ \mu\text{m}$ x $20\ \mu\text{m}$ diameter and the petri dish. The purple cross-section indicates an extraction over the center of the cell (taken as $x = 0$), while the blue and green cross-sections are extractions taken at a distance of $r/2$ and r away from the cell center, respectively. The red line represents an extraction taken over the petri dish at a distance of $2r$. For these experimental extractions, $x > 2r$ away from the cell center was taken ($x \gg r$). (B) The 2D and 3D simulated PACs to the center of the cell are compared, validating the 3D simulation model. (D)-(E) are the corresponding simulated PACs over the color-specified locations in (A). As the electrode gets further from the cell center, the electrochemical feedback becomes weaker..... 35

Figure. 2.4. Optical images of a (A) T24 cell (red circle) and (B) approach of a $10\ \mu\text{m}$ Pt UME which is in close proximity to the cell (black circle). (C) A typical SECM depth scan image of the T24 cells obtained using the redox mediator FcCOO^- , as detected by the $10\ \mu\text{m}$ Pt UME. 37

Figure 2.5. (A) The SECM depth scan image of a T24 cell using FcCOO^- as the redox mediator, as detected by a $10\ \mu\text{m}$ Pt UME with RG 3. The scale bar in the image represents $10\ \mu\text{m}$. The PACs illustrated in (B) correspond to the vertical cross-sections taken over the

cell (blue) and over the dish (purple) overlaid onto theoretical insulating curves (black solid lines)..... 39

Figure 2.6. Distribution of the heights of the T24 cells, where the average was found to be $8.7 \pm 3.3 \mu\text{m}$ for $N = 22$ cells..... 40

Figure 2.7. (A) Illustrative representation of the parametric sweep of the cell height against a fixed cell diameter ($20 \mu\text{m}$). (B) An experimental PAC overlaid onto simulated curves to directly determine the cell's height. This particular cell has a diameter of $20 \mu\text{m}$ and a height of $14 \mu\text{m}$ (green circles)..... 41

Figure 2.8. (A) An optical micrograph of a T24 cell under study with the cell encircled in red. (B) The corresponding SECM depth scan image taken across the cell using a $5 \mu\text{m}$ Pt UME, with the vertical cross-sectional lines identified for PAC extractions. The purple cross-section represents the center of the cell ($x = 0$), which can be characterized with the traditional 2D-Axial simulations. The blue, green and red extractions require the 3D simulations ($x = r/2$, r , and $\gg r$, respectively). The extracted experimental PACs overlaid onto their respective simulated curves, at $x =$ (C) 0 (purple), (D) $r/2$ (blue), and (E) r (green) and (F) $\gg r$ (red)..... 43

Figure 2.9. Simulated concentration maps of horizontal UME sweeps $1 \mu\text{m}$ above the cell at electrode x positions of (A) $15 \mu\text{m}$ away from cell center, $x = 1.5r$, (B) $10 \mu\text{m}$ away from the cell center (cell edge), $x = r$, (C) $5 \mu\text{m}$ away from the cell center, $x = r/2$, and (D) directly above cell center, at $x = 0r$ 46

Figure 2.10. (A) A horizontally-labelled SECM depth scan image taken across the cell using a $5 \mu\text{m}$ Pt UME. The blue line is taken at the edge of the image, the red and black lines taken 5 and $10 \mu\text{m}$ above the blue line respectively. (B) Simulated and experimental SECM horizontal sweeps across the cell. The UME probe distances (above the cell) in micrometers are indicated in the legend for the simulated curves. (C) The vertically-labelled SECM depth scan image above the center of the cell. (D) The simulated and experimental PACs extracted over the center of the cell..... 47

Figure 2.11. (A) Experimental and (B) simulated depth scans collected with a 5 μm UME with an RG of 3 approaching a single cell with a height of 8 μm and a diameter of 20 μm . The theoretical UME approaches to 2.0 μm from the highest point on the cell during its closest horizontal sweep. The experimental depth scan is determined to approach to a height of 2.6 μm above the cell..... 49

Figure 3.1. A schematic of the 2D axial geometry simulated in COMSOL 3.5a. c_R and c_{R1} are the bulk concentrations outside and inside the cell, respectively. The boundary conditions at the cell membrane are the inward and outward fluxes of FcCH_2OH across the cell membrane: $f_{\text{in}} = P_m (c_R - c_{R1})$ and $f_{\text{out}} = P_m (c_{R1} - c_R)$ 60

Figure 3.2. Optical micrographs of T24 cells (A) unexposed to Cd^{2+} and (B) exposed to 10 mM Cd^{2+} for 12 h..... 63

Figure 3.3. (A) An optical micrograph of control T24 cells. The black spot in the image is the UME, which is to the right of the cell of interest (circled). (B) A typical SECM depth scan image of a T24 cell unexposed to Cd^{2+} (control). (C) An experimental probe approach curve to a control T24 cell, taken at the vertical line above the cell as shown in (B). The experimental PAC is overlaid onto simulated curves of known membrane permeability coefficients..... 64

Figure 3.4. Optical micrographs of a T24 cell (A) before and (B) after exposure to 1 mM Cd^{2+} for 50 min, the UME is located to the right of the cell of interest. (C) A SECM depth scan image of the T24 cell as in (A) after 50 min of Cd^{2+} exposure. (D) PACs to the cell before (red, extracted along the vertical line in (C)) and 45 min after exposure to 1 mM Cd^{2+} (blue)..... 66

Figure 3.5. Optical micrographs of a T24 cell (A) before and (B) after exposing to 10 mM Cd^{2+} for 45 min, where the UME is to the right of the cell. (C) A SECM depth scan image of the T24 cell as in (A) after 50 min of Cd^{2+} exposure. PACs to the cell before (red in (D)), extracted along the vertical line in (C)) and 45 min after exposing to 1 mM Cd^{2+} (blue in (D))..... 68

Figure 3.6. Permeability of FcCH₂OH as a function of time for T24 cells treated with 1.0 and 7.5 mM Cd²⁺. Note, the membrane permeability at t = 5 min was removed due to the intense current spike which occurs immediately after the addition of 7.5 mM Cd²⁺ 69

Figure 4.1. Typical SECM depth scan images of single T24 collected using redox mediators: (A) FcCOO⁻, (B) Fc(COO)₂²⁻, and (C) Ru(NH₃)₆³⁺. The scale bar in each SECM image represents 10 μm. The corresponding experimental PACs extracted at each arrow in (A-C) is overlaid onto theoretical PACs generated to an insulating cell, where the redox mediator is (D) FcCOO⁻ (purple), (E) Fc(COO)₂²⁻ (blue), and (F) Ru(NH₃)₆³⁺ (green). Please note, the color map (current) for Ru(NH₃)₆³⁺ in (C) appears inverted from the ferrocene carboxylates (A-B) due to the opposing redox chemistry occurring at the UME tip. 82

Figure 4.2. The average P_m of T24 cells pre-incubated with 25 μM Cd²⁺ plotted as a function of incubation time using the following molecular probes: (A) FcCOO⁻ (purple squares), (B) Fc(COO)₂²⁻ (blue diamonds), (C) Ru(NH₃)₆³⁺ (green triangles), and (D) FcCH₂OH (red circles). A typical SECM depth scan image of a T24 cell after 6 hours of Cd²⁺ treatment and its corresponding PAC overlaid onto a curve of known P_m , are included as an inset for each molecular probe (A-D). The scale bar in each SECM image represents 10 μm. Each SECM live cell experiment produces a single depth scan image, which provides a P_m to be used in determining the average P_m for that particular molecular probe at the respective Cd²⁺ treatment period (A-D). 85

Figure 4.3. Optical micrographs of T24 cells grown in the (A) absence of Cd²⁺ treatment and (B) after 4 hours of Cd²⁺ treatment. The T24 cells treated with 4 hours of 25 μM Cd²⁺ appear to have more blebbing throughout the cell, indicating cellular stress and/or damage. The scale bar in each optical image represents 40 μm. 88

Figure 4.4. Cell viability of T24 cells treated with 25 μM Cd²⁺ was measured by the MTT cell proliferation assay. The mean ± RSD of 5 separate experiments (8 replicates per experiment) is shown. 90

Figure 4.5. Typical SECM depth scan images of T24 cells treated with 4.4 mM Cd²⁺ for 1 hour detected using the following molecular probes: (A) FcCOO⁻, (B) Fc(COO)₂²⁻, and (C)

$\text{Ru}(\text{NH}_3)_6^{3+}$. The scale bar in each SECM image represents 10 μm . The arrows in (A)-(C) indicate where the vertical cross section was taken to extract the PACs in (D)-(F) respectively. The experimental PACs were overlaid onto simulated curves to quantify their P_m . Graphical representation of the changes in the average P_m to the redox mediators after acute Cd^{2+} exposure are shown in (G)-(I), in the same order as (A)-(C) and (D)-(F). 91

Figure 4.6. Cell viability of T24 cells treated with acute Cd^{2+} concentrations for 1 hour was measured by the MTT assay. The mean \pm RSD of 3 separate experiments (6 replicates per experiment) is shown. 93

Figure 5.1. Typical SECM depth scan images of single T24 cells treated with (A) 10 μM and (B) 400 μM Zn^{2+} using FcCH_2OH as the redox mediator. The scale bar in each image represents 10 μm . The arrows in (A) and (B) indicate where the PACs were extracted for P_m quantification along with simulated ones in (C) and (D), respectively. The colors of the arrows in the depth images (A-B) match the obtained PACs (diamonds in C-D). 108

Figure 5.2. Average membrane permeability to (A) FcCH_2OH and (B) $\text{Ru}(\text{NH}_3)_6^{3+}$ in T24 cells treated with Zn^{2+} between the ranges of 0-400 μM for 24 hours. The inset in (A) includes two optical micrographs of methanol-fixed T24 cells treated with 0 μM Zn^{2+} (left) and 400 μM Zn^{2+} (right) and (B) the zoomed in view of the P_m changes in 100-400 μM Zn^{2+} . The scale bar in the optical images represents 20 μm 110

Figure 5.3. Cellular viability of Zn^{2+} -treated T24 cells using ReadyProbes® NucBlue and NucGreen. NucBlue is membrane permeable which therefore allows measurement of total cell count while NucGreen can only permeate a cell with a compromised cell membrane. The ratio of cells expressing NucGreen to NucBlue is compared to that of the control cells and is used to indicate cellular viability. 113

Figure 5.4. Statistical validation of T24 cells treated with (A) 0 (control), (B) 100, (C) 200 and (D) 400 μM Zn^{2+} undergoing apoptosis. The externalized PS is visible by the fluorochrome PE of Annexin V PE, while the fluorochrome 7-AAD indicates those cells with compromised cell membranes. 115

Figure 5.5. Percentage of T24 cells undergoing (A) apoptosis and (B) necrosis after treatment with Zn^{2+} . Apoptotic cells were identified through the expression of CellEvent™ Caspase-3/7, while necrotic cells were identified through the expression of ReadyProbes® NucRed (propidium iodide). ReadyProbes® NucBlue (Hoescht 33342) was used to identify the cells (nuclei). 118

Figure 6.1. The model geometries of the SECM analysis of an IAME sample (A) parallel to the UME tip and (B) at a 10° tilt relative to the electrode. (C) A zoomed in and labelled model of the Pt and glass microband electrodes of the IAME. (D) The 3D perspective view illustrating the symmetry plane in the simulation model. (E) The tetrahedrally-meshed simulation model with further refinement at the electrode tip and the IAME microbands to improve the accuracy of the simulation. (F) An example of a simulated concentration map of the IAME with the SECM probe positioned in bulk solution. 130

Figure 6.2. (A) The CV obtained in 10 mM $Ru(NH_3)_6^{3+}$ and 0.1 M KCl as the supporting electrolyte in ultrapure deionized water testing for electrode conductivity. (B) A horizontal line scan obtained across 1 grid square, where the first 30 μm is over the Ni portion of the grid and the second half of the scan (30-60 μm) is over the “hole” portion of the grid. The inset is an optical image of the TEM grid with the scan path of the SECM probe identified in red arrow. The blue scale bar in the image represents 40 μm 134

Figure 6.3. (A) An SEM image of a freshly pulled NE. The 25 nm diameter Pt wire can be seen to be recessed 7 μm within the pulled quartz capillary tip. (B) A SEM image of a FIB-milled laser-pulled Pt NE with Pt tip exposed by FIB-milling. The indicated area in (B) provides an estimate of ~25 nm for the diameter of the Pt wire with an RG > 30. 135

Figure 6.4. (A) and (B) are the constant height SECM images of two alternating pairs of Pt and glass microbands collected in 10 mM $Ru(NH_3)_6^{3+}$ solution with 0.1 M KCl as the supporting electrolyte by a 250 nm diameter Pt NE with RG 30. (A) is the 2D current map view and (B) is a 3D view of (A), providing stronger visualization of the electrochemical behavior of the Pt and glass microbands. The scale bars in the images represent 4 μm and the current scale bar in (A) is been normalized against the steady state current. (C)-(E) are the

horizontal line scans taken at the locations specified in (A), that are overlaid over simulated curves generated at 0.50, 0.75, 1.00, 2.00 and 3.00 μm above the sample. From successful overlays, the 250 nm Pt NE was scanned approximately 0.75 μm above the sample. The simulation geometry of the working electrode was simplified to a 250 nm Pt NE with an RG of 10. 137

Figure 6.5. (A) SECM depth scan image towards the glass and Pt microbands of the IAME with a 250 nm Pt probe (RG30). A horizontal line scan (red pentagons) is extracted near the end of the scan. (B) The experimental horizontal scan is overlaid onto theoretical curves to quantify tip-to-sample distance. 140

Figure 6.6. Theoretical PACs of a 250 nm Pt NE's approach to the Pt and glass microbands (red and black) of the IAME. 141

Figure 6.7. An optical micrograph of the (A) Pt and glass microbands of an IAME sample with a scale bar of 40 μm . (B) The corresponding SECM constant height image taken above the IAME collected using a 4.4 μm Pt UME (RG3) with FcCH_2OH as the redox mediator. The scale bar in the image represents 10 μm . Note, our SECM instrument moves the electrode from right to left, resulting in an inverted SECM image (with respect to the optical micrograph). 142

Figure 6.8. (A) A horizontally-labelled SECM depth scan image taken across the IAME surface using a 4.4 μm Pt UME (RG3). The purple line is taken at the edge of the image, while the green, blue, and red lines are taken 1.4, 5, and 10 μm above the purple line respectively. (B) and (C) are the simulated horizontal sweeps across the IAME with the experimental SECM data overlaid on top. (B) Displays a wide range of curves (0.5 to 30 μm) while the (C) is magnified from (B), focused on the normalized current range between 1.00 and 1.20 and the electrode position between 80 and 120 μm . From this plot, the purple and green experimental horizontal scans are removed for improved clarity. 144

Figure 6.9. (A) A SECM depth scan image taken across the microbands of the IAME using a 4.4 μm Pt UME with a RG value of 3, with the vertical cross-sectional lines identified. The blue and purple cross-sections represents a PAC extracted to the center of a Pt and glass

microband respectively, while the green cross-section represents a PAC extracted to the transition region between the two microbands 147

Figure 6.10. The comparison of the experimental PACs extracted to the (A) Pt and (B) glass microbands. In each of these figures, a PAC to the glass neighboring the IAME is also included (pure insulator). 149

Figure 6.11. (A) A schematic illustration of the redox cycling occurring at the IAME when the SECM probe is over the insulating glass microband. The Pt UME acts as the electron generator while the Pt microband acts as an electron collector. (B) and (C) are the concentration maps of the UME over the direct center of a Pt and glass microband, respectively. 150

Figure 6.12. (A) The SECM depth scan image of the IAME with the two vertical cross-sections labelled as detected by a 4.4 μm Pt UME (RG3). The PACs illustrated in (B) and (C) corresponds to the vertical cross-sections taken beside the microbands (red and blue respectively in (A)) overlaid onto theoretical curves generated at the same distances relative to the microbands. 152

Figure 6.13. (A) The simulated 3D current maps of a 4.4 μm UME approach towards a fixed IAME sample with the experimental horizontal sweep tilted at 0.76° overlaid directly on top (red curve). (B) The 3D mapping of a tilted IAME sample (0.75°) with the experimental horizontal sweep overlaid directly on top (red curve). 153

List of Appendices

Appendix I. Chapter 1: Introduction.....	168
Appendix II. Chapter 2: Determining Live Cell Topography by Scanning Electrochemical Microscopy.....	169
Appendix III. Chapter 3: A Time Course Study of Cadmium Effect on Membrane Permeability of Single Human Bladder Cancer Cells Using Scanning Electrochemical Microscopy.....	200
Appendix IV. Chapter 4: Probing Cd ²⁺ -Stressed Live Cell Membrane Permeability with Various Redox Mediators in Scanning Electrochemical Microscopy.....	223
Appendix V. Chapter 5: Zn ²⁺ -Induced Apoptosis in Single Human Bladder Cancer Cells Interrogated by Scanning Electrochemical Microscopy:	232
Appendix VI. Chapter 6: Scanning Electrochemical Microscopy with Laser-Pulled Submicron Pt Probes	234

List of Abbreviations

Abbreviation	Definition
A	Amperes or Amps
<i>a</i>	Radius of electrode
Abs	Absorbance
CE	Counter/auxiliary electrode
COS-7	Monkey kidney cells
CV	Cyclic voltammetry or cyclic voltammogram
D	Diffusion coefficient (m ² /s)
<i>d</i>	Tip-to-sample distance
DMSO	Dimethyl sulfoxide
DNA	Deoxyribonucleic acid
EDTA	Ethylenediaminetetraacetic acid
F	Faraday constant (96,485 C/mol)
FBS	Fetal bovine serum
Fc	Ferrocene
Fc ⁺	Ferrocenium cation
FcCH ₂ OH	Ferrocenemethanol
FcCOO ⁻	Ferrocenecarboxylate anion

FcCOOH	Ferrocenecarboxylic acid
Fc(COO) ₂ ²⁻	1,1'-ferrocene dicarboxylate anion
Fc(COOH) ₂	1,1'-ferrocene dicarboxylic acid
FEA	Finite elemental analysis (finite elemental method)
FEM	Finite elemental method (finite elemental analysis)
FIB	Focused ion beam
GSH	Glutathione
GSSG	Glutathione disulfide
HeLa	Human cervical cancer cells
I	Normalized current
<i>i</i> _∞	Steady state (bulk) current
IAME	Independently addressable microband electrodes
<i>iR</i>	resistivity
<i>i</i> _{ss}	Steady state current
I _T	Normalized current
KCl	Potassium chloride
L	Normalized distance
MTT	3-(4,5-dimethylthiazol-2-yl)-2,5-diphenyltetrazolium bromide
N	Number of individual cell measurements
<i>n</i>	Number of electrons transferred in the redox reaction

NE	Nanoelectrode
O	Oxidized species
PAC	Probe approach curve
PBS	Phosphate buffered saline
<i>Pm</i>	Membrane permeability coefficient
R	Reduced species
RSD	Relative standard deviation
RE	Reference electrode
RG	The ratio of the glass sheathing radius to the conductive wire radius
RNS	Reactive nitrogen species
ROS	Reactive oxygen species
$\text{Ru}(\text{NH}_3)_6^{3+}$	Hexaaminetruthenium(III) cation
$\text{Ru}(\text{NH}_3)_6\text{Cl}_3$	Hexaamineruthenium trichloride
σ	Standard deviation
SDS	Sodium dodecyl sulfate
SE	Standard error
SECM	Scanning electrochemical microscopy
SEM	Scanning electron microscopy
SNOM	Scanning near-field optical microscopy
SPM	Scanning probe microscopy

T24 cells	Human bladder cancer cells
TEM	Transmission electron microscopy
UME	Ultramicroelectrode
WE	Working electrode

Chapter 1

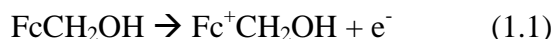
1 Introduction

1.1 Background of SECM

Scanning electrochemical microscopy (SECM), a member of the scanning probe microscopy (SPM) family, was first introduced in the late 1980s by the Bard¹⁻² and Engstrom³⁻⁴ Research Groups. Since then, SECM has been greatly developed by the Bard Lab and many other scientific researchers within many interdisciplinary fields, with applications ranging from chemical to biological studies.^{1, 3-14} SECM has since emerged as a powerful electroanalytical technique that has found applications in kinetic studies, chemical activity imaging and microfabrications. Within the last decade, peer-reviewed scientific reports have been averaging over a hundred publications a year and over two thousand articles, including reviews^{10-11, 15-16} and textbooks,⁵ have been published overall.

1.2 SECM Principles

The electrochemical signals and lateral resolution of SECM are directly dependent on the probes employed. Ultramicroelectrodes (UMEs), electrodes with a radius, a , on the order of a few nm to 12.5 μm , are used as the probes in this technique.^{6, 11} By using probes of these sizes, the steady state redox currents can be quickly obtained ($\sim a^2/D$, where D is the diffusion coefficient of the redox mediator) and resistive drops (iR) in solution during the passage of current are negligible, since the current is small (typically on the order of nA to pA range).^{5, 10} Figure 1.1A shows a cyclic voltammogram (CV) of 0.9 mM ferrocenemethanol (FcCH_2OH) with 0.1 M KCl supporting electrolyte in deionized water, collected using a 25 μm Pt UME. Upon sufficient potential bias, the one electron oxidation reaction of FcCH_2OH occurs:



This results in a steady state oxidative current at applied potentials greater than 0.20 V (vs. Ag/AgCl). In this plateau region, the conversion (or consumption) of FcCH_2OH in the

vicinity of the UME tip is converted directly to $\text{Fc}^+\text{CH}_2\text{OH}$ in a diffusion-controlled manner (eqn 1.1).

When these biased probes are several tip radii distances away from a substrate (or sample), the mass transport of the redox mediator from the bulk solution replenishes any FcCH_2OH consumed at the tip (Figure 1.1A). In other words, the resulting current is controlled by the mass transfer rate of diffusion of the electroactive species from the bulk solution towards the electrode surface. This diffusion layer is described as hemispherical in nature and the steady state current (i_{ss}) for a planar disk electrode with a large glass sheath can be described by:⁵

$$i_{ss} = 4nFDac \quad (1.2)$$

where n is the number of electrons transferred in the redox reaction, F is the Faraday constant (96,485 C/mol), and c is the concentration of the electroactive species. The steady-state current for other tip shapes, such as spherical or hemispherical, can be defined similarly.⁵

As the biased SECM probe approaches a sample, the feedback current becomes influenced by the sample's electrically conductive or insulating properties. Hemispherical diffusion of the mediator from the bulk solution to electrode tip becomes partially hindered by the sample and the feedback current will deviate from steady state depending on the electrical properties of the sample. This is often characterized in the form of probe approach curves (PACs), where the normalized current (I) is plotted against the normalized distance (L), eqns 1.3 and 1.4, respectively:

$$\text{Normalized Current, } I = \frac{i_t}{i_\infty} \quad (1.3)$$

$$\text{Normalized Distance, } L = \frac{\text{tip-to-sample distance, } d}{\text{electrode radius, } a} \quad (1.4)$$

For instance, Figure 1.1B shows a typical PAC of an SECM probe approaching a conductive substrate. When the probe is several tip radii away ($L > 4$), the steady state current is detected ($I \approx 1$). However, once the probe is in close proximity to the sample ($L < 2$), increased feedback current is detected ($I \gg 1$). This is due to the oxidized $\text{Fc}^+\text{CH}_2\text{OH}$

species (produced at the biased electrode tip) diffusing to the conductive sample, where it becomes reduced, regenerating the mediator. This rate of regeneration by the substrate will increase as the tip-to-sample distance is decreased. The reduced species can diffuse back to the electrode tip, where it can drive the reaction forward (eqn 1.1), contributing to increased feedback current (positive feedback, $I \gg 1$). If the sample is insulating, the resulting PAC will show a decrease in normalized current as the probe approaches the sample since reduction of the oxidized species cannot occur and hemispherical diffusion remains partially blocked by the sample ($I < 1$, Figure 1.1C). It is expected that the normalized tip current will reach 0 at a tip-to-sample distance of 0 ($L = 0$).

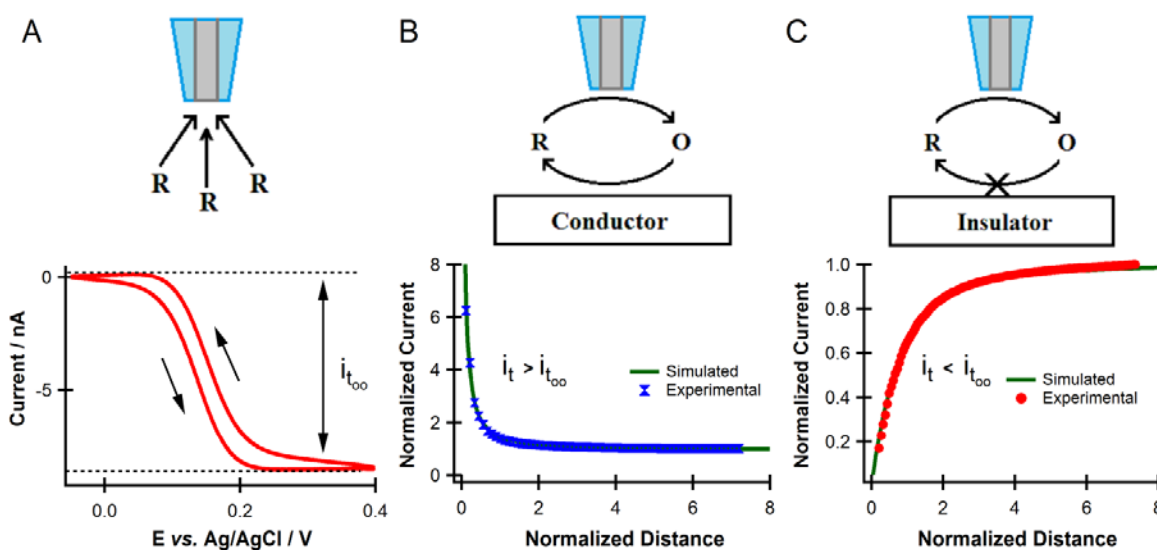


Figure 1.1. Principles of SECM illustrating (A) top: hemispherical diffusion of a reduced redox mediator from the bulk solution to the electrode tip, bottom: a CV of 0.90 mM FcCH₂OH with 0.100 M KCl in deionized water, (B) top: positive feedback between the electrode tip and conductive sample (redox cycling), bottom: the corresponding experimental and simulated PACs approaching a conductive sample and (C) top: illustration of negative feedback principle between the electrode tip and insulating sample, bottom: the corresponding experimental and simulated PACs approaching a non-conductive (insulating) sample. All data shown were collected with a 25 μm Pt UME (RG3).

1.3 Simulations

Quantitative SECM theory has been developed to allow treatments for both diffusion-controlled properties and finite kinetics.⁵ The first theoretical treatment of SECM data was reported by Kwak and Bard in 1989 using the finite element method (FEM).² These simulations solved the tip currents as the SECM probe approached a conductive or insulating substrate, similar to the simulated PACs presented in Figures 1.1B and C. Kwak and Bard demonstrated that the experimental PACs can be overlaid onto simulated curves, generated based on the experimental conditions, to quantify sample and electrode properties, such as the absolute tip-to-substrate distances and RG (ratio of insulating sheathing to conductive wire) effects on the UME.² For example, the experimental PACs obtained to a conductor and insulator shown in Figures 1.1B and C indicate a tip-to-sample distance of 1.41 μm ($L = 0.11$) and 2.69 μm ($L = 0.22$), respectively. Since 1989, the theory and FEM simulations of SECM have become well developed and are now systematic.^{2, 17-19} The theory of feedback mode of SECM was extended to include, but not limited to, finite heterogeneous electron transfer kinetics at microscopic substrates,²⁰ transient (chronoamperometric) feedback modes,¹⁹ and rate constants for irreversible heterogeneous processes.²⁰⁻²¹

In the Ding Lab, the FEM is used with SECM to solve for kinetic parameters, such as rate constants for reactive oxygen species evolution²²⁻²³ and membrane permeability in single live cells.²⁴⁻²⁵ These simulation models were generated using 2D axially symmetric geometry and coordinates system, which limits the SECM probe to a linear path of motion that is centered over a symmetric substrate. Simulations of asymmetric models were previously limited due to their high demand on computer resources, where memory utilization and long compute times restricted their use.²⁶⁻²⁷ However, progression into 3D modelling in FEM now allows simulations for the quantification of experimental off-axis PACs and horizontal sweeps.²⁶⁻²⁷

1.4 Modes of Operation for SECM

There are several modes of operation in SECM, the tip generation/substrate collection (TG/SC), substrate generation/tip collection (SG/TC) and feedback modes.^{5, 11} In the TG/SC mode, the tip is biased at a potential where a redox reaction occurs and the substrate is biased

at a different potential, where the product from the reaction at the tip drives the substrate reaction forward.²⁸ In most cases, the substrate is considerably larger than the tip, so the collection efficiency is essentially 1 ($i_{\text{substrate}}/i_{\text{tip}} = 100\%$).⁵ If the tip product does not diffuse directly to the substrate, this collection efficiency decreases and the determination of the rate constant of the homogenous reaction is possible. In the alternative mode, SG/TC, the substrate behaves as the generator and the tip is the collector (Figure 1.2B).

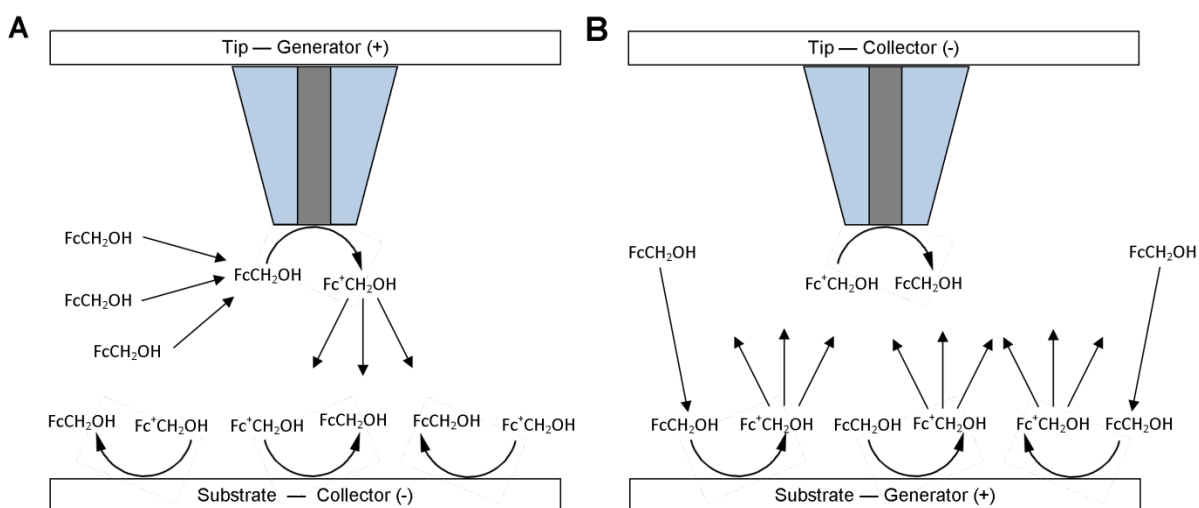


Figure 1.2. Schematic illustrations of the (A) tip generation/substrate collection (TG/SC) and (B) substrate generation/tip collection (SG/TC) modes of SECM.

In (A) the tip acts as the generator, where it is biased at a positive potential to drive the one electron oxidation reaction of FcCH₂OH to Fc⁺CH₂OH forward. The oxidized product Fc⁺CH₂OH can diffuse to the substrate, where it gets reduced back to FcCH₂OH. In (B) the substrate acts as the generator, oxidizing FcCH₂OH at its surface. The oxidized species can diffuse to the tip, where it becomes reduced. The consumption of FcCH₂OH at the (A) electrode tip and (B) substrate are replenished by the diffusion of the species from the bulk solution.

The most frequently used mode of operation of SECM is the feedback mode, where only the current of the biased tip is monitored. When in close proximity to a substrate, there is blockage of the hemispherical diffusion of the redox species to the tip (negative feedback, Figure 1.1C) or regeneration of the redox species by the substrate occurs (positive feedback, Figure 1.1B). This effectively allows investigation into both electrically insulating and

conducting surfaces, as well as the reactions that occur there. In this dissertation, the feedback mode of SECM is used for all projects reported within.

1.5 Conventional Imaging Modes of SECM

Conventionally, most research groups use one of two SECM imaging modes: the constant height or constant distance modes, which utilize the feedback mode of SECM (Figure 1.3). In the traditional constant height mode, the biased probe is held at a constant tip-to-sample distance and is scanned along the sample surface in an x - y sweep to electrochemically study its topography and properties (Figure 1.3A). However, one major drawback of this method is the convolution of the faradaic processes and the probe-to-sample distance effects if there is an uneven sample surface. It is possible that the variations in the sample topography may influence the current changes observed in the SECM image. There is also risk that the probe may crash against an uneven sample, which can lead to unwanted tip or sample damage. To overcome the inherent shortcomings of the constant height mode, the constant distance mode was developed (Figure 1.3B).⁵ In this mode, the probe will maintain a constant distance from the sample, moving up or down accordingly to maintain a constant normalized current. This allows deconvolution of the varying sample heights through the faradaic processes. These two imaging modes produce a current map in the x - y plane (Figure 1.4A).

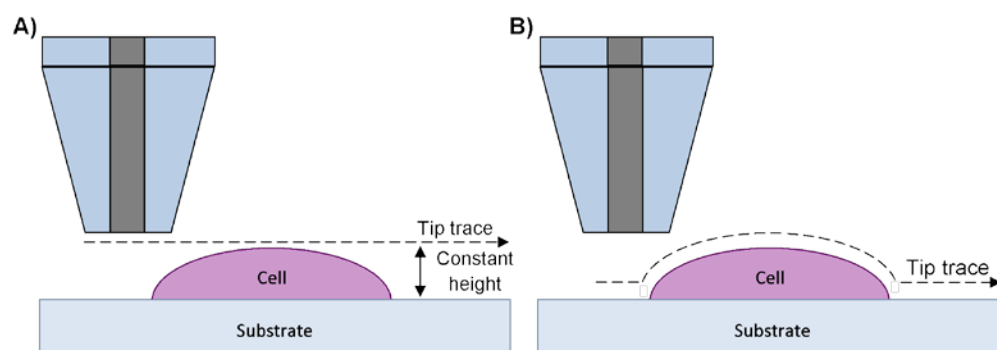


Figure 1.3. The schematic illustrations of the SECM operating in the (A) constant height and (B) constant distance modes. In constant height mode, the probe is scanned at a fixed height relative to the z -axis of the positioning system, while the probe in constant distance mode will be scanned to maintain a constant normalized current and therefore tip-to-sample distance. The dotted line represents the probe's scan path.

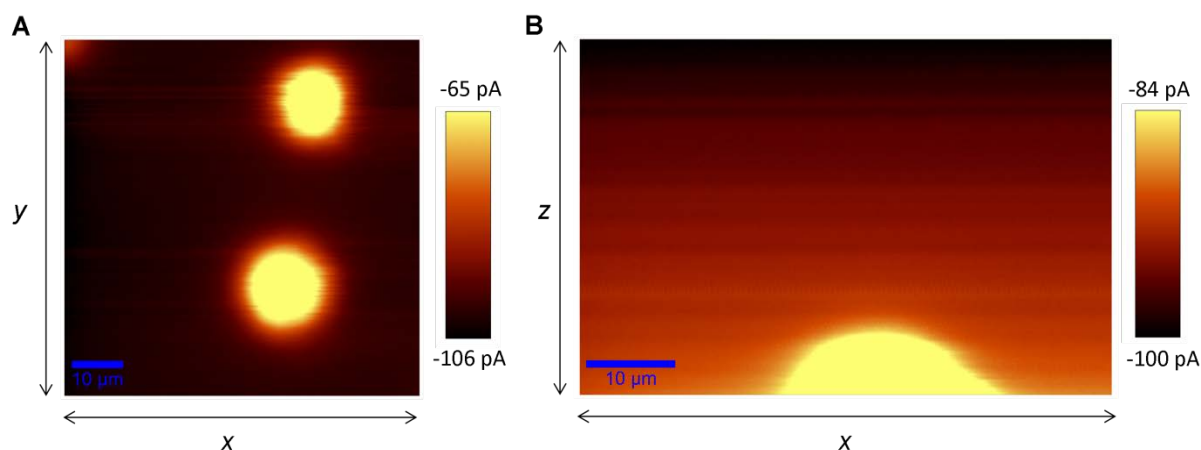


Figure 1.4. SECM current map images of T24 cells collected using the (A) constant height and (B) depth scan imaging modes.

An alternative to the conventional SECM imaging methods is the depth scan mode, which was developed and is frequently used by the Ding Lab (Figure 1.4B).^{22-23, 29} In this mode, the probe performs a series of horizontal line scans in the x direction, where with each consecutive line scan, the probe is moved in the z direction to minimize the tip-to-sample distance. This mode generates a current map in the x,z -plane in real-time. The visualization of the SECM probe's approach can allow the experimentalist to prevent a potential collision between the probe and sample based on the current detection at the electrode tip. In addition, since each pixel in the SECM image is comprised of both the tip current and its x,z coordinates, multiple PACs and horizontal line scans can be analyzed after the collection of a single image. In combination with FEM, this allows quantification of sample properties.

1.6 SECM Instrumental Setup

SECM instrumentation consists of three main components: (i) the electrochemical system, (ii) a precise positioning system and (iii) the data acquisition system (Figure 1.5). The electrochemical system is comprised of a low current electrochemical analyzer (e.g. bipotentiostat) that is employed to control and monitor the applied potential and faradaic current at the probe and/or substrate. As a member of the SPM family, a precise positioning system is employed to control the SECM probe's movements since high spatial resolution is required. Often, the movement of the probes is governed by inchworm motors or piezoelectric positioners. Initially, inchworm motors were used to control the movement of

the probe, which is created through the sequential activation of three piezo components where the outer two piezo elements act as clamps and the central piezo element expands and contracts along the motor shaft when voltage is applied. Most modern SECM instruments utilize a piezoelectric scanners; the electromechanical device undergoes a dimensional change when voltage is applied. These precise positioning systems offer the high spatial resolution, on the order of submicron scale, when the SECM probe is scanned across a sample. A computer with a data acquisition system is utilized to control the three components, while collecting and compiling the experimental data from all sources. In addition to these three components, SECM instruments are often placed within a Faraday cage, provided with electrical isolation and common grounding, and placed on a vibration-free optical table to avoid electromagnetic noises and environmental vibration.^{5, 30}

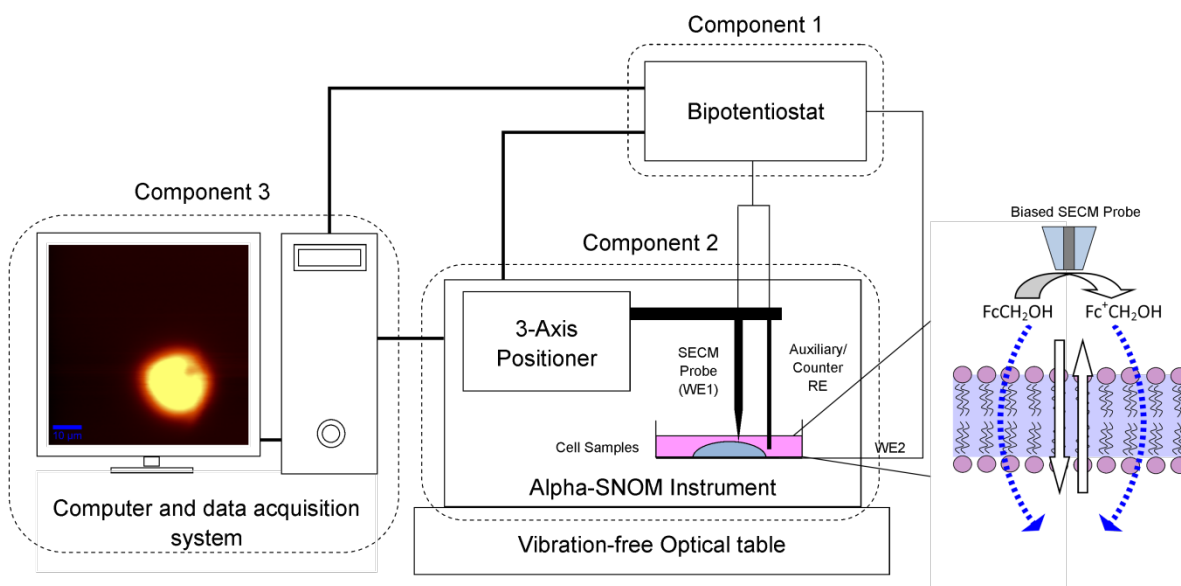


Figure 1.5. A schematic illustration of the SECM setup used throughout this dissertation with the 3 components identified: (1) the electrochemical system, (2) a precise positioning system and (3) the data acquisition system.

For this dissertation, an electrochemical analyzer with a picoamp booster is used to monitor electrochemical response (Component 1). The piezoelectric positioning stage and piezo-stepper motors of an Alpha-SNOM instrument were used to control the movement of the

probe and samples (Component 2). A computer holds the data acquisition system which controls the SECM components and records the experimental data (Component 3).

1.7 Ultramicroelectrodes

These probes are fabricated with a conductive wire (typically noble metal) or fiber that is sheathed with insulating material, such as glass or plastic. The detailed fabrication procedure of UMEs has been reported by many electrochemistry groups.³¹⁻³⁵ Briefly, there are four main steps in their fabrication: (1) a conductive wire (or fiber) is heat-sealed in a pulled glass capillary, (2) the extension of the internal electrical connections, (3) the tip is manually polished to expose the wire (or fiber) and (4) the glass sheathing is polished to reduce its tip diameter to maintain a RG between 2-10. There are several key advantages offered by maintaining these RG ratios, such as electrode tilt during experimentation becomes less of a concern, which can reduce the chances of physical collision with the sample, and smaller tip-to-sample distances can be reached.

1.8 Application of SECM

Since this dissertation focuses mainly on the use of SECM to the study the membrane response in live cells, herein, the focus will be on the biological applications of SECM. In this regard, SECM offers several unique advantages over other bioanalytical techniques. For instance, SECM provides non-invasive and non-destructive investigations on biological samples. It is also possible to maintain the physiological temperature and pH (buffered solutions) requirements of the samples, preventing external environmental stimulation. SECM also provides the ability to study singular cells, in addition to cell monolayers and tissues, due to the small probe size required in SECM studies.⁵ There exists a wide selection of redox mediators that can be used in SECM, allowing a range of different sample characteristics to be assessed. This permits the experimentalist to study a particular response in the biological samples, such as membrane integrity in cells, without mediator-induced toxicity.³⁶

In biological studies, SECM can be used to: 1) quantify the flux of molecules across the cell membrane, 2) probe the local electrochemical reactions occurring at or inside cells,

and 3) perform repeated or multiple measurements on biological samples due to its non-invasive nature.^{7-8, 12, 37} These studies have included, but are not limited to, investigations of electron transfer kinetics,³⁸⁻³⁹ molecular transport,⁴⁰ neurotransmitter release,⁴¹⁻⁴² reactive oxygen^{23, 43-46} or nitrogen species release⁴⁴ and assessment of drug resistance in biological cells.^{8, 23, 47-48}

For instance, Liebetrau *et al.* were able to use SECM to monitor the morphological changes in PC12 cells after initiating neuronal differentiation with nerve growth factor.⁴¹⁻⁴² The high resolution of SECM allowed morphological changes, such as neurite extensions from the cell bodies to be detected in real time, which were not identifiable by light-based microscopy.⁴¹⁻⁴² The Suzuki Group has also reported a similar study where the neurite imaging of living PC12 cells in a hybrid SECM/near-field scanning optical microscopy (NSOM)/atomic force microscopy (AFM) techniques.⁴⁹ Using their SECM/NSOM/AFM system, improved resolution imaging, such that varicosity-like structures and the distribution of Ca²⁺ located at the neurite extensions, were now possible.⁴⁹

Other groups have used SECM to monitor the extracellular and intracellular responses of live cells upon chemical stimulation or with the redox mediator themselves. For example, the Schuhmann Group has used SECM to monitor the release of nitric oxide from single transformed human umbilical vein endothelial cells upon stimulation with bradykinin,⁵⁰⁻⁵² as well as neurotransmitters (catecholamines, adrenaline, noradrenaline and dopamine) after PC12 cells were stimulated with K⁺.⁵³ In the Ding Group, extracellular reactive oxygen species (ROS) have been used as a label free SECM mediator.^{22, 54-55} The sensitivity and selectivity offered by this electrochemistry technique allows for ROS quantification in single cells by SECM (Figure S1.1 in Appendix I). The effects of cadmium-induced stress on plant cells have also been investigated through the release of these species from the stoma.⁴³ Specifically, the number of stoma and ROS release in cadmium-treated plants decreased. Since cancer cells reportedly have higher levels of ROS,⁵⁶ the Ding Lab has used these species as a means to investigate the effectiveness of anti-cancer drugs (cisplatin)²³ and bacterial-induced (*Escherichia coli*) effects on cancer cells.⁵⁵

The Mirkin Group used SECM to distinguish between non-metastatic and metastatic breast cells based on their redox reactivity with the SECM mediators.⁵⁷⁻⁶¹ From their studies, the Mirkin Group was able to identify bimolecular reactions between the extracellular redox species in solution and intracellular redox moieties in the cells as a contributing factor to mediator regeneration at the UME tip.⁵⁷ They were also able to recognize diffusion of the redox species through live cells as one of the possible contributing factors to mediator regeneration at the UME tip.⁵⁷ The Amemiya Group confirmed that the passive transport of redox molecules across the permeable double-membraned nuclear envelope of *Xenopus laevis* oocytes were limited by the rate of diffusion across the membrane.⁶²

Using SECM mediators, $\text{IrCl}_6^{2-/3-}$ and $\text{Fe}(\text{CN})_6^{4-/3-}$, the Shao Group were able to gain insight into the interactions between Ag nanoparticles and human cervical cancer (HeLa) cells.⁶³ The mediator IrCl_6^{2-} , which can be produced *in situ*, can react with the Ag nanoparticles on the HeLa cells, while $\text{Fe}(\text{CN})_6^{4-}$ cannot. Since $\text{Fe}(\text{CN})_6^{4-}$ remained impermeable to HeLa cells with Ag nanoparticles deposited on them, the researchers demonstrated that the kinetic rate constants between IrCl_6^{2-} and the Ag nanoparticles on the HeLa cells could be evaluated by SECM. Similarly, the Bard Group investigated Ag^+ uptake in bacterial and mammalian cells by SECM.⁶⁴⁻⁶⁶ Zhan, Fan and Bard demonstrated that Ag^+ uptake can be enhanced by 4-aminopyridine, a voltage sensitive potassium channel blocker.⁵⁶ Using SECM, the researchers found that the uptake rate in 3T3 fibroblast cells increased from 4.8×10^7 ions/cell·s to 1.0×10^8 ions/cell·s (0.2 mM 4-aminopyridine) and 1.5×10^4 ions/cell·s to 3.5×10^4 ions/cell·s (0.5 mM 4-aminopyridine) in *Escherichia coli* cells.

Koley and Bard demonstrated that SECM can be used to monitor changes in cell morphology, membrane permeability and viability in HeLa cells after their exposure to Triton X-100, a nonionic surfactant.³⁶ Upon exposure, the HeLa cells were reported to undergo irreversible permeabilization of the cell membrane and structural collapse. The infiltration of a hydrophilic redox mediator, $\text{Fe}(\text{CN})_6^{4-}$, into the cell provided insight into the viability of individual HeLa cells and additional quantitative information on the cell membrane permeability.³⁶ Utilizing the relationship between the redox mediator and membrane permeability, the Mauzeroll Group has demonstrated that SECM can be used to investigate multidrug resistance-associated protein 1 (MRP1), which is overexpressed in

cancer cells.^{47-48, 67} Specifically, SECM confirmed the interaction between the redox mediator, FcCH₂OH and the cells, was dependent on the expression of MRP1. SECM has since shown great promise as a technique in studying the effects of toxins and anti-cancer drugs on cells through the induction of membrane permeability.^{36, 68-70}

1.9 SECM Study on Single Live Cells

In SECM studies on single live cells, three types of measurements are most widely used: (i) SECM imaging of the cells in which the current is measured and mapped as a function of probe coordinates (often *x-y* plane), revealing the electrochemical topography of the adhered cells^{45-46, 71-72} and/or the spatial profile of extracellular redox active species;^{22, 45-46, 55, 73-74} (ii) PACs are used to quantitatively determine kinetic parameters⁷⁵⁻⁷⁶ of a redox-active species across the cell membrane,^{36, 62, 72, 77} and (iii) current-time curves (chronoamperometry) at specific tip-to-cell distances to study the evolutionary trend of cellular topography,⁷⁴ reactivity,⁷⁸ monitoring very fast bursts of redox active species released by cells⁷⁸⁻⁷⁹ and membrane permeability studies of single live cells.³⁶

1.10 SECM Membrane Permeability

The choice of redox mediators in SECM live cell experiments is crucial, since it can provide insight into cell membrane properties. Redox mediators that are hydrophilic and charged, e.g. hexaamineruthenium(III) (Ru(NH₃)₆³⁺),⁸⁰ ferrocenecarboxylate (FcCOO⁻)⁵⁷ and ferrocyanide (Fe(CN)₆⁴⁻),^{36, 63} have been confirmed to be impermeable to healthy and intact cells through several biology-based techniques, including SECM (insulator, negative feedback).^{36, 66} Therefore, the permeation of these hydrophilic and charged species by SECM (partially positive feedback, Figure 1.6) signifies substantial membrane integrity loss, such as pore formation or structural collapse of the cell membrane.³⁶ On the other hand, water soluble mediators exhibiting more oleophilic properties (membrane-permeable), such as ferrocenemethanol (FcCH₂OH),^{47, 66, 80} 1,2-naphthaquinone (C₁₀H₆O₂),⁵⁷ and menadione (C₆H₄(CO)₂C₂H(CH₃))^{57, 81} can be used to monitor more subtle changes in the cell membrane than that of the hydrophilic and charged redox mediators.

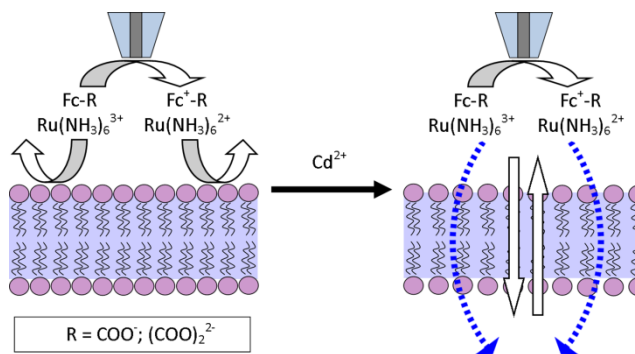


Figure 1.6. Schematic illustration of increased membrane permeability to hydrophilic redox mediators, FcCOO^- , $\text{Fc}(\text{COO})_2^{2-}$ and $\text{Ru}(\text{NH}_3)_6^{3+}$ after treatment with Cd^{2+} .

1.11 Exposure to Heavy Metals

Cells exposed to toxic heavy metals are known to incur membrane integrity loss,⁸²⁻⁸³ membrane permeability changes,⁸⁴⁻⁸⁵ and cellular death.^{82-83, 86} Dyes, such as, propidium iodide⁸² or trypan blue,⁸⁷ can provide insight into the membrane integrity and cellular viability since these dyes cannot permeate healthy cells. Unfortunately, these methods tend to be destructive and cannot give quantification from a singular cell standpoint. Therefore, it becomes ideal to use the non-invasive SECM technique to investigate the effects of the heavy metals exposure on single live cells through membrane permeability studies. This will provide both insights into the membrane integrity in single live cells, as well as quantification of the membrane permeability coefficient to the redox mediator.

1.12 Human Bladder Cancer (T24) Cells

Experimental studies on laboratory animals have demonstrated that the presence of the toxic heavy metal cadmium (Cd^{2+}) can be confirmed through the analysis of their urinary excretion. This commonly represents 0.01-0.02 % of the total body burden upon long-term exposure.⁸⁸ Similarly in humans, Cd^{2+} is often detected through its presence in urinary excretion which indicates approximately 0.01% of the total body burden.⁸⁹ Therefore, it becomes attractive to use the bladder as the basis of the experimental (model) system as a means to study the effects of toxic heavy metals. In particular, the induced cellular membrane responses in single, live human bladder cancer (T24) cells (ATCC[®] HTB-4[™]), were investigated by SECM. This cell line was selected since the bladder is one of several

organs in which heavy metals may bioaccumulate, as well as a key organ that is involved in their excretion from the body.⁸⁸⁻⁸⁹

In addition, the use of a cell line as the experimental (model) system is cost-effective, while providing a large supply of cells of similar genotypes and phenotypes.⁹⁰ Human cancer cell lines also retain the hallmarks of the original cancer, while the pure population of cells can provide more reproducible results across numerous passages when identical protocols are used.⁹¹ In addition, there becomes no ethical concern associated with their use, unlike those implicated in animal or human studies. The use of this cell line as a model system provides an effective means to investigate the heavy metal induced membrane changes by SECM.

1.13 Scope of Dissertation

The scope of this dissertation focuses on the investigation of the cell membrane responses in single live human bladder cancer (T24) cells before and after their exposure to heavy metals.

Firstly, Chapter 2 focuses on the use of SECM to investigate the cellular topography of T24 cells in the absence of any heavy metal treatment. Using the membrane-impermeable redox mediator, FcCOO⁻, the cellular geometry and topography was confirmed through three approaches. The first method is the more traditional approach which compared two different PACs, one to the cell's center and another to the petri dish next to the cell, while the second approach relied on the direct fitting of a PAC to the center of the cell to simulated curves towards cells of varying heights. A 3D simulation model was also used to quantify cellular topography across the cell to confirm cellular geometry.

Cd²⁺, a toxic heavy metal, is well known to cause detrimental effects in living organisms, such as the membrane integrity loss in cells and cellular death. Chapter 3 focuses on the use of time-lapsed SECM to monitor the membrane permeability changes in T24 cells after their exposure to acute (1-10 mM) Cd²⁺. This response was further investigated in Chapter 4, using membrane-impermeable redox mediators, FcCOO⁻, Fc(COO)₂²⁻ and Ru(NH₃)₆³⁺. The successful permeation of these redox mediators into T24 cells after both low (25 μM, t ≤ 6 hrs) and acute (0-5 mM, t = 1 hr) Cd²⁺ exposure, confirmed a loss in the

membrane integrity of these cells. This weakening of the membrane integrity identified through the permeation of these SECM mediators was correlated to a decrease in the cellular viability by the MTT cell proliferation assay. This directly linked the membrane permeability changes in SECM to Cd^{2+} -induced cellular death.

Following these studies on the toxic metal Cd^{2+} , Chapter 5 focuses on the effects of the trace essential metal, zinc (Zn^{2+}) on membrane permeability. SECM revealed minimal effects on the membrane permeability to redox mediators, FcCH_2OH and $\text{Ru}(\text{NH}_3)_6^{3+}$ after treatment to 0-75 μM Zn^{2+} (24 hrs). Exceeding this concentration range, the role of Zn^{2+} was no longer therapeutic or essential, but toxic, which is evident based on the increased permeability to the redox mediators. This loss in membrane integrity correlated to a Zn^{2+} -induced cellular death process. Due to the treatment length and SECM results, it was hypothesized the cellular death pathway was apoptosis. Through complementary biological techniques, such as cellular viability assays, flow cytometry, and immunofluorescence, both Zn^{2+} -induced cellular death and apoptosis as the primary mechanism was confirmed. This Chapter demonstrates the powerful nature of SECM, which can be used to assist in the identification of a cellular death mechanism.

Chapter 6 focuses on the fabrication of nanometer-sized SECM probes designed to improve the resolution of the SECM in the Ding Lab. The development of this fabrication method yielded SECM probes that had thousand times reduction in Pt diameter size. Successful FEM simulations using 3D model geometry was also completed. This allowed a more in depth analysis of the 2D SECM data set, which was previously limited to 2D axially symmetric models. This advancement allowed investigation into the effects of redox cycling between the alternating insulating glass and conductive microbands of an independently addressable microband electrodes sample and SECM probes, one significantly smaller and one similar in size to the bands (250 nm and 4.4 μm probes).

Finally, Chapter 7 provides a collective summary to the aforementioned work, as well as future works to be considered.

1.14 References

1. Bard, A. J.; Fan, F.-R. F.; Kwak, J.; Lev, O., Scanning Electrochemical Microscopy. Introduction and Principles. *Anal. Chem.* **1989**, *61*, 132-138.
2. Kwak, J.; Bard, A., Scanning Electrochemical Microscopy. Theory of the Feedback Mode. *Anal. Chem.* **1989**, *61*, 1221-1227.
3. Engstrom, R. C.; Weber, M.; Wunder, D. J.; Burgess, R.; Winkquist, S., Measurements within the Diffusion Layer Using a Microelectrode Probe. *Anal. Chem.* **1986**, *58*, 844-848.
4. Engstrom, R. C.; Meaney, T.; Tople, R.; Wightman, R. M., Spatiotemporal Description of the Diffusion Layer with a Microelectrode Probe. *Anal. Chem.* **1987**, *59*, 2005-2010.
5. Bard, A. J.; Mirkin, M. V., *Scanning Electrochemical Microscopy*; Marcel Dekker: New York, 2001.
6. Amemiya, S.; Bard, A. J.; Fan, F.-R. F.; Mirkin, M. V.; Unwin, P. R., Scanning Electrochemical Microscopy. *Annu. Rev. Anal. Chem.* **2008**, *1*, 95-131.
7. Bergner, S.; Vatsyayan, P.; Matysik, F. M., Recent Advances in High Resolution Scanning Electrochemical Microscopy of Living Cells - A Review. *Anal. Chim. Acta* **2013**, *775*, 1-13.
8. Beaulieu, I.; Kuss, S.; Mauzeroll, J.; Geissler, M., Biological Scanning Electrochemical Microscopy and Its Application to Live Cell Studies. *Anal. Chem.* **2011**, *83*, 1485-1492.
9. Torisawa, Y. S.; Kaya, T.; Takii, Y.; Oyamatsu, D.; Nishizawa, M.; Matsue, T., Scanning Electrochemical Microscopy-Based Drug Sensitivity Test for a Cell Culture Integrated in Silicon Microstructures. *Anal. Chem.* **2003**, *75*, 2154-2158.
10. Polcari, D.; Dauphin-Ducharme, P.; Mauzeroll, J., Scanning Electrochemical Microscopy: A Comprehensive Review of Experimental Parameters from 1989 to 2015. *Chem. Rev.* **2016**, *116*, 13234-13278.
11. Zoski, C. G., Review - Advances in Scanning Electrochemical Microscopy (SECM). *J. Electrochem. Soc.* **2015**, *163*, H3088-H3100.
12. Schulte, A.; Schuhmann, W., Single-Cell Microelectrochemistry. *Angew. Chem. Int. Ed.* **2007**, *46*, 8760-8777.
13. Schulte, A.; Nebel, M.; Schuhmann, W., Scanning Electrochemical Microscopy in Neuroscience. *Annu. Rev. Anal. Chem.* **2010**, *3*, 299-318.

14. Zhao, C.; Wittstock, G., An SECM Detection Scheme with Improved Sensitivity and Lateral Resolution: Detection of Galactosidase Activity with Signal Amplification by Glucose Dehydrogenase. *Angew. Chem. Int. Ed.* **2004**, *43*, 4170-4172.
15. Ebejer, N.; Guell, A. G.; Lai, S. C.; McKelvey, K.; Snowden, M. E.; Unwin, P. R., Scanning Electrochemical Cell Microscopy: A Versatile Technique for Nanoscale Electrochemistry and Functional Imaging. *Annu. Rev. Anal. Chem.* **2013**, *6*, 329-351.
16. Mirkin, M. V., Peer Reviewed: Recent Advances in Scanning Electrochemical Microscopy. *Anal. Chem.* **1997**, *68*, 177A-182A.
17. Unwin, P. R.; Bard, A. J., Scanning Electrochemical Microscopy. 9. Theory and Application of the Feedback Mode to the Measurement of Following Chemical Reaction Rates in Electrode Processes. *J. Phys. Chem.* **1991**, *95*, 7814-7824.
18. Mirkin, M. V.; Yang, H.; Bard, A. J., Borohydride Oxidation at a Gold Electrode. *J. Electrochem. Soc.* **1992**, *139*, 2212-2217.
19. Bard, A. J.; Denuault, G.; Friesner, R. A.; Dornblaser, B. C.; Tuckerman, L. S., Scanning Electrochemical Microscopy: Theory and Application of the Transient (Chronoamperometric) SECM Response. *Anal. Chem.* **1991**, *63*, 1282-1288.
20. Bard, A. J.; Mirkin, M. V.; Unwin, P. R.; Wipf, D. O., Scanning Electrochemical Microscopy. 12. Theory and Experiment of the Feedback Mode with Finite Heterogeneous Electron-Transfer Kinetics and Arbitrary Substrate Size. *J. Phys. Chem.* **1992**, *96*, 1861-1868.
21. Oleinick, A.; Yu, Y.; Svir, I.; Mirkin, M. V.; Amatore, C., Theory and Simulations for the Electron-Transfer/Ion-Transfer Mode of Scanning Electrochemical Microscopy in the Presence or Absence of Homogenous Kinetics. *ChemElectroChem* **2017**, *4*, 287-295.
22. Zhao, X.; Zhang, M.; Long, Y.; Ding, Z., Redox Reactions of Reactive Oxygen Species in Aqueous Solutions as the Probe for Scanning Electrochemical Microscopy of Single Live T24 Cells. *Can. J. Chem.* **2010**, *88*, 569-576.
23. Zhang, M. M. N.; Long, Y.-T.; Ding, Z., Cisplatin Effects on Evolution of Reactive Oxygen Species from Single Human Bladder Cancer Cells Investigated by Scanning Electrochemical Microscopy. *J. Inorg. Biochem.* **2012**, *108*, 115-122.
24. Koley, D.; Bard, A. J., Inhibition of the MRP1-Mediated Transport of the Menadione-Glutathione Conjugate (Thiodione) in HeLa Cells as Studied by SECM. *Proc. Natl. Acad. Sci. U. S. A.* **2012**, *109*, 11522-11527.
25. Zhang, M.-N.; Ding, Z.; Long, Y.-T., Sensing Cisplatin-Induced Permeation of Single Live Human Bladder Cancer Cells by Scanning Electrochemical Microscopy. *Analyst* **2015**, *140*, 6054-6060.

26. Filice, F. P.; Li, M. S. M.; Henderson, J. D.; Ding, Z., Three-Dimensional Electrochemical Functionality of an Interdigitated Array Electrode by Scanning Electrochemical Microscopy. *J. Phys. Chem. C* **2015**, *119*, 21473-21482.
27. Filice, F. P.; Li, M. S. M.; Henderson, J. D.; Ding, Z., Mapping Cd²⁺-Induced Membrane Permeability Changes of Single Live Cells by Means of Scanning Electrochemical Microscopy. *Anal. Chim. Acta* **2016**, *908*, 85-94.
28. Zoski, C. G.; Liu, B.; Bard, A. J., Scanning Electrochemical Microscopy: Theory and Characterization of Electrodes of Finite Conical Geometry. *Anal. Chem.* **2004**, *76*, 3646-3654.
29. Zhao, X.; Diakowski, P.; Ding, Z., Deconvoluting Topography and Spatial Physiological Activity of Live Macrophage Cells by Scanning Electrochemical Microscopy in Constant-Distance Mode. *Anal. Chem.* **2010**, *82*, 8371-8373.
30. Wipf, D. O., Scanning Electrochemical Microscopy. In *Encyclopedia of Imaging Science and Technology*, John Wiley & Sons, Inc.: 2002.
31. Danis, L.; Polcari, D.; Kwan, A.; Gateman, S. M.; Mauzeroll, J., Fabrication of Carbon, Gold, Platinum, Silver, and Mercury Ultramicroelectrodes with Controlled Geometry. *Anal. Chem.* **2015**, *87*, 2565-2569.
32. Mauzeroll, J.; Hueske, E. A.; Bard, A. J., Scanning Electrochemical Microscopy. 48. Hg/Pt Hemispherical Ultramicroelectrodes: Fabrication and Characterization. *Anal. Chem.* **2003**, *75*, 3880-3889.
33. Zoski, C. G., Ultramicroelectrodes: Design, Fabrication, and Characterization. *Electroanalysis* **2002**, *14*, 1041-1051.
34. Holt, K. B.; Hu, J.; Foord, J. S., Fabrication of Boron-Doped Diamond Ultramicroelectrodes for Use in Scanning Electrochemical Microscopy Experiments. *Anal. Chem.* **2007**, *79*, 2556-2561.
35. Liu, B.; Rolland, J. P.; DeSimone, J. M.; Bard, A. J., Fabrication of Ultramicroelectrodes Using a "Teflon-Like" Coating Material. *Anal. Chem.* **2005**, *77*, 3013-3017.
36. Koley, D.; Bard, A. J., Triton X-100 Concentration Effects on Membrane Permeability of a Single HeLa Cell by Scanning Electrochemical Microscopy (SECM). *Proc. Natl. Acad. Sci. U. S. A.* **2010**, *107*, 16783-16787.
37. Cortes-Salazar, F.; Momotenko, D.; Girault, H. H.; Lesch, A.; Wittstock, G., Seeing Big with Scanning Electrochemical Microscopy. *Anal. Chem.* **2011**, *83*, 1493-1499.
38. Nioradze, N.; Kim, J.; Amemiya, S., Quasi-Steady-State Voltammetry of Rapid Electron Transfer Reactions at the Macroscopic Substrate of the Scanning Electrochemical Microscope. *Anal. Chem.* **2010**, *83*, 828-835.

39. Cannan, S.; Cervera, J.; Steliaros, R. J.; Bitziou, E.; Whitworth, A. L.; Unwin, P. R., Scanning Electrochemical Microscopy (SECM) Studies of Catalytic EC [Prime or Minute] Processes: Theory and Experiment for Feedback, Generation/Collection and Imaging Measurements. *Phys. Chem. Chem. Phys.* **2011**, *13*, 5403-5412.
40. Matrab, T.; Hauquier, F.; Combellas, C.; Kanoufi, F., Scanning Electron Microscopy Investigation of Molecular Transport and Reactivity within Polymer Brushes. *ChemPhysChem* **2010**, *11*, 670-682.
41. Liebetrau, J. M.; Miller, H. M.; Baur, J. E.; Takacs, S. A.; Anupunpisit, V.; Garris, P. A.; Wipf, D. O., Scanning Electrochemical Microscopy of Model Neurons: Imaging and Real-Time Detection of Morphological Changes. *Anal. Chem.* **2003**, *75*, 563-571.
42. Kurulugama, R. T.; Wipf, D. O.; Takacs, S. A.; Pongmayteegul, S.; Garris, P. A.; Baur, J. E., Scanning Electrochemical Microscopy of Model Neurons: Constant Distance Imaging. *Anal. Chem.* **2005**, *77*, 1111-1117.
43. Zhu, R.; Macfie, S. M.; Ding, Z., Cadmium-Induced Plant Stress Investigated by Scanning Electrochemical Microscopy. *J. Exp. Bot.* **2005**, *56*, 2831-2838.
44. Wang, Y.; Noël, J.-M.; Velmurugan, J.; Nogala, W.; Mirkin, M. V.; Lu, C.; Guille Collignon, M.; Lemaître, F.; Amatore, C., Nanoelectrodes for Determination of Reactive Oxygen and Nitrogen Species inside Murine Macrophages. *Proc. Natl. Acad. Sci. U. S. A.* **2012**, *109*, 11534-11539.
45. Zhao, X.; Petersen, N. O.; Ding, Z., Comparison Study of Live Cells by Atomic Force Microscopy, Confocal Microscopy, and Scanning Electrochemical Microscopy. *Can. J. Chem.* **2007**, *85*, 175-183.
46. Zhao, X.; Diakowski, P. M.; Ding, Z., Deconvoluting Topography and Spatial Physiological Activity of Live Macrophage Cells by Scanning Electrochemical Microscopy in Constant-Distance Mode. *Anal. Chem.* **2010**, *82*, 8371-8373.
47. Kuss, S.; Polcari, D.; Geissler, M.; Brassard, D.; Mauzeroll, J., Assessment of Multidrug Resistance on Cell Coculture Patterns Using Scanning Electrochemical Microscopy. *Proc. Natl. Acad. Sci. U. S. A.* **2013**, *110*, 9249-9254.
48. Kuss, S.; Cornut, R.; Beaulieu, I.; Mezour, M. A.; Annabi, B.; Mauzeroll, J., Assessing Multidrug Resistance Protein 1-Mediated Function in Cancer Cell Multidrug Resistance by Scanning Electrochemical Microscopy and Flow Cytometry. *Bioelectrochemistry* **2011**, *82*, 29-37.
49. Ueda, A.; Niwa, O.; Maruyama, K.; Shindo, Y.; Oka, K.; Suzuki, K., Neurite Imaging of Living PC12 Cells with Scanning Electrochemical/Near-Field Optical/Atomic Force Microscopy. *Angew. Chem. Int. Ed.* **2007**, *46*, 8238-8241.

50. Isik, S.; Schuhmann, W., Detection of Nitric Oxide Release from Single Cells by Using Constant-Distance-Mode Scanning Electrochemical Microscopy. *Angew. Chem. Int. Ed.* **2006**, *45*, 7451-7454.
51. Isik, S.; Etienne, M.; Oni, J.; Blöchl, A.; Reiter, S.; Schuhmann, W., Dual Microelectrodes for Distance Control and Detection of Nitric Oxide from Endothelial Cells by Means of Scanning Electrochemical Microscope. *Anal. Chem.* **2004**, *76*, 6389-6394.
52. Pailleret, A.; Oni, J.; Reiter, S.; Isik, S.; Etienne, M.; Bedioui, F.; Schuhmann, W., In Situ Formation and Scanning Electrochemical Microscopy Assisted Positioning of No-Sensors above Human Umbilical Vein Endothelial Cells for the Detection of Nitric Oxide Release. *Electrochem. Commun.* **2003**, *5*, 847-852.
53. Hengstenberg, A.; Blöchl, A.; Dietzel, I. D.; Schuhmann, W., Spatially Resolved Detection of Neurotransmitter Secretion from Individual Cells by Means of Scanning Electrochemical Microscopy. *Angew. Chem., Int. Ed.* **2001**, *40*, 905-908.
54. Zhang, M.; Long, Y.-T.; Ding, Z., Filming a Live Cell by Scanning Electrochemical Microscopy: Label-Free Imaging of the Dynamic Morphology in Real Time. *Chem. Cent. J.* **2012**, *6*, 20.
55. Zhao, X.; Lam, S.; Jass, J.; Ding, Z., Scanning Electrochemical Microscopy of Single Human Urinary Bladder Cells Using Reactive Oxygen Species as Probe of Inflammatory Response. *Electrochem. Commun.* **2010**, *12*, 773-776.
56. Pelicano, H.; Carney, D.; Huang, P., Ros Stress in Cancer Cells and Therapeutic Implications. *Drug Resist. Update* **2004**, *7*, 97-110.
57. Liu, B.; Rotenberg, S. A.; Mirkin, M. V., Scanning Electrochemical Microscopy of Living Cells: Different Redox Activities of Nonmetastatic and Metastatic Human Breast Cells. *Proc. Natl. Acad. Sci. U. S. A.* **2000**, *97*, 9855-9860.
58. Liu, B.; Cheng, W.; Rotenberg, S. A.; Mirkin, M. V., Scanning Electrochemical Microscopy of Living Cells: Part 2. Imaging Redox and Acid/Basic Reactivities. *J. Electroanal. Chem.* **2001**, *500*, 590-597.
59. Liu, B.; Rotenberg, S. A.; Mirkin, M. V., Scanning Electrochemical Microscopy of Living Cells. 4. Mechanistic Study of Charge Transfer Reactions in Human Breast Cells. *Anal. Chem.* **2002**, *74*, 6340-6348.
60. Feng, W.; Rotenberg, S. A.; Mirkin, M. V., Scanning Electrochemical Microscopy of Living Cells. 5. Imaging of Fields of Normal and Metastatic Human Breast Cells. *Anal. Chem.* **2003**, *75*, 4148-4154.
61. Rotenberg, S. A.; Mirkin, M. V., Scanning Electrochemical Microscopy: Detection of Human Breast Cancer Cells by Redox Environment. *J. Mammary Gland Biol. Neoplasia* **2004**, *9*, 375-382.

62. Guo, J.; Amemiya, S., Permeability of the Nuclear Envelope at Isolated Xenopus Oocyte Nuclei Studied by Scanning Electrochemical Microscopy. *Anal. Chem.* **2005**, *77*, 2147-2156.
63. Chen, Z.; Xie, S.; Shen, L.; Du, Y.; He, S.; Li, Q.; Liang, Z.; Meng, X.; Li, B.; Xu, X., et al., Investigation of the Interactions between Silver Nanoparticles and HeLa Cells by Scanning Electrochemical Microscopy. *Analyst* **2008**, *133*, 1221-1228.
64. Zhan, D.; Fan, F. R.; Bard, A. J., The K_v Channel Blocker 4-Aminopyridine Enhances Ag⁺ Uptake: A Scanning Electrochemical Microscopy Study of Single Living Cells. *Proc. Natl. Acad. Sci. U. S. A.* **2008**, *105*, 12118-12122.
65. Holt, K. B.; Bard, A. J., Interaction of Silver(I) Ions with the Respiratory Chain of Escherichia Coli: An Electrochemical and Scanning Electrochemical Microscopy Study of the Antimicrobial Mechanism of Micromolar Ag⁺. *Biochemistry* **2005**, *44*, 13214-13223.
66. Li, X.; Bard, A. J., Scanning Electrochemical Microscopy of HeLa Cells - Effects of Ferrocene Methanol and Silver Ion. *J. Electroanal. Chem.* **2009**, *628*, 35-42.
67. Polcari, D.; Hernandez-Castro, J. A.; Li, K.; Geissler, M.; Mauzeroll, J., Determination of the Relationship between Expression and Functional Activity of Multidrug Resistance-Associated Protein 1 Using Scanning Electrochemical Microscopy. *Anal. Chem.* **2017**, *89*, 8988-8994.
68. Liebetrau, J. M.; Miller, H. M.; Baur, J. E.; Takacs, S. A.; Anupunpisit, V.; Garris, P. A.; Wipf, D. O., Scanning Electrochemical Microscopy of Model Neurons: Imaging and Real-Time Detection of Morphological Changes. *Anal. Chem.* **2003**, *75*, 563-571.
69. Li, X.; Bard, A. J., Scanning Electrochemical Microscopy of HeLa Cells – Effects of Ferrocene Methanol and Silver Ion. *J. Electroanal. Chem.* **2009**, *628*, 35-42.
70. Zhang, M. N.; Ding, Z.; Long, Y. T., Sensing Cisplatin-Induced Permeation of Single Live Human Bladder Cancer Cells by Scanning Electrochemical Microscopy. *Analyst* **2015**, *140*, 6054-6060.
71. Bard, A. J.; Li, X.; Zhan, W., Chemically Imaging Living Cells by Scanning Electrochemical Microscopy. *Biosens. Bioelectron.* **2006**, *22*, 461-472.
72. Amemiya, S.; Guo, J.; Xiong, H.; Gross, D., Biological Applications of Scanning Electrochemical Microscopy: Chemical Imaging of Single Living Cells and Beyond. *Anal. Bioanal. Chem.* **2006**, *386*, 458-471.
73. Zhu, R.; Macfie, S. M.; Ding, Z., Effects of Cadmium on Photosynthetic Oxygen Evolution from Single Stomata in Brassica Juncea (L.) Czern. *Langmuir* **2008**, *24*, 14261-14268.

74. Diakowski, P. M.; Ding, Z. F., Interrogation of Living Cells Using Alternating Current Scanning Electrochemical Microscopy (AC-SECM). *Phys. Chem. Chem. Phys.* **2007**, *9*, 5966-5974.
75. Shao, Y.; Mirkin, M. V., Probing Ion Transfer at the Liquid/Liquid Interface by Scanning Electrochemical Microscopy (SECM). *J. Phys. Chem. B* **1998**, *102*, 9915-9921.
76. Barker, A. L.; Macpherson, J. V.; Slevin, C. J.; Unwin, P. R., Scanning Electrochemical Microscopy (SECM) as a Probe of Transfer Processes in Two-Phase Systems: Theory and Experimental Applications of SECM-Induced Transfer with Arbitrary Partition Coefficients, Diffusion Coefficients, and Interfacial Kinetics. *J. Phys. Chem. B* **1998**, *102*, 1586-1598.
77. Yasukawa, T.; Uchida, I.; Matsue, T., Permeation of Redox Species through a Cell Membrane of a Single, Living Algal Protoplast Studied by Microamperometry. *Biochim. Biophys. Acta* **1998**, *1369*, 152-158.
78. Kasai, S.; Shiku, H.; Torisawa, Y.-S.; Noda, H.; Yoshitake, J.; Shiraishi, T.; Yasukawa, T.; Watanabe, T.; Matsue, T.; Yoshimura, T., Real-Time Monitoring of Reactive Oxygen Species Production During Differentiation of Human Monocytic Cell Lines (THP-1). *Anal. Chim. Acta* **2005**, *549*, 14-19.
79. Hu, R.; Guille, M.; Arbault, S.; Lin, C. J.; Amatore, C., In Situ Electrochemical Monitoring of Reactive Oxygen and Nitrogen Species Released by Single MG63 Osteosarcoma Cell Submitted to a Mechanical Stress. *Phys. Chem. Chem. Phys.* **2010**, *12*, 10048-10054.
80. Bergner, S.; Wegener, J.; Matysik, F.-M., Monitoring Passive Transport of Redox Mediators across a Confluent Cell Monolayer with Single-Cell Resolution by Means of Scanning Electrochemical Microscopy. *Anal. Methods* **2012**, *4*, 623-629.
81. Mauzeroll, J.; Bard, A. J., Scanning Electrochemical Microscopy of Menadione-Glutathione Conjugate Export from Yeast Cells. *Proc. Natl. Acad. Sci. U. S. A.* **2004**, *101*, 7862-7867.
82. López, E.; Figueroa, S.; Oset-Gasque, M. J.; González, M. P., Apoptosis and Necrosis: Two Distinct Events Induced by Cadmium in Cortical Neurons in Culture. *Br. J. Pharmacol.* **2003**, *138*, 901-911.
83. Yeh, J.-H.; Huang, C.-C.; Yeh, M.-Y.; Wang, J.-S.; Lee, J.-K.; Jan, C.-R., Cadmium-Induced Cytosolic Ca²⁺ elevation and Subsequent Apoptosis in Renal Tubular Cells. *Basic Clin. Pharmacol. Toxicol.* **2009**, *104*, 345-351.
84. Li, M. S. M.; Filice, F. P.; Ding, Z., A Time Course Study of Cadmium Effect on Membrane Permeability of Single Human Bladder Cancer Cells Using Scanning Electrochemical Microscopy. *J. Inorg. Biochem.* **2014**, *136*, 177-183.

85. Henderson, J. D.; Filice, F. P.; Li, M. S. M.; Ding, Z., Tracking Live Cell Response to Cadmium (II) Concentrations by Scanning Electrochemical Microscopy. *J. Inorg. Biochem.*, **2016**, *158*, 92-98.
86. Chen, L.; Liu, L.; Huang, S., Cadmium Activates the Mitogen-Activated Protein Kinase (MAPK) Pathway Via Induction of Reactive Oxygen Species and Inhibition of Protein Phosphatases 2A and 5. *Free Radic. Biol. Med.* **2008**, *45*, 1035-1044.
87. Strober, W., Trypan Blue Exclusion Test of Cell Viability. In *Current Protocols in Immunology*, John Wiley & Sons, Inc.: 2001.
88. Sarkar, B., *Heavy Metals in the Environment*; Marcel Dekker: New York, 2002.
89. Thévenod, F.; Lee, W.-K., Toxicology of Cadmium and Its Damage to Mammalian Organs. In *Cadmium: From Toxicity to Essentiality*, Sigel, A.; Sigel, H.; Sigel, R. K. O., Eds. Springer Netherlands: 2013; Vol. 11, pp 415-490.
90. Masters, J. R. W., Human Cancer Cell Lines: Fact and Fantasy. *Nat. Rev. Mol. Cell Biol.* **2000**, *1*, 233-236.
91. van Staveren, W. C. G.; Solís, D. Y. W.; Hébrant, A.; Detours, V.; Dumont, J. E.; Maenhaut, C., Human Cancer Cell Lines: Experimental Models for Cancer Cells in Situ? For Cancer Stem Cells? *Biochim. Biophys. Acta* **2009**, *1795*, 92-103.

Chapter 2

2 Determining Live Cell Topography by Scanning Electrochemical Microscopy

(A version of this work has been published in the *Journal of Electroanalytical Chemistry*
Li, M.S.M.; Filice, F.P.; Ding, Z. *J. Electroanal. Chem.* **2016**, 779, 176-186.)

2.1 Introduction

Scanning electrochemical microscopy (SECM) is a non-invasive analytical technique of the scanning probe microscopy family.¹⁻³ This technique operates by moving a biased ultramicroelectrode (UME, ≤ 25 μm in diameter) over a sample (or substrate) with extreme precision. Changes in the faradaic current are monitored relative to the UME position. By biasing the UME at a particular potential such that the redox species is oxidized or reduced in a diffusion-controlled process, a steady state current can be detected. If the biased UME approaches a conductive sample, this current can be amplified (regeneration of the redox species, positive feedback) or decreased if the sample has insulating-characteristics (negative feedback).⁴

Developed greatly by Bard *et al.* since 1989,⁴ SECM has been employed for a wide range of chemical studies, such as studying surface and interface interactions,⁵⁻⁷ substrate kinetics,⁸ and microstructure fabrication.^{9,10} Recent advancements towards biological applications have been greatly pursued.¹¹⁻¹⁷ Coupling SECM with the study of living cells has led to significant insight into understanding biological mechanisms, such as electron transfer kinetics and molecular transports,¹⁸⁻²⁰ extracellular reactive oxygen/nitrogen²¹⁻²⁶ and neurotransmitter release,^{27,28} and the pre-assessment of drugs.^{13,14,26}

In our group, a different mode of SECM was developed which is known as the SECM depth scan mode.²⁶ This mode passes the UME in the x -direction to perform a horizontal line scan at a particular height in the z plane. The electrode is then lowered by a set distance and another horizontal line scan is collected. This action is repeated until the desired depth is reached, producing a 2D image of the current as a function of UME's x, z coordinates. This

real-time imaging technique allows for the tip-to-sample distance to be more easily gauged throughout the experiment, removing the limitation of conventional SECM approach methods. As each pixel in the image provides the specific tip current and its coordinates, hundreds of usable probe approach curves (PACs) can be obtained, limited only by user defined resolution. By simply extracting vertical cross-sections from the SECM image, experimental PACs can be obtained.

This SECM mode is parallel to the Schuhmann group's 4D shearforce-based constant distance mode, where multiple constant distance images are obtained above the sample.²⁹ The tip-to-sample distance is controlled by the retractions of the tip based on the shearforce of the SECM probe.²⁹ A comprehensive 4D data set of the current-tip coordinates is generated, allowing for the extraction of different types of plots, such as depth scan images, whereas our method collects these 2D depth scan images directly.

Typically, quantification of physiological processes, such as membrane permeability^{12,30,31} and molecular transport of species,²⁰ by SECM are assessed by overlaying experimental PACs onto simulated theoretical curves. Since simulations are based on the experimental geometry and parameters, successful overlay of these curves allows for the quantification of these properties. The generation of these simulated PACs is typically done in advanced finite elemental analysis software, such as COMSOL Multiphysics or MATLAB, as 2D-axially symmetric simulations. A limitation to these 2D-axially symmetric models is that only one experimental PAC (to the direct center of the sample) is usable, severely limiting the advantages of our depth scan mode. By progressing towards 3D simulations, complete control of the electrode's position and model geometry, with no imposed symmetry restrictions, become possible.^{32,33}

Experimentally, we will present the use of a hydrophilic and charged redox mediator, ferrocene carboxylate (FcCOO^-), to study the cellular topography in human bladder cancer (T24) cells by means of SECM. As an impermeable redox agent, FcCOO^- can provide insights into the cellular heights of the adhered T24 cells through the comparison of the PACs to the direct center of the cell and the petri dish. The use of 3D modelling would also allow PACs to be assessed at any location over the cell.^{32,33} Herein for the first time, we will

demonstrate the utilization of a 3D model to determine the cell height and topography across the cell. Confirmation of the 3D model was carried out through a comparison of the PAC to the center of the cell against the previously established 2D axially symmetric model. We will also utilize a separate simulation model where the cell diameter is fixed according to its exact geometry, followed by parameterizing the cell height. The fitting of experimental PACs to these curves will yield the cell height directly. These methods will quantify the cell height over the center of the cell, however 3D simulations will also allow further cell heights across the cell to be assessed. Also as a result of 3D simulations, we were able to confirm cellular geometry and topography by means of horizontal sweeps across the cells.

2.2 Experimental Section

2.2.1 Materials

Ferrocenecarboxylic acid (97%) and sodium dodecyl sulfate (SDS, 99+%) were acquired from Sigma-Aldrich (Mississauga, ON), while potassium chloride (99%) was acquired from Alfa Aesar (Ward Hill, MA). All chemicals were used as received. 3-(4,5-dimethylthiazol-2-yl)-2,5-diphenyltetrazolium bromide (MTT) was acquired from R&D Systems Inc. (Minneapolis, MN) in the TACS® MTT Cell Proliferation Assay Kit. Spectroscopic grade dimethyl sulfoxide (DMSO) was used to dissolve the formazan crystals (Caledon Laboratory Ltd, Georgetown, ON).

2.2.2 Cell Culture

Human bladder carcinoma (T24) cells (ATCC® HTB-4™) were purchased from American Type Culture Collection (ATCC, Manassas, VA) and maintained in McCoy's 5a medium modified with addition of 10% fetal bovine serum (FBS). T24 cells were grown directly on uncoated T25 flasks (Becton Dickinson, Franklin Lakes, NJ) and at 80-100% confluency, cells were washed with phosphate buffered saline (PBS, 10 mM, pH 7.4) followed by trypsinization (0.25 % trypsin and 0.03 % ethylenediaminetetraacetic acid solution) and subcultured weekly. T24 cells were grown in a humidified incubator maintained at 37 °C and 5 % CO₂ (Sanyo, Japan). McCoy's 5a medium modified was purchased from ATCC, while all other culture solutions and serums were purchased from

Invitrogen (Burlington, ON, Canada). All media preparation and cell culturing were performed in a sterilized laminar flow hood.

For live cell SECM measurements, T24 cells were plated in glass bottom petri dishes (P50-G-0-30-F, MatTek Corporation, Ashland, MA). All cultured cells were washed with PBS (1x PBS) and refilled with 0.5 mM FcCOO⁻ and 0.1 M KCl in PBS immediately prior to SECM experiments. For valid comparison, all SECM live cell experiments were completed using the cells from a narrow passage range (within 5 passages).

2.2.3 Cellular Viability

The effects of FcCOO⁻ on cellular viability was assessed using the MTT cell proliferation assay.³⁴ Briefly, 2×10^4 T24 cells/well were seeded onto Corning Scientific Costar™ 96-well polystyrol flat bottom plates. After 24 hours, the growth medium was aspirated and replaced with new growth medium containing 0.5 mM FcCOO⁻ or SDS (0.05, 0.10, 0.15, or 0.20 mg/mL), which was used as a positive control in the assay.

After treatment, the growth medium was carefully aspirated and replaced with 100 μ L of fresh growth medium (absent of phenol red) and an additional 10 μ L of the MTT reagent. After 6 hours, the MTT solution was carefully aspirated and the formazan crystals were dissolved with 50 μ L of spectroscopic grade DMSO. The absorbance at 540 nm was read by a M1000 PRO plate reader (Tecan Switzerland) following 1 s of shaking at 2 mm amp and 654 rpm. To remove the background media effects, empty (blank) wells were also treated according to the MTT protocol. The results reported here are the mean \pm relative standard deviations (RSD) from at least 4 experiments (8 replicates of each treatment period).

2.2.4 Electrode Fabrication

The 5 and 10 μ m diameter Pt UMEs used in this Chapter were fabricated in house and has been previously published elsewhere in great detail.^{12,25,35} Briefly, Pt UMEs were fabricated by inserting a 5 or 10 μ m diameter Pt wire (Goodfellow Metals, Cambridge, UK) into a pulled and heat-sealed end of a borosilicate glass capillary (o.d.: 2.00 mm, i.d.: 1.16 mm, length: 10.00 cm, Sutter Instrument, Novato, CA). The capillary assembly was then vacuum-pumped through the open end and the glass sheathing on the opposite end was

melted onto the Pt wire using the tungsten coil from a micropipette puller (PP-83, Narishige, Japan). The Pt tip was exposed by manually polishing the sealed tip on a homemade polishing wheel attached with abrasive alumina-coated polishing pads (3.0, 0.3, and 0.05 μm , Buehler, Whitby, ON). The ratio of the surrounding glass radius to that of the Pt wire (RG) was manually polished to approximately 3 (eqn 2.1):

$$RG = \frac{\text{Radius of glass insulator}}{\text{Radius of Pt wire}} \quad (2.1)$$

The electrode tip was examined using optical microscopy and tested for functionality using cyclic voltammetry during the fabrication and polishing processes.

2.2.5 SECM Instrumentation

All SECM experiments were conducted using a modified Alpha-SNOM microscope (WITec, Ulm, Germany) adapted with a home-made electrode holder.^{12,31,33,36} Using the Alpha-SNOM positioning system along with an inverted Nikon objective lens (50x lens, N.A.: 0.55, W.D.: 10.1 mm, Japan), the UME's approach to the T24 cells was visualized and controlled to avoid cellular penetration. The electrochemical experiments were performed using an electrochemical analyzer (CHI 800B, CH Instruments, Austin, TX) combined with a CHI 200 Picoamp Booster to reduce noise (CH Instruments), which signal was fed directly into the data acquisition channel of the Alpha-SNOM instrument. For all electrochemical experiments described in this Chapter, the Pt UMEs were used as the working electrode and a Ag/AgCl electrode was used as the combined auxiliary and reference electrode.

2.2.6 SECM Experiments

SECM measurements were obtained by mounting the petri dish onto the scanning stage (P-517K064, Polytec PI, Germany) of the microscope, maintained at 37.0 ± 0.2 °C (Bioscience Tools, San Diego, CA). Using the inverted objective lens, individual T24 cells were located and the UME was then brought in close proximity to the cell. The biased UME (0.500 V) approached the cell using the depth scan feature of the WITec software, resulting in a 2D current-distance (x, z) image. Each image has 128 x 128 pixels, scan width and depth of 60 μm and 80 μm , respectively and an integration time of 0.01 s. All petri dishes and cells were discarded within 1.5 hours of experiments.

2.2.7 SECM Data Analysis

PACs were obtained by extracting the vertical cross-sections above the cells from their respective SECM depth scan images. To quantify cell height, experimental PACs were overlapped onto simulated curves generated by COMSOL Multiphysics v.5.1, a finite element analysis software.^{37,38} A total of 22 T24 cells were analyzed to determine the average \pm standard deviation cell height and diameter.

2.2.8 The Simulation Workstation Computer

COMSOL Multiphysics v.5.1 (COMSOL, Boston, MA) was used for all simulations. A custom-built workstation computer was used which included an Intel Core I7 4930K (6-core, 12-thread) processor and 32 GB Kingston HyperX Fury Black memory. A Mushkin Chronos 480 GB SSD was used to increase swap speeds for the large simulations that demanded more than 32GB RAM. Ubuntu Linux 14.04.1 LTS was used as a stable and reliable operating system for running simulations. All components used in the workstation PC are consumer available, “gaming grade” parts. Components were selected, acquired and assembled in-house with specific optimization for COMSOL simulation.

2.3 Theory and Simulations

2.3.1 2D Axially Symmetric Simulation Model Geometry

The simulation model for PACs to the center of the cell was constructed in 2D axial symmetry in COMSOL Multiphysics. The model geometry was designed to be representative of the physical dimensions of all objects involved in the live cell SECM experiments, Figure 2.1. The electrode in the simulation reflected the fabricated UMEs used (Figure 2.1A): a 2.5 (or 5) μm radius of Pt wire was surrounded by an insulating glass sheathing with a radius of 7.5 (or 15) μm , maintaining the RG ratio of 3. The electrode tip-to-cell distance was parameterized, allowing for the automated simulation of the electrode’s approach to the cell and the generation of PACs. The T24 cell was represented as a nominal semi-oblate ellipsoid that was 8 μm in height and 10 μm in radius, which is representative of the average T24 cell studied. The cell height and diameter were defined as parameters allowing for ease of modification to match specific cell dimensions. The parametric nature

of the cell diameter and height also allows for the automated simulation of multiple cell heights and diameters (see Figures S2.1 and S2.2 in Appendix II).

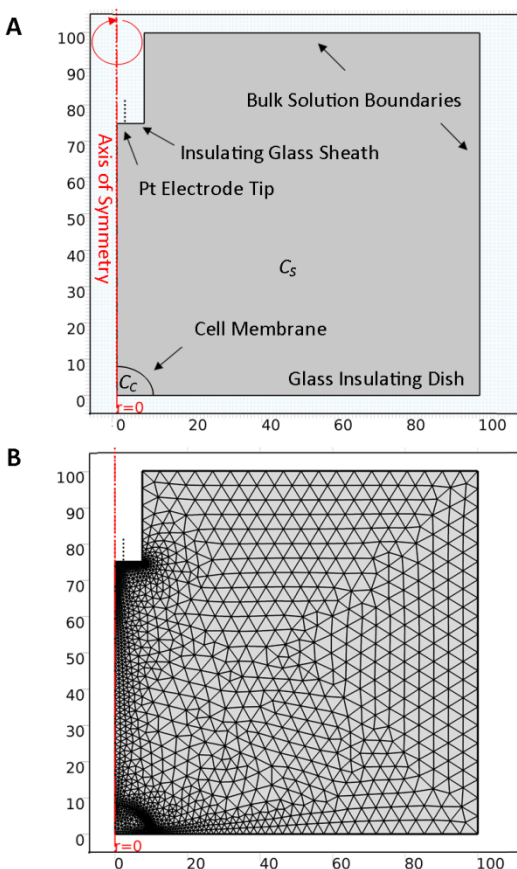


Figure 2.1. (A) An illustration of the 2D axially symmetric model of a T24 cell in COMSOL Multiphysics v5.1. c_s and c_c are the bulk concentrations outside and inside the cell, respectively. At the cell membrane, the membrane flux, f , is defined as a no flux boundary, where f is $0 \text{ mol}\cdot\text{m/L}\cdot\text{s}$. (B) A typical meshed 2D SECM model, with finer meshing located in the areas of interest (Pt tip and cell membrane).

2.3.2 3D Simulation Model Geometry

To perform PAC simulations at locations other than the cell's central axis (or a horizontal sweep of the electrode across the cell), a full 3D model geometry is needed. Many of the parameters for the 3D model geometry match those of the 2D axially symmetric model detailed above. The simulation was performed inside of a quarter sphere solution domain with a symmetry boundary (Figure 2.2A). As the electrode positioning was only performed

in the x,z plane, a plane of symmetry was present in the semi-spherical model. The model geometry could therefore be optimized to a quarter sphere, halving the number of meshing elements required for this simulation, greatly reducing system memory load (Figure 2.2B).³⁹ The model is mirrored across the symmetry boundary during simulation, allowing for the flux of FcCOO^- species across this boundary. The top $10\ \mu\text{m}$ of the quarter sphere domain was removed to reduce the complexity of the mesh at the point the cylindrical electrode would normally intersect the curved domain boundary.

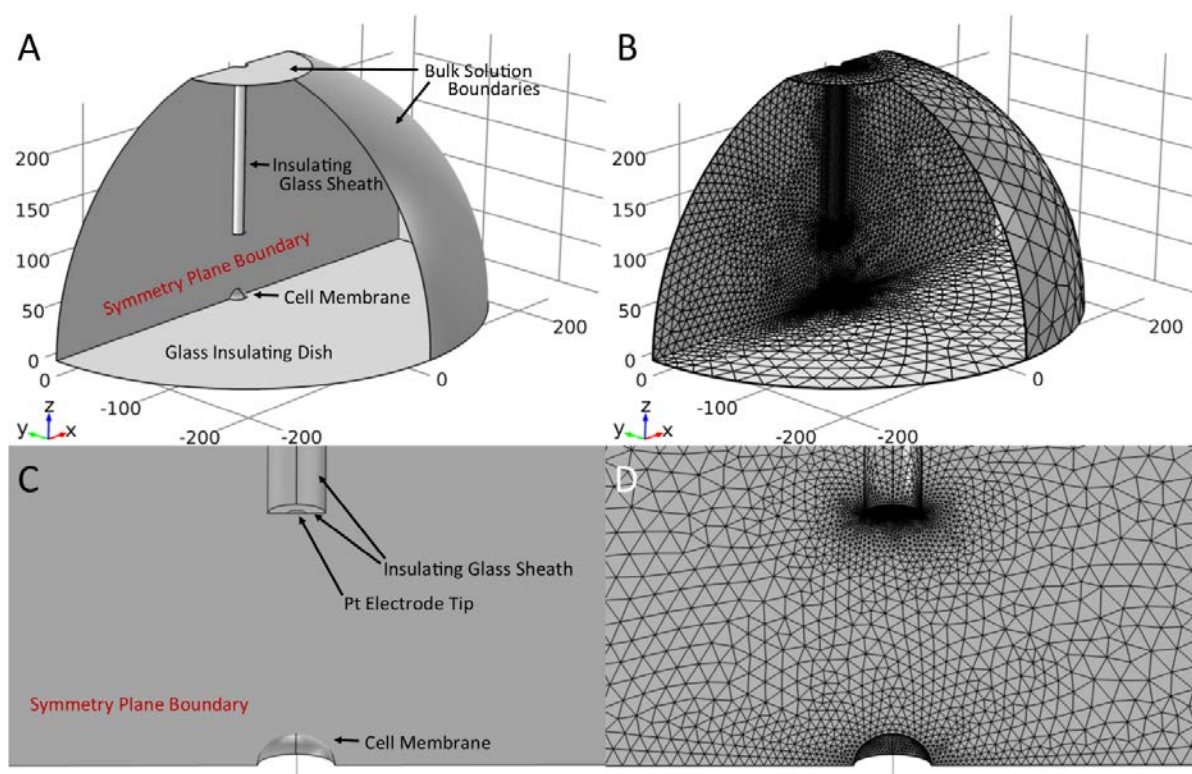


Figure 2.2. (A) The labelled 3D model geometry of an SECM electrode's approach to a single live cell. (B) Mesh of the full 3D model. (C) Zoomed-in view of the 3D model geometry focusing on the electrode tip and cell membrane (D) Mesh of the zoomed in 3D model.

Similar to the 2D axially symmetric simulations, the 3D simulation geometry reflects those of the experimental physical dimensions. The electrode is a Pt semi-circular disk with a diameter of 5 (or 10) μm that has an RG of 3 (Figures 2.2C and D). As a result of the semi-circular Pt electrode at the symmetry boundary, the surface area of the electrode tip boundary

is halved. The electrode's x and z positions are parameterized in the study conditions for the model, allowing for parametric movement of the electrode position in both directions. The T24 cell was represented as a nominal semi-oblate ellipsoid with a parameterized $8\ \mu\text{m}$ in height and $20\ \mu\text{m}$ in diameter.

2.3.3 Simulation Methodology

Due to the charged nature of the redox mediator, there is no membrane flux for the FcCOO^- under normal conditions. The cell interior and exterior domains in this case do not interact with each other, i.e. the cell acts as an insulator. As a result, the cell interior domain can be ignored, requiring only the specification and simulation of the physics and concentrations of the cell exterior. The cell membrane was defined as an insulating “no flux” boundary. The diffusion coefficient, D , was set to $5.7 \times 10^{-10}\ \text{m}^2/\text{s}$ for FcCOO^- species.⁴⁰ The solution domain follows Fick's second law of diffusion, eqns 2.2 (for 2D axial symmetry) and 2.3 (for full 3D):

$$\frac{\partial c_s(r,z)}{\partial t} = D \left(\frac{\partial^2 c_s(r,z)}{\partial r^2} + \frac{1}{r} \left(\frac{\partial c_s(r,z)}{\partial r} \right) + \frac{\partial^2 c_s(r,z)}{\partial z^2} \right) \quad (2.2)$$

$$\frac{\partial c_s(x,y,z)}{\partial t} = D \left(\frac{\partial^2 c_s(x,y,z)}{\partial x^2} + \frac{\partial^2 c_s(x,y,z)}{\partial y^2} + \frac{\partial^2 c_s(x,y,z)}{\partial z^2} \right) \quad (2.3)$$

where c_s represents the concentration of FcCOO^- in the solution domains. The variables r and z are the cylindrical coordinates used in 2D axially symmetric modelling, where x , y and z are the Cartesian coordinates used in full 3D modelling, and t is time.

The bulk concentration of FcCOO^- was set to $0.5\ \text{mM}$, which is the concentration of the mediator used in these experiments. The simulation study performed was a stationary phase (steady state) simulation. The electrode tip boundary was set to consume the mediator, generating a concentration of $0\ \text{M}$. The bulk solution boundaries were set to generate the initial mediator concentration of $0.5\ \text{mM}$. This simulates the bulk solution concentration with a theoretically infinite size relative to the size of region of interest: the electrode tip and cell membrane. Since the glass sheathing and petri dish both have insulating characteristics, they were set as no flux boundaries.

The simulation models are finely meshed with a triangular mesh for 2D or tetrahedral mesh for 3D. Further refinement in the meshing elements at the regions of interest (electrode tip and cell membrane) prior to computation was completed to provide greater accuracy and precision (Figures 2.1B and 2.2B). A convergence plot of the meshing error can be found in Appendix II (Figure S2.3).

To generate the theoretical PACs, numerous data points are acquired at tip-to-cell distances between the range 0.2 and 60 μm . The UME's z position was parameterized using the parametric sweep function, allowing the specification of a range of electrode positions to be simulated as one large set. The electrode's x position was also parameterized in the 3D model to allow for horizontal sweep generation and the simulation of full x,z plane depth scans. Cell heights and diameters were also parametrized for comparison of PACs generated on approach to cells of different dimensions. For a more detailed report of the simulation process is included in Appendix II.

In the 2D model, the tip current was obtained by integration of the simulated concentration flux, eqn 2.4:¹²

$$i = nDF \int_0^a r \left[\frac{\partial c_s(r,z,\varphi)}{\partial z} \right] dr \quad (2.4)$$

where, n is the number of electrons transferred and F is Faraday's constant (96,485 C/mol). In the 3D model, the electrochemical current can be calculated by integrating the concentration flux versus the electrode surface area:³³

$$i = 2nFD \int_0^a \left[\frac{\partial c}{\partial z} \right]_z da \quad (2.5)$$

To normalize the PACs, the tip current was normalized (I) against the steady state current (i_{ss}), while the tip-to-cell distances (d) were normalized with respect to the electrode radius (a , eqns 2.6 and 2.7, respectively).

$$I = \frac{i}{i_{ss}} \quad (2.6)$$

$$\text{Normalized Distance, } L = \frac{\text{Tip-to-Sample distance, } d}{\text{Electrode Radius, } a} \quad (2.7)$$

For the off axis simulations, the normalized distances were calculated relative to the position of the substrate directly below the electrode disk center. As a result, the simulations performed to the cell edge or further ($x \geq 1r$) were offset from the highest point on the cell by the cell height (cellH), ie. simulated relative to the position of the dish (see Figure S2.4). Calculation of the offset for any position over the cell follows the equation for an ellipse and is dependent on the cell dimensions:

$$offset = cellH - \sqrt{\left(1 - \frac{x^2}{r^2}\right) * cellH^2} \quad (2.8)$$

where x is the distance from the cell center that the vertical cross-section is taken at and the offset is the height difference between the cell at position x and the center of the cell. Due to the characteristic shape of an ellipse, offset values at $x = r/2$ do not cause substantial deviation of tip-to-substrate distance from the electrode position centered over the cell relative to the total cell height. At the $x = r$ position, an offset of the full cell height is provided by this formula.

2.3.4 Validation of the 3D Model

While the geometry for the UME's approach towards an individual cell can be simplified to a 2D axially symmetric model, this simulation can only provide quantification over the direct center of the cell. The 2D axially symmetric model, while computationally efficient, severely limits the advantage of our SECM depth scan mode. To take full advantage of our SECM technique, 3D modelling has been shown to be the most promising.³³

As described in the above simulation section, PACs were generated using the 3D model at specific positions relative to the cell center as illustrated in Figure 2.3A. The purple vertical cross-section at the center of the cell was taken as $x = 0$. The blue cross-section represents a PAC extracted at a distance of $r/2$ away from the cell center, while the green line indicates a full r distance away. To determine cellular height, a vertical cross-section to the petri dish is extracted at a distance of $x > 2r$ away ($x \gg r$, red).

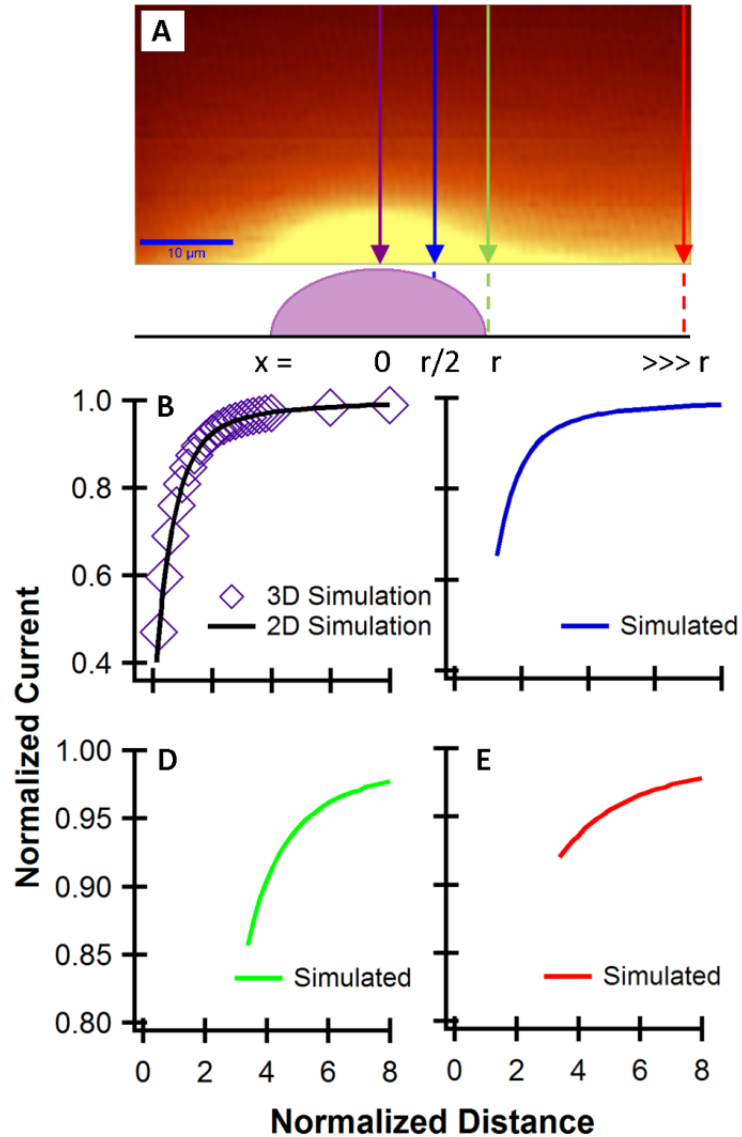


Figure 2.3. (A) Graphical representation of the 4 vertical cross-section locations over a T24 cell of height $8\ \mu\text{m}$ x $20\ \mu\text{m}$ diameter and the petri dish. The purple cross-section indicates an extraction over the center of the cell (taken as $x = 0$), while the blue and green cross-sections are extractions taken at a distance of $r/2$ and r away from the cell center, respectively. The red line represents an extraction taken over the petri dish at a distance of $2r$. For these experimental extractions, $x > 2r$ away from the cell center was taken ($x \gg r$). (B) The 2D and 3D simulated PACs to the center of the cell are compared, validating the 3D simulation model. (D)-(E) are the corresponding simulated PACs over the color-specified locations in (A). As the electrode gets further from the cell center, the electrochemical feedback becomes weaker.

To validate the 3D simulations, the PAC extracted over the center of the cell was compared with that from the 2D simulation model (Figure 2.3B), which showed excellent agreement.¹⁶ Figures 2.3C-E are the corresponding simulated PACs generated at the color-specific locations indicated in Figure 2.3A. When the electrode is over the direct center of the cell at its highest point, the electrochemical feedback is strongest (Figure 2.3B). As the UME sweeps away the cell, the electrochemical feedback weakens (Figures 2.3C and D), where it will eventually display the same electrochemical feedback as the insulating petri dish (Figure 2.3E).

2.4 Results and Discussion

2.4.1 Determining Cell Diameter through Optical Micrographs

Our instrumental set-up provides optical assistance in locating potential T24 cells prior to SECM study. Figure 2.4A shows a typical optical micrograph of a T24 cell (focused to the cell of interest, encircled in red). Using the optical micrographs, the diameter of the T24 cells can be determined, for instance, the cell in Figure 2.4A (and B) has a diameter of 20.6 μm . The average cell diameter of all tested cells was determined to be $20.1 \pm 3.8 \mu\text{m}$ ($N = 22$ cells). The simulations were completed using an average diameter of 20.0 μm since it is within this $\pm 3.8 \mu\text{m}$ range: the average diameter has little effect on the simulated PACs (see Figure S2.2). After T24 cells are located, the SECM probe was placed in its vicinity (solid black circle to the right of the cell, Figure 2.4B). The SECM depth scan images were then collected as the probe performed horizontal line scans above the cell (Figure 2.4C).

When the UME is far from the cell (and petri dish) a steady state oxidative current can be detected, which is indicated by the stable red-brown color in the image when $d > 20 \mu\text{m}$ (or $L > 4$). Once the UME is in closer proximity ($L_{\text{cell}} < 4$), the electrochemical influence can be detected as indicated by the yellow semi-elliptical shape in the SECM image (Figure 2.4C). While the glass bottom petri dish has insulating characteristics, it is less noticeable at the same location in the x - z scan due to the height differences between the cell and the dish.

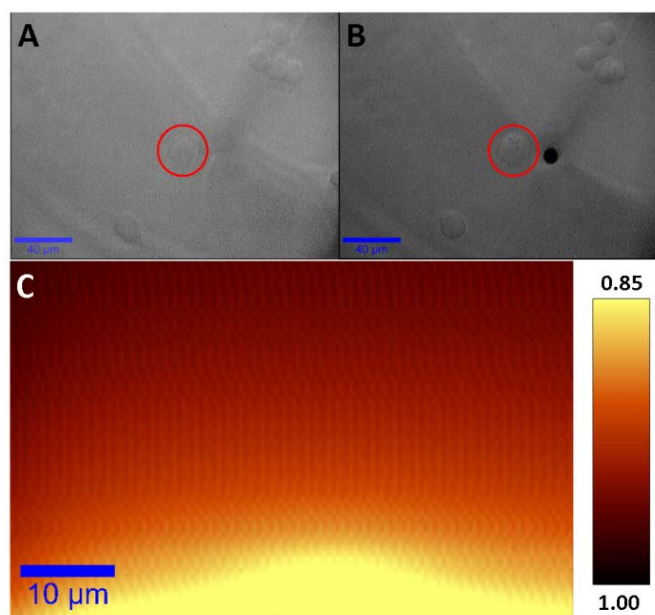


Figure 2.4. Optical images of a (A) T24 cell (red circle) and (B) approach of a 10 μm Pt UME which is in close proximity to the cell (black circle). (C) A typical SECM depth scan image of the T24 cells obtained using the redox mediator FcCOO^- , as detected by the 10 μm Pt UME.

2.4.2 Extraction of Cell Heights by Traditional Methods

In literature, the simulated cellular geometry has varied widely, appearing as a flat substrate³⁵ to rectangular⁴¹ to elliptical shape.^{12,16} In fact, the simulated geometry can have a significant effect on the curvature of the PAC: approaching a flat *vs.* elliptical cell, the PACs would be more pronounced as L approaches 0 (See Figure S2.5). Since the cell geometry can have an effect on theoretical PACs, it is important for the theoretical geometries (electrode and cells) to be carefully tuned to match the experimental system.

Previously, we estimated the average cell height based on the experimental observations, noting the difference between the tip-to-cell and tip-to-substrate distances.^{12,26,31} However, cellular height can also be determined quantitatively by SECM. The traditional approach is to use two PACs: one to the cell and one to the petri dish (in the vicinity of the cell to avoid dish tilting effects). In our previous studies, the hydrophobic redox mediator ferrocenemethanol was used to study the effects of the anti-cancer drug, cisplatin and heavy metal cytotoxicity on T24 cells.^{12,26,31} However, since hydrophobic

redox mediators can permeate into the cell, it is extremely difficult to assess the cell height based on the use of these agents without requiring multiple, higher complexity simulations. An alternative to this is to use a hydrophilic and charged redox mediator, such as FcCOO^- against healthy T24 cells. The FcCOO^- species cannot readily cross the cell membrane, thus the cell behaves similarly to an insulating sample which allows for simpler and less computationally demanding simulations.

Since each pixel embedded into an SECM depth scan image holds the tip current and probe coordinates, PACs can be extracted as vertical cross-sections taken from the image (blue and purple lines in Figure 2.5A). Using 2D axially symmetric simulation models, the PACs are limited to the center of the cell and to the insulating dish (through a separate simulation). Since FcCOO^- is impermeable to the cell, the simulation of an UME's approach to an insulating cell will provide its simulated PAC. To determine cell height using this method, a simulation model was designed based on the exact geometries of the electrodes and the average cell determined as a height of $8\ \mu\text{m}$ by $20\ \mu\text{m}$ diameter. The difference between the normalized distances to the dish and cell quantifies the height of the cell (Figure 2.5).

The tip-to-cell distance can be determined by overlaying the experimental PAC from the center cell (blue arrow in Figure 2.5A) onto the simulated curve (Figure 2.5B): here a tip-to-cell distance of $4.4\ \mu\text{m}$ ($L = 0.88$) was achieved (eqn 2.7). When the experimental PAC to the petri dish (blue arrow in Figure 2.5B) is overlaid onto its theoretical insulating curve (Figure 2.5B), a tip-to-dish distance of $15.9\ \mu\text{m}$ ($L = 3.2$) was achieved. The difference between these two approaches would quantify the cell's height. For this particular T24 cell, the cell height was determined to be $11.5\ \mu\text{m}$.

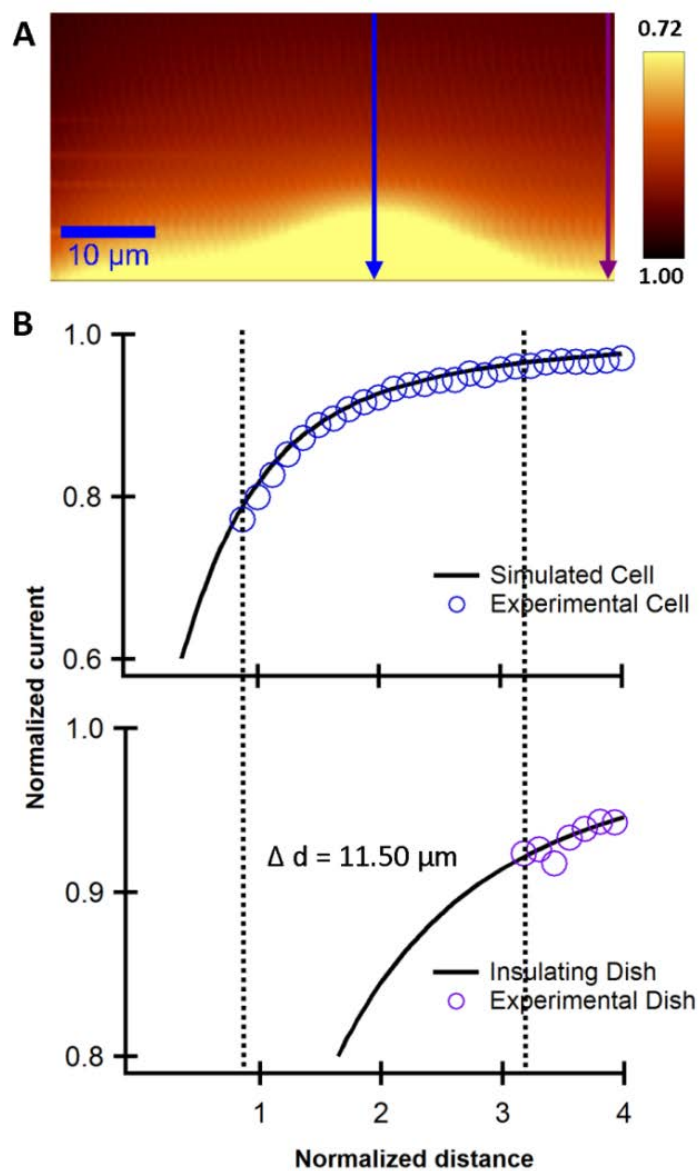


Figure 2.5. (A) The SECM depth scan image of a T24 cell using FcCOO^- as the redox mediator, as detected by a $10 \mu\text{m}$ Pt UME with RG 3. The scale bar in the image represents $10 \mu\text{m}$. The PACs illustrated in (B) correspond to the vertical cross-sections taken over the cell (blue) and over the dish (purple) overlaid onto theoretical insulating curves (black solid lines).

Using this PAC comparison method, a wide distribution range of cell heights was found: 4 to 15 μm (Figure 2.6). The average cell height was found to be $8.7 \pm 3.3 \mu\text{m}$ ($N = 22$ cells). One possible explanation to the wide range of cell heights could be due to the different post-incubational times of the cells prior to their testing by SECM. For each tested petri dish, three to seven individual cells were studied prior to discarding after one and a half hours of SECM experiments. The cells were in a PBS electrolytic solution containing 0.5 mM FcCOO^- and 0.1 M KCl as the supporting electrolyte. The addition of the supporting electrolyte could induce an effect on the solution's ionic strength causing duress to the cells, thereby affecting the cell height. It is also possible that the cells were in different cellular stages contributing to different heights. Any of these factors could have contributed to the cells rounding up and resulting in a larger cell height. To verify FcCOO^- did not have any toxic effects on the T24 cells during the SECM experiments, the established MTT cell proliferation assay was used to assess cellular viability. No changes in cell viability were detected during treatment periods up 2.5 hours (Figure S2.6).

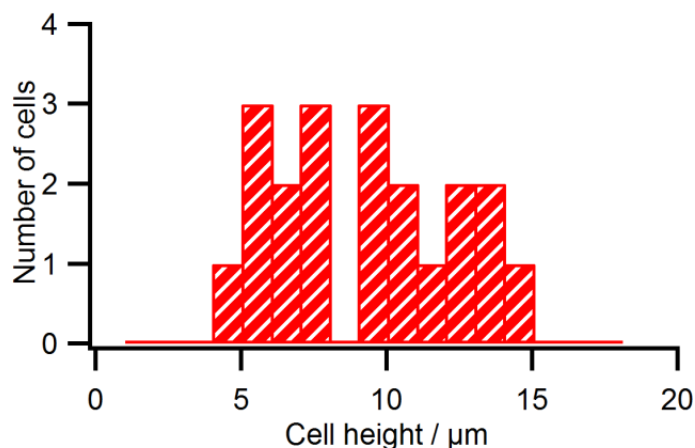


Figure 2.6. Distribution of the heights of the T24 cells, where the average was found to be $8.7 \pm 3.3 \mu\text{m}$ for $N = 22$ cells.

2.4.3 Determining Cell Heights by Parameterizing Heights

Here, we established an alternative method to assess the cells' height, directly comparing the PAC at the cell center to simulated PACs generated with varying heights (against a fixed cell diameter, Figure 2.7). This approach will directly quantify the cell's

height, requiring only a single PAC. The height of the simulated cell was varied from 3 to 15 μm (only shown for 13, 14 and 15 μm , Figure 2.7, full set shown in Figure S2.2) which confirms the height of the cell can affect the simulated PACs.

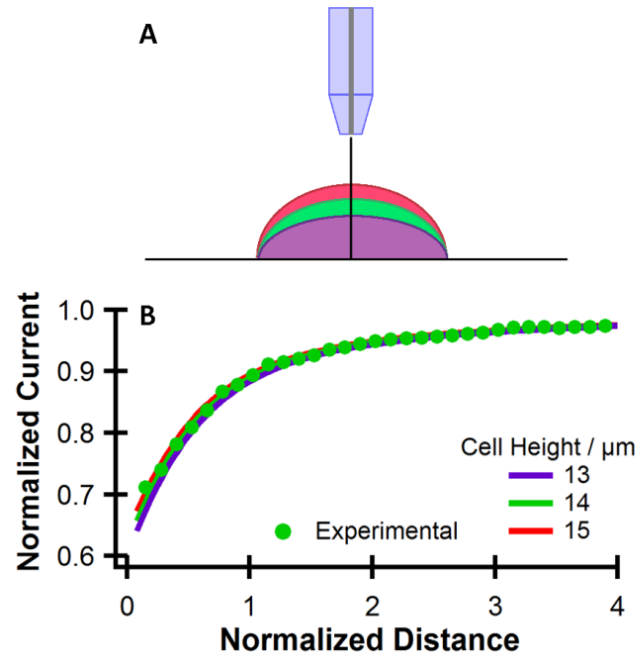


Figure 2.7. (A) Illustrative representation of the parametric sweep of the cell height against a fixed cell diameter (20 μm). (B) An experimental PAC overlaid onto simulated curves to directly determine the cell's height. This particular cell has a diameter of 20 μm and a height of 14 μm (green circles).

The experimental cell in Figure 2.7 fits quite well to the cell with a height of 14 μm (experimental PAC is comprised of green circles, which is overlain onto the solid green simulated curve). For this particular cell, the traditional method yields a cell height of 12.8 μm (based on the 2D simulation model previously described). These two methods yielded similar cell heights (within 10 % deviation, Table 2.1).

Table 2.1. Comparison of the cell heights quantified by the PAC extraction method (2D vs. 3D models) and parameterizing the cell heights method.

Cell Height (μm) Determined by		Traditional PAC Method				Parametrizing Cell Height
		2D Model		3D Model		
		$x = 0$	$x = 0$	$x = r/2$	$x = r$	
Cell 1	10	11.5	11.8	10.3	1.5	11
Cell 2	10	12.8	13.5	11.8	2.8	14
Cell 3	5	9.7	10.6	9.0	1.9	10
Cell 4	5	8.1	8.9	7.3	0.9	8

2.4.4 3D Mapping of Cell Topography

Utilizing 3D simulations, PACs over any point of the cell can now be extracted and studied. Potential T24 cells were identified in a similar fashion as previously described, first cells were located optically (Figure 2.8A) followed by the SECM depth scan experiments (Figure 2.8B). Four vertical cross-sections were chosen: one to the direct center of the cell ($x = 0$); one half a radii distance away from the center of the cell ($x = r/2$); one a full radii away ($x = r$) and one above the petri dish, which was taken at a distance greater than 2 radii away from the center of the cell ($x \geq 2r$, purple, blue, green and red lines respectively in Figure 2.8B). The electrochemical feedback can be seen to differ across the sample's topography in the SECM image, becoming less pronounced the further away from the cell.

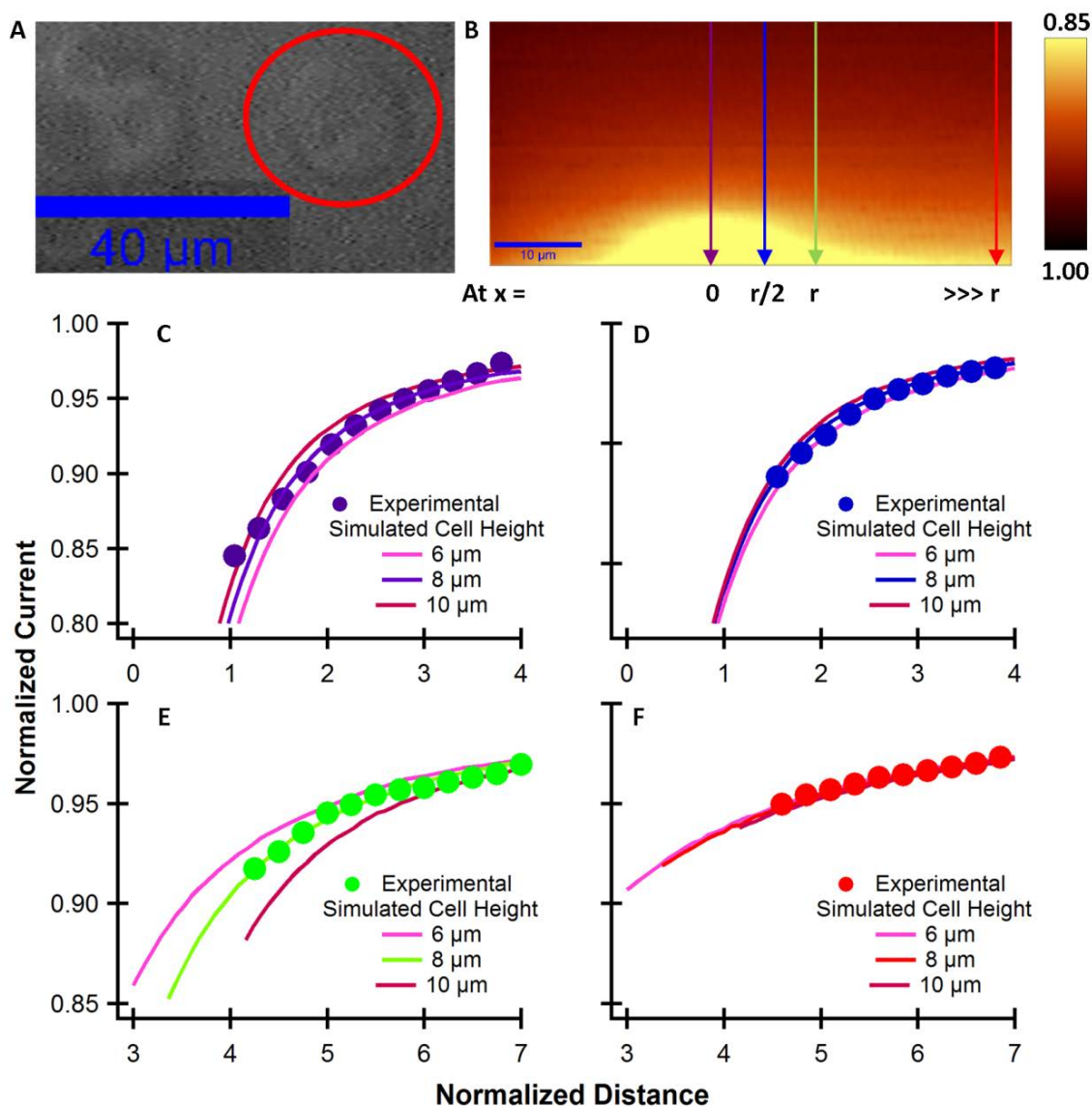


Figure 2.8. (A) An optical micrograph of a T24 cell under study with the cell encircled in red. (B) The corresponding SECM depth scan image taken across the cell using a 5 μm Pt UME, with the vertical cross-sectional lines identified for PAC extractions.

The purple cross-section represents the center of the cell ($x = 0$), which can be characterized with the traditional 2D-Axial simulations. The blue, green and red extractions require the 3D simulations ($x = r/2$, r , and $\gg r$, respectively). The extracted experimental PACs overlaid onto their respective simulated curves, at $x =$ (C) 0 (purple), (D) $r/2$ (blue), and (E) r (green) and (F) $\gg r$ (red).

The extracted experimental PACs were overlaid onto a set of theoretical PACs simulated at the same geometric position relative to the cell center in Figure 2.8. This allowed quantification of tip-to-sample distances at their respective locations. From the SECM image and the corresponding PAC over the direct center of the cell, the height of the cell is at its maxima, achieving a tip-to-sample distance of 2.6 μm (Figure 2.8C). When the PAC is extracted at a distance half a radii away, the tip-to-sample distance becomes greater (3.9 μm) confirming the cell is flatter at this region (Figure 2.8D). Taking a PAC at the edge of the cell ($x = r$, determined by horizontal cross-section) the tip-to-sample distance becomes 10.6 μm (Figure 2.8E), whereas a PAC to the dish itself ($x \gg r$, Figure 2.8F) revealed a tip-to-sample distance of 11.5 μm . The discrepancy between the tip-to-sample distances at the cell edge and the petri dish is due to the cell's influence on this location's PAC, since extracted PACs taken at a distance of $x < 2r$ from the cell center can still influence the curves.⁴² We can also conclude through the PACs that when the UME is furthest away from the cell center (x direction), the curvature or chemical feedback influence from the sample or substrate is weakened. Over the petri dish, the electrochemical feedback is at its weakest since the SECM probe is furthest away from the substrate. The full extended set of theoretical PACs in Figures 2.8C-F is included in Appendix II (Figure S2.7).

Similar to the 2D methodology in determining the height of the cells, the heights across the cell can be also be assessed by the 3D simulation method. For instance, through comparison of the closest approach to the cell and the petri dish, the cell bears a height of 8.9 μm (eqn 2.9), while the parametric cell height method quantifies this cell as having a height of 8 μm (Figure 2.8C). Quantifying the cellular height based on the traditional PAC extraction approach and parametric cell height method produce similar cell heights, within approximately 10 % agreement (Table 2.1). However, the 2D methodology limits these PAC extractions to the direct center of the cell, whereas 3D simulations allow cellular height to be accessed across the depth scan image. At a distance of $x = r/2$ away from the cell center, the height of the cell is 7.3 μm , while $x = r$ away is 0.9 μm (eqn 2.9)

$$\text{Cell height, at } x = (L_{\text{petri dish}} - L_x) * a \quad (2.9)$$

This would confirm that this particular cell is indeed more ellipsoidal in shape as opposed to the hemispherical shape. While the electrochemical feedback in the SECM image (Figure 2.8B) may suggest a larger cell, the resolution limitation of the electrode makes the electrochemical feedback appear greater.⁴²

The precision of the cell heights determined through these SECM/simulation methodologies agrees quite well with experimental observations, where the electrode was physically lowered to the petri dish by approximately 10 μm . While smaller electrodes do provide higher resolution, a closer approach to the substrate is required. With significant difference between the height of the cell and the petri dish, it becomes more difficult to accurately gauge the fitting of the PAC to the dish since a steady state current is detected at these tip-to-sample distances.

2.4.5 Horizontal Sweeps across the Cell

While vertical PACs are the more commonly used to study sample characteristics in SECM depth scan mode,^{12,26} horizontal cross-sections can also provide insights into cell topography. For example, horizontal cross-sections taken across the SECM image can be utilized to study the variations in cellular height across the cell, thereby allowing the cell's highest point to be located prior to the use of PACs extractions. Coupling 3D modelling in COMSOL such that full control of UME position over the cell surface is possible, the tip-to-cell distance or cellular geometry can be confirmed. Horizontal cross-sections can be simulated by moving the UME across the substrate at a fixed height (Figure 2.9). The UME's x position is parameterized allowing for the entire horizontal sweep to be performed as an automated sequence of simulations.

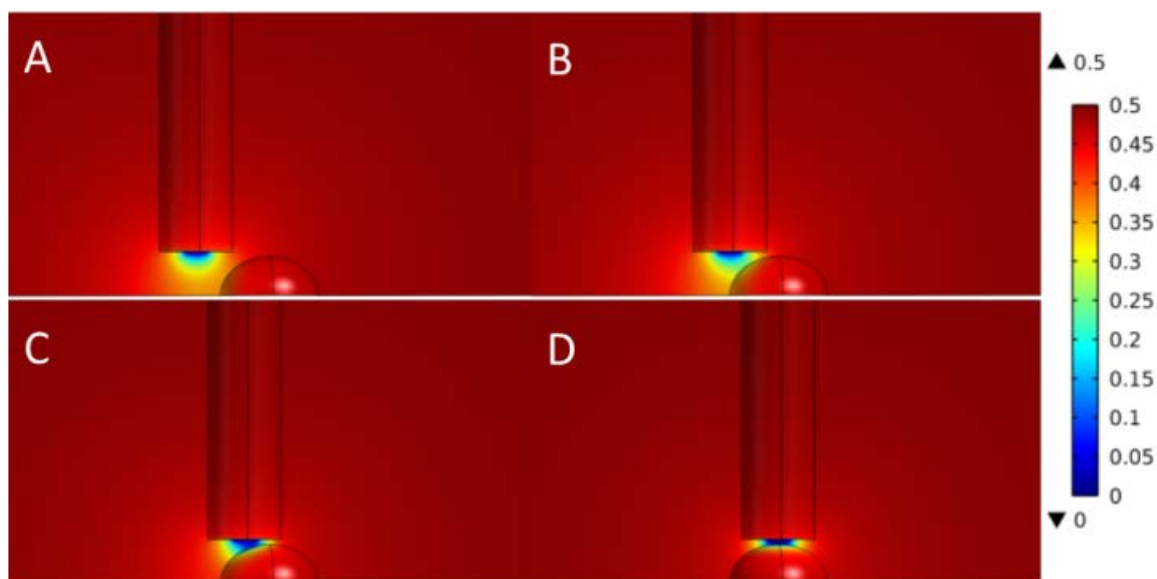


Figure 2.9. Simulated concentration maps of horizontal UME sweeps 1 μm above the cell at electrode x positions of (A) 15 μm away from cell center, $x = 1.5r$, (B) 10 μm away from the cell center (cell edge), $x = r$, (C) 5 μm away from the cell center, $x = r/2$, and (D) directly above cell center, at $x = 0r$.

Simulating a horizontal sweep 1 μm above the cell, for locations where the electrode is far from the cell ($x \geq 2r$, Figure 2.10A), the detected faradaic current (red region) is more or less typical of a horizontal sweep across the insulating glass petri dish at the same tip-to-substrate distance. Once the UME is in close proximity to the cell (Figures 2.10B-D), the limited diffusion effects from the cell causes a current drop that results in increased negative feedback. As the electrode sweeps directly over the cell, the current depletion region becomes visually reduced. Utilizing these simulated horizontal line scans, we can determine the obtained tip-to-cell distances accurately (Figure 2.10).

Three horizontal cross-sections were taken above the cell, one at the edge of the scan window (blue) and two horizontal cross-sections 5 and 10 μm above this height (red and black respectively, Figure 2.10B). To normalize these currents, a current reading from the SECM image 80 μm above the dish was used (steady state current region). Horizontal sweep curves of the UME were simulated at a number of distances (0.5-60.0 μm) above the cell and plotted together (1.5-10.0 μm shown in Figure 2.10B, for the full set please see Figure S2.8 in Appendix II).

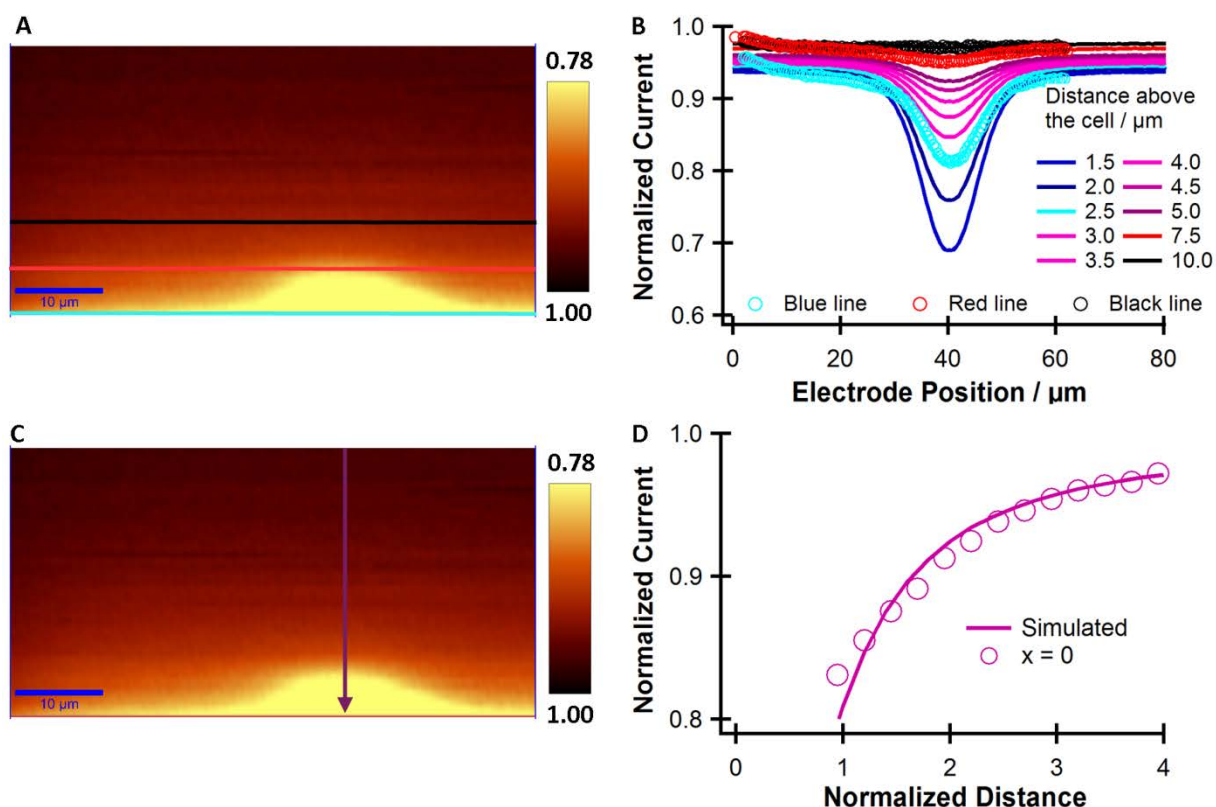


Figure 2.10. (A) A horizontally-labelled SECM depth scan image taken across the cell using a 5 μm Pt UME. The blue line is taken at the edge of the image, the red and black lines taken 5 and 10 μm above the blue line respectively. (B) Simulated and experimental SECM horizontal sweeps across the cell. The UME probe distances (above the cell) in micrometers are indicated in the legend for the simulated curves. (C) The vertically-labelled SECM depth scan image above the center of the cell. (D) The simulated and experimental PACs extracted over the center of the cell.

Over the flat insulating portion of the petri dish ($0 \mu\text{m} < x < 30 \mu\text{m}$ and $50 \mu\text{m} > x > 60 \mu\text{m}$, absent of any cell), the steady state oxidative current was detected since $d_{\text{petri dish}} = d_{\text{Cell}} + 8 \mu\text{m}$ ($L_{\text{petri dish}} = L_{\text{Cell}} + 3.2$) for a 5 μm Pt UME. For the 5 μm Pt UME, any substrate effects on the current are subtle, almost negligible. When the electrode is positioned over the cell ($30 \mu\text{m} < x < 50 \mu\text{m}$), the electrochemical influence can be observed; when the UME probe is over the direct center of the cell, the largest electrochemical feedback is detected (at approximately 40 μm , Figure 2.10B). This suggests that the smallest

tip-to-cell distance is achieved, defining the minimal L value for all electrode positions across the particular SECM image.

Extracting a horizontal cross-section above the cell (blue) at the edge of the image, the experimental curve overlaps to the simulated horizontal sweep $2.5\ \mu\text{m}$ above the cell (blue circles in Figure 2.10B). Extracting other experimental horizontal cross-sections 5 and $10\ \mu\text{m}$ above the blue line (red and black lines respectively in Figure 2.10B), the curves overlapped quite well to the corresponding simulated curves at probe distances 7.5 and $10.0\ \mu\text{m}$ above the cell. At a simulated horizontal sweep greater than $10\ \mu\text{m}$ above the cell ($L > 4$), the stimulated and experimental horizontal sweeps were indistinguishable from one another, which explains why the black experimental sweep overlaps well a probe-to-cell distance of $10\ \mu\text{m}$ (as opposed to $12.5\ \mu\text{m}$).

Similar to the effects of an SECM probe's approach to an interdigitated array of electrodes,³³ the amplitude of the curve increased as the tip-to-sample distance of the horizontal sweep decreased. In the case of the cell, the amplitude of the curve was largest at the direct center, suggesting this region of cell was at its most maximum height. With the successful overlaying of the experimental curve to simulated horizontal sweeps, it is believed the cellular geometry is indeed elliptical.

To confirm the horizontal sweep was simulated correctly, a comparison of the PAC to the center of the cell was made (purple line in Figure 2.10C). Overlaying the PAC onto its simulated curve, it can be seen that a distance of $2.4\ \mu\text{m}$ was achieved (Figure 2.10D). The fitting of the horizontal sweep (tip-to-cell distance of $2.5\ \mu\text{m}$, Figure 2.10B) is in close agreement to the fitting of the vertical PAC. This demonstrates the validity of the 3D horizontal sweep simulations.

2.4.6 Horizontal Imaging of the Cell

The UME's x axis parametric sweep can be nested inside of another parametric sweep in COMSOL, controlling the UME's z direction movement. The electrode height is fixed at the first defined height in the outer parametric sweep, performing a full horizontal sweep at this z position. On completion of this inner parametric sweep of the x position, the outer

parametric sweep increments to the next z position, repeating the horizontal sweep process. This process continues until all combinations of electrode's x and z positions within the desired ranges are simulated. A matrix of the UME tip current at all electrode positions can be generated from the nested parametric sweep simulation, allowing for the simulation of entire depth scan images (Figure 2.11).

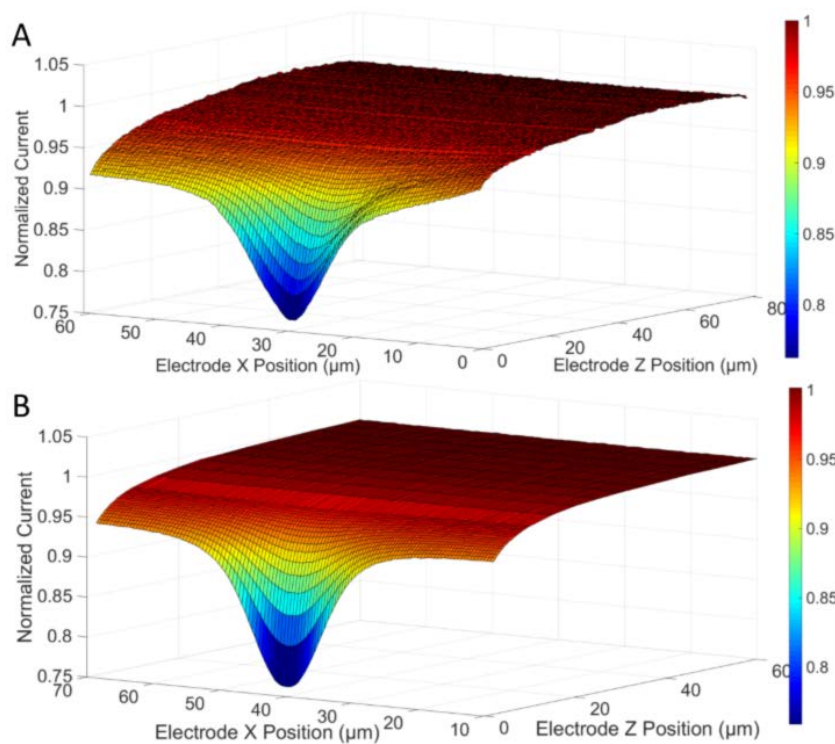


Figure 2.11. (A) Experimental and (B) simulated depth scans collected with a 5 μm UME with an RG of 3 approaching a single cell with a height of 8 μm and a diameter of 20 μm . The theoretical UME approaches to 2.0 μm from the highest point on the cell during its closest horizontal sweep. The experimental depth scan is determined to approach to a height of 2.6 μm above the cell.

The experimental depth scan images (Figure 2.11A) can be compared to simulated depth scans (Figure 2.11B) for the general cell shape and individual cross-sections which can be obtained from images in either the x or z directions. From Figure 2.11A, we can see the experimental SECM scan lies in close agreement to the simulated cell when the SECM probe is 2.0 μm above (bottom curve in Figure 2.11B). We can see from both the experimental and simulation images, the diffusion of the FcCOO^- is most hindered when the UME is above the

center of the cell (blue region in image). From the shape of experimental sweep and its agreement to the simulated curves (Figures 2.10B and 2.11B), we can confirm the cellular geometry appears to be elliptical in shape.

2.5 Conclusions

3D simulation models were used to assess the cellular height across different locations over the cell. This 3D simulation model allowed us to access additional approaches by SECM depth scan imaging, previously inaccessible by the traditional 2D axially symmetric models. These simulations allowed for the fitting of both the vertical PACs and horizontal sweeps across the cell and petri dish surface.

Using an impermeable non-toxic redox agent as a molecular sensor we were able to determine cellular geometry and topography, as well as access the accuracy of the SECM probe-to-cell distances (from PACs). Cell heights were determined using two different methods: (1) the traditional approach, where the comparison of the PACs to the cell and dish (using both 2D and 3D simulations) yields the cell height and (2) direct comparison of the experimental PAC to simulated curves, where the height is parameterized, yields the cell height. Both methods produce similar cell heights, regardless of the simulation method used (within 10% difference). We confirmed that the cell was at its highest height at the direct center of the cell, detecting the strongest electrochemical feedback at this location. While stronger feedback can be detected using a smaller electrode, more error is associated with the fitting of the PAC further away from the cell, since $L_{\text{petri dish}} > 3.2$ for 5 μm (vs. 1.6 for a 10 μm electrode).

In addition, 3D simulations of the cell allowed more PACs from the depth scan images to be accessible. Through height quantification across the cell we were able to determine that these tested individual live cells appeared to be more elliptical in morphology when adhered onto a surface. It is anticipated that the topography of individual cells without elliptical symmetry can be assessed by means of 3D simulations.

2.6 References

1. Bard, A. J.; Faulkner, L. R. *Electrochemical Methods: Fundamentals and Applications, 2nd Edition*. 2 ed.; John Wiley & Sons, Inc.: 2001.
2. Bard, A. J.; Mirkin, M. V. *Scanning Electrochemical Microscopy*. 2 ed.; CRC Press: 2012.
3. Zoski, C. G. Review - Advances in Scanning Electrochemical Microscopy (SECM). *J. Electrochem. Soc.* **2015**, *163*, H3088-H3100.
4. Bard, A.; Fan, F.; Kwak, J.; Lev, O. Scanning Electrochemical Microscopy. Introduction and Principles. *Anal. Chem.* **1989**, *61*, 132-138.
5. Nowierski, C.; Noël, J. J.; Shoesmith, D. W.; Ding, Z. Correlating Surface Microstructures with Reactivity on Commercially Pure Zirconium using Scanning Electrochemical Microscopy and Scanning Electron Microscopy. *Electrochem. Commun.* **2009**, *11*, 1234-1236.
6. Yin, Y.; Niu, L.; Lu, M.; Guo, W.; Chen, S. In Situ Characterization of Localized Corrosion of Stainless Steel by Scanning Electrochemical Microscope. *Appl. Surf. Sci.* **2009**, *255*, 9193-9199.
7. Combellas, C.; Fuchs, A.; Kanoufi, F. Scanning Electrochemical Microscopy with a Band Microelectrode: Theory and Application. *Anal. Chem.* **2004**, *76*, 3612-3618.
8. Ding, Z.; Quinn, B. M.; Bard, A. J. Kinetics of Heterogeneous Electron Transfer at Liquid/Liquid Interfaces as Studied by SECM. *J. Phys. Chem. B* **2001**, *105*, 6367-6374.
9. Tang, J.; Zheng, J.-J.; Yu, Y.-T.; Chen, L.; Zhang, N.; Tian, Z. Selective Etching of ZnO Films on an ITO Substrate using a Scanning Electrochemical Microscope. *Electrochim. Acta* **2012**, *83*, 247-252.
10. Eifert, A.; Mizaikoff, B.; Kranz, C. Advanced Fabrication Process for Combined Atomic Force-Scanning Electrochemical Microscopy (AFM-SECM) Probes. *Micron* **2015**, *68*, 27-35.
11. Amemiya, S.; Guo, J.; Xiong, H.; Gross, D. Biological Applications of Scanning Electrochemical Microscopy: Chemical Imaging of Single Living Cells and Beyond. *Anal. Bioanal. Chem.* **2006**, *386*, 458-471.
12. Li, M. S. M.; Filice, F. P.; Ding, Z. A Time Course Study of Cadmium Effect on Membrane Permeability of Single Human Bladder Cancer Cells using Scanning Electrochemical Microscopy. *J. Inorg. Biochem.* **2014**, *136*, 177-183.

13. Kuss, S.; Polcari, D.; Geissler, M.; Brassard, D.; Mauzeroll, J. Assessment of Multidrug Resistance on Cell Coculture Patterns using Scanning Electrochemical Microscopy. *Proc. Natl. Acad. Sci. U. S. A.* **2013**, *110*, 9249-9254.
14. Kuss, S.; Cornut, R.; Beaulieu, I.; Mezour, M. A.; Annabi, B.; Mauzeroll, J. Assessing Multidrug Resistance Protein 1-Mediated Function in Cancer Cell Multidrug Resistance by Scanning Electrochemical Microscopy and Flow Cytometry. *Bioelectrochemistry* **2011**, *82*, 29-37.
15. Beaulieu, I.; Kuss, S.; Mauzeroll, J.; Geissler, M. Biological Scanning Electrochemical Microscopy and Its Application to Live Cell Studies. *Anal. Chem.* **2011**, *83*, 1485-1492.
16. Koley, D.; Bard, A. J. Triton X-100 Concentration Effects on Membrane Permeability of a Single HeLa Cell by Scanning Electrochemical Microscopy (SECM). *Proc. Natl. Acad. Sci. U. S. A.* **2010**, *107*, 16783-16787.
17. Liu, B.; Rotenberg, S. A.; Mirkin, M. V. Scanning Electrochemical Microscopy of Living Cells: Different Redox Activities of Nonmetastatic and Metastatic Human Breast Cells. *Proc. Natl. Acad. Sci. U. S. A.* **2000**, *97*, 9855-9860.
18. Nioradze, N.; Kim, J.; Amemiya, S. Quasi-Steady-State Voltammetry of Rapid Electron Transfer Reactions at the Macroscopic Substrate of the Scanning Electrochemical Microscope. *Anal. Chem.* **2011**, *83*, 828-835.
19. Cannan, S.; Cervera, J.; Steliaros, R. J.; Bitziou, E.; Whitworth, A. L.; Unwin, P. R. Scanning Electrochemical Microscopy (SECM) Studies of Catalytic EC [Prime or Minute] Processes: Theory and Experiment for Feedback, Generation/Collection and Imaging Measurements. *Phys. Chem. Chem. Phys.* **2011**, *13*, 5403-5412.
20. Matrab, T.; Hauquier, F.; Combellas, C.; Kanoufi, F. Scanning Electron Microscopy Investigation of Molecular Transport and Reactivity within Polymer Brushes. *ChemPhysChem* **2010**, *11*, 670-682.
21. Zhu, R.; Macfie, S. M.; Ding, Z. Cadmium-Induced Plant Stress Investigated by Scanning Electrochemical Microscopy. *J. Exp. Bot.* **2005**, *56*, 2831-2838.
22. Wang, Y.; Noël, J.-M.; Velmurugan, J.; Nogala, W.; Mirkin, M. V.; Lu, C.; Guille Collignon, M.; Lemaître, F.; Amatore, C. Nanoelectrodes for Determination of Reactive Oxygen and Nitrogen Species Inside Murine Macrophages. *Proc. Natl. Acad. Sci. U. S. A.* **2012**, *109*, 11534-11539.
23. Zhao, X.; Lam, S.; Jass, J.; Ding, Z. Scanning Electrochemical Microscopy of Single Human Urinary Bladder Cells using Reactive Oxygen Species as Probe of Inflammatory Response. *Electrochem Comm* **2010**, *12*, 773-776.

24. Zhao, X.; Petersen, N. O.; Ding, Z. Comparison Study of Live Cells by Atomic Force Microscopy, Confocal Microscopy, and Scanning Electrochemical Microscopy. *Can. J. Chem.* **2007**, *85*, 175-183.
25. Zhao, X.; Diakowski, P.; Ding, Z. Deconvoluting Topography and Spatial Physiological Activity of Live Macrophage Cells by Scanning Electrochemical Microscopy in Constant-Distance Mode. *Anal. Chem.* **2010**, *82*, 8371-8373.
26. Zhang, M. M. N.; Long, Y.-T.; Ding, Z. Cisplatin Effects on Evolution of Reactive Oxygen Species from Single Human Bladder Cancer Cells Investigated by Scanning Electrochemical Microscopy. *J. Inorg. Biochem.* **2012**, *108*, 115-122.
27. Liebetrau, J. M.; Miller, H. M.; Baur, J. E.; Takacs, S. A.; Anupunpisit, V.; Garris, P. A.; Wipf, D. O. Scanning Electrochemical Microscopy of Model Neurons: Imaging and Real-Time Detection of Morphological Changes. *Anal. Chem.* **2002**, *75*, 563-571.
28. Kurulugama, R. T.; Wipf, D. O.; Takacs, S. A.; Pongmayteegul, S.; Garris, P. A.; Baur, J. E. Scanning Electrochemical Microscopy of Model Neurons: Constant Distance Imaging. *Anal. Chem.* **2005**, *77*, 1111-1117.
29. Nebel, M.; Eckhard, K.; Erichsen, T.; Schulte, A.; Schuhmann, W. 4D Shearforce-Based Constant-Distance Mode Scanning Electrochemical Microscopy. *Anal. Chem.* **2010**, *82*, 7842-7848.
30. Yasukawa, T.; Uchida, I.; Matsue, T. Permeation of Redox Species through a Cell Membrane of a Single, Living Algal Protoplast Studied by Microamperometry. *Biochim. Biophys. Acta* **1998**, *1369*, 152-158.
31. Zhang, M. N.; Ding, Z.; Long, Y. T. Sensing Cisplatin-Induced Permeation of Single Live Human Bladder Cancer Cells by Scanning Electrochemical Microscopy. *Analyst* **2015**, *140*, 6054-6060.
32. Sklyar, O.; Wittstock, G. Numerical Simulations of Complex Nonsymmetrical 3D Systems for Scanning Electrochemical Microscopy Using the Boundary Element Method. *J. Phys. Chem. B* **2002**, *106*, 7499-7508.
33. Filice, F. P.; Li, M. S. M.; Henderson, J. D.; Ding, Z., Three-Dimensional Electrochemical Functionality of an Interdigitated Array Electrode by Scanning Electrochemical Microscopy. *J. Phys. Chem. C* **2015**, *119*, 21473-21482.
34. Mosmann, T. Rapid Colorimetric Assay for Cellular Growth and Survival: Application to Proliferation and Cytotoxicity Assays. *J. Immunol. Methods* **1983**, *65*, 55-63.
35. Zhu, R.; Macfie, S. M.; Ding, Z. Effects of Cadmium on Photosynthetic Oxygen Evolution from Single Stomata in *Brassica Juncea* (L.) Czern. *Langmuir* **2008**, *24*, 14261-14268.

36. Zhang, M. M.; Long, Y. T.; Ding, Z. Filming a Live Cell by Scanning Electrochemical Microscopy: Label-Free Imaging of the Dynamic Morphology in Real Time. *Chem. Cent. J.* **2012**, *6*, 20.
37. Li, M. S. M.; Filice, F. P.; Henderson, J. D.; Ding, Z. F. Probing Cd²⁺-Stressed Live Cell Membrane Permeability with Various Redox Mediators in Scanning Electrochemical Microscopy. *J. Phys. Chem. C* **2016**, *120*, 6094-6103.
38. Li, M. S. M.; Filice, F. P.; Ding, Z. F. Determining Live Cell Topography by Scanning Electrochemical Microscopy. *J. Electroanal. Chem.* **2016**, *779*, 176-186.
39. Adam, C.; Kanoufi, F.; Sojic, N.; Etienne, M. Shearforce Positioning of Nanoprobe Electrode Arrays for Scanning Electrochemical Microscopy Experiments. *Electrochim. Acta* **2015**, *179*, 45-56.
40. Rossier, J. S.; Vollet, C.; Carnal, A.; Lager, G.; Gobry, V.; Girault, H. H.; Michel, P.; Reymond, F. Plasma Etched Polymer Microelectrochemical Systems. *Lab Chip* **2002**, *2*, 145-150.
41. Guo, J.; Amemiya, S. Permeability of the Nuclear Envelope at Isolated Xenopus Oocyte Nuclei Studied by Scanning Electrochemical Microscopy. *Anal. Chem.* **2005**, *77*, 2147-2156.
42. Filice, F. P.; Li, M. S. M.; Henderson, J. D.; Ding, Z. Mapping Cd²⁺-Induced Membrane Permeability Changes of Single Live Cells by Means of Scanning Electrochemical Microscopy. *Anal. Chim. Acta* **2016**, *908*, 85-94.

Chapter 3

3 A Time Course Study of the Cadmium Effects on Membrane Permeability in Single Human Bladder Cancer Cells Using Scanning Electrochemical Microscopy

(A version of this work has been published in the *Journal of Bioinorganic Chemistry*

Li, M.S.M.; Filice, F.P.; Ding, Z. *J. Inorg. Biochem.* **2014**, *136*, 177-183.)

3.1 Introduction

Scanning electrochemical microscopy (SECM) is a powerful electroanalytical technique that can be used to non-invasively study biological samples through the generation or regeneration of redox mediated species.¹⁻² Developed greatly by Bard *et al.* in 1989,³ it has progressed from chemical-based studies to being applied in biological systems^{1, 4-6} including, but not limited to, electron transfer kinetics and molecular transport studies,⁷⁻⁹ neurotransmitter,¹⁰⁻¹¹ reactive oxygen, and nitrogen species (ROS and RNS, respectively) release by live cells,¹²⁻¹⁶ as well as the assessment of drug resistance in biological cells.^{14, 17-18} SECM utilizes an ultramicroelectrode (UME) with a diameter less than 25 μm , that is biased at a potential at which a redox active species can be found in either its oxidized or reduced form. As the UME approaches the substrate, the current signal can be amplified if the UME probe approaches a conductive surface (regeneration of the non-oxidized or reduced form, positive feedback) or decreased if the UME probe approaches an insulating surface (blocked regeneration, negative feedback).

In literature, most research groups use one of the two common SECM imaging modes: constant height or constant distance. In constant height mode, the UME probe is held at a constant height and is scanned along the sample surface to study its topography. However, one major drawback of this method is the convolution of the faradaic processes and probe-to-sample distance effects that can occur if there is an uneven surface or if the sample is adhered to a substrate at varying heights. The UME probe can collide against the sample causing damage to either the sample and/or the electrode itself. In constant distance

mode, the UME probe will maintain a constant distance from the substrate and move up or down accordingly, deconvoluting the varying heights through the faradaic processes.

In SECM studies of live cells, three types of measurements are most widely used: (1) SECM imaging of the cells in which the current is measured and mapped as a function of the probe coordinates (horizontal plane), thus revealing the topography of the adhered cell^{15-16, 19-20} and/or the spatial profile of extracellular redox active species;^{15-16, 21-24} (2) probe approach curves (PACs), which are normalized current *vs.* normalized probe-to-cell distance plots, used to quantitatively determine kinetic parameters²⁵⁻²⁶ of a species across the cell membrane;^{20, 27-29} and (3) current-time curves (chronoamperometry) at specific probe-to-cell distances to study the evolutionary trend of cellular topography,²⁴ reactivity,³⁰ and the monitoring of very fast bursts of redox active species released by cells.³⁰⁻³¹ SECM has recently been used to investigate anti-cancer drugs and their treatment of cancers using ROS as the probe.¹⁴ However, the redox potentials of the ROS species are very close together which makes selectivity problematic.¹⁴ Another study conducted by Koley and Bard reported the successful investigation of membrane permeability in single live HeLa cells after their exposure to Triton X-100.²⁷ As the cell membrane is the first cellular barrier that anti-cancer drugs will interact with, it is important to study membrane permeability in live cells. Progression into membrane permeability research with SECM could widen the study of the interactions between cancerous cells and potential anti-cancer drugs, as well as preventative measures.^{27-29, 32}

Cadmium poisoning or intoxication can lead to numerous health issues, such as: cancers, immunodepression, and neurodegeneration.³³⁻³⁴ Cadmium can also affect gene expression by interacting with various transcription and translation factors,³⁵ both of which are important for successful DNA replication and protein synthesis in healthy cells. Studies have shown that Cd²⁺ intoxication can lead to increased oxidative stress through amplified ROS generation,³⁶⁻³⁷ which is already reported to be higher in cancerous cells.³⁸ Here, we look into the effects of Cd²⁺ intoxication on membrane permeability. We then compared the obtained results with previous SECM studies, in particular those involving cisplatin-induced cell death, as those studies were able to distinguish the means of cellular death by the extrinsic apoptosis pathway.³⁹⁻⁴¹

We have previously developed a SECM depth scan method where contacting of the UME with the sample is minimized by means of approaching the UME to the cells in the x - z or y - z plane.¹⁴ In this report, we use this SECM depth scan mode to approach single human bladder cancer (T24) cells and assess the changes in the permeability to ferrocenemethanol (FcCH₂OH), a non-toxic compound,^{15, 21} after Cd²⁺ treatment.

3.2 Experimental

The experimental details discussed here are the project-specific details briefly summarized. A more detailed report of the Experimental is included in Chapter 2.

3.2.1 Materials

Cadmium chloride (anhydrous grade) and FcCH₂OH (97%) were purchased from Sigma-Aldrich (Mississauga, ON), while potassium chloride (99%) was purchased from Alfa Aesar (Ward Hill, MA). Stock solutions of 1 M CdCl₂ was prepared in deionized water (18 MΩ.cm, MilliQ water, Millipore, Etobicoke, ON), while 0.45 mM FcCH₂OH with 0.05 M KCl (supporting electrolyte) were prepared in 1x phosphate buffered saline (PBS, 10 mM, pH 7.4). McCoy's 5A medium was purchased from American Type Culture Collection (ATCC, Manassas, VA), while all other culture solutions and serums were purchased from Invitrogen (Burlington, ON). All SECM live cell experiments were carried out at 37.0 ± 0.2 °C unless otherwise stated.

3.2.2 Electrochemical Measurements

A 5 μm Pt UME with RG2 (ratio of glass sheathing to conductive wire) was used for all electrochemical experiments described in this Chapter. Its fabrication procedure has been described in detail in Chapter 2. A Ag/AgCl wire was used as a combined auxiliary/reference electrode. Optical microscopy and cyclic voltammetry was used to examine the UME tip quality and functionality respectively.

Electrochemical experiments were performed using an electrochemical analyzer (CHI 800B, CH Instruments, Austin, TX) with a CHI 200 Picoamp Booster to reduce noise (CH Instruments), which was recorded by the Alpha-SNOM instrument (WITec, Ulm, Germany).^{14, 42} The steady state oxidative potential of FcCH₂OH (0.300 V vs. Ag/AgCl) was

identified from a cyclic voltammogram of 0.45 mM FcCH₂OH with 0.05 M KCl as the supporting electrolyte in 1x PBS.

3.2.3 SECM Measurements

For the SECM experiments, T24 cells (ATCC® HTB-4™) were plated on glass bottom dishes (P35G-0-20C, MatTek Corporation, Ashland, MA) and allowed to adhere and grow overnight. The growth medium, McCoy's 5A media supplemented with 10% fetal bovine serum, was removed and T24 cells were washed 3x with 1x PBS. The growth medium was then replaced with 0.45 mM FcCH₂OH and 0.05 M KCl in PBS.

The petri dish was mounted onto the scanning stage (P-517K064, Polytec PI, Germany) of the Alpha-SNOM and maintained at 37.0 ± 0.2 °C (Bioscience Tools, San Diego, CA). Using the Alpha-SNOM positioning system along with an inverted objective lens (Nikon, 50x magnification, N.A.: 0.55, Japan), prospective single live T24 cells were located. The distance between a single cell and the UME probe was optimized by using SECM depth scans. Experimental PACs were obtained by drawing vertical lines above the cell and studied immediately after each scan to confirm no contact with the cell was being made.

Once optical cell-probe distance was determined, another T24 cell (on the same petri dish) was studied for its response to Cd²⁺ stimulation. The first SECM depth scan of this cell was declared to be taken at $t = 0$ min. This was followed by the injection of Cd²⁺ directly into the mediator solution at $t = 5$ min. SECM depth scans were taken every 5 min for 50 min. Each SECM depth scan image has 128 x 128 pixels, a scan scale of 60 μm in width and either 20 or 25 μm in depth. An integration time of 0.01 s was chosen for these scans. These SECM scans had a tip speed of 6.19 and 7.73 μm/s for depth scans of depth 20 and 25 μm respectively.

3.3 Simulations

In the simulation process, we assume a simple one-electron oxidation reaction of FcCH₂OH (reduced species, R) to Fc⁺CH₂OH (oxidized species, O) at the UME surface:



Since the oxidation of FcCH₂OH is a diffusion-controlled process at 0.300 V vs. Ag/AgCl, the concentrations of FcCH₂OH outside the cell, $c_R(r, z, t)$, and inside the cell, $c_{R1}(r, z, t)$, follow Fick's second law of diffusion:

$$\frac{\partial c_R(r,z,t)}{\partial t} = D_R \left(\frac{\partial^2 c_R(r,z,t)}{\partial r^2} + \frac{1}{r} \frac{\partial c_R(r,z,t)}{\partial r} + \frac{\partial^2 c_R(r,z,t)}{\partial z^2} \right) \quad (3.2)$$

$$\frac{\partial c_{R1}(r,z,t)}{\partial t} = D_{R1} \left(\frac{\partial^2 c_{R1}(r,z,t)}{\partial r^2} + \frac{1}{r} \frac{\partial c_{R1}(r,z,t)}{\partial r} + \frac{\partial^2 c_{R1}(r,z,t)}{\partial z^2} \right) \quad (3.3)$$

where r and z are the axial symmetric coordinates, t is the time, and D is the diffusion coefficient of FcCH₂OH, which was assumed to be the same for both inside and outside of the cell ($7.6 \times 10^{-10} \text{ m}^2/\text{s}$).^{28, 43}

In the simulation model, the T24 cell is represented as a nominal semi-oblate spheroid with polar and equatorial lengths of 8 and 15 μm , respectively. We assumed 2D axial symmetry at the center of the cell (Figure 3.1). Since the concentration of oxidized species (O) generated at the UME tip is very small outside the cell, it is therefore negligible inside the cell.

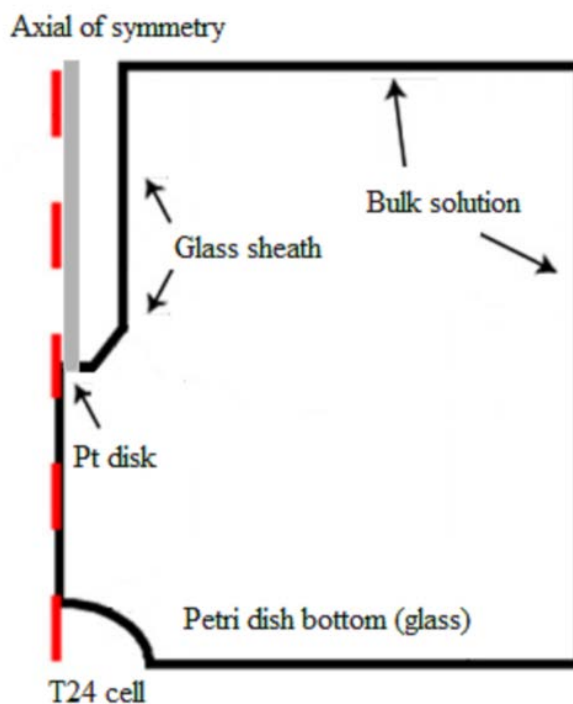


Figure 3.1. A schematic of the 2D axial geometry simulated in COMSOL 3.5a. c_R and c_{R1} are the bulk concentrations outside and inside the cell, respectively. The boundary conditions at the cell membrane are the inward and outward fluxes of FcCH_2OH across the cell membrane: $f_{\text{in}} = P_m (c_R - c_{R1})$ and $f_{\text{out}} = P_m (c_{R1} - c_R)$.

The boundary conditions are described as the following:

When $t = 0$ min and $E = 0.000$ V at the UME tip, the concentration of FcCH_2OH inside the cell is:

$$c_{R1} = 0 \text{ mol/m}^3 \quad (3.4)$$

The concentration of FcCH_2OH in the outer solution is:

$$c_R = 0.45 \text{ mol/m}^3 \quad (3.5)$$

When $0 < t \leq 10$ min and $E = 0.000$ V, the inward and outward fluxes of FcCH_2OH across the cell membrane are:^{27, 29}

$$f_{\text{in}} = P_m (c_R - c_{R1}) \quad (3.6)$$

$$f_{\text{out}} = P_m (c_{R1} - c_R) \quad (3.7)$$

where f_{in} and f_{out} are the inward and outward fluxes of FcCH₂OH relative to the cell and P_m is the permeability coefficient.

Since no potential is applied to the UME at this moment, the Pt surface is equivalent to an insulating surface. The concentration gradient of FcCH₂OH at the Pt surface is therefore:

$$\frac{\partial c_R(r,z,t)}{\partial z} = \frac{\partial c_R(r,z,t)}{\partial r} = 0 \quad (3.8)$$

The concentration gradients of FcCH₂OH at glass sheath and petri dish are the same as eqn 3.8.

The concentration gradient of FcCH₂OH at the axis of symmetry is:

$$\left[\frac{\partial c_R(r,z,t)}{\partial r} \right]_{r=0} = 0 \quad (3.9)$$

When $t > 10$ min and $E = 0.300$ V, the inward and outward fluxes of FcCH₂OH across the cell membrane follows eqns 3.6 and 3.7, respectively.

Under the applied potential of 0.300 V, FcCH₂OH is oxidized at the diffusion-controlled rate. Therefore the concentration of FcCH₂OH at the Pt surface is

$$c_R(r, z, t) = 0 \quad (3.10)$$

The tip current, i , can be obtained by integrating the flux towards the Pt surface:

$$i = 2\pi nDF \int_0^a r \left[\frac{\partial c_R(r,z,t)}{\partial z} \right] dr \quad (3.11)$$

where n is the number of electrons transferred in the oxidation of FcCH₂OH (1), F is Faraday constant (96,485 C/mol), and a is the radius of the Pt surface.

The simulation model was solved by running finite elemental analysis using COMSOL Multiphysics v.3.5 (COMSOL Inc., Burlington, MA). In general practice, for each permeability value, P_m , a simulated PAC was obtained by plotting the normalized current versus the normalized distances (as discussed in Chapter 2).

For each simulated PAC, no FcCH₂OH was assumed to be inside the cell at $t = 0$ min. For the first 10 min, the concentration profiles of FcCH₂OH both inside and outside of the cell were calculated under the assumption that the UME was far from the cell and inactive.²⁷ At $t = 10$ min, the previously calculated concentration profiles were used as the initial parameters for the internal and external domains. When the UME tip is biased at 0.300 V, the steady state diffusion-controlled oxidation reaction of FcCH₂OH occurs at this boundary.²⁷ Sequential simulations with known P_m values and their respective normalized probe-cell distances and tip currents were performed to generate the simulated PACs.

The simulation mesh statistics included: 83,896 mesh points, 343,041 degrees of freedom, 167,315 elements (triangular), 4,442 boundary elements, 9 vertex elements, and a minimum element quality of 0.668. A COMSOL report on the details of the simulation code can be found in Appendix III.

3.4 Results and Discussion

3.4.1 Cadmium concentration addition

Cd²⁺ has been shown to increase the ROS generated in various cancer cell lines, such as PC12 and SH-SY5Y, activating cellular pathways which can ultimately lead to cellular death.³⁶ According to a paper by Chen *et al.*,³⁶ Cd²⁺ concentrations greater than 80 μ M can cause SH-SY5Y cells to undergo cellular death within several hours of exposure. Keeping this in mind, we wanted to use Cd²⁺ concentrations that would not generate a response too quickly in the cells that cannot be measured directly by SECM (due to scan length), but high enough to be informative.

Our initial experiments with Cd²⁺ were carried out in culture, growing the T24 cells in the presence of 10 mM Cd²⁺ (Figure 3.2), a concentration much higher than those presented in literature (often in the μ M range at an incubation time of several days).^{36, 44} The physiological appearance of the Cd²⁺-treated T24 cells became unhealthy and slightly contracted, possibly indicating that they are undergoing cellular death (Figure 3.2A and B).

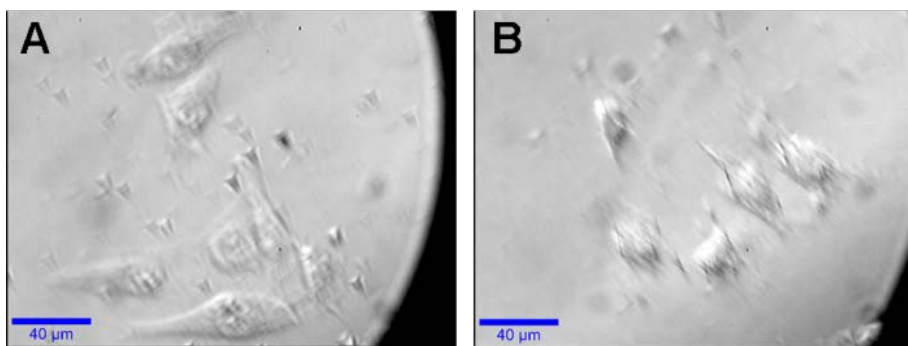


Figure 3.2. Optical micrographs of T24 cells (A) unexposed to Cd²⁺ and (B) exposed to 10 mM Cd²⁺ for 12 h.

After the addition of 10 mM Cd²⁺ to the biological media, the media quickly became acidic, as indicated by the change of the phenol red indicator in the media to a yellow-red color, while the control (unexposed) sample remained red. The SECM experiments were then planned as a time course study in order to examine the changes in the membrane permeability to FcCH₂OH upon immediate stimulation to Cd²⁺. The effects of Cd²⁺ on the T24 cells should be slow enough for a SECM depth scan (3.25 min) but fast enough to provide a better understanding of the change in membrane permeability.

3.4.2 SECM for time course measurements of membrane permeability

Figure 3.3A shows a typical optical micrograph of the control T24 cells, with the SECM probe located to the right of a T24 cell (encircled black spot). The SECM depth scan image in Figure 3.3B demonstrates a decreased current profile as the UME approached the T24 cell; this observation follows the SECM negative feedback principle. When the electrode was far from the cell (and substrate), hemispherical diffusion can occur to the electrode tip, resulting in a steady state current. When the electrode approached the cell, the hemispherical diffusion of the redox mediator to the electrode tip was blocked by the cell which results in a decreased tip current. This trend can be verified by the experimental PAC in Figure 3.3C, which was obtained by simply drawing a vertical line above the cell as illustrated in Figure 3.3B. To determine the membrane permeability coefficient, the experimental PACs were overlaid onto simulated theoretical PACs with preset permeability values (0.0 m/s to 1.0 x 10⁻³ m/s). Non-stimulated control T24 cells maintained constant

membrane permeability to FcCH_2OH , with a value of approximately $5.0 \times 10^{-5} \text{ m/s}$ up to 50 min (Figure 3.3C).

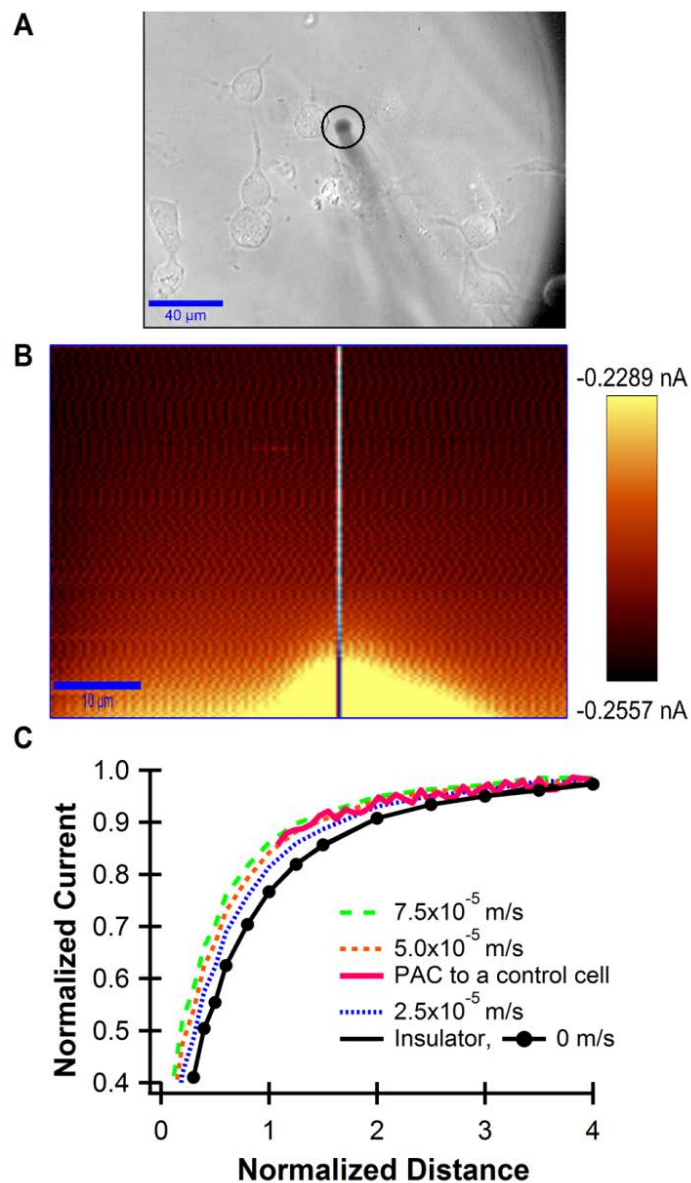


Figure 3.3. (A) An optical micrograph of control T24 cells. The black spot in the image is the UME, which is to the right of the cell of interest (circled). (B) A typical SECM depth scan image of a T24 cell unexposed to Cd^{2+} (control). (C) An experimental probe approach curve to a control T24 cell, taken at the vertical line above the cell as shown in (B). The experimental PAC is overlaid onto simulated curves of known membrane permeability coefficients.

In our SECM depth scans, while there is movement of our UME probe (in both the x and z direction), we assumed that convective transport is not a concern for the UME size.⁴⁵ The scanning of the biased UME in the x and z directions (previously described) generates the SECM depth scan image, which is collected across the entire cell body. Another advantage in using SECM in the depth scan imaging mode is it allow us to assess the membrane permeability changes in these live cells in a time course manner, simply by drawing a vertical line over the same location above the cell in each consecutive scan. Cell changes in their height during their “breath” processes do not affect their PAC measurements, provided that the cell does not make contact with the UME. When overlapping the experimental PACs to theoretical ones, we can take into account the “breath” process of the cell based on the shift in negative feedback curvature (L axis).

3.4.3 Time course study of Cd^{2+} effect on membrane permeability

Since T24 cells maintained constant membrane permeability to FcCH_2OH over time in the absence of any stimuli, any changes in membrane permeability after the addition of Cd^{2+} can solely be contributed to the interaction of Cd^{2+} with the cells. We assess any feedback changes observed in the PACs to be due to the increase or decrease of FcCH_2OH flux in or out of the cell as a result of the Cd^{2+} stimulation to the T24 cells. Other redox species native to the cell, such as ROS release from the cell, are not affected at the potential bias of 0.300 V (*vs.* Ag/AgCl).²² In a previous study, FcCH_2OH exposure in monkey kidney (COS-7) cells led to no morphological changes;¹⁵ it was also observed in this study to have no effect on the physical morphology of the T24 cells.

For this time course study of Cd^{2+} on T24 cell membrane permeability, FcCH_2OH was held constant at a final concentration of 0.45 mM, while Cd^{2+} was added in-situ at increasing final concentrations of 1.0, 2.5, 5.0, 7.5 and 10.0 mM. Time-lapsed SECM depth scans were obtained at time intervals of 5 min (3.25 min per scan, followed by 1.75 min rest period) for 50 min to study Cd^{2+} effects on the membrane permeability in T24 cells. 50 min was chosen as the experimental duration since the experimental PACs had stabilized well before 45 min (*ie.* no further changes in membrane permeability).

When 1.0 mM Cd^{2+} was added in-situ to the T24 cells, it was observed that there were very little morphological changes over the duration of the SECM experiments (Figures 3.4A and B). PACs extracted from the depth scan above the center of the cell (Figure 3.4C) revealed that the PACs displayed the same partial negative feedback curvature over 50 min (Figure 3.4D). This suggests that at this concentration and for this duration of Cd^{2+} exposure, the cell membrane permeability is constant (2.5×10^{-5} m/s, Figure 3.4D).

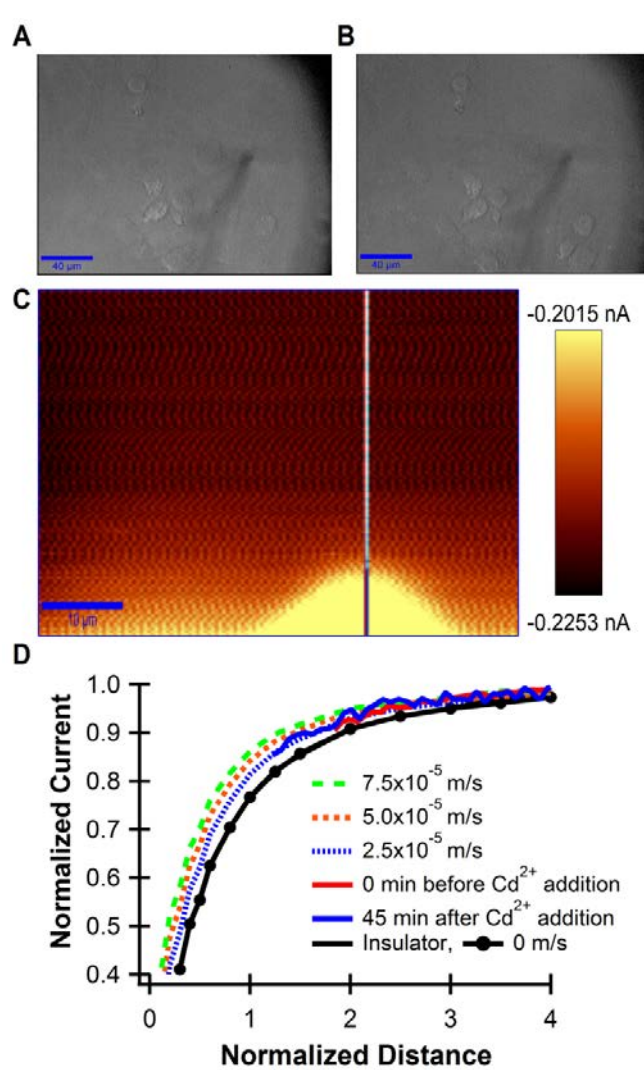


Figure 3.4. Optical micrographs of a T24 cell (A) before and (B) after exposure to 1 mM Cd^{2+} for 50 min, the UME is located to the right of the cell of interest. (C) A SECM depth scan image of the T24 cell as in (A) after 50 min of Cd^{2+} exposure. (D) PACs to the cell before (red, extracted along the vertical line in (C)) and 45 min after exposure to 1 mM Cd^{2+} (blue).

When the T24 cells are exposed to higher concentrations of Cd^{2+} , the membrane permeability also increased (Table 3.1).

Table 3.1. The initial and final membrane permeability of T24 cells exposed to various concentrations of Cd^{2+} .

$[\text{Cd}^{2+}]$ (mM)	Initial membrane permeability \pm standard deviation (m/s)	Final membrane permeability \pm standard deviation after the addition of Cd^{2+} (m/s)
1.0	$(2.5 \pm 0.3) \times 10^{-5}$	$(2.5 \pm 0.3) \times 10^{-5}$
2.5	$(5.0 \pm 0.3) \times 10^{-5}$	$(1.0 \pm 0.3) \times 10^{-4}$
5.0	$(5.0 \pm 0.3) \times 10^{-5}$	$(1.5 \pm 0.7) \times 10^{-4}$
7.5	$(5.0 \pm 0.3) \times 10^{-5}$	$(3.5 \pm 2.1) \times 10^{-4}$
10.0	$(3.8 \pm 1.8) \times 10^{-5}$	$(2.0 \pm 0.3) \times 10^{-4}$

The initial (control) average membrane permeability in all the single live cells experiments were $(4.3 \pm 1.1) \times 10^{-5}$ m/s. An increase in membrane permeability up to 3.5×10^{-4} m/s (7.5 mM Cd^{2+} , Table 3.1) suggested there is increased flux of FcCH_2OH from the cell to the UME tip.

For instance, when T24 cells were treated with 2.5 mM Cd^{2+} , the membrane permeability increased from 5.0×10^{-5} m/s to 1.0×10^{-4} m/s (Table 3.1). The higher the Cd^{2+} stimulation, it was observed that T24 cells would decreased in height (requiring the lowering of the electrode), as well as an increased in the surface area they occupied on the petri dishes. For example, in one of the 10.0 mM Cd^{2+} experiments, the T24 cell became flattened and its spreading over the petri dish increased so significantly (Figures 3.5A and B), the electrode was required to be lowered 14 μm to obtain feedback.

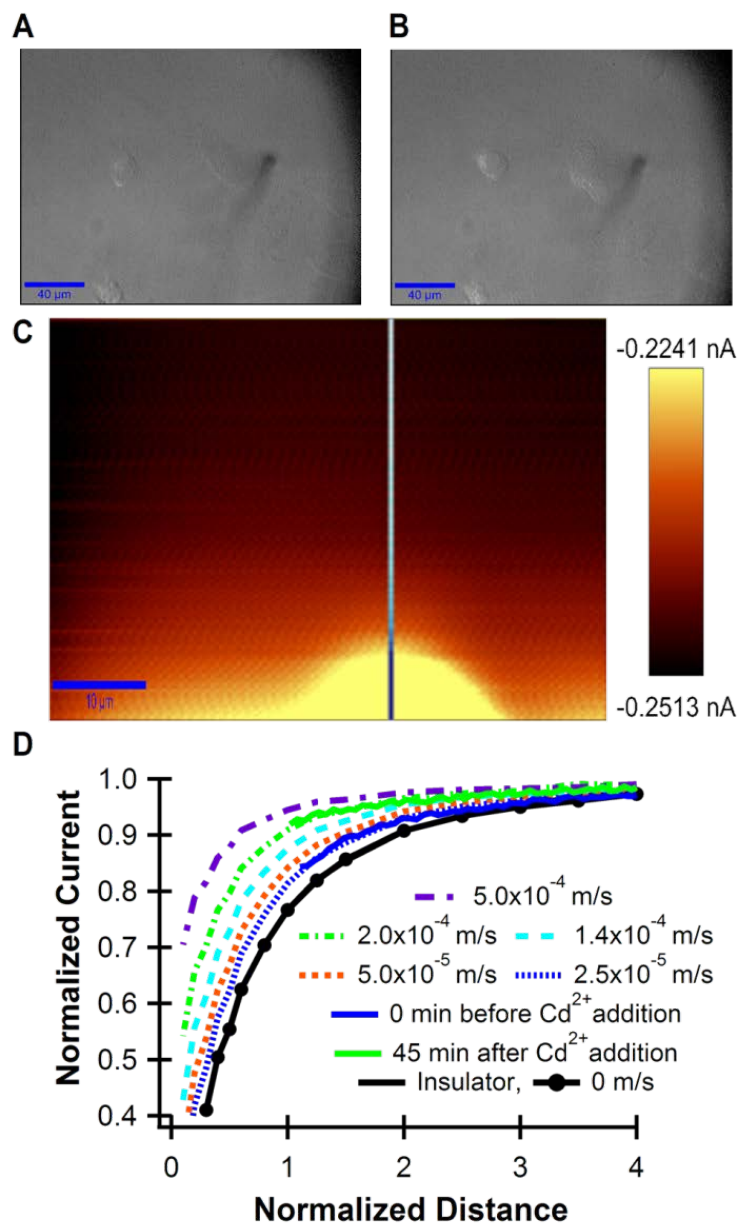


Figure 3.5. Optical micrographs of a T24 cell (A) before and (B) after exposing to 10 mM Cd²⁺ for 45 min, where the UME is to the right of the cell. (C) A SECM depth scan image of the T24 cell as in (A) after 50 min of Cd²⁺ exposure. PACs to the cell before (red in (D)), extracted along the vertical line in (C)) and 45 min after exposing to 1 mM Cd²⁺ (blue in (D)).

It was interesting to note that after higher Cd^{2+} treatments and longer exposure times, the nucleus of the T24 cell was observable without the aid of immunocytochemistry (see Figure S3.1 in Appendix III). When the membrane permeability to FcCH_2OH is increased, there is more flux of FcCH_2OH from the cell to the UME tip, making the partial negative feedback more partially positive (more conductor-like). This is due to the spreading of the membrane phospholipids heads, allowing more FcCH_2OH molecules to enter and leave the cell.

SECM could be used to quantitatively measure the membrane permeability. Figure 3.6 illustrates the time course changes in membrane permeability after 1.0 mM and 7.5 mM Cd^{2+} treatments.

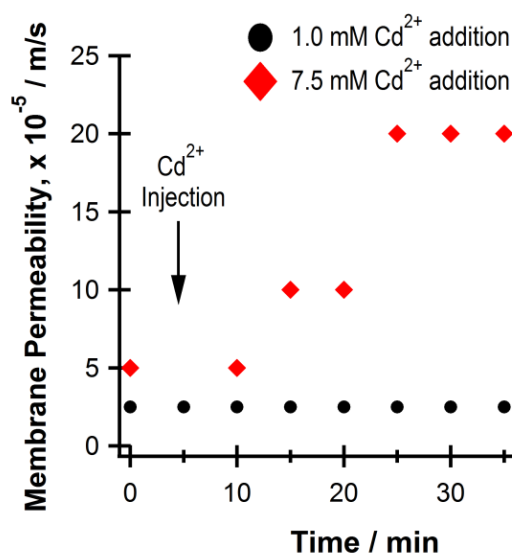


Figure 3.6. Permeability of FcCH_2OH as a function of time for T24 cells treated with 1.0 and 7.5 mM Cd^{2+} . Note, the membrane permeability at $t = 5$ min was removed due to the intense current spike which occurs immediately after the addition of 7.5 mM Cd^{2+} .

From Figure 3.6, it can be seen that the membrane permeability to FcCH_2OH does not change in the case of 1 mM Cd^{2+} -treated cells (black dots), which is similar to that of the control T24 cells. From the membrane permeability trend depicting a T24 cell's exposure to 7.5 mM Cd^{2+} (red diamonds), it can be seen that while the membrane permeability remains constant for the first 10 min (5 min of Cd^{2+} exposure). At 15 min, the membrane permeability increases from 5.0×10^{-5} m/s to 1.0×10^{-4} m/s, where it stayed constant for

10 min. This is followed by a steady membrane permeability of 2.0×10^{-4} m/s for the remainder of the experiment. Note, the membrane permeability value at $t = 5$ was removed due to the intense current spike which occurred immediately after the addition of 7.5 mM Cd^{2+} (amperometric i-t curve).

As reported by Chen *et al.*,³⁶ concentrations of Cd^{2+} greater than 80 μM can initiate necrosis in PC12 and SH-SY5Y cells within hours of exposure. Using much higher concentrations, we observed significant increases in membrane permeability of FcCH_2OH within minutes. We believe this is in response to Cd^{2+} cytotoxicity, where Cd^{2+} can induce a cellular death response similar to cisplatin-induced cellular death in the T24 cells.¹⁴

It is widely known that cadmium interacts with a large number of genes, transcription and translation factors vital to healthy cells.³⁵ Major response genes activated by Cd^{2+} are involved in the synthesis of metallothioneins, a family of small cysteine rich proteins, which have been shown to have roles in toxic metal detoxification and protection against oxidative stress.⁴⁶ We suspect that in the above experiments, because of the extremely high and toxic concentrations of Cd^{2+} , there is more Cd^{2+} entering the cell and forming an acute case of toxicity (*vs.* chronic). This potentially results in the overloading of the metallothioneins found in the cells. Once saturation of the metallothioneins is reached, there would be free Cd^{2+} ions being found in the cell, which can trigger cellular death. It would be interesting to see if the pretreatment of T24 cells with anti-oxidants, such as vitamin C, which has been shown to decrease ROS generation,⁴⁷ can lessen the cytotoxic effects of Cd^{2+} . This may lessen the toxic effects of Cd^{2+} on the membrane permeability in T24 cells.

3.5 Conclusion

Upon examination of the results reported in this Chapter, a correlation between Cd^{2+} treatment and membrane permeability was identified: Cd^{2+} treatment can increase the membrane permeability to FcCH_2OH in T24 cells. High Cd^{2+} concentrations appeared to induce morphological changes, such as increased spreading and flattening of the cell (increased radius), possibly leading to cellular death. After 45 minutes of exposure, the lowest Cd^{2+} treatment (1.0 mM) led to almost negligible changes in the membrane permeability, as well as the morphology of these Cd^{2+} -treated T24 cells. For each

concentration studied, the effects of Cd^{2+} on membrane permeability appeared to have stabilized well within the 50 min experiment. As the membrane permeability is increased, there is increased spreading between the neighboring phospholipid heads of the plasma membrane, which will allow for increased flux of FcCH_2OH in and out of the cell.

It is also interesting to note that when morphological flattening and spreading of the cellular bodies were observed, the nuclei of these T24 cells became more profound and easily identifiable without the aid of immunocytochemistry. This work here illustrates SECM's potential in time course studies of membrane permeability to redox mediators. It is plausible that biological SECM studies have great potential as a tool in studying the diffusion of a chemical agent through the cellular membranes for disease diagnostics and potential drug testing.

3.6 References

1. Beaulieu, I.; Kuss, S.; Mauzeroll, J.; Geissler, M., Biological Scanning Electrochemical Microscopy and Its Application to Live Cell Studies. *Anal. Chem.* **2011**, *83*, 1485-1492.
2. Cortes-Salazar, F.; Momotenko, D.; Girault, H. H.; Lesch, A.; Wittstock, G., Seeing Big with Scanning Electrochemical Microscopy. *Anal. Chem.* **2011**, *83*, 1493-1499.
3. Bard, A. J.; Fan, F. R. F.; Kwak, J.; Lev, O., Scanning Electrochemical Microscopy. Introduction and Principles. *Anal. Chem.* **1989**, *61*, 132-138.
4. Schulte, A.; Schuhmann, W., Single-Cell Microelectrochemistry. *Angew. Chem. Int. Ed.* **2007**, *46*, 8760-8777.
5. Schulte, A.; Nebel, M.; Schuhmann, W., Scanning Electrochemical Microscopy in Neuroscience. *Annu. Rev. Anal. Chem.* **2010**, *3*, 299-318.
6. Zhao, C.; Wittstock, G., An SECM Detection Scheme with Improved Sensitivity and Lateral Resolution: Detection of Galactosidase Activity with Signal Amplification by Glucose Dehydrogenase. *Angew. Chem. Int. Ed.* **2004**, *43*, 4170-4172.
7. Nioradze, N.; Kim, J.; Amemiya, S., Quasi-Steady-State Voltammetry of Rapid Electron Transfer Reactions at the Macroscopic Substrate of the Scanning Electrochemical Microscope. *Anal. Chem.* **2011**, *83*, 828-835.
8. Cannan, S.; Cervera, J.; Steliaros, R. J.; Bitziou, E.; Whitworth, A. L.; Unwin, P. R., Scanning Electrochemical Microscopy (SECM) Studies of Catalytic EC [Prime or

- Minute] Processes: Theory and Experiment for Feedback, Generation/Collection and Imaging Measurements. *Phys. Chem. Chem. Phys.* **2011**, *13*, 5403-5412.
9. Matrab, T.; Hauquier, F.; Combellas, C.; Kanoufi, F., Scanning Electron Microscopy Investigation of Molecular Transport and Reactivity within Polymer Brushes. *ChemPhysChem* **2010**, *11*, 670-682.
 10. Liebetrau, J. M.; Miller, H. M.; Baur, J. E.; Takacs, S. A.; Anupunpisit, V.; Garris, P. A.; Wipf, D. O., Scanning Electrochemical Microscopy of Model Neurons: Imaging and Real-Time Detection of Morphological Changes. *Anal. Chem.* **2002**, *75*, 563-571.
 11. Kurulugama, R. T.; Wipf, D. O.; Takacs, S. A.; Pongmayteegul, S.; Garris, P. A.; Baur, J. E., Scanning Electrochemical Microscopy of Model Neurons: Constant Distance Imaging. *Anal. Chem.* **2005**, *77*, 1111-1117.
 12. Zhu, R.; Macfie, S. M.; Ding, Z., Cadmium-Induced Plant Stress Investigated by Scanning Electrochemical Microscopy. *J. Exp. Bot.* **2005**, *56*, 2831-2838.
 13. Wang, Y.; Noël, J.-M.; Velmurugan, J.; Nogala, W.; Mirkin, M. V.; Lu, C.; Guille Collignon, M.; Lemaître, F.; Amatore, C., Nanoelectrodes for Determination of Reactive Oxygen and Nitrogen Species inside Murine Macrophages. *Proc. Natl. Acad. Sci. U. S. A.* **2012**, *109*, 11534-11539.
 14. Zhang, M. M. N.; Long, Y.-T.; Ding, Z., Cisplatin Effects on Evolution of Reactive Oxygen Species from Single Human Bladder Cancer Cells Investigated by Scanning Electrochemical Microscopy. *J. Inorg. Biochem.* **2012**, *108*, 115-122.
 15. Zhao, X.; Petersen, N. O.; Ding, Z., Comparison Study of Live Cells by Atomic Force Microscopy, Confocal Microscopy, and Scanning Electrochemical Microscopy. *Can. J. Chem.* **2007**, *85*, 175-183.
 16. Zhao, X.; Diakowski, P. M.; Ding, Z., Deconvoluting Topography and Spatial Physiological Activity of Live Macrophage Cells by Scanning Electrochemical Microscopy in Constant-Distance Mode. *Anal. Chem.* **2010**, *82*, 8371-8373.
 17. Kuss, S.; Cornut, R.; Beaulieu, I.; Mezour, M. A.; Annabi, B.; Mauzeroll, J., Assessing Multidrug Resistance Protein 1-Mediated Function in Cancer Cell Multidrug Resistance by Scanning Electrochemical Microscopy and Flow Cytometry. *Bioelectrochemistry* **2011**, *82*, 29-37.
 18. Kuss, S.; Polcari, D.; Geissler, M.; Brassard, D.; Mauzeroll, J., Assessment of Multidrug Resistance on Cell Coculture Patterns Using Scanning Electrochemical Microscopy. *Proc. Natl. Acad. Sci. U. S. A.* **2013**, *110*, 9249-9254.
 19. Bard, A. J.; Li, X.; Zhan, W., Chemically Imaging Living Cells by Scanning Electrochemical Microscopy. *Biosens. Bioelectron.* **2006**, *22*, 461-472.

20. Amemiya, S.; Guo, J.; Xiong, H.; Gross, D. A., Biological Applications of Scanning Electrochemical Microscopy: Chemical Imaging of Single Living Cells and Beyond. *Anal. Bioanal. Chem.* **2006**, *386*, 458-471.
21. Zhao, X.; Lam, S.; Jass, J.; Ding, Z., Scanning Electrochemical Microscopy of Single Human Urinary Bladder Cells Using Reactive Oxygen Species as Probe of Inflammatory Response. *Electrochem. Commun.* **2010**, *12*, 773-776.
22. Zhao, X.; Zhang, M.; Long, Y.; Ding, Z., Redox Reactions of Reactive Oxygen Species in Aqueous Solutions as the Probe for Scanning Electrochemical Microscopy of Single Live T24 Cells. *Can. J. Chem.* **2010**, *88*, 569-576.
23. Zhu, R.; Macfie, S. M.; Ding, Z., Effects of Cadmium on Photosynthetic Oxygen Evolution from Single Stomata in Brassica Juncea (L.) Czern. *Langmuir* **2008**, *24*, 14261-14268.
24. Diakowski, P. M.; Ding, Z. F., Interrogation of Living Cells Using Alternating Current Scanning Electrochemical Microscopy (AC-SECM). *Phys. Chem. Chem. Phys.* **2007**, *9*, 5966-5974.
25. Shao, Y.; Mirkin, M. V., Probing Ion Transfer at the Liquid/Liquid Interface by Scanning Electrochemical Microscopy (SECM). *J. Phys. Chem. B* **1998**, *102*, 9915-9921.
26. Barker, A. L.; Macpherson, J. V.; Slevin, C. J.; Unwin, P. R., Scanning Electrochemical Microscopy (SECM) as a Probe of Transfer Processes in Two-Phase Systems: Theory and Experimental Applications of SECM-Induced Transfer with Arbitrary Partition Coefficients, Diffusion Coefficients, and Interfacial Kinetics. *J. Phys. Chem. B* **1998**, *102*, 1586-1598.
27. Koley, D.; Bard, A. J., Triton X-100 Concentration Effects on Membrane Permeability of a Single HeLa Cell by Scanning Electrochemical Microscopy (SECM). *Proc. Natl. Acad. Sci. U. S. A.* **2010**, *107*, 16783-16787.
28. Guo, J.; Amemiya, S., Permeability of the Nuclear Envelope at Isolated Xenopus Oocyte Nuclei Studied by Scanning Electrochemical Microscopy. *Anal. Chem.* **2005**, *77*, 2147-2156.
29. Yasukawa, T.; Uchida, I.; Matsue, T., Permeation of Redox Species through a Cell Membrane of a Single, Living Algal Protoplast Studied by Microamperometry. *Biochim. Biophys. Acta* **1998**, *1369*, 152-158.
30. Kasai, S.; Shiku, H.; Torisawa, Y.-S.; Noda, H.; Yoshitake, J.; Shiraishi, T.; Yasukawa, T.; Watanabe, T.; Matsue, T.; Yoshimura, T., Real-Time Monitoring of Reactive Oxygen Species Production During Differentiation of Human Monocytic Cell Lines (THP-1). *Anal. Chim. Acta* **2005**, *549*, 14-19.

31. Hu, R.; Guille, M.; Arbault, S.; Lin, C. J.; Amatore, C., In Situ Electrochemical Monitoring of Reactive Oxygen and Nitrogen Species Released by Single MG63 Osteosarcoma Cell Submitted to a Mechanical Stress. *Phys. Chem. Chem. Phys.* **2010**, *12*, 10048-10054.
32. Gonsalves, M.; Macpherson, J. V.; O'Hare, D.; Winlove, C. P.; Unwin, P. R., High Resolution Imaging of the Distribution and Permeability of Methyl Viologen Dication in Bovine Articular Cartilage Using Scanning Electrochemical Microscopy. *Biochim. Biophys. Acta* **2000**, *1524*, 66-74.
33. López, E.; Figueroa, S.; Oset-Gasque, M. J.; González, M. P., Apoptosis and Necrosis: Two Distinct Events Induced by Cadmium in Cortical Neurons in Culture. *Br. J. Pharmacol.* **2003**, *138*, 901-911.
34. Chuang, S.-M.; Wang, I.-C.; Yang, J.-L., Roles of JNK, P38 and ERK Mitogen-Activated Protein Kinases in the Growth Inhibition and Apoptosis Induced by Cadmium. *Carcinogenesis* **2000**, *21*, 1423-1432.
35. Hartwig, A., Metal Interaction with Redox Regulation: An Integrating Concept in Metal Carcinogenesis? *Free Radic. Biol. Med.* **2013**, *55*, 63-72.
36. Chen, L.; Liu, L.; Huang, S., Cadmium Activates the Mitogen-Activated Protein Kinase (MAPK) Pathway Via Induction of Reactive Oxygen Species and Inhibition of Protein Phosphatases 2A and 5. *Free Radic. Biol. Med.* **2008**, *45*, 1035-1044.
37. Chen, L.; Liu, L.; Yin, J.; Luo, Y.; Huang, S., Hydrogen Peroxide-Induced Neuronal Apoptosis Is Associated with Inhibition of Protein Phosphatase 2A and 5, Leading to Activation of MAPK Pathway. *Int. J. Biochem. Cell Biol.* **2009**, *41*, 1284-1295.
38. Pelicano, H.; Carney, D.; Huang, P., Ros Stress in Cancer Cells and Therapeutic Implications. *Drug Resist. Update* **2004**, *7*, 97-110.
39. Lacour, S.; Hammann, A.; Grazide, S.; Lagadic-Gossmann, D.; Athias, A.; Sergent, O.; Laurent, G.; Gambert, P.; Solary, E.; Dimanche-Boitrel, M.-T., Cisplatin-Induced CD95 Redistribution into Membrane Lipid Rafts of HT29 Human Colon Cancer Cells. *Cancer Res.* **2004**, *64*, 3593-3598.
40. Huang, C.-R.; Jin, Z.-X.; Dong, L.; Tong, X.-P.; Yue, S.; Kawanami, T.; Sawaki, T.; Sakai, T.; Miki, M.; Iwao, H., et al., Cisplatin Augments FAS-Mediated Apoptosis through Lipid Rafts. *Anticancer Res.* **2010**, *30*, 2065-2071.
41. Vondálová Blanářová, O.; Jelínková, I.; Szöör, Á.; Skender, B.; Souček, K.; Horváth, V.; Vaculová, A.; Anděra, L.; Sova, P.; Szöllösi, J., et al., Cisplatin and a Potent Platinum(IV) Complex-Mediated Enhancement of TRAIL-Induced Cancer Cells Killing is Associated with Modulation of Upstream Events in the Extrinsic Apoptotic Pathway. *Carcinogenesis* **2011**, *32*, 42-51.

42. Zhang, M. M.; Long, Y. T.; Ding, Z., Filming a Live Cell by Scanning Electrochemical Microscopy: Label-Free Imaging of the Dynamic Morphology in Real Time. *Chem. Cent. J.* **2012**, *6*, 20.
43. Miao, W.; Ding, Z.; Bard, A. J., Solution Viscosity Effects on the Heterogeneous Electron Transfer Kinetics of Ferrocenemethanol in Dimethyl Sulfoxide-Water Mixtures. *J. Phys. Chem. B* **2002**, *106*, 1392-1398.
44. Yeh, C.-M.; Hsiao, L.-J.; Huang, H.-J., Cadmium Activates a Mitogen-Activated Protein Kinase Gene and MBP Kinases in Rice. *Plant Cell Physiol.* **2004**, *45*, 1306-1312.
45. Amatore, C.; Pebay, C.; Thouin, L.; Wang, A.; Warkocz, J. S., Difference between Ultramicroelectrodes and Microelectrodes: Influence of Natural Convection. *Anal. Chem.* **2010**, *82*, 6933-6939.
46. Sutherland, D. E. K.; Stillman, M. J., The "Magic Numbers" of Metallothionein. *Metallomics* **2011**, *3*, 444-463.
47. Grosicki, A., Influence of Vitamin C on Cadmium Absorption and Distribution in Rats. *J. Trace Elem. Med Biol.* **2004**, *18*, 183-187.

Chapter 4

4 Probing Cd²⁺-Stressed Live Cell Membrane Permeability with Various Redox Mediators in Scanning Electrochemical Microscopy

(A version of this work has been published in the *Journal of Physical Chemistry C* Li, M.S.M.; Filice, F.P.; Ding, Z. *J. Phys. Chem. C.* **2016**, *120*, 6094-6103.)

4.1 Introduction

Cd²⁺ has no physiological uses in the body; instead, Cd²⁺ exposure can lead to numerous health issues.¹⁻³ Short-term or acute exposure (typically >15 mg/L or 0.133 mM) can lead to flu-like symptoms.³ While long-term or chronic exposure leads to more severe health issues, including bone diseases, organ dysfunctions and cancers.^{1,4} A huge underlying problem in Cd²⁺ cytotoxicity is its long biological half-life of 10-30 years, which often leads to life-long complications.¹⁻³

Cd²⁺ may enter the body through the consumption of contaminated foods or water, cigarette smoke, and exposure to Cd²⁺-coated metallic items.² Once exposed, it can enter cells through various ion channels, such as those intended for Ca²⁺, Zn²⁺, Fe²⁺ and Cu²⁺.⁵ It can compete with the essential metals (e.g. Zn²⁺), displacing them in metalloenzymes or metalloproteins, resulting in their dysfunctions.^{1, 5} On the cellular level, Cd²⁺ has been shown to induce membrane integrity loss,⁶⁻⁷ membrane permeability changes,⁸⁻⁹ and cellular death.^{6-7, 10} Dyes, such as, propidium iodide⁶ or trypan blue,¹¹ can provide insight into cell viability, as these dyes cannot permeate healthy cells (dye exclusion methods). Unfortunately, these methods tend to be destructive and cannot give quantification from a singular cell standpoint. Here, we use non-invasive scanning electrochemical microscopy (SECM) to study the effects of Cd²⁺-induced stress on membrane permeability.

SECM utilizes an ultramicroelectrode (UME, ≤ 25 μm diameter) that can be biased at particular potentials such that a redox active species is being oxidized or reduced in a diffusion-controlled process.¹²⁻¹³ As the UME approaches the sample (or substrate), the

faradaic current can be amplified from the diffusion-controlled steady state current if the substrate is conductive (cyclic regeneration effect, positive feedback) or decreased if the substrate is insulating (blocked diffusion, negative feedback). Greatly developed by Bard *et al.* since 1989,¹² SECM has provoked a number of applications, including but not limited to, surface and interface studies,¹⁴⁻¹⁵ kinetic studies,¹⁶ and microstructure fabrication.¹⁷⁻¹⁸ SECM studies have progressed towards biological systems,¹⁹⁻²⁴ including: electron transfer kinetics and molecular transports,²⁵⁻²⁷ extracellular reactive oxygen/nitrogen species²⁸⁻³⁴ and neurotransmitter release,³⁵⁻³⁶ and the assessment of drugs on biological cells.^{33, 37-38}

In the SECM study of live cells, three measurements are most widely used: (1) the 2D imaging of the cells, where the current is mapped as a function of the SECM probe coordinates revealing either cellular topography^{31-32, 39-40} and/or the spatial profile of extracellular redox active species;^{30-32, 41-42} (2) probe approach curves (PACs) which plot the normalized current (I) against the normalized probe-to-cell distance (L), allowing for the quantification of kinetic parameters⁴³⁻⁴⁴ of redox species across the cell membrane^{40, 45-47} and; (3) chronoamperometry at specific probe-to-cell distances to study the evolutionary trend of cellular topography,⁴⁸ reactivity,⁴⁹ and monitoring the generation of redox active species from the cells.⁴⁹⁻⁵⁰

In 2000, the Mirkin Group was able to identify diffusion of the redox species through live cells as one of the possible contributing factors in mediator regeneration at the UME tip.⁵¹ They also assessed bimolecular reactions between the extracellular redox species in solution and intracellular redox moieties in the cells as another contributing factor.⁵¹ In 2005, the Amemiya Group was able to determine that passive transport of the redox molecules across the permeable double-membraned nuclear envelope of *Xenopus laevis* oocytes was actually limited by the rate of diffusion.⁴⁶ This was later confirmed by Li and Bard for human cervical cancer (HeLa) cells.⁵² SECM has since shown great promise as a technique in studying the effects of toxins and anti-cancer drugs on cells through the induction of membrane permeability.^{8, 35, 45, 52-53}

We have previously used ferrocenemethanol (FcCH₂OH) as a molecular probe to investigate membrane permeability changes in single live human bladder cancer (T24) cells

under Cd^{2+} and cisplatin stimulations.^{8-9, 33, 53} While relative changes in permeability can be observed, the molecular probe itself is permeable to the cell. It becomes attractive to select a sensing agent that will display strong contrast between the control (impermeable) and stressed cells (permeable). Large uncharged polar molecules and ions are initially impermeable to the hydrophobic cell membrane, requiring facilitated diffusion or special transport channels to allow entrance into the cell.

Here we demonstrate the quantification of hydrophilic and charged redox mediators, ferrocene carboxylate (FcCOO^-), 1,1'-ferrocene dicarboxylate (Fc(COO)_2^{2-}) and hexaamineruthenium(III) ($\text{Ru(NH}_3)_6^{3+}$) as molecular probes in SECM to study the toxic effects of Cd^{2+} on T24 cells. With an abundance of literature verifying the effects of Cd^{2+} on membrane permeability and integrity,^{1, 6, 8-10} investigation on the permeation of these redox mediators after sufficient Cd^{2+} exposure is expected. We explored this through two SECM-membrane permeability studies: (1) a time-dependent exposure to low Cd^{2+} concentration treatment; and (2) a concentration-dependent exposure to acute Cd^{2+} treatment. The induction of membrane permeability through the incubation of T24 cells with low Cd^{2+} concentration for several hours should mirror the effects of short duration acute Cd^{2+} treatments. A comparison of the exposure treatments will also be made, correlating membrane permeability and cellular viability.

4.2 Experimental Section

The experimental details discussed here are the project-specific details briefly summarized. A more detailed report of the Experimental is included in Chapter 2.

4.2.1 Materials

Cadmium chloride, FcCH_2OH (97%), FcCOOH (97%), and $\text{Ru(NH}_3)_6\text{Cl}_3$ (98%) were purchased from Sigma-Aldrich (Mississauga, ON), while potassium chloride (KCl, 99%) and Fc(COOH)_2 (98%) were purchased from Alfa Aesar (Ward Hill, MA) and Santa Cruz Biotechnology, Inc. (Dallas, TX) respectively.

Stock solutions of CdCl_2 were prepared in deionized water (18.2 M Ω .cm, MilliQ water, Millipore, Etobicoke, ON) and syringe-filtered for sterility using a 0.2 μm Supor[®]

Membrane (PALL Corporation, Mississauga, ON) prior to live cell treatment. 0.5 mM FcCOO^- , 0.5 mM $\text{Fc}(\text{COO})_2^{2-}$, 0.9 mM FcCH_2OH and 1.0 mM $\text{Ru}(\text{NH}_3)_6^{3+}$, all with 0.1 M KCl as the supporting electrolyte, were prepared in phosphate buffered saline (PBS, 10 mM and pH 7.4).

4.2.2 Electrode Fabrication

The UMEs (working electrodes) were fabricated in house and its procedure has been previously published in detail;^{8, 32, 41} additional information can found in Chapter 2. Two working electrodes were used in this study: a 10 μm Pt UME for the time-dependent study and a 5 μm Pt UME for the concentration-dependent study. The RG (ratio of the surrounding glass radius to that of the Pt wire) of the UMEs were polished to approximately 3. The electrode tips were examined using optical microscopy and tested for functionality using cyclic voltammetry.

4.2.3 Cell Culture

T24 cells were cultured as discussed in Chapter 2 and the project specific details are listed here. Prior to the live cell SECM measurements, T24 cells were plated on a glass bottom petri dish (P50-G-0-30-F, MatTek Corporation, Ashland, MA) during subculturing. Cells were allowed to adhere and grow overnight prior to the SECM experiments. T24 cells were incubated with 25 μM Cd^{2+} at the desired exposure times (time-dependent study) or acute concentrations for 1 hr prior to the SECM experiments. All cultured cells were washed 3x with 2 mL of PBS and refilled with 4 mL of the desired mediator solution.

4.2.4 Cell Viability

Cell viability was assessed using the MTT cell proliferation assay⁵⁴ and its procedure was described in detail in Chapter 2. Briefly, the project specific details are discussed here: 2×10^4 T24 cells were treated with 25 μM Cd^{2+} for incubation periods of 0 (control), 1, 2, 4, and 6 hours (time-dependent study) or 0, 1.0, 2.5, 5.0, and 7.5 mM Cd^{2+} for 1 hour (concentration-dependent study). 0.05, 0.10, 0.15, or 0.20 mg/mL SDS was prepared and used as a positive control in the assay. In the 6 hour treatment period, SDS reached 0 % viability for cells treated with 0.15 and 0.20 mg/mL, confirming sensitivity of the assay. The

results shown here are the mean values \pm relative standard deviation (RSD) from at least 5 different experiments completed in sets of eight (time-dependent study) or 3 experiments completed in sets of six (concentration-dependent study).

4.2.5 SECM Instrumentation

All SECM experiments were conducted using a modified Alpha-SNOM instrument (WITec, Ulm, Germany) as detailed in Chapter 2.^{8, 33, 53, 55} Electrochemical experiments were performed using an electrochemical analyzer (CHI 800B, CH Instruments, Austin, TX) with a CHI 200 Picoamp Booster to reduce noise (CH Instruments) and recorded by the Alpha-SNOM instrument. For all electrochemical experiments described in this Chapter, a Ag/AgCl wire was used as a combined auxiliary/reference electrode.

4.2.6 SECM Experiments

SECM measurements were obtained by mounting the petri dish onto the scanning stage (P-517K064, Polytec PI, Germany) of the Alpha-SNOM and maintained at 37.0 ± 0.2 °C (Bioscience Tools, San Diego, CA). The UMEs were biased in either the oxidation plateau region of the ferrocene-based compounds or the reduction plateau region of $\text{Ru}(\text{NH}_3)_6^{3+}$ (Table 4.1). The UME was approached in close proximity to the cell by the WITec instrument. Each depth scan image has 128 x 128 pixels, a scan width of 60 μm , depth of 80 μm , and an integration time of 0.01 s. All cell samples were discarded within 1.5 hours of experimentation. Further details about the SECM instrumentation and sample preparation can be found in Chapter 2.

Table 4.1. Experimental Parameters of the SECM Redox Mediators Studied

Probe	At pH 7	Electrochemical reaction	c [mM]	E [V]	D [m ² /s]
FcCH₂OH	FcCH ₂ OH	FcCH ₂ OH → Fc ⁺ CH ₂ OH + e ⁻	0.9	+0.300	7.6 x 10 ⁻¹⁰ ^{46, 56}
FcCOOH	FcCOO ⁻	FcCOO ⁻ → Fc ⁺ COO ⁻ + e ⁻	0.5	+0.500	5.7 x 10 ⁻¹⁰ ⁵⁷
Fc(COOH)₂	Fc(COO) ₂ ²⁻	Fc(COO) ₂ ²⁻ → Fc(COO) ₂ ⁻ + e ⁻	0.5	+0.600	5.3 x 10 ⁻¹⁰ ^[a]
Ru(NH₃)₆Cl₃	Ru(NH ₃) ₆ ³⁺	Ru(NH ₃) ₆ ³⁺ + e ⁻ → Ru(NH ₃) ₆ ²⁺	1.0	-0.350	6.7 x 10 ⁻¹⁰ ⁵⁸

[a] for Fc(COO)₂²⁻, D was determined through its steady state voltammogram (see Supporting Information, Figures S4.1 and S4.2 in Appendix IV).

4.2.7 SECM Data Analysis

PACs were obtained by extracting vertical cross-sections above the center of the cells from their respective SECM depth scan images. Experimental curves were overlapped onto simulated PACs generated using COMSOL Multiphysics v.4.4, a finite element analysis software, to quantify their membrane permeability coefficients, P_m . All P_m values reported here are the averages of 4 or more cell measurements unless otherwise stated. In each average membrane permeability plot, the error bars represent the mean ± standard error (SE, $SE = \sigma / \sqrt{N}$, where σ is the standard deviation and N is the number of individual cell measurements).

4.2.8 Simulations of PACs

For the purpose of theoretical PAC generation, a simulation model in 2D axial symmetry was constructed using COMSOL (Figure S4.3). The model geometry was designed to be representative of the physical dimensions of all objects in the live cell SECM experiments (Figures S4.4 and S4.5). A detailed description of the model geometry, simulation parameters, and post-processing steps has been previously described in great detail ^{8-9, 59} and is discussed in Appendix IV. To quantify P_m , the experimental PACs were overlaid onto simulated theoretical curves (a sample set is shown in Figure S4.6).

4.3 Results and Discussion

4.3.1 Quantification of the Membrane Permeability to the Three Hydrophilic Redox Mediators

Hydrophilic, polar or charged molecules do not favor permeation across the hydrophobic cell membrane through passive diffusion.⁴⁵ As a result, hydrophilic and charged redox mediators, such as FcCOO^- , $\text{Fc}(\text{COO})_2^{2-}$ and $\text{Ru}(\text{NH}_3)_6^{3+}$ are posed to serve as great SECM sensing agents to study the effects of toxins on membrane permeability. In SECM depth scan mode, the changes in electrochemical behavior can be monitored as the UME tip approaches a sample from above, displayed in the form of a 2D current-distance image. Figure 4.1 displays typical SECM depth scan images with their corresponding extracted PACs to the top of the cells.

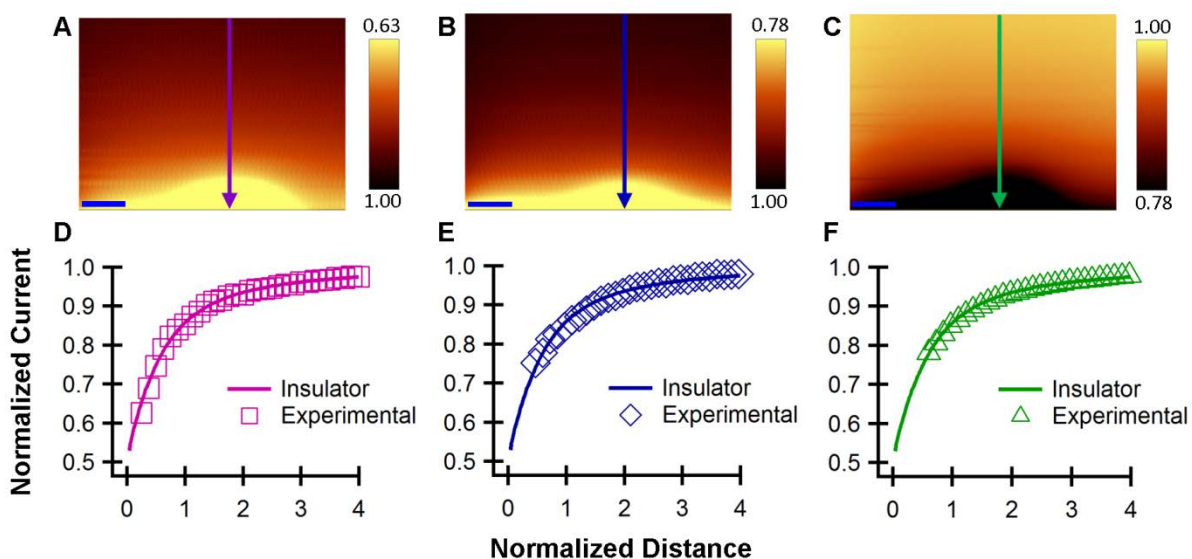


Figure 4.1. Typical SECM depth scan images of single T24 collected using redox mediators: (A) FcCOO^- , (B) $\text{Fc}(\text{COO})_2^{2-}$, and (C) $\text{Ru}(\text{NH}_3)_6^{3+}$. The scale bar in each SECM image represents 10 μm . The corresponding experimental PACs extracted at each arrow in (A-C) is overlaid onto theoretical PACs generated to an insulating cell, where the redox mediator is (D) FcCOO^- (purple), (E) $\text{Fc}(\text{COO})_2^{2-}$ (blue), and (F) $\text{Ru}(\text{NH}_3)_6^{3+}$ (green). Please note, the color map (current) for $\text{Ru}(\text{NH}_3)_6^{3+}$ in (C) appears inverted from the ferrocene carboxylates (A-B) due to the opposing redox chemistry occurring at the UME tip.

In the SECM depth scan images (Figures 4.1A-C), when the UME is far from the cell ($d > 20 \mu\text{m}$) the detected current is influenced by neither the cell nor the dish: thus, a steady state current (i_{∞}) is observed. However, we can see the clear electrochemical definition of a cell (yellow or black semi-ellipse for the ferrocene carboxylates and $\text{Ru}(\text{NH}_3)_6^{3+}$, respectively) with decreased current as the UME approaches the cell ($d \leq 10 \mu\text{m}$). Please note, the color scales appear inverted between the ferrocene carboxylates and $\text{Ru}(\text{NH}_3)_6^{3+}$ images due to the opposing redox chemistry occurring at the tip. This decrease in the faradaic current would suggest that the cells are behaving similar to an insulating substrate, displaying negative electrochemical feedback characteristics.

To quantify the P_m values, the experimental PACs were extracted from the SECM depth scan images by taking vertical cross-sections centered over the cell (the arrows in Figures 4.1A-C). Once normalized, the PACs can be overlaid onto the simulated curves generated with known permeability coefficients quantifying P_m for the cell under study (Figures 4.1D-F). These PACs demonstrate that there was no flux of the sensing agents across the cell membrane since the experimental PACs overlap well with a simulated cell having a P_m of 0 m/s or a purely insulating cell. This result was expected as these molecular probes are hydrophilic, polar and charged, all of which make them unfavorable to cross the cell membrane by passive diffusion. The successful overlay of the experimental PACs to an insulating cell also suggests there is no additional redox chemistry occurring at the cellular membrane, such as the reverse redox reactions listed in Table 4.1.

To verify the impermeable nature of these sensing agents, a similar SECM depth scan study was performed using the known membrane-permeable and hydrophobic mediator, FcCH_2OH .^{8-9, 52-53} The initial average P_m of this molecular probe was found to be $(5.0 \pm 3.5) \times 10^{-5}$ m/s. This value, along with that in our previously report⁸ confirms the permeable nature of FcCH_2OH . The membrane permeability to FcCH_2OH in T24 cells is similar to the value reported by Matsue *et al.* for single algal protoplast (5.00×10^{-5} m/s).⁴⁷

4.3.2 Time-Dependent Effects of Cadmium Treatment on Membrane Permeability

4.3.2.1 Hydrophilic Redox Probes

From a previous study conducted in our lab, it was determined that the pretreatment of T24 cells with 10 μM Cd^{2+} induced changes in membrane permeability to FcCH_2OH after 1 hour of incubation, despite its low concentration.⁹ However, in the following time-dependent experiments, a higher concentration of 25 μM Cd^{2+} was used to ensure it can induce a measurable effect for the hydrophilic molecular probes. The membrane permeability of T24 cells were measured using the SECM depth scan imaging mode after the cells were incubated with 25 μM Cd^{2+} for 0 to 6 hours (Figure 4.2).

Upon Cd^{2+} treatment, T24 cells displayed an increased growth trend in the membrane permeability to these hydrophilic probes (Figures 4.2A-C). FcCOO^- for example, had an impermeable region where the T24 cells exposed to 25 μM Cd^{2+} for less than 2 hours had no effect on membrane permeability (Figure 4.2A). However, after 2 hours, the permeability to FcCOO^- was found to increase, having an onset value of 2.0×10^{-5} m/s. Permeability then increased exponentially, reaching a plateau value of 6.3×10^{-5} m/s after 4 hours, which remained unaffected by additional Cd^{2+} exposure.

Surprisingly, the more negatively charged, $\text{Fc}(\text{COO})_2^{2-}$ began to enter the cell the fastest of the three hydrophilic redox mediators (Figure 4.2B); displaying some efflux of these species after 1 hour of Cd^{2+} treatment (2.1×10^{-5} m/s). It was expected for $\text{Fc}(\text{COO})_2^{2-}$ to diffuse across the membrane slower than FcCOO^- due to the negatively charged phosphate in the lipid membrane. This could be due to the higher attractive interaction between the positively charged electrode and $\text{Fc}(\text{COO})_2^{2-}$ than FcCOO^- . After 2 hours, Cd^{2+} increased the membrane permeability to 4.4×10^{-5} m/s, which plateaued at approximately 6.7×10^{-5} m/s soon after.

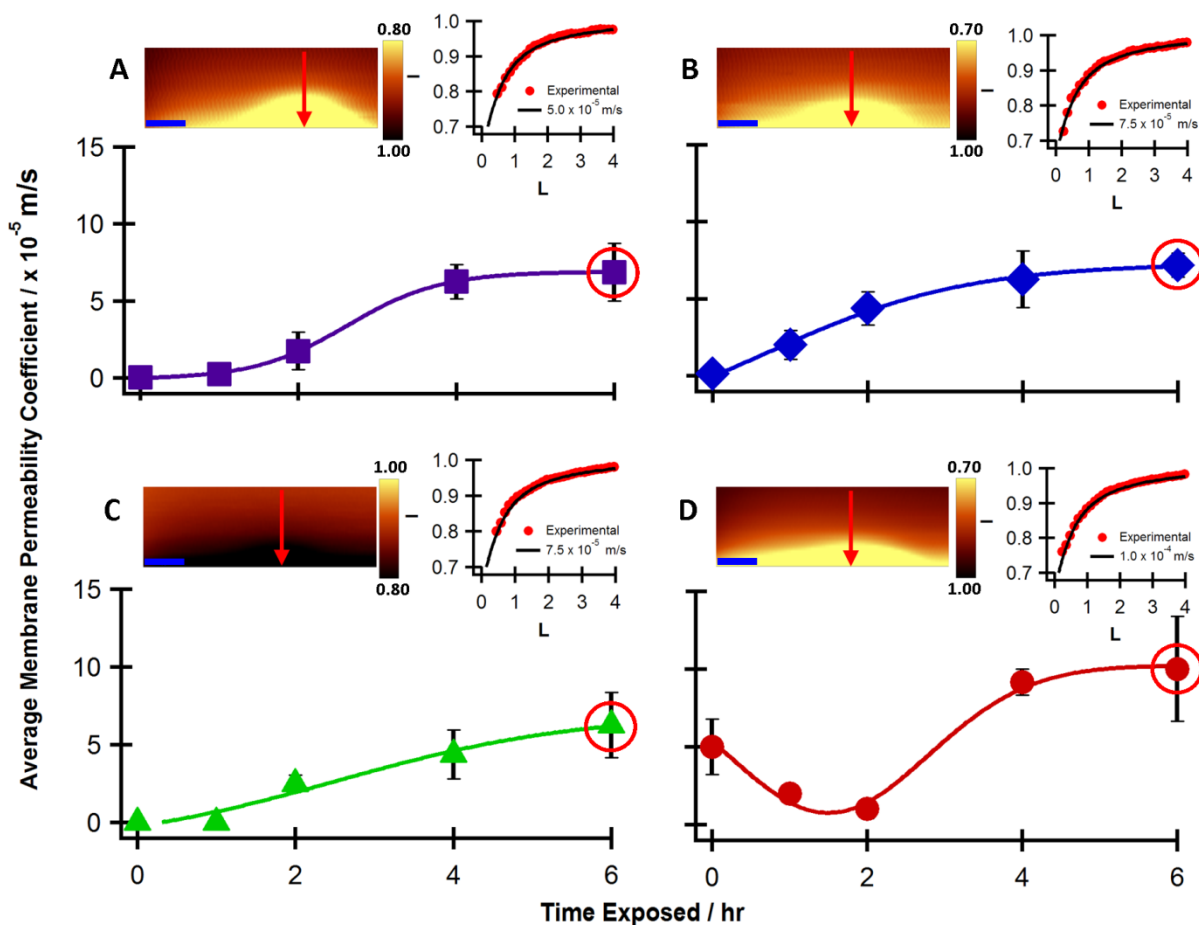


Figure 4.2. The average P_m of T24 cells pre-incubated with $25 \mu\text{M Cd}^{2+}$ plotted as a function of incubation time using the following molecular probes: (A) FcCOO⁻ (purple squares), (B) Fc(COO)₂²⁻ (blue diamonds), (C) Ru(NH₃)₆³⁺ (green triangles), and (D) FcCH₂OH (red circles). A typical SECM depth scan image of a T24 cell after 6 hours of Cd^{2+} treatment and its corresponding PAC overlaid onto a curve of known P_m , are included as an inset for each molecular probe (A-D). The scale bar in each SECM image represents $10 \mu\text{m}$. Each SECM live cell experiment produces a single depth scan image, which provides a P_m to be used in determining the average P_m for that particular molecular probe at the respective Cd^{2+} treatment period (A-D).

The most positively charged molecular probe, $\text{Ru}(\text{NH}_3)_6^{3+}$, showed the slowest growth pattern: one hour of Cd^{2+} exposure was not sufficient to induce permeability changes in the T24 cells (Figure 4.2C). It seems that the favorable static interactions between the cathode biased at -0.35 V (Table 4.1) and the cation does not play an important role in the efflux of $\text{Ru}(\text{NH}_3)_6^{3+}$ from the cell to the electrode. It is possible that the negatively charged phosphate group in the lipid membrane may retain the positively charged molecular probe. This observation is likely the balance between the two static interactions. After 2 hours, $\text{Ru}(\text{NH}_3)_6^{3+}$ began to permeate across the cell, displaying the lowest permeability coefficient of all the three hydrophilic redox mediators at this time period (2.5×10^{-5} m/s). After 4 hours, the permeability to $\text{Ru}(\text{NH}_3)_6^{3+}$ approached 4.4×10^{-5} m/s, followed by 6.3×10^{-5} m/s after 6 hours of Cd^{2+} treatment.

While differing in the sigmoidal growth trends, these three hydrophilic redox mediators achieved and maintained similar maximum average permeability coefficients (approximately 7×10^{-5} m/s, Figures 4.2A-C). It appears that the charge of the molecular probe has an effect on its rate of entrance into the cell after sufficient Cd^{2+} exposure and its detection by SECM depends on this rate, along with the static interactions between the phosphate groups of the cell membrane and the molecular probes. Interestingly, these sigmoidal growth trends were similar to a previous study, where the membrane permeability to FcCH_2OH in T24 cells was studied in direct response to acute Cd^{2+} stimulations.⁸

4.3.2.2 Hydrophobic Redox Mediator

To confirm the induction of hydrophilic species through the cell membrane, a concurrent set of experiments were completed, testing the membrane permeability to the more hydrophobic redox mediator, FcCH_2OH (Figure 4.2D). For the first two hours of Cd^{2+} treatment, the membrane permeability decreased from 5.0×10^{-5} m/s to 1.0×10^{-5} m/s. This decrease suggests a slight contraction or improvement in the integrity of the cell membrane.⁶⁰ We suspect at this low exposure, an improvement in membrane integrity is a possible defense mechanism of the T24 cells to prevent Cd^{2+} entrance into the cells.⁶¹ However, after prolonged Cd^{2+} exposure ($t > 4$ hours), the membrane permeability increased to approximately 1.0×10^{-4} m/s and remained constant regardless of the prolonged Cd^{2+}

treatment. This trend was similar to a concentration-dependent study of Cd^{2+} in the range of 1 μM to 1 mM .⁹ Cd^{2+} concentrations induced the following membrane permeability changes: (1) no effect (stable), (2) decreased (membrane contraction) and (3) increased (membrane relaxation).⁹ The initial region of stability was not observed in this work since 25 μM Cd^{2+} was already known to induce a decrease in membrane permeability to FcCH_2OH within the first hour of exposure.⁹

The inset SECM depth scan images of T24 cells treated with 25 μM Cd^{2+} for 6 hours (Figure 4.2) suggest that when hydrophilic molecular probes are used, the electrochemical feedback from the T24 cells appears more round in shape than the hydrophobic FcCH_2OH molecular probe. However, there was a wide range of electrochemical feedback shapes observed within each set of mediators (ranging from hemispherical to a near flat elliptical geometry). At this time, we cannot attribute these electrochemical shapes to be caused exclusively by the presence of the molecular probes. The corresponding PACs for these SECM images represent one experimental trial, which was used to determine the average membrane permeability coefficients.

4.3.3 Compromised Structure of the Cell Membrane

Here, Cd^{2+} was used as a toxin to increase the membrane permeability to the hydrophilic redox mediators, which are normally unable to enter the cell. Increasing the membrane permeability to chemicals has been previously established to be indicative of membrane integrity loss.^{45, 60, 62-63} Typically, membrane integrity is assessed by the transfer of an impermeable species into the cell, such as dye exclusion viability studies.⁶ Propidium iodide, for example, can only permeate the cell when the membrane integrity is lost, ruptured or cellular death has occurred.^{6, 62, 64}

In 2010, Koley and Bard⁴⁵ demonstrated SECM can be used to monitor membrane integrity loss through the induction of ferrocyanide ($\text{Fe}(\text{CN})_6^{4-}$) into HeLa cells, after their exposure to the surfactant Triton X-100. As a surfactant, Triton X-100 is able to lyse cells for the extraction of intracellular proteins and organelles or induce higher permeability of the membrane to allow for transfection.⁴⁵ The infiltration of this hydrophilic $\text{Fe}(\text{CN})_6^{4-}$ species

into the cell was believed to be due to the structural collapse or pore formation within the membrane upon exposure to Triton X-100.⁴⁵

While optically, we did not observe significant changes in confluency (viability) of our tested T24 cells, our SECM results suggested compromised cell membranes after Cd^{2+} treatment. This loss in membrane integrity has allowed the permeation of not only the tested hydrophilic mediators, but perhaps other available ions and species in the electrolytic solution through non-specific diffusion channels or pore formations in the cell membrane.^{45, 65} It is likely the permeation of available ions and molecules into the cell will have a biological consequence, since homeostasis will be disrupted. In fact, even at this low concentration, it was observed for Cd^{2+} to induce small morphological changes in the T24 cells (Figure 4.3).

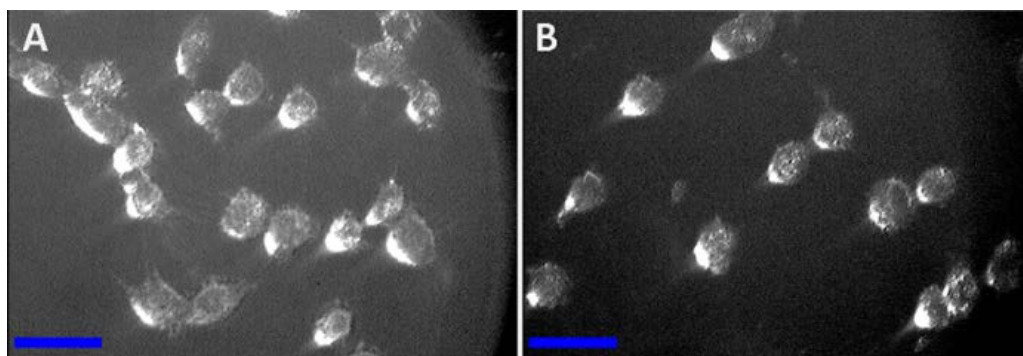


Figure 4.3. Optical micrographs of T24 cells grown in the (A) absence of Cd^{2+} treatment and (B) after 4 hours of Cd^{2+} treatment. The T24 cells treated with 4 hours of 25 μM Cd^{2+} appear to have more blebbing throughout the cell, indicating cellular stress and/or damage. The scale bar in each optical image represents 40 μm .

In the absence of Cd^{2+} , the T24 cells had their typical epithelial morphology (Figure 4.3A). Upon sufficient Cd^{2+} treatment, the T24 cells appeared slightly smaller and more round in shape, while localized blebbing in the center of the cells were observed (Figure 4.3B). The appearances of the blebs were likely caused by the Cd^{2+} treatment, since it can induce a variety of harmful effects on organisms. Effects of Cd^{2+} poisoning can include increasing lipid peroxidation of the cell membranes and disruption of the antioxidant defense system, which can cause oxidative damage.⁶⁶ Huang *et al.* also previously demonstrated that

alterations in the membrane-cytoskeleton linkers can lead to the formation and detachment of membrane blebs through weakening of the membrane-cytoskeleton interactions in isolated rabbit proximal tubule cells.⁶⁷ It is plausible that the presence of these blebs in our Cd²⁺-treated cells are indicative of this Cd²⁺-induced stress.

Since Cd²⁺ is known to induce morphological changes in living organisms, to prevent drastic changes from occurring during the SECM-live cell experiments, T24 cells were pretreated with Cd²⁺ immediately prior to experimentation. By incubating the cells with Cd²⁺, it was hypothesized that the major morphological changes would occur during this period rather than during the SECM experiments.⁸ The geometric model used in these simulations was designed based on the average cell size determined optically and by SECM (Figures S4.4 and S4.5). Additional PACs were generated based on a range of values greater than average \pm standard deviation of the cell height and diameter respectively, confirming minimal effect on the curves (Figures S4.7 and S4.8). While our results suggest the cell membrane is compromised upon Cd²⁺ exposure, biological changes in proteins or the cell membrane (pore formation/collapse) are undetectable by the UMEs used in this study. The micron-sized UMEs detect the average membrane permeability across the cell membrane due to the size of the electrodes. Any biological changes that are occurring on the submicron scale cannot be detected by these UMEs.

4.3.4 Time-Dependent Effects of Cd²⁺ on Cellular Viability

Since morphological changes were induced, it was important to determine if the overall health of the T24 cells is affected by Cd²⁺ exposure. To evaluate cell viability, the MTT cell proliferation assay was used (Figure 4.4).

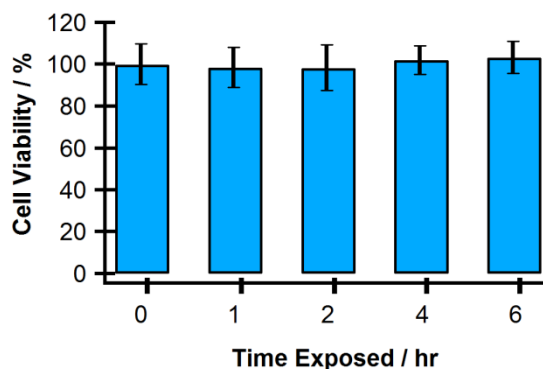


Figure 4.4. Cell viability of T24 cells treated with 25 μM Cd^{2+} was measured by the MTT cell proliferation assay. The mean \pm RSD of 5 separate experiments (8 replicates per experiment) is shown.

Cell survival or viability was determined by comparing the Cd^{2+} -treated T24 cells to the untreated cells (eqn 4.1):

$$\text{Cell Viability (\%)} = \frac{\text{Abs}_{\text{sample}} - \text{Abs}_{\text{blank}}}{\text{Abs}_{\text{control}} - \text{Abs}_{\text{blank}}} \times 100 \% \quad (4.1)$$

where Abs represents absorbance. The cell viability remains constant at approximately 100 % throughout all tested incubation periods. This indicates that the T24 cells did not die as a direct response to the low Cd^{2+} concentration stimulation. In fact, while our SECM results may indicate there is a loss in membrane integrity, these viability studies confirm that the T24 cells are still viable during the SECM experiments. With higher treatment and dosage times, Cd^{2+} is likely to induce cellular death (apoptosis or necrosis) in the T24 cell line similar to other cell lines.^{6, 10, 68}

4.3.5 Cd^{2+} Concentration-Dependence of Membrane Permeability

To confirm induction of the membrane permeability to the three hydrophilic redox mediators, the effects of acute Cd^{2+} -cytotoxicity was also explored. In this study, T24 cells were pretreated with acute Cd^{2+} concentrations in the range of 1-5 mM for a duration of 1 hour (Figure 4.5).

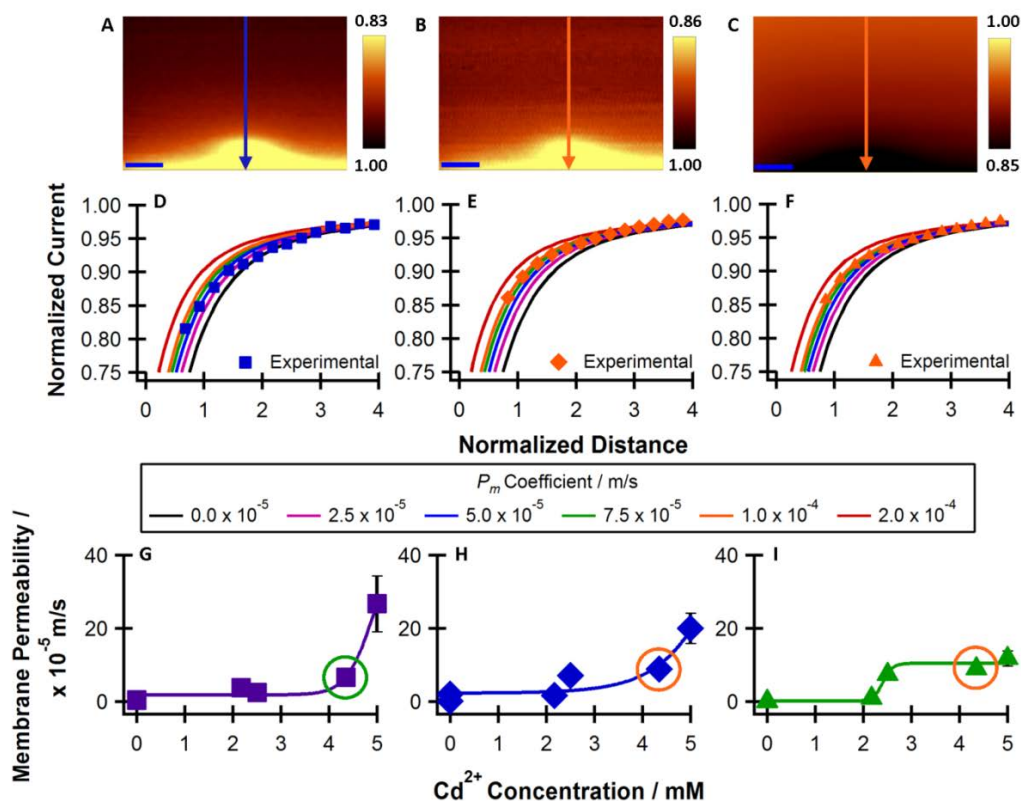


Figure 4.5. Typical SECM depth scan images of T24 cells treated with 4.4 mM Cd²⁺ for 1 hour detected using the following molecular probes: (A) FcCOO⁻, (B) Fc(COO)₂²⁻, and (C) Ru(NH₃)₆³⁺. The scale bar in each SECM image represents 10 μm. The arrows in (A)-(C) indicate where the vertical cross section was taken to extract the PACs in (D)-(F) respectively. The experimental PACs were overlaid onto simulated curves to quantify their P_m . Graphical representation of the changes in the average P_m to the redox mediators after acute Cd²⁺ exposure are shown in (G)-(I), in the same order as (A)-(C) and (D)-(F).

From Figures 4.5A-C, it can be seen that the detected electrochemical feedback from the T24 cells appear more flat and elliptical-like while displaying similar normalized currents. Taking vertical cross-sections above the center of the cell (green and red arrows in Figures 4.5A-C), the corresponding experimental PACs are quantified to have a membrane permeability coefficient of 7.5×10^{-5} m/s, 1.0×10^{-4} m/s and 1.0×10^{-4} m/s to FcCOO⁻ (Figure 4.5C), Fc(COO)₂²⁻ (Figure 4.5D) and Ru(NH₃)₆³⁺ (Figure 4.5E), respectively.

However, the induction of these hydrophilic probes is only possible once sufficient Cd^{2+} exposure is met.

Initially, T24 cells displayed a region of stability where these mediators remained unable to cross the membrane (Figures 4.5G-I). For the ferrocene carboxylates, this stable region consisted of Cd^{2+} treatments less than 4 mM, followed by an exponential growth region exceeding 4 mM Cd^{2+} treatment (Figures 4.5G and H). While similar in structure, the growth trend in membrane permeability to FcCOO^- is slower than that of $\text{Fc}(\text{COO})_2^{2-}$, which is consistent to the results in the time-dependent study. This might be due to the higher attractive interactions between the positively charged electrode to $\text{Fc}(\text{COO})_2^{2-}$ than to FcCOO^- . Another difference aside from the growth rate was the final membrane permeability values to each of these ferrocene carboxylates: FcCOO^- reached a higher permeability coefficient of 2.7×10^{-4} m/s, whereas $\text{Fc}(\text{COO})_2^{2-}$ reached 2.0×10^{-4} m/s, suggesting FcCOO^- is slightly more favorable to enter the cell.

$\text{Ru}(\text{NH}_3)_6^{3+}$, however, as a permeability probe behaved quite differently upon acute Cd^{2+} stimulation (Figure 4.5I): the membrane permeability trend displayed sigmodal growth as opposed to exponential growth observed for the ferrocene carboxylates. The T24 cells displayed a smaller impermeable region when treated with Cd^{2+} concentrations less than 2 mM. After treatment with 2 mM Cd^{2+} , the membrane permeability increased to approximately 1.0×10^{-4} m/s and remained unchanged regardless of further stimulation. It is interesting to note that the membrane permeability to the hydrophilic redox species induced by acute Cd^{2+} is similar to that by the low, but longer exposure of Cd^{2+} in the time-dependent study. With no evident physiological benefit,¹⁻³ this toxin can have severe detrimental effects on cells and organisms, altering the homeostatic balance and ultimately leading to cell death.

4.3.6 Concentration-Dependent Effects of Cd^{2+} on Cellular Viability

Since acute Cd^{2+} lead to more cell loss and higher overall membrane permeability, it was important to assess the cellular viability (Figure 4.6). Once again, the untreated T24 cells were considered to be the control sample, assuming 100 % viability. When treated with 1.0 and 2.5 mM Cd^{2+} , the T24 cells showed an increase in proliferation (Figure 4.6). From

our previous work, where acute Cd^{2+} was injected into the electrolyte solutions and membrane permeability was detected every 5 mins up to 45 mins, the membrane permeability was more resistant to changes at these low concentrations.⁸ In both the previous⁸ and present work, during these low acute concentration exposures, we had observed no significant morphological changes as a result of Cd^{2+} cytotoxicity. Within the low end of the acute Cd^{2+} concentration range (1-4 mM), the hydrophilic redox mediators remained mostly impermeable to the cell membrane, possibly correlating to the increased proliferation. However, once surpassing this concentration range (greater than 4 mM Cd^{2+}), the membrane permeability to these mediators significantly increased (approximately 2×10^{-4} m/s), which corresponded to higher cellular death (68 % after 7.5 mM treatment for 1 hour) as confirmed by the MTT assay.

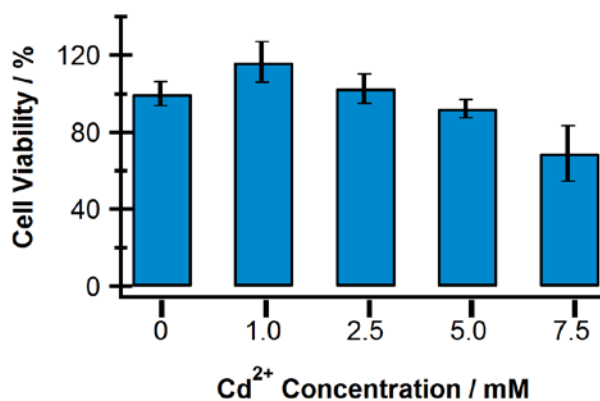


Figure 4.6. Cell viability of T24 cells treated with acute Cd^{2+} concentrations for 1 hour was measured by the MTT assay. The mean \pm RSD of 3 separate experiments (6 replicates per experiment) is shown.

4.3.7 Comparison of the Time-Dependent vs. Concentration-Dependent Studies

The membrane permeability to the three hydrophilic redox mediators was higher after acute exposure than in the time-dependent study, approximately 2×10^{-4} vs. 7×10^{-5} m/s, respectively. The lower membrane permeability in the time-dependent study could be explained by two possibilities: (1) the cells are capable of resisting or combating the cytotoxic effects of the low 25 μM Cd^{2+} dosage or (2) the membrane permeability could be increased further. If the second possibility holds true, the T24 cells were able to resist the

cytotoxic effects between hours 4-6 and longer treatment is required to induce permeability to match those found after acute Cd^{2+} treatment.⁸

The cell viability of T24 cells appeared to be unaffected when treated with 25 μM Cd^{2+} up to 6 hours, whereas significant cell death occurred within 1 hour when treated with acute concentrations. Since higher membrane permeability is indicative of membrane integrity loss, the increase in membrane permeability (concentration *vs.* time dependent studies) correlates well with cellular death. Whether Cd^{2+} is inducing membrane integrity loss through pore formation, structural collapse or the allowing available, yet unwanted ions and molecules into the cell through non-specific diffusion channels, hydrophilic redox probes are ideal candidates in toxin testing.

4.3.8 Effects on Flux/Membrane Permeability

The dominating factor contributing to increased membrane permeability detectable by SECM is the result of the redox mediator's diffusion into the cell.⁵² There are, of course, other contributing factors such as redox mediated processes (both extra- and intra- cellular) which can affect the rate of the mediator flux into the cell.⁵¹

When FcCH_2OH has diffused into a living cell, it is known to promote intracellular regeneration of the antioxidant, glutathione (GSH).^{37-38, 69} GSH can be reduced from glutathione disulfide, GS-SG by the following reaction:



Upon the increase in intracellular regeneration of GSH, the homeostatic balance is disrupted such that an enhanced GSH efflux from the cell was initiated.³⁷⁻³⁸ The extracellular GSH present can reduce the oxidized $\text{Fc}^+\text{CH}_2\text{OH}$ back to its reduced FcCH_2OH form, leading to enhanced electrochemical feedback near the cell membrane.³⁷⁻³⁸

Charged and hydrophilic species behave differently from the neutral FcCH_2OH sensing agent since these species may only enter the cell once sufficient membrane integrity is lost. While initially the charge effect on the influx of the agents into the cell is complex, our results indicate minor influence besides the static interactions between the electrode and

the molecular probe, as well as that between the molecular probe and the negatively charged cell membrane. In the time-dependent experiments, after 6 hours of 25 μM Cd^{2+} treatment, the membrane permeability to the redox mediators plateaued at approximately 7×10^{-5} m/s, while after a short treatment period of 1 hour with acute Cd^{2+} concentrations, the membrane permeability increased to approximately 2×10^{-4} m/s. It is evident that once the membrane integrity is sufficiently lost, the membrane does not discriminate charge species entering. It is also possible that once the hydrophilic mediators have entered the cell, intracellular redox proteins are interacting with the charged redox species. If these intracellular redox processes are occurring, activation or complications on other biological pathways are also possible, causing disruptions in homeostasis. This can lead to further detrimental oxidative stress or damage of the cells.

4.4 Conclusions

SECM depth scan mode was used to demonstrate hydrophilic redox mediators are ideal molecular probes in the testing of toxins since increased membrane permeability is indicative of membrane integrity loss. Species that are charged, polar or hydrophilic, such as FcCOO^- , $\text{Fc}(\text{COO})_2^{2-}$, and $\text{Ru}(\text{NH}_3)_6^{3+}$, are not favorable in crossing healthy membranes through passive diffusion. However, upon sufficient Cd^{2+} -treatment, the membrane integrity in T24 cells is weakened, allowing these foreign redox mediators to enter into the cell through non-specific diffusion channels, pore formations or the structural collapse of the cell membrane.

After long Cd^{2+} incubation treatments (25 μM , up to 6 hours), all hydrophilic redox mediators entered the cell at the same average membrane permeability coefficient, approximately 7×10^{-5} m/s. While Cd^{2+} and the hydrophilic mediators had entered T24 cells, the viability of the cells remains unaffected: the only morphological change observed was the localized swelling (blebs) in the center of cells. However when the cells were treated with acute Cd^{2+} concentrations for 1 hour, both the viability and permeability become greatly affected. The membrane permeability was found to increase to 2×10^{-4} m/s after exposure to 5 mM Cd^{2+} , while the viability of the cells decreased as Cd^{2+} concentration increased (68 %). Long durations of low Cd^{2+} treatment or a short exposure to acute Cd^{2+} leads to a similar

outcome: the membrane permeability was augmented sufficiently to allow the entry of these foreign hydrophilic species into the cells. In both these studies, beside the static interaction between the electrode and the redox mediator, the membrane permeability to the mediators reached similar maxima, which suggested that the effect of the molecular charge may not influence the rate of its flux into the cell. This would support their influx into the cell is through non-specific diffusion channels, pore formation or the structural collapse of the membrane. The use of hydrophilic redox mediators in SECM may lead to insight into potential drug interactions and testing in single live cells.

4.5 References

1. Hartwig, A., Metal Interaction with Redox Regulation: An Integrating Concept in Metal Carcinogenesis? *Free Radic. Biol. Med.* **2013**, *55*, 63-72.
2. Thévenod, F.; Lee, W.-K., Toxicology of Cadmium and Its Damage to Mammalian Organs. In *Cadmium: From Toxicity to Essentiality*, Sigel, A.; Sigel, H.; Sigel, R. K. O., Eds. Springer Netherlands: 2013.
3. Sarkar, B., *Heavy Metals in the Environment*; Marcel Dekker: New York, 2002.
4. Thevenod, F.; Lee, W. K., Cadmium and Cellular Signaling Cascades: Interactions between Cell Death and Survival Pathways. *Arch. Toxicol.* **2013**, *87*, 1743-1786.
5. Thévenod, F., Catch Me If You Can! Novel Aspects of Cadmium Transport in Mammalian Cells. *Biometals* **2010**, *23*, 857-875.
6. López, E.; Figueroa, S.; Oset-Gasque, M. J.; González, M. P., Apoptosis and Necrosis: Two Distinct Events Induced by Cadmium in Cortical Neurons in Culture. *Br. J. Pharmacol.* **2003**, *138*, 901-911.
7. Yeh, J.-H.; Huang, C.-C.; Yeh, M.-Y.; Wang, J.-S.; Lee, J.-K.; Jan, C.-R., Cadmium-Induced Cytosolic Ca²⁺ elevation and Subsequent Apoptosis in Renal Tubular Cells. *Basic Clin. Pharmacol. Toxicol.* **2009**, *104*, 345-351.
8. Li, M. S. M.; Filice, F. P.; Ding, Z., A Time Course Study of Cadmium Effect on Membrane Permeability of Single Human Bladder Cancer Cells Using Scanning Electrochemical Microscopy. *J. Inorg. Biochem.* **2014**, *136*, 177-183.
9. Henderson, J. D.; Filice, F. P.; Li, M. S. M.; Ding, Z., Tracking Live Cell Response to Cadmium (II) Concentrations by Scanning Electrochemical Microscopy. *J. Inorg. Biochem.* **2016**, *158*, 92-98.

10. Chen, L.; Liu, L.; Huang, S., Cadmium Activates the Mitogen-Activated Protein Kinase (MAPK) Pathway Via Induction of Reactive Oxygen Species and Inhibition of Protein Phosphatases 2A and 5. *Free Radic. Biol. Med.* **2008**, *45*, 1035-1044.
11. Strober, W., Trypan Blue Exclusion Test of Cell Viability. In *Current Protocols in Immunology*, John Wiley & Sons, Inc.: 2001.
12. Bard, A.; Fan, F.; Kwak, J.; Lev, O., Scanning Electrochemical Microscopy. Introduction and Principles. *Anal. Chem.* **1989**, *61*, 132-138.
13. Bard, A. J.; Mirkin, M. V., *Scanning Electrochemical Microscopy*; Marcel Dekker: New York, 2001.
14. Nowierski, C.; Noël, J. J.; Shoesmith, D. W.; Ding, Z., Correlating Surface Microstructures with Reactivity on Commercially Pure Zirconium Using Scanning Electrochemical Microscopy and Scanning Electron Microscopy. *Electrochem. Commun.* **2009**, *11*, 1234-1236.
15. Yin, Y.; Niu, L.; Lu, M.; Guo, W.; Chen, S., In Situ Characterization of Localized Corrosion of Stainless Steel by Scanning Electrochemical Microscope. *Appl. Surf. Sci.* **2009**, *255*, 9193-9199.
16. Ding, Z.; Quinn, B. M.; Bard, A. J., Kinetics of Heterogeneous Electron Transfer at Liquid/Liquid Interfaces as Studied by SECM. *J. Phys. Chem. B* **2001**, *105*, 6367-6374.
17. Tang, J.; Zheng, J.-J.; Yu, Y.-T.; Chen, I.; Zhang, N.; Tian, Z., Selective Etching of Zn Films on an ITO Substrate Using a Scanning Electrochemical Microscope. *Electrochim. Acta* **2012**, *83*, 247-252.
18. Eifert, A.; Mizaikoff, B.; Kranz, C., Advanced Fabrication Process for Combined Atomic Force-Scanning Electrochemical Microscopy (AFM-SECM) Probes. *Micron* **2015**, *68*, 27-35.
19. Beaulieu, I.; Kuss, S.; Mauzeroll, J.; Geissler, M., Biological Scanning Electrochemical Microscopy and Its Application to Live Cell Studies. *Anal. Chem.* **2011**, *83*, 1485-1492.
20. Schulte, A.; Schuhmann, W., Single-Cell Microelectrochemistry. *Angew. Chem. Int. Ed.* **2007**, *46*, 8760-8777.
21. Schulte, A.; Nebel, M.; Schuhmann, W., Scanning Electrochemical Microscopy in Neuroscience. *Annu. Rev. Anal. Chem.* **2010**, *3*, 299-318.
22. Zhao, C.; Wittstock, G., An SECM Detection Scheme with Improved Sensitivity and Lateral Resolution: Detection of Galactosidase Activity with Signal Amplification by Glucose Dehydrogenase. *Angew. Chem. Int. Ed.* **2004**, *43*, 4170-4172.

23. Wu, Z.-Q.; Jia, W.-Z.; Wang, K.; Xu, J.-J.; Chen, H.-Y.; Xia, X.-H., Exploration of Two-Enzyme Coupled Catalysis System Using Scanning Electrochemical Microscopy. *Anal. Chem.* **2012**, *84*, 10586-10592.
24. Matsumae, Y.; Arai, T.; Takahashi, Y.; Ino, K.; Shiku, H.; Matsue, T., Evaluation of the Differentiation Status of Single Embryonic Stem Cells Using Scanning Electrochemical Microscopy. *Chem. Commun.* **2013**, *49*, 6498-6500.
25. Nioradze, N.; Kim, J.; Amemiya, S., Quasi-Steady-State Voltammetry of Rapid Electron Transfer Reactions at the Macroscopic Substrate of the Scanning Electrochemical Microscope. *Anal. Chem.* **2010**, *83*, 828-835.
26. Cannan, S.; Cervera, J.; Steliaros, R. J.; Bitziou, E.; Whitworth, A. L.; Unwin, P. R., Scanning Electrochemical Microscopy (SECM) Studies of Catalytic EC [Prime or Minute] Processes: Theory and Experiment for Feedback, Generation/Collection and Imaging Measurements. *Phys. Chem. Chem. Phys.* **2011**, *13*, 5403-5412.
27. Matrab, T.; Hauquier, F.; Combellas, C.; Kanoufi, F., Scanning Electron Microscopy Investigation of Molecular Transport and Reactivity within Polymer Brushes. *ChemPhysChem* **2010**, *11*, 670-682.
28. Zhu, R.; Macfie, S. M.; Ding, Z., Cadmium-Induced Plant Stress Investigated by Scanning Electrochemical Microscopy. *J. Exp. Bot.* **2005**, *56*, 2831-2838.
29. Wang, Y.; Noël, J.-M.; Velmurugan, J.; Nogala, W.; Mirkin, M. V.; Lu, C.; Guille Collignon, M.; Lemaître, F.; Amatore, C., Nanoelectrodes for Determination of Reactive Oxygen and Nitrogen Species inside Murine Macrophages. *Proc. Natl. Acad. Sci. U. S. A.* **2012**, *109*, 11534-11539.
30. Zhao, X.; Lam, S.; Jass, J.; Ding, Z., Scanning Electrochemical Microscopy of Single Human Urinary Bladder Cells Using Reactive Oxygen Species as Probe of Inflammatory Response. *Electrochem. Comm.* **2010**, *12*, 773-776.
31. Zhao, X.; Petersen, N. O.; Ding, Z., Comparison Study of Live Cells by Atomic Force Microscopy, Confocal Microscopy, and Scanning Electrochemical Microscopy. *Can. J. Chem.* **2007**, *85*, 175-183.
32. Zhao, X.; Diakowski, P.; Ding, Z., Deconvoluting Topography and Spatial Physiological Activity of Live Macrophage Cells by Scanning Electrochemical Microscopy in Constant-Distance Mode. *Anal. Chem.* **2010**, *82*, 8371-8373.
33. Zhang, M. M.; Long, Y. T.; Ding, Z., Filming a Live Cell by Scanning Electrochemical Microscopy: Label-Free Imaging of the Dynamic Morphology in Real Time. *Chem. Cent. J.* **2012**, *6*, 20.
34. Salamifar, S. E.; Lai, R. Y., Use of Combined Scanning Electrochemical and Fluorescence Microscopy for Detection of Reactive Oxygen Species in Prostate Cancer Cells. *Anal. Chem.* **2013**, *85*, 9417-9421.

35. Liebetrau, J. M.; Miller, H. M.; Baur, J. E.; Takacs, S. A.; Anupunpisit, V.; Garris, P. A.; Wipf, D. O., Scanning Electrochemical Microscopy of Model Neurons: Imaging and Real-Time Detection of Morphological Changes. *Anal. Chem.* **2002**, *75*, 563-571.
36. Kurulugama, R. T.; Wipf, D. O.; Takacs, S. A.; Pongmayteegul, S.; Garris, P. A.; Baur, J. E., Scanning Electrochemical Microscopy of Model Neurons: Constant Distance Imaging. *Anal. Chem.* **2005**, *77*, 1111-1117.
37. Kuss, S.; Cornut, R.; Beaulieu, I.; Mezour, M. A.; Annabi, B.; Mauzeroll, J., Assessing Multidrug Resistance Protein 1-Mediated Function in Cancer Cell Multidrug Resistance by Scanning Electrochemical Microscopy and Flow Cytometry. *Bioelectrochemistry* **2011**, *82*, 29-37.
38. Kuss, S.; Polcari, D.; Geissler, M.; Brassard, D.; Mauzeroll, J., Assessment of Multidrug Resistance on Cell Coculture Patterns Using Scanning Electrochemical Microscopy. *Proc. Natl. Acad. Sci. U. S. A.* **2013**, *110*, 9249-9254.
39. Bard, A.; Li, X.; Zhan, W., Chemically Imaging Living Cells by Scanning Electrochemical Microscopy. *Biosens. Bioelectron.* **2006**, *22*, 461-472.
40. Amemiya, S.; Guo, J.; Xiong, H.; Gross, D., Biological Applications of Scanning Electrochemical Microscopy: Chemical Imaging of Single Living Cells and Beyond. *Anal. Bioanal. Chem.* **2006**, *386*, 458-471.
41. Zhu, R.; Macfie, S. M.; Ding, Z., Effects of Cadmium on Photosynthetic Oxygen Evolution from Single Stomata in Brassica Juncea (L.) Czern. *Langmuir* **2008**, *24*, 14261-14268.
42. Zhao, X.; Zhang, M.; Long, Y.; Ding, Z., Redox Reactions of Reactive Oxygen Species in Aqueous Solutions as the Probe for Scanning Electrochemical Microscopy of Single Live T24 Cells. *Can. J. Chem.* **2010**, *88*, 569-576.
43. Shao, Y.; Mirkin, M. V., Probing Ion Transfer at the Liquid/Liquid Interface by Scanning Electrochemical Microscopy (SECM). *J. Phys. Chem. B* **1998**, *102*, 9915-9921.
44. Barker, A. L.; Macpherson, J. V.; Slevin, C. J.; Unwin, P. R., Scanning Electrochemical Microscopy (SECM) as a Probe of Transfer Processes in Two-Phase Systems: Theory and Experimental Applications of SECM-Induced Transfer with Arbitrary Partition Coefficients, Diffusion Coefficients, and Interfacial Kinetics. *J. Phys. Chem. B* **1998**, *102*, 1586-1598.
45. Koley, D.; Bard, A. J., Triton X-100 Concentration Effects on Membrane Permeability of a Single HeLa Cell by Scanning Electrochemical Microscopy (SECM). *Proc. Natl. Acad. Sci. U. S. A.* **2010**, *107*, 16783-7.

46. Guo, J.; Amemiya, S., Permeability of the Nuclear Envelope at Isolated Xenopus Oocyte Nuclei Studied by Scanning Electrochemical Microscopy. *Anal. Chem.* **2005**, *77*, 2147-2156.
47. Yasukawa, T.; Uchida, I.; Matsue, T., Permeation of Redox Species through a Cell Membrane of a Single, Living Algal Protoplast Studied by Microamperometry. *Biochim. Biophys. Acta* **1998**, *1369*, 152-158.
48. Diakowski, P. M.; Ding, Z. F., Interrogation of Living Cells Using Alternating Current Scanning Electrochemical Microscopy (AC-SECM). *Phys. Chem. Chem. Phys.* **2007**, *9*, 5966-5974.
49. Kasai, S.; Shiku, H.; Torisawa, Y.-S.; Noda, H.; Yoshitake, J.; Shiraishi, T.; Yasukawa, T.; Watanabe, T.; Matsue, T.; Yoshimura, T., Real-Time Monitoring of Reactive Oxygen Species Production During Differentiation of Human Monocytic Cell Lines (THP-1). *Anal. Chim. Acta* **2005**, *549*, 14-19.
50. Hu, R.; Guille, M.; Arbault, S.; Lin, C. J.; Amatore, C., In Situ Electrochemical Monitoring of Reactive Oxygen and Nitrogen Species Released by Single MG63 Osteosarcoma Cell Submitted to a Mechanical Stress. *Phys. Chem. Chem. Phys.* **2010**, *12*, 10048-10054.
51. Liu, B.; Rotenberg, S. A.; Mirkin, M. V., Scanning Electrochemical Microscopy of Living Cells: Different Redox Activities of Nonmetastatic and Metastatic Human Breast Cells. *Proc. Natl. Acad. Sci. U. S. A.* **2000**, *97*, 9855-9860.
52. Li, X.; Bard, A. J., Scanning Electrochemical Microscopy of HeLa Cells – Effects of Ferrocene Methanol and Silver Ion. *J. Electroanal. Chem.* **2009**, *628*, 35-42.
53. Zhang, M. N.; Ding, Z.; Long, Y. T., Sensing Cisplatin-Induced Permeation of Single Live Human Bladder Cancer Cells by Scanning Electrochemical Microscopy. *Analyst* **2015**, *140*, 6054-6060.
54. Mosmann, T., Rapid Colorimetric Assay for Cellular Growth and Survival: Application to Proliferation and Cytotoxicity Assays. *J. Immunol. Methods* **1983**, *65*, 55-63.
55. Filice, F. P.; Li, M. S. M.; Henderson, J. D.; Ding, Z., Three-Dimensional Electrochemical Functionality of an Interdigitated Array Electrode by Scanning Electrochemical Microscopy. *J. Phys. Chem. C* **2015**, *119*, 21473-21482.
56. Miao, W.; Ding, Z.; Bard, A. J., Solution Viscosity Effects on the Heterogeneous Electron Transfer Kinetics of Ferrocenemethanol in Dimethyl Sulfoxide – Water Mixtures. *J. Phys. Chem. B* **2002**, *106*, 1392-1398.
57. Rossier, J. S.; Vollet, C.; Carnal, A.; Lager, G.; Gobry, V.; Girault, H. H.; Michel, P.; Reymond, F., Plasma Etched Polymer Microelectrochemical Systems. *Lab Chip* **2002**, *2*, 145-150.

58. Mauzeroll, J.; Hueske, E. A.; Bard, A. J., Scanning Electrochemical Microscopy. 48. Hg/Pt Hemispherical Ultramicroelectrodes: Fabrication and Characterization. *Anal. Chem.* **2003**, *75*, 3880-3889.
59. Filice, F. P.; Li, M. S. M.; Henderson, J. D.; Ding, Z., Mapping Cd²⁺-Induced Membrane Permeability Changes of Single Live Cells by Means of Scanning Electrochemical Microscopy. *Anal. Chim. Acta* **2016**, *908*, 85-94.
60. Gauthier, N. C.; Rossier, O. M.; Mathur, A.; Hone, J. C.; Sheetz, M. P., Plasma Membrane Area Increases with Spread Area by Exocytosis of a GPI-Anchored Protein Compartment. *Mol. Biol. Cell* **2009**, *20*, 3261-3272.
61. Dela Vega, A. L.; Delcour, A. H., Polyamines Decrease Escherichia Coli Outer Membrane Permeability. *J. Bacteriol.* **1996**, *178*, 3715-3721.
62. Sridhar, A.; de Boer, H. L.; van den Berg, A.; Le Gac, S., Microstamped Petri Dishes for Scanning Electrochemical Microscopy Analysis of Arrays of Microtissues. *PLoS ONE* **2014**, *9*, e93618.
63. Gauthier, N. C.; Fardin, M. A.; Roca-Cusachs, P.; Sheetz, M. P., Temporary Increase in Plasma Membrane Tension Coordinates the Activation of Exocytosis and Contraction During Cell Spreading. *Proc. Natl. Acad. Sci. U. S. A.* **2011**, *108*, 14467-14472.
64. McNeil, P. L.; Steinhardt, R. A., Plasma Membrane Disruption: Repair, Prevention, Adaptation. *Annu. Rev. Cell Dev. Biol.* **2003**, *19*, 697-731.
65. Nikaido, H.; Luckey, M.; Rosenberg, E. Y., Nonspecific and Specific Diffusion Channels in the Outer Membrane of Escherichia Coli. *J. Supramol. Struct.* **1980**, *13*, 305-313.
66. Karabulut-Bulan, O.; Bolkent, S.; Yanardag, R.; Bilgin-Sokmen, B., The Role of Vitamin C, Vitamin E, and Selenium on Cadmium-Induced Renal Toxicity of Rats. *Drug Chem. Toxicol.* **2008**, *31*, 413-426.
67. Chen, J.; Wagner, M. C., Altered Membrane-Cytoskeleton Linkage and Membrane Blebbing in Energy-Depleted Renal Proximal Tubular Cells. *Am. J. Physiol. Renal. Physiol.* **2001**, *280*, F619-F627.
68. Galán, A.; García-Bermejo, L.; Troyano, A.; Vilaboa, N. E.; Fernández, C.; de Blas, E.; Aller, P., The Role of Intracellular Oxidation in Death Induction (Apoptosis and Necrosis) in Human Promonocytic Cells Treated with Stress Inducers (Cadmium, Heat, X-Rays). *Eur. J. Cell Biol.* **2001**, *80*, 312-320.
69. Kuss, S.; Trinh, D.; Mauzeroll, J., High-Speed Scanning Electrochemical Microscopy Method for Substrate Kinetic Determination: Application to Live Cell Imaging in Human Cancer. *Anal. Chem.* **2015**, *87*, 8102-8106.

Chapter 5

5 Zn²⁺-Induced Apoptosis in Single Human Bladder Cancer Cells Interrogated by Scanning Electrochemical Microscopy

(A version of this work has been prepared for publication

Li, M.S.M.; Filice, F.P.; Ding, Z. Zn²⁺-Induced Apoptosis in Single Human Bladder Cancer Cells Interrogated by Scanning Electrochemical Microscopy, **2017**. *Upon Submission*.)

5.1 Introduction

Zn is one of the most important and abundant trace elements found in the body.¹⁻³ It is known to be an essential component of many metalloenzymes, metalloproteins and transcription factors. Its biological role in the body is widespread, including but not limited to, structural and catalytic roles in various metalloenzymes, facilitating protein function, maturation and degradation, as well as playing a role in DNA transcription and regulation.²⁻³

As a trace essential element, it is important that homeostatic levels of Zn²⁺ are maintained. When deviations from safe levels of Zn²⁺ occurs, either by an increase or decrease in cellular concentrations, disruptions in biological processes can occur, potentially leading to disease or death.³⁻⁴ For instance, Vazquez *et al.* reported the effects of Zn²⁺ on human Burkitt lymphoma B cells were concentration-dependent: low Zn²⁺ (<50 μ M) inhibited caspase-3 activation and apoptosis, while higher concentrations appeared to induce apoptosis.⁴ Han *et al.* reported similar Zn²⁺ effects in mouse embryonic stem cells, where moderate concentrations of Zn²⁺ (≥ 4 μ M) increased cellular proliferation, while higher Zn²⁺ concentrations (≥ 200 μ M) blocked this effect.¹

Upon metal overloading (excess), essential trace elements are known to become toxic to the organism. This can contribute to the disturbance of cellular redox homeostasis, either through the induction of oxidative stress or the metals interacting with proteins involved in cellular redox regulation.⁵ Disrupting the homeostatic redox levels can lead to additional oxidative stress (reactive oxygen and nitrogen species generation). This damage can lead to

lipid peroxidation of the cell membrane and eventual membrane integrity loss, allowing increased permeation to chemical agents. Furthermore, Zn^{2+} is now well recognized as an important cofactor in regulation of apoptosis⁶⁻⁷ and is known to have an anticancer effect by inducing apoptosis in prostate and bladder cancer cells.⁸

Scanning electrochemical microscopy (SECM) has emerged as a powerful tool in the investigation of biological cells.⁹⁻¹⁵ A large number of these studies have focused on the analysis of the cell membrane properties, such as membrane integrity, through the permeability of redox mediators in and out of the cell. Redox mediators that are hydrophilic and charged, e.g. hexaamineruthenium(III) ($\text{Ru}(\text{NH}_3)_6^{3+}$),¹⁶ ferrocenecarboxylate (FcCOO^-)¹⁷ and ferrocyanide ($\text{Fe}(\text{CN})_6^{4-}$),¹⁸⁻¹⁹ have been confirmed to be impermeable to healthy and intact cells through several modes in SECM (insulator, negative feedback).^{16-18, 20-21} The permeation of these hydrophilic and charged species by SECM (partial positive feedback) signifies substantial membrane integrity loss, such as pore formation or structural collapse of the cell membrane.¹⁸ On the other hand, water soluble mediators exhibiting more oleophilic properties (membrane-permeable), such as 1,2-naphthaquinone ($\text{C}_{10}\text{H}_6\text{O}_2$),¹⁷ menadione ($\text{C}_6\text{H}_4(\text{CO})_2\text{C}_2\text{H}(\text{CH}_3)$)^{17, 22} and ferrocenemethanol (FcCH_2OH),^{16, 20, 23} can be used to monitor the more subtle changes in the cell membrane than that of the hydrophilic and charged redox mediators.

Using a membrane permeable and an impermeable redox mediator (FcCH_2OH and $\text{Ru}(\text{NH}_3)_6^{3+}$, respectively), herein we investigate the effects of various Zn^{2+} concentration on single live human bladder cancer (T24) cells for the first time. Since it is known that a correlation between membrane permeability and cellular viability exists, this study focuses on how SECM can be used to assist in the identification of the Zn^{2+} -induced cellular death mechanism (apoptosis or necrosis). It is discovered that Zn^{2+} exposure increases the membrane permeability to the redox mediators detected by SECM and causes the subsequent morphological and biological changes which lead to cellular apoptosis. This SECM membrane permeability study gives insight into physiology and pathology of the single live cell model.

5.2 Experimental

The experimental details discussed here are the project-specific details briefly summarized. A more detailed report of the Experimental is included in Chapter 2.

5.2.1 Materials

Zinc chloride (anhydrous, $\geq 97\%$), FcCH₂OH (97%), Ru(NH₃)₆·Cl₃ (98%) and sodium dodecyl sulfate (SDS, 99+%) were acquired from Sigma-Aldrich (Mississauga, ON) and used as received. Stock solutions of 0.9 mM FcCH₂OH or 1 mM Ru(NH₃)₆³⁺ were prepared in 1x phosphate buffered saline (PBS, 10 mM, pH 7.4). 3-(4,5-dimethylthiazol-2-yl)-2,5-diphenyltetrazolium bromide (MTT) was acquired from R&D Systems Inc. (Minneapolis, MN) in the TACS[®] MTT Cell Proliferation Assay Kit. Dimethyl sulfoxide (DMSO, spectroscopic grade, Caledon Laboratory Ltd, Georgetown, ON) was used to dissolve the formazan crystals in the MTT assays. The PE Annexin V Apoptosis Detection Kit with 7-AAD was purchased from BioLegend[®] (San Diego, CA). All ReadyProbes[™] and CellEvent[™] Caspase-3/7 were purchased from ThermoFisher Scientific (Burlington, ON)

5.2.2 Electrode Fabrication

Pt ultramicroelectrodes (UMEs) were fabricated in-house using a P-2000 laser-based micropipette puller system (Sutter Instrument, Novato, CA).²⁴⁻²⁵ Briefly, a 25 μm Pt wire (Goodfellow Metals, Cambridge, U.K.) was heat-sealed and pulled within a quartz capillary, producing two Pt tips sheathed in quartz.²⁵ Following internal electrical connections and reinforcement of the quartz capillary, manual polishing of the tip ensured a flat, smooth Pt surface was exposed. The tip was polished to have a Pt diameter of 4.4 μm with an RG (glass to wire ratio) of 3. The quality of the UME was optically assessed and electrochemically tested using 0.9 mM FcCH₂OH and 1 mM Ru(NH₃)₆³⁺ in PBS via cyclic voltammetry.

5.2.3 Cell Culture

T24 cells (ATCC[®] HTB-4[™]) were acquired from American Type Culture Collection (ATCC, Manassas, VA) and maintained in accordance to their protocol. All culture solutions and serums were acquired from Invitrogen (Burlington, ON) with the exception of McCoy's

5A medium (ATCC). For the SECM experiments, T24 cells were plated on glass bottom petri dishes (P35G-0-20C, MatTek Corporation, Ashland, MA) and allowed to adhere overnight. The culture medium was then replaced with new medium supplemented with Zn^{2+} . Following 24 hr treatment, the cells were washed 3x with PBS and replaced with PBS containing 0.9 mM FcCH_2OH and 1 mM $\text{Ru}(\text{NH}_3)_6^{3+}$ for SECM analysis.

5.2.4 SECM Instrumentation and Experimentation

SECM experiments were performed on an Alpha-SNOM instrument (WITec, Ulm, Germany) adapted with a custom-made electrode mount. A 4.4 μm Pt UME was used as the SECM probe (working electrode) and a Ag/AgCl wire was used as a combined auxiliary/reference electrode. All electrochemical experiments were performed using a CHI 800B with a CHI 200 Picoamp Booster (CH Instruments, Austin, TX), which current signals were fed into one data acquisition channel of the Alpha-SNOM instrument. The details of this SECM instrumentation and operation procedure has been described elsewhere in great detail.²⁶⁻²⁹ Briefly, SECM measurements were obtained by mounting the petri dishes onto the scanning stage (P-517K064, Polytec PI, Germany) of the Alpha-SNOM instrument, maintained at 37.0 ± 0.2 °C (Bioscience Tools, San Diego, CA). Individual T24 cells and the Pt UME were located using the inverted Nikon objective lens (50x, N.A. = 0.55, Japan) of the instrument. Using the confocal setting within the WITec software, SECM depth scan experiments were conducted. This allowed the biased UME to perform a 2D (x , z) sweep over the cells, performing a horizontal line scan at each vertical stepping upon approach. Each SECM depth scan image has 128 x 64 pixels, scan width and depth of 60 μm and 40 μm respectively, and an integration time of 0.03 s. All petri dishes and cells were discarded within 1.5 hours of experiments.

5.2.5 SECM Data Analysis

Probe approach curves (PACs) were obtained by extracting the vertical cross-sections above the center of the cells from their respective SECM depth scan images. To quantify the membrane permeability coefficients, P_m , experimental PACs were overlapped onto simulated curves generated by COMSOL Multiphysics v.5.0, a finite element analysis software.^{21, 30} For the purpose of the simulated PAC data sets, the simulation model is representative of the

SECM experiments and was designed in 2D axial symmetry, with the symmetry plane through the center of the cell and electrode. Detailed descriptions of the model geometry, simulation parameters, and post-processing steps have been previously reported in great detail.^{28, 31} All P_m values reported here are the averages of 2-6 individual cell measurements, unless otherwise stated. In each average membrane permeability plot, the error bars represent the mean \pm standard error (SE, $SE = \sigma/\sqrt{N}$, where σ is the standard deviation and N is the number of individual cell measurements).

5.2.6 Optical Imaging

Methanol-fixed, Zn^{2+} -treated T24 cells were optically imaged with a Zeiss LSM 510 META multiphoton confocal laser scanning microscope. For these images, a 63x Nikon objective (N.A. = 0.75, Japan) was used.

5.2.7 Immunofluorescence

The Countess II FL Automated Cell Counter (ThermoFisher Scientific) was used to monitor cellular viability in Zn^{2+} -treated T24 cells. For insight into the membrane integrity of the Zn^{2+} -treated T24 cells, ReadyProbes[®] NucGreen (membrane-impermeable) was used. To identify apoptotic and necrotic cells, CellEvent[™] Caspase-3/7Green ReadyProbes[®] reagent and ReadyProbes[®] NucRed (propidium iodide), respectively were used as their indicators. For all immunofluorescence experiments, ReadyProbes[®] NucBlue (Hoechst 33342, membrane-permeable) was used to identify the total number of cells per sample. These reagents were used according to supplier's protocol (ThermoFisher Scientific).

5.2.8 MTT Cell Proliferation Assay

Cellular viability of Zn^{2+} -treated T24 cells were assessed using the MTT cell proliferation assay.³² Briefly, 2×10^4 cells/well were seeded onto Corning Scientific Costar[™] 96-well polystyrol flat bottom plates. After 24 hours, the growth medium was aspirated and replaced with new media containing Zn^{2+} or SDS (0.05, 0.10, 0.15, or 0.20 mg/mL), which was used as the positive control. After treatment, the media was carefully aspirated and replaced with 100 μ L of fresh media (absent of phenol red) and 10 μ L of the MTT reagent. After 6 hours, the MTT solution was carefully removed and the formazan

crystals were dissolved with 50 μ L DMSO. The absorbance at 540 nm was read by a M1000 PRO plate reader (Tecan Switzerland) following 1 s of shaking at 2 mm amp and 654 rpm. To remove the background media effects, empty (blank) wells were also treated in accordance to the MTT protocol.³³

5.2.9 Flow Cytometry

Apoptosis, as the primary death mechanism, was confirmed using the Biolegend® PE Annexin V Apoptosis Detection Kit with 7-AAD. Briefly, 3×10^5 T24 cells were plated into individual wells of a 6-well plate (0-75 μ M Zn^{2+} -treatment) or 9×10^5 T24 cells in T25 flasks for the acute concentrations (100-400 μ M Zn^{2+} , with 1 control sample at 0 μ M). After 24 hours, the growth medium was aspirated and replaced with new growth medium containing Zn^{2+} for 24 hours, paralleling the SECM and cell viability experiments. Another set of T24 cells were exposed to 12 hours of Zn^{2+} treatment, which was prepared similarly to the acute treatment previously mentioned.

For flow cytometry experiments, the cells were trypsinized to detach the Zn^{2+} -treated T24 cells from their dishes and resuspended in cold cell staining buffer and centrifuged at 800 rpm for 5 mins. The cell staining buffer was decanted and resuspended in Annexin V binding buffer. 7-AAD and Annexin V PE were added to the cell samples, followed by incubation at room temperature for 15 mins in the dark. Annexin V buffer was then added to each tube according to Biolegend® protocol. The only exception to their protocol was half the volumes of Annexin V PE and 7-AAD were used. Cells were gently vortexed prior to testing on a FACSCanto (BD Biosciences, USA) and data was analyzed with the software FlowJo VX (FlowJo, LLC, USA). 50,000 cell events were targeted for Zn^{2+} -treated T24 cells (0-400 μ M for 24 hours); however approximately 36,000 and 30,100 cell events could be reached after 200 μ M and 400 μ M Zn^{2+} -treatment. For the 12 hour Zn^{2+} -treatment, 20,000 cell events were analyzed.

5.3 Results and Discussion

5.3.1 Zn²⁺ Effects on Cell Membrane Permeability

5.3.1.1 SECM with Ferrocenemethanol (Permeable)

SECM depth scans,^{25, 29, 34-35} where the UME is scanned repeatedly in the horizontal plane (x -axis, image width) at various z positions upon approach to the substrate (image depth), were carried out on single Zn²⁺-treated T24 cells. Using this SECM mode, the cell P_m to FcCH₂OH, a partially permeable electrochemical mediator, was quantified (Figures 5.1A and B).

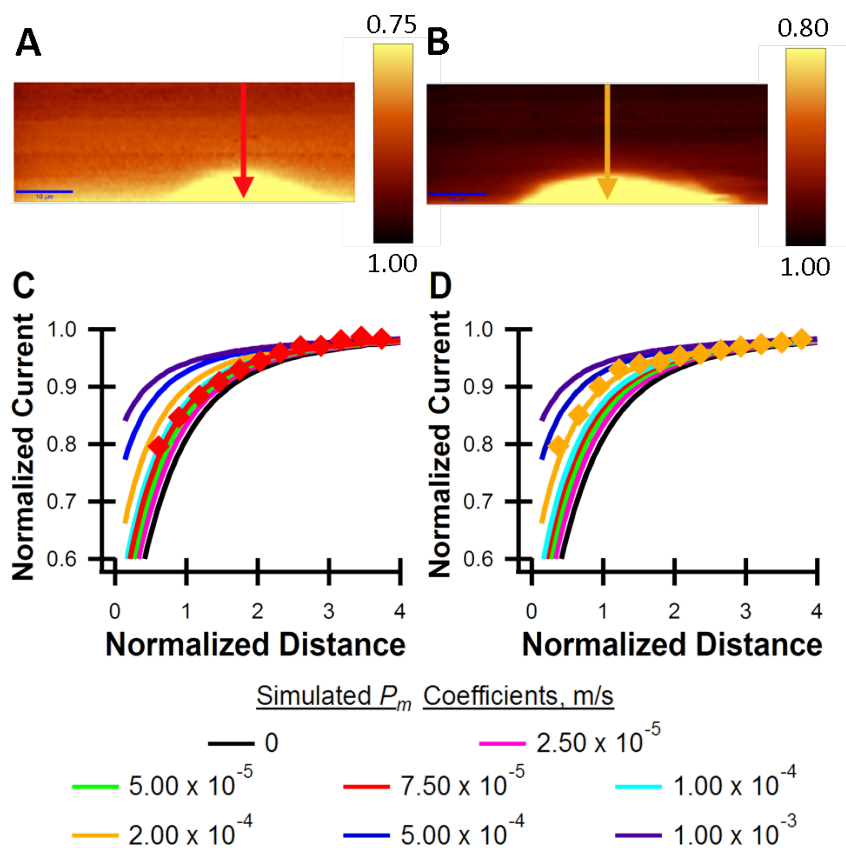


Figure 5.1. Typical SECM depth scan images of single T24 cells treated with (A) 10 μM and (B) 400 μM Zn²⁺ using FcCH₂OH as the redox mediator. The scale bar in each image represents 10 μm. The arrows in (A) and (B) indicate where the PACs were extracted for P_m quantification along with simulated ones in (C) and (D), respectively.

The colors of the arrows in the depth images (A-B) match the obtained PACs (diamonds in C-D).

Vertical cross-sections (current vs. tip-to-sample distance) were extracted from the SECM depth scan images. The UME tip current was normalized against the steady state (bulk) current and the tip-to-sample distances were normalized against the electrode radius to obtain the so-called PACs. This allows the quantification of cellular properties, such as membrane permeability¹⁸ and cell height,³⁰ when overlaid onto simulated curves generated with defined geometry and permeability coefficients.

From Figure 5.1A, the experimental PAC to a T24 cell treated with 10 μM Zn^{2+} (red arrow) revealed a P_m of 7.5×10^{-5} m/s (red, Figure 5.1C), similar to that of the untreated (control) T24 cells.^{21, 28} This confirms that FcCH_2OH can passively diffuse across the cell membrane, entering and leaving the cell on its own. Passive diffusion of the redox mediator from the cell interior, across the membrane, returns the redox species back into solution. This contributes to an increased tip current relative to an ideally insulating (no flux) surface of the same geometry (region of decreased feedback, yellow, Figures 5.1A and B). When the SECM tip is scanned horizontally across the cell the increase in redox species provides a noticeable response in the form of a reduced tip current. When T24 cells were treated with increasing Zn^{2+} concentrations, the membrane permeability to FcCH_2OH was also observed to increase. For example, a PAC to a T24 cell treated with 400 μM Zn^{2+} (orange arrow, Figure 5.1B) revealed an experimental P_m value of 2.0×10^{-4} m/s (orange, Figure 5.1D). This increase in membrane permeability coefficient indicates a higher efflux of the redox species from the cell to the SECM tip (higher tip current, Figures 5.1C vs. 5.1D), therefore a higher degree of passive diffusion across the membrane.

Overall, SECM revealed a trend that Zn^{2+} altered the membrane permeability to FcCH_2OH (N = 2-6 cells) in a two-stage manner (Figure 5.2A).

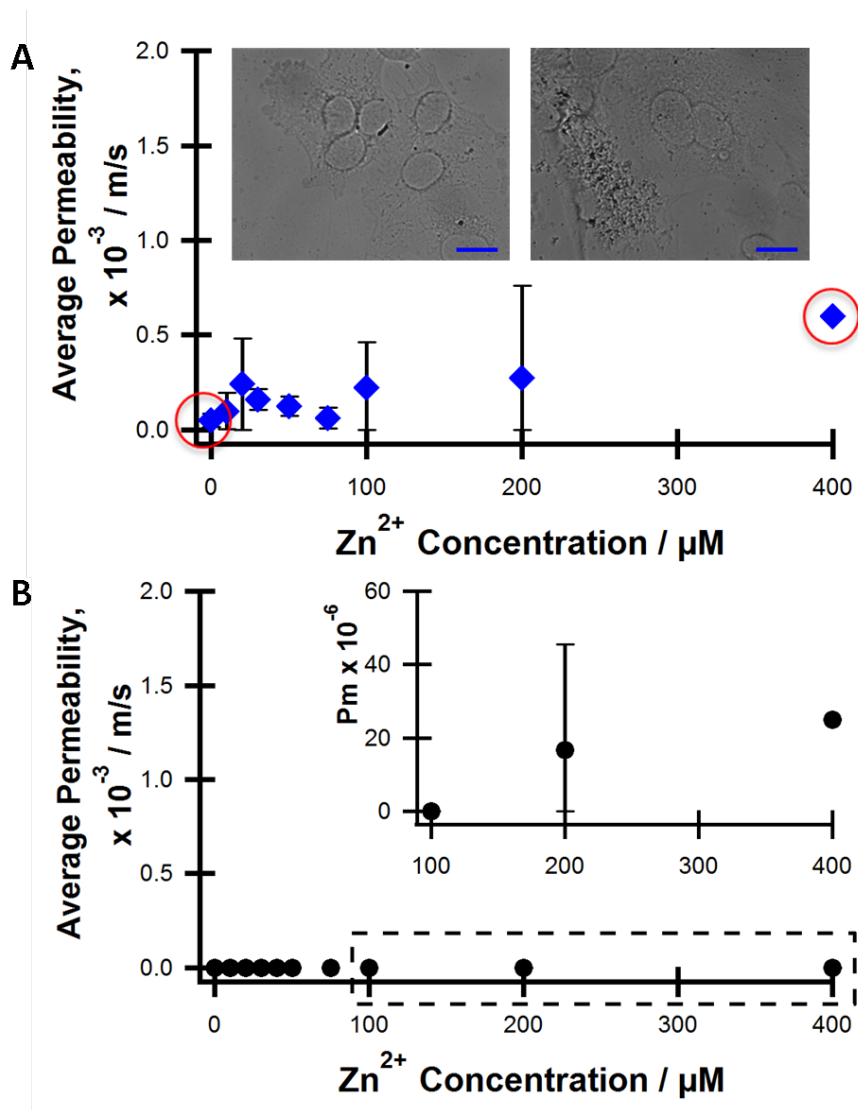


Figure 5.2. Average membrane permeability to (A) FcCH₂OH and (B) Ru(NH₃)₆³⁺ in T24 cells treated with Zn²⁺ between the ranges of 0-400 μM for 24 hours. The inset in (A) includes two optical micrographs of methanol-fixed T24 cells treated with 0 μM Zn²⁺ (left) and 400 μM Zn²⁺ (right) and (B) the zoomed in view of the P_m changes in 100-400 μM Zn²⁺. The scale bar in the optical images represents 20 μm.

Firstly, in the absence of Zn^{2+} -treatment, T24 cells had an average P_m of 5.0×10^{-5} m/s (Figure 5.2A), the same as our previously reported values^{21, 28} and similar to the permeability coefficient in single algal protoplast reported by Matsue *et al.*³⁶ (i) With low Zn^{2+} -treatment (10-75 μM), the average membrane permeability to FcCH_2OH resisted significant change, holding an average P_m between 5.0×10^{-5} m/s and 1.3×10^{-4} m/s. In this concentration range, Zn^{2+} appeared to have minimal to no adverse effects on membrane permeability or the observed cell viability. This agrees very closely with the cellular behavior and gene expression results presented in Zhu *et al.*'s study on human smooth muscle cells treated with low concentrations of Zn^{2+} (<80 μM).³⁷ In their case, low Zn^{2+} did not induce any adverse effects in the smooth muscle cells, however, the additional Zn^{2+} acted therapeutically, promoting cellular adhesion, spreading and viability.³⁷ (ii) In this study, after high Zn^{2+} -treatment (>75 μM), the membrane permeability trend increased in a dose-dependent manner, where the average P_m was found between 2.3×10^{-4} (100 μM) and 5.9×10^{-4} m/s (400 μM). It is possible this increase is due to the Zn^{2+} inducing biological and morphological changes within the cell (insets, Figure 5.2A). For example, if Zn^{2+} induces the generation of reactive oxygen species,³⁸ the antioxidant defense system may become overwhelmed and lead to subsequent oxidative damage.¹ One possible consequence is the lipid peroxidation of the cell membrane.¹ Ultimately, this can lead to membrane integrity loss and therefore, increased permeation to chemical species.^{1, 39} It is also likely in this concentration range, Zn^{2+} no longer behaves therapeutically but rather toxically since cellular viability was observed to decrease as Zn^{2+} concentrations increased (>75 μM , *see Zn²⁺ Effects on Cellular Viability*).

5.3.1.2 SECM with Hexaamineruthenium(III) (Impermeable)

The membrane integrity of Zn^{2+} -treated T24 cells were assessed using $\text{Ru}(\text{NH}_3)_6^{3+}$ as the SECM mediator (Figure 5.2B).^{17-18, 21} $\text{Ru}(\text{NH}_3)_6^{3+}$ is a highly charged (3+) and hydrophilic species which is excluded by healthy and intact cells.¹⁸ It was discovered that $\text{Ru}(\text{NH}_3)_6^{3+}$ remains impermeable (0 m/s) to the cell between 0-100 μM Zn^{2+} -treatment (Figure 5.2B). Exceeding this concentration, higher tip current was detected as $\text{Ru}(\text{NH}_3)_6^{3+}$ permeated across the cell through passive diffusion. The observed higher current

corresponded to increased membrane permeability coefficients: 1.67×10^{-5} m/s (200 μ M) and 2.5×10^{-5} m/s (400 μ M).

The membrane permeability trend to FcCH₂OH at these Zn²⁺ concentrations followed a similar profile, where greater dosages leads to higher permeability. The increase in membrane permeability to both FcCH₂OH and Ru(NH₃)₆³⁺ at the high Zn²⁺ concentrations (Figure 5.2) confirmed a weakening of the membrane integrity, which may lead to the eventual death of T24 cells.^{18, 20-21} It has been noted that intra- or extra- cellular redox reactions can occur between the oxidized FcCH₂OH in other cell lines,^{17, 40} however it does not appear to contribute significantly to the membrane permeability change detected in these Zn²⁺-treated T24 cells.

5.3.2 Zn²⁺ Effects on Cellular Viability

T24 cells required 24 hours of exposure to high Zn²⁺ concentration levels (>75 μ M) to initiate membrane integrity loss and overpermeabilization (Figure 5.2). This differed from previous SECM heavy metal studies, where T24 cells exposed to toxic Cd²⁺ or Cr₂O₇²⁻, at much lower concentrations, suffered from induced membrane changes within 1 hour of exposure.^{21, 28, 41-42} In a similar manner, Koley and Bard were able to monitor the membrane response in HeLa cells almost immediately after their exposure to Triton X-100, a known nonionic surfactant that can be used to permeabilize cells.¹⁸

The weakening of the membrane integrity after high Zn²⁺-treatment correlated well with the observed morphological changes (insets, Figure 5.2A) and cellular loss as a result of the Zn²⁺-treatment. Membrane integrity loss was confirmed through two additional methods: (i) immunofluorescence via the permeation of a normally membrane impermeable fluorochrome against a membrane permeable fluorochrome (ReadyProbes™ NucGreen and NucBlue, respectively, Figure 5.3) and (ii) the MTT proliferation assay (Figure S5.1 in Appendix V).

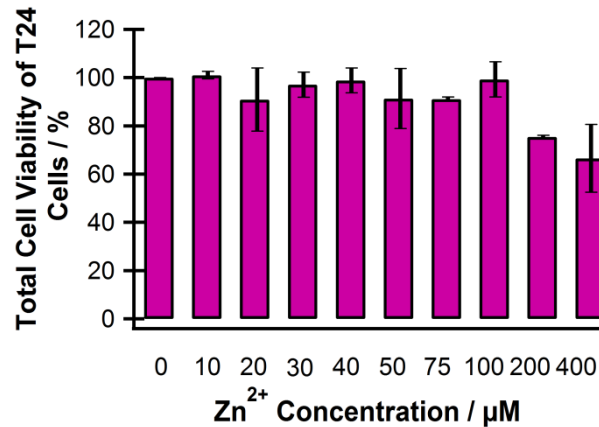


Figure 5.3. Cellular viability of Zn²⁺-treated T24 cells using ReadyProbes® NucBlue and NucGreen. NucBlue is membrane permeable which therefore allows measurement of total cell count while NucGreen can only permeate a cell with a compromised cell membrane. The ratio of cells expressing NucGreen to NucBlue is compared to that of the control cells and is used to indicate cellular viability.

After low Zn²⁺-treatment (10-100 µM), there was minimal effect on cellular viability relative to the control T24 cells (approximately 100 % viability). T24 cells were identified through the expression of ReadyProbes® NucBlue (Hoescht 33342), while NucGreen expression signified those Zn²⁺-treated cells that had a compromised cell membrane. Higher Zn²⁺-treatment allowed the permeation of NucGreen into the cell, confirming a loss in cellular viability: 25% and 33% after 200 µM and 400 µM Zn²⁺-treatment, respectively (Figure 5.3). Similarly, the results of the MTT proliferation assay mirrored those of the immunofluorescence experiments, where significant cell death occurred at the higher Zn²⁺ concentrations (>100 µM, Figure S5.1). This concentration is in close agreement with the accepted Zn²⁺ toxicity concentration in most cell types (100 µM, in vitro).^{1, 37, 43-45}

5.3.2.1 Correlation to Membrane Permeability

The observed increase in Zn²⁺-induced cellular death after high Zn²⁺ treatments (>100 µM) correlated well with the membrane permeability trend observed in SECM. Therefore, it is likely, those T24 cells exposed to high Zn²⁺ concentrations in the SECM membrane permeability experiments were also undergoing cellular death, possibly through the necrotic or apoptotic mechanisms. However, since necrosis is closely linked to severe

and acute injuries (environmentally-induced),⁴⁶⁻⁴⁷ we suspect that Zn^{2+} -induced necrosis would likely occur shortly after the introduction of Zn^{2+} . If this is the case, the experimental preparation should remove these cells, leaving primarily healthy or apoptotic cells to be tested via SECM. In this concentration range, the membrane integrity of Zn^{2+} -treated T24 cells was confirmed to be weakened, allowing permeation of a hydrophilic and charged species ($\text{Ru}(\text{NH}_3)_6^{3+}$) that is normally impermeable to cells. The results also indicated T24 cells maintained a near-to-intact cell membrane since these permeability changes were minor (Figure 5.2B). Therefore, we hypothesized that our SECM membrane permeability study are to Zn^{2+} -induced apoptotic cells.

5.3.3 Confirmation of Apoptosis

5.3.3.1 Flow Cytometry

Flow cytometry was used to investigate Zn^{2+} -induced apoptosis in T24 cells using the fluorescent stains, Annexin V Phycoerythrin (Annexin V PE) and 7-aminoactinomycin (7-AAD, Figure 5.4; the complete concentration series is shown in Figure S5.2).

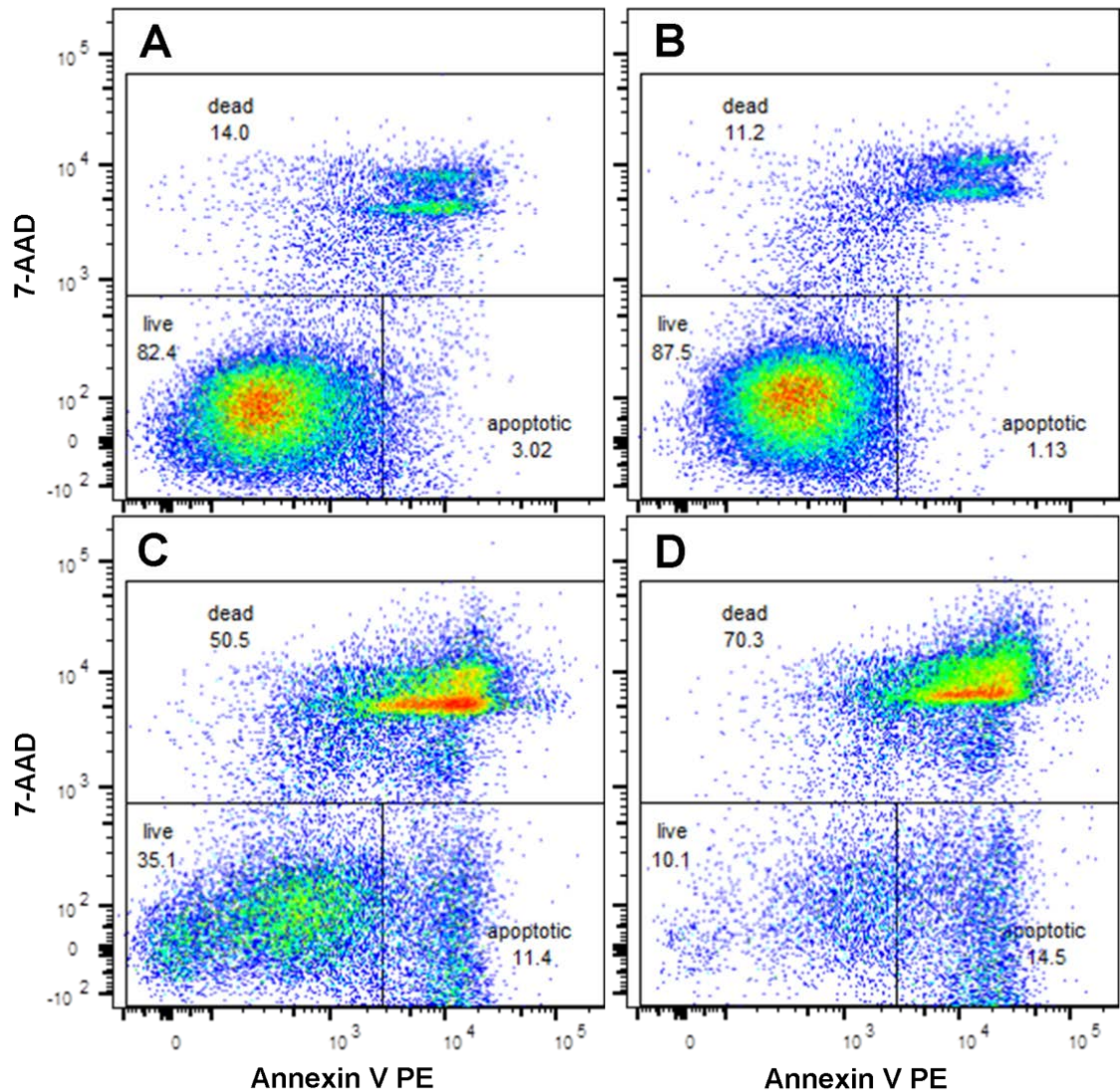


Figure 5.4. Statistical validation of T24 cells treated with (A) 0 (control), (B) 100, (C) 200 and (D) 400 μM Zn^{2+} undergoing apoptosis. The externalized PS is visible by the fluorochrome PE of Annexin V PE, while the fluorochrome 7-AAD indicates those cells with compromised cell membranes.

Figures 5.4A and S5.2A shows the majority of non-treated T24 cells are viable (82.4%), since these cells do not express externalized phosphatidylserine (PS, an early indicator of apoptosis) nor a compromised cell membrane (bottom left quadrant, Annexin V PE⁻/7-AAD⁻). 3.0% of the control cells displayed signs of early apoptosis, however their membrane integrity was maintained (bottom right quadrant,

Annexin V PE⁺/7-AAD⁻). Additionally, 14.0% of the control cells expressed both externalized PS and compromised cell membranes, indicating these cells are dead or nonviable (Annexin V PE⁺/7-AAD⁺). We correlate these early apoptotic and nonviable T24 cells to normal cellular loss which occurs in culturing and experimental preparation.

From Figures 5.4B and S5.2B-H, it can be seen that the majority of T24 cells treated with 10-100 μM Zn^{2+} were found to be healthy and intact (~80%). Approximately 15% of cells were nonviable, while a smaller population of Zn^{2+} -treated T24 cells were found to display signs of early apoptosis (~3%). Since these populations of cells were similar to the control sample (Figures 5.4A and S5.2A), we correlate the early apoptotic and nonviable cells to sample preparation rather than Zn^{2+} exposure.

Higher Zn^{2+} -treatment lead to a significant decrease in the population of viable and intact cells: 35.1% and 10.1% for 200 and 400 μM Zn^{2+} -treatment, respectively (Figures 5.4C-D and S5.2I-J). More T24 cells began to display signs of early apoptosis (PS externalization), which appeared to be concentration-dependent: 11.4% (200 μM) and 14.5% (400 μM). Similarly, the percentage of nonviable cells significantly increased: 50.5% (200 μM) and 70.3% (400 μM). From Figures 5.4B-D, the migration of viable cells (lower left quadrant) towards cellular death (lower right quadrant and upper quadrant) is visible as the concentration of Zn^{2+} increases.

During sample preparation for the SECM experiments, we had observed lower cellular confluency as the concentration of Zn^{2+} increased. Therefore, higher seeding densities of the T24 cells (3x) were used for the flow cytometry experiments in attempt to maintain the same number of cell events for characterization. For T24 cells treated between 0 and 100 μM Zn^{2+} (24 hours), 50,000 cell events were easily analyzed (Figure 5.4). As the Zn^{2+} concentration increased, it became evident that cellular viability decreased in a dose-dependent manner since the acquisition time per sample lengthened. However, the higher seeding densities used for Zn^{2+} concentrations greater than 100 μM were unable to compensate for the significant cell death that occurred and the targeted cell events were not reached. Instead 36,000 cells and 30,100 cells were analyzed for 200 and 400 μM Zn^{2+} -

treated T24 cells, respectively. This confirmed the toxicity power of Zn^{2+} in the high concentration ranges (Figures 5.4 and S5.2).

5.3.3.2 Correlation to Membrane Permeability and Cellular Viability

The concentration at which Zn^{2+} toxicity occurred was identified in the flow cytometry experiments to be greater than 100 μM (Figure 5.4). This was similar to the concentration identified in our SECM study, where $\text{Ru}(\text{NH}_3)_6^{3+}$ became permeable (Figure 5.2B) and in the cell viability experiments (Figures 5.3 and S5.1). Furthermore, flow cytometry experiments identified apoptosis as the primary cellular death mechanism through the externalization of PS in the T24 cells (Annexin V PE⁺). Since membrane asymmetry in apoptotic cells occurs prior to membrane integrity loss,⁴⁶ it is possible membrane asymmetry began earlier in the 24 hour treatment period. This was confirmed through the fluorescent stains of Zn^{2+} -treated T24 cells (0, 100, 200, and 400 μM) for 12 hours (Figure S5.3). The membrane integrity loss can subsequently lead to an increase in the passive transport of the redox mediators across the membrane and an increased membrane permeability trend detectable by SECM.

5.3.3.3 Immunofluorescence

Immunofluorescence was used to further confirm the apoptotic and necrotic tendencies of Zn^{2+} -treated T24 cells (Figure 5.5). It can be seen that as the concentration of Zn^{2+} increased, T24 cells expressed higher caspase-3/7 cleavage (Figure 5.5A). These caspases are apoptotic effectors that can drive apoptosis in human cells.⁴⁸⁻⁴⁹ Activation of these caspases can distinguish between apoptosis and other forms of cell death.⁴⁷ While a small percentage of control T24 cells appear to have undergone apoptosis (approximately 10%), 40% of the T24 cells have undergone apoptosis after treatment with 400 μM Zn^{2+} . This further reiterated the correlation between Zn^{2+} exposure and apoptosis.

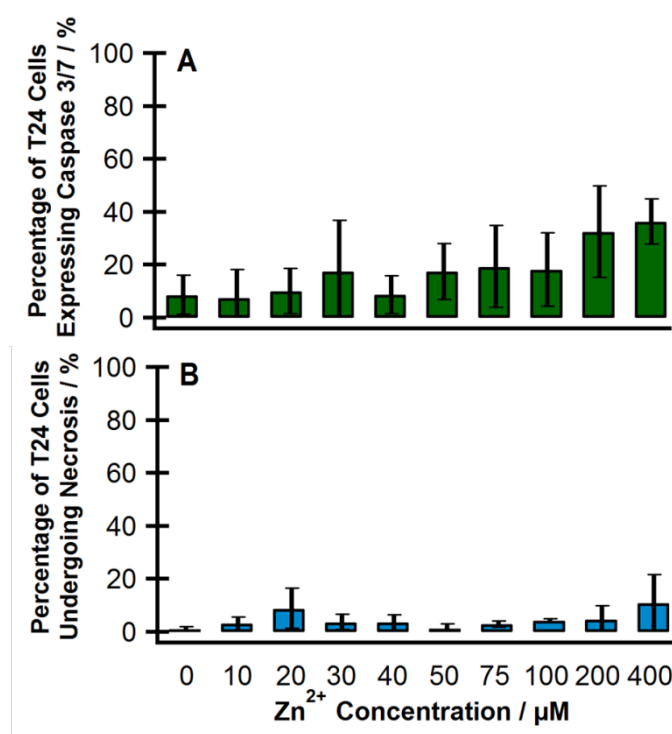


Figure 5.5. Percentage of T24 cells undergoing (A) apoptosis and (B) necrosis after treatment with Zn²⁺. Apoptotic cells were identified through the expression of CellEvent™ Caspase-3/7, while necrotic cells were identified through the expression of ReadyProbes® NucRed (propidium iodide). ReadyProbes® NucBlue (Hoescht 33342) was used to identify the cells (nuclei).

In addition, the fluorescent dye propidium iodide was unable to permeate the membranes of control T24 cells (Figure 5.5B). This indicates that none of the control cells were undergoing necrosis. As the concentration of Zn²⁺ increased towards 400 μM, the percentage of T24 cells that had undergone necrosis increased to 10.1%. The only exception to this was the T24 cells treated with 20 μM, which had indicated 8.9% of the cells to be necrotic. In these immunofluorescence experiments, ReadyProbes® NucBlue (Hoescht 33342, membrane permeable) was used to identify the total number of cells through fluorescence labelling of their nuclei.

5.3.3.4 Correlation to Membrane Permeability and Cellular Viability

Overall, the total number of T24 cells treated with 0-75 μM Zn^{2+} that are undergoing cell death appeared minimal, mirroring the cellular viability experiments. The majority of the apoptotic or necrotic cells were found after treatment with high Zn^{2+} ($>100 \mu\text{M}$). There was a higher population of Zn^{2+} -treated T24 cells expressing caspase 3/7 cleavage than propidium iodide expression. This reiterates that our SECM study on the high Zn^{2+} -treated T24 cells are performed to apoptotic cells rather than necrotic cells. The greater population of cells expressing caspase 3/7 cleavage (apoptosis) is also in agreement with our flow cytometry results. The proteolytic cleavage of caspase 3 and 7 can lead to distinctive morphological changes associated with apoptosis, which includes membrane blebbing (bulging), PS externalization and cytoplasmic condensation.^{48, 50-53} These can lead to the morphological changes observed in Zn^{2+} -treated T24 cells (inset, Figure 5.2A). It is possible, as a result of Zn^{2+} -induced apoptosis, membrane integrity loss contributes to the increased membrane permeability trend detected by SECM.

5.4 Conclusions

Here, SECM depth scan mode was used to investigate the effects of Zn^{2+} exposure on apoptosis in single live T24 cells. Utilizing membrane permeable (FcCH_2OH) and membrane-impermeable ($\text{Ru}(\text{NH}_3)_6^{3+}$) redox mediators, SECM provided insight into the membrane integrity of these Zn^{2+} -treated cells. Low Zn^{2+} -treatment (10-75 μM) brought no significant changes in membrane permeability, while the acute concentration range (100-400 μM) increased the passive diffusion of the redox mediators across the cell membrane. The apoptosis-induced morphological changes led to the weakening of the membrane integrity, which was confirmed by the permeation surge to $\text{Ru}(\text{NH}_3)_6^{3+}$ after exposure to acute Zn^{2+} concentrations. These SECM findings correlated with the observed morphological variations and decreases in cellular viability.

Unlike the effects of toxic heavy metal exposures, the permeability changes in T24 cells occurred after 24 hour treatment, and overpermeabilization only occurred in those cells exposed to the acute Zn^{2+} concentrations ($>75 \mu\text{M}$). Therefore, it was hypothesized that the acute Zn^{2+} -treated T24 cells studied by SECM primarily underwent the apoptotic death route.

Flow cytometry and immunofluorescence experiments confirmed this pathway through the externalization of PS and cleavage of caspase-3/7, respectively, which are early signs of apoptosis. These results indicate that although Zn^{2+} is critical to biological systems and while some concentrations may be therapeutic, prolonged exposure to high concentrations can be toxic to cells.

5.5 References

1. Ryu, J. M.; Lee, M. Y.; Yun, S. P.; Han, H. J., Zinc Chloride Stimulates DNA Synthesis of Mouse Embryonic Stem Cells: Involvement of PI3K/Akt, MAPKs, and mTOR. *J. Cell. Physiol.* **2009**, *218*, 558-567.
2. Farrell, N., Biomedical Uses and Applications of Inorganic Chemistry. An Overview. *Coord. Chem. Rev.* **2002**, *232*, 1-4.
3. Huber, K. L.; Hardy, J. A., Mechanism of Zinc-Mediated Inhibition of Caspase-9. *Protein Sci.* **2012**, *21*, 1056-1065.
4. Schrantz, N.; Auffredou, M. T.; Bourgeade, M. F.; Besnault, L.; Leca, G.; Vazquez, A., Zinc-Mediated Regulation of Caspases Activity: Dose-Dependent Inhibition or Activation of Caspase-3 in the Human Burkitt Lymphoma B Cells (Ramos). *Cell Death Differ.* **2001**, *8*, 152-161.
5. Hartwig, A., Metal Interaction with Redox Regulation: An Integrating Concept in Metal Carcinogenesis? *Free Radic. Biol. Med.* **2013**, *55*, 63-72.
6. Kimura, E.; Aoki, S.; Kikuta, E.; Koike, T., A Macrocyclic Zinc(II) Fluorophore as a Detector of Apoptosis. *Proc. Natl. Acad. Sci. U. S. A.* **2003**, *100*, 3731-3736.
7. Truong-Tran, A. Q.; Carter, J.; Ruffin, R. E.; Zalewski, P. D., The Role of Zinc in Caspase Activation and Apoptotic Cell Death. *BioMetals* **2001**, *14*, 315-330.
8. Hong, S.-H.; Choi, Y. S.; Cho, H. J.; Lee, J. Y.; Hwang, T.-K.; Kim, S. W., Induction of Apoptosis of Bladder Cancer Cells by Zinc-Citrate Compound. *Korean J. Urol.* **2012**, *53*, 800-806.
9. Bard, A. J.; Mirkin, M. V., *Scanning Electrochemical Microscopy*, 2 ed.; CRC Press, 2012.
10. Beaulieu, I.; Kuss, S.; Mauzeroll, J.; Geissler, M., Biological Scanning Electrochemical Microscopy and Its Application to Live Cell Studies. *Anal Chem* **2011**, *83*, 1485-1492.

11. Wittstock, G.; Burchardt, M.; Kirchner, C. N., Chapter 37 Scanning Electrochemical Microscopy in Biosensor Research. In *Comprehensive Analytical Chemistry*, Alegret, S.; Merkoçi, A., Elsevier: 2007.
12. Schulte, A.; Nebel, M.; Schuhmann, W., Scanning Electrochemical Microscopy in Neuroscience. *Annu. Rev. Anal. Chem.* **2010**, *3*, 299-318.
13. Zhan, D.; Fan, F.-R. F.; Bard, A. J., The K_v Channel Blocker 4-Aminopyridine Enhances Ag⁺ Uptake: A Scanning Electrochemical Microscopy Study of Single Living Cells. *Proc. Natl. Acad. Sci. U. S. A.* **2008**, *105*, 12118-12122.
14. Takahashi, Y.; Shevchuk, A. I.; Novak, P.; Babakinejad, B.; Macpherson, J.; Unwin, P. R.; Shiku, H.; Gorelik, J.; Klenerman, D.; Korchev, Y. E., et al., Topographical and Electrochemical Nanoscale Imaging of Living Cells Using Voltage-Switching Mode Scanning Electrochemical Microscopy. *Proc. Natl. Acad. Sci. U. S. A.* **2012**, *109*, 11540-11545.
15. Guo, J.; Amemiya, S., Permeability of the Nuclear Envelope at Isolated Xenopus Oocyte Nuclei Studied by Scanning Electrochemical Microscopy. *Anal. Chem.* **2005**, *77*, 2147-2156.
16. Bergner, S.; Wegener, J.; Matysik, F.-M., Monitoring Passive Transport of Redox Mediators across a Confluent Cell Monolayer with Single-Cell Resolution by Means of Scanning Electrochemical Microscopy. *Anal. Methods* **2012**, *4*, 623-629.
17. Liu, B.; Rotenberg, S. A.; Mirkin, M. V., Scanning Electrochemical Microscopy of Living Cells: Different Redox Activities of Nonmetastatic and Metastatic Human Breast Cells. *Proc. Natl. Acad. Sci. U. S. A.* **2000**, *97*, 9855-9860.
18. Koley, D.; Bard, A. J., Triton X-100 Concentration Effects on Membrane Permeability of a Single HeLa Cell by Scanning Electrochemical Microscopy (SECM). *Proc. Natl. Acad. Sci. U. S. A.* **2010**, *107*, 16783-16787.
19. Chen, Z.; Xie, S.; Shen, L.; Du, Y.; He, S.; Li, Q.; Liang, Z.; Meng, X.; Li, B.; Xu, X., et al., Investigation of the Interactions between Silver Nanoparticles and HeLa Cells by Scanning Electrochemical Microscopy. *Analyst* **2008**, *133*, 1221-1228.
20. Li, X.; Bard, A. J., Scanning Electrochemical Microscopy of HeLa Cells - Effects of Ferrocene Methanol and Silver Ion. *J. Electroanal. Chem.* **2009**, *628*, 35-42.
21. Li, M. S. M.; Filice, F. P.; Henderson, J. D.; Ding, Z. F., Probing Cd²⁺-Stressed Live Cell Membrane Permeability with Various Redox Mediators in Scanning Electrochemical Microscopy. *J. Phys. Chem. C* **2016**, *120*, 6094-6103.
22. Mauzeroll, J.; Bard, A. J., Scanning Electrochemical Microscopy of Menadione-Glutathione Conjugate Export from Yeast Cells. *Proc. Natl. Acad. Sci. U. S. A.* **2004**, *101*, 7862-7867.

23. Kuss, S.; Polcari, D.; Geissler, M.; Brassard, D.; Mauzeroll, J., Assessment of Multidrug Resistance on Cell Coculture Patterns Using Scanning Electrochemical Microscopy. *Proc. Natl. Acad. Sci. U. S. A.* **2013**, *110*, 9249-9254.
24. Danis, L.; Snowden, M. E.; Tefashe, U. M.; Heinemann, C. N.; Mauzeroll, J., Development of Nano-Disc Electrodes for Application as Shear Force Sensitive Electrochemical Probes. *Electrochim. Acta* **2014**, *136*, 121-129.
25. Li, M. S. M.; Filice, F. P.; Ding, Z. F., Scanning Electrochemical Microscopy Imaging with Laser-Pulled Probes. *J. Electroanal. Chem.* **2016**, *781*, 126-135.
26. Zhang, M. M.; Long, Y. T.; Ding, Z., Filming a Live Cell by Scanning Electrochemical Microscopy: Label-Free Imaging of the Dynamic Morphology in Real Time. *Chem. Cent. J.* **2012**, *6*, 20.
27. Zhang, M. N.; Ding, Z.; Long, Y. T., Sensing Cisplatin-Induced Permeation of Single Live Human Bladder Cancer Cells by Scanning Electrochemical Microscopy. *Analyst* **2015**, *140*, 6054-6060.
28. Li, M. S. M.; Filice, F. P.; Ding, Z., A Time Course Study of Cadmium Effect on Membrane Permeability of Single Human Bladder Cancer Cells Using Scanning Electrochemical Microscopy. *J. Inorg. Biochem.* **2014**, *136*, 177-183.
29. Filice, F. P.; Li, M. S. M.; Henderson, J. D.; Ding, Z., Three-Dimensional Electrochemical Functionality of an Interdigitated Array Electrode by Scanning Electrochemical Microscopy. *J. Phys. Chem. C* **2015**, *119*, 21473-21482.
30. Li, M. S. M.; Filice, F. P.; Ding, Z. F., Determining Live Cell Topography by Scanning Electrochemical Microscopy. *J. Electroanal. Chem.* **2016**, *779*, 176-186.
31. Filice, F. P.; Li, M. S. M.; Henderson, J. D.; Ding, Z., Mapping Cd²⁺-Induced Membrane Permeability Changes of Single Live Cells by Means of Scanning Electrochemical Microscopy. *Anal. Chim. Acta* **2016**, *908*, 85-94.
32. Mosmann, T., Rapid Colorimetric Assay for Cellular Growth and Survival: Application to Proliferation and Cytotoxicity Assays. *J. Immunol. Methods* **1983**, *65*, 55-63.
33. Soleimani, A.; Moustafa, M. M. A. R.; Borecki, A.; Gillies, E. R., A Comparison of Covalent and Noncovalent Strategies for Paclitaxel Release Using Poly(Ester Amide) Graft Copolymer Micelles. *Can. J. Chem.* **2015**, *93*, 399-405.
34. Zhao, X.; Diakowski, P. M.; Ding, Z., Deconvoluting Topography and Spatial Physiological Activity of Live Macrophage Cells by Scanning Electrochemical Microscopy in Constant-Distance Mode. *Anal. Chem.* **2010**, *82*, 8371-8373.

35. Zhang, M. M. N.; Long, Y.-T.; Ding, Z., Cisplatin Effects on Evolution of Reactive Oxygen Species from Single Human Bladder Cancer Cells Investigated by Scanning Electrochemical Microscopy. *J. Inorg. Biochem.* **2012**, *108*, 115-122.
36. Yasukawa, T.; Uchida, I.; Matsue, T., Permeation of Redox Species through a Cell Membrane of a Single, Living Algal Protoplast Studied by Microamperometry. *Biochim. Biophys. Acta* **1998**, *1369*, 152-158.
37. Ma, J.; Zhao, N.; Zhu, D., Bioabsorbable Zinc Ion Induced Biphasic Cellular Responses in Vascular Smooth Muscle Cells. *Sci. Rep.* **2016**, *6*, 26661.
38. Sensi, S. L.; Yin, H. Z.; Carriedo, S. G.; Rao, S. S.; Weiss, J. H., Preferential Zn²⁺ Influx through Ca²⁺-Permeable AMPA/Kainate Channels Triggers Prolonged Mitochondrial Superoxide Production. *Proc. Natl. Acad. Sci. U. S. A.* **1999**, *96*, 2414-2419.
39. Cordeiro, R. M., Reactive Oxygen Species at Phospholipid Bilayers: Distribution, Mobility and Permeation. *Biochim. Biophys. Acta* **2014**, *1838*, 438-444.
40. Kuss, S.; Cornut, R.; Beaulieu, I.; Mezour, M. A.; Annabi, B.; Mauzeroll, J., Assessing Multidrug Resistance Protein 1-Mediated Function in Cancer Cell Multidrug Resistance by Scanning Electrochemical Microscopy and Flow Cytometry. *Bioelectrochemistry* **2011**, *82*, 29-37.
41. Henderson, J. D.; Filice, F. P.; Li, M. S. M.; Ding, Z., Tracking Live-Cell Response to Hexavalent Chromium Toxicity by Using Scanning Electrochemical Microscopy. *ChemElectroChem* **2017**, *4*, 856-863.
42. Henderson, J. D.; Filice, F. P.; Li, M. S. M.; Ding, Z., Tracking Live Cell Response to Cadmium (II) Concentrations by Scanning Electrochemical Microscopy. *J. Inorg. Biochem.* **2016**, *158*, 92-98.
43. O, T. M.; Lou, M. S.; Ma, Y., Zinc Effect on Human Lymphatic Malformation Cells in Vitro. *Int. J. Pediatr. Otorhinolaryngol.* **2016**, *80*, 33-38.
44. Telford, W. G.; Fraker, P. J., Preferential Induction of Apoptosis in Mouse CD4⁺CD8⁺αβTCR^{lo}CD3ε^{lo} Thymocytes by Zinc. *J. Cell. Physiol.* **1995**, *164*, 259-270.
45. Sargazi, M.; Shenkin, A.; Roberts, N. B., Zinc Induced Damage to Kidney Proximal Tubular Cells: Studies on Chemical Speciation Leading to a Mechanism of Damage. *J. Trace Elem. Med Biol.* **2013**, *27*, 242-248.
46. Kroemer, G.; Dallaporta, B.; Resche-Rigon, M., The Mitochondrial Death/Life Regulator in Apoptosis and Necrosis. *Annu Rev Physiol* **1998**, *60*, 619-642.
47. Krysko, D. V.; Vanden Berghe, T.; D'Herde, K.; Vandenabeele, P., Apoptosis and Necrosis: Detection, Discrimination and Phagocytosis. *Methods* **2008**, *44*, 205-221.

48. Julien, O.; Wells, J. A., Caspases and Their Substrates. *Cell Death Differ.* **2017**, *24*, 1380-1389.
49. Gray, D. C.; Mahrus, S.; Wells, J. A., Activation of Specific Apoptotic Caspases with an Engineered Small-Molecule-Activated Protease. *Cell* **2010**, *142*, 637-646.
50. Porter, A. G.; Janicke, R. U., Emerging Roles of Caspase-3 in Apoptosis. *Cell Death Differ.* **1999**, *6*, 99-104.
51. Lakhani, S. A.; Masud, A.; Kuida, K.; Porter, G. A., Jr.; Booth, C. J.; Mehal, W. Z.; Inayat, I.; Flavell, R. A., Caspases 3 and 7: Key Mediators of Mitochondrial Events of Apoptosis. *Science* **2006**, *311*, 847-851.
52. Hristov, G.; Marttila, T.; Durand, C.; Niesler, B.; Rappold, G. A.; Marchini, A., Shox Triggers the Lysosomal Pathway of Apoptosis Via Oxidative Stress. *Hum. Mol. Genet.* **2014**, *23*, 1619-1630.
53. Liu, X. S.; Zou, H.; Slaughter, C.; Wang, X. D., DFF, a Heterodimeric Protein That Functions Downstream of Caspase-3 to Trigger DNA Fragmentation During Apoptosis. *Cell* **1997**, *89*, 175-184.

Chapter 6

6 Scanning Electrochemical Microscopy with Laser-Pulled Submicron Pt Probes

(Part of this work has been prepared for publication

Li, M.S.M.; Filice, F.P.; Ding, Z. Electrochemical Functionality of Microband Electrodes Imaged by Scanning Electrochemical Microscopy with Submicron Probes, **2017**.

Upon Submission.

Part of this work has been published in the *Journal of Electroanalytical Chemistry*

Li, M.S.M.; Filice, F.P.; Ding, Z. *J. Electroanal. Chem.* **2016**, 781, 126-135.)

6.1 Introduction

Scanning probe microscopy is a family of techniques that utilizes a physical probe to scan above a sample, characterizing its topography and physicochemical features. Scanning electrochemical microscopy (SECM) is a member of this family.¹⁻⁶ Since its emergence, SECM has been used in a wide range of applications, including but not limited to microfabrication,⁷⁻⁸ kinetic studies,⁹⁻¹⁰ and chemical imaging.¹¹⁻¹⁵ SECM utilizes a biased electrode (less than 25 μm in diameter) that is scanned over a sample that is submerged in an electrolyte solution (containing a redox mediator) with extreme precision.^{2, 13, 16} The relationship between the electrode position and tip current is observed and can be represented as single line scans or multi axes current maps (images).

As a result of the potential bias, the redox mediator is converted to its oxidized or reduced form at the electrode tip in an electrochemically-driven process. When the biased SECM probe is far from the sample, the resulting faradaic current will be constant since it is diffusion-controlled. However, when the probe approaches a conductive sample, the current will be amplified due to the cyclic regeneration of the mediator at the sample-electrolyte interface (positive feedback). If the sample is insulating, the current will decay due to the depletion of the mediator at the electrode tip (diffusion-limited, negative feedback).

The two most common imaging modes of SECM are collected using the constant height or constant distance modes.^{2-3, 17} As their names suggest, the constant height mode entails that the electrode is scanned above a sample at a constant height (fixed z position), while the constant distance mode entails a constant tip-to-sample distance throughout the scan, which is achieved by moving the electrode up or down to maintain a constant current. Other modes have since emerged over the years, such as Schuhmann's 4D shearforce-based constant distance mode,¹⁸ where the retractions of the tip (shearforce-based) generate a comprehensive 4D data set and images, and the depth scan mode, established in the Ding Research Group, which reports the current *vs.* tip-to-sample distances as a single 2D image.¹⁹⁻²¹

The biased electrode in SECM depth scan mode performs multiple horizontal line scans above the sample, where with each consecutive scan the electrode takes a downward step in the z -direction. As a result of the real-time generation of the depth scan image, we are able to monitor the electrode's approach towards the sample, avoiding collisions that can potentially harm the electrode and/or sample. Another advantage to this mode is that since each pixel in the SECM image is comprised of both the tip current and its coordinates, a single depth scan image can provide several hundreds of probe approach curves (PACs) and horizontal line scans. Combined with finite elemental analysis simulations, simulated curves allow researchers to quantitatively analyze sample traits, such as physical properties and reaction kinetics, which cannot be obtained directly from the SECM experiments.²²

Since the resolution of the SECM image is directly dependent on electrode size, the attractiveness of nanoelectrodes (NEs) as probes are becoming increasingly popular.²³ By using NEs as opposed to ultramicroelectrodes (UMEs, micron scale) in SECM imaging, submicron size structures are no longer lost. Many research groups have developed their own NE fabrication methods,²⁴ including laser pulling,²⁵⁻²⁶ chemical vapor deposition,²⁷⁻²⁸ and focus-ion-beam (FIB) milling²⁹ techniques. While each method holds its own advantages and disadvantages, the NEs used in this Chapter for SECM analysis were prepared by the laser pulling method. Some of the NEs were used as prepared, while others were exposed to a secondary step of either FIB-milling or manual polishing. As SECM utilizes the redox cycling principle, where the probe acts as the generator and the sample, the

collector, coupling SECM with microstructure arrays, such as independently addressable microband electrodes (IAMEs) or electrode arrays³⁰ can lead to high amplification of the oxidative/reductive current at the electrode tip.³¹⁻³⁵ In the case of a reversible redox reaction, the amplification of the current is only dependent on the dimensions of the electrodes in the array and interdigit (glass) space between them.

The SECM probe selected to image a sample must be smaller than the individual features that require resolving (for instance, the conductive and glass microbands of the IAMEs). An SECM probe that is much larger than the area(s) of interest (on the sample) will average out the finer features and display either mostly conductive or insulating properties, depending on the nature of the sample. Choosing IAMEs and SECM probes that are close in size, exploration of the redox cycling phenomena can be anticipated. Utilizing an unbiased IAME (sample), the effects of redox cycling should be noticeable when a PAC is extracted to the insulating glass between the two Pt microbands. A comparison between the effects of redox cycling detected by a Pt UME will be compared against a Pt NE that is significantly smaller in size to the microbands of the IAME. Variation between the tip-to-sample distances can cause discrepancies in the tip feedback current. Therefore, the presence of a tilted IAME sample can lead to inconsistent results. These inconsistencies become greater as the tip diameter decreases. Herein, we also explore the use of simulation models to quantify the sample tilt in three different methods: 1) the traditional PAC extraction approach; 2) an experimentally tilted horizontal line scan against a non-tilted simulated depth scan map; and 3) simulated tilted sample depth scan maps against non-tilted experimental data.

6.2 Experimental Section

The experimental details discussed here are the project-specific details briefly summarized. A more detailed report of the Experimental is included in Chapter 2.

6.2.1 Materials

Ferrocenemethanol (FcCH_2OH , 97%) and hexaamineruthenium(III) chloride ($\text{Ru}(\text{NH}_3)_6\cdot\text{Cl}_3$, 98%) were acquired from Sigma-Aldrich (Mississauga, ON), while potassium chloride (KCl, 99%) was obtained from Alfa Aesar (Ward Hill, MA). Stock solutions of 0.9 mM FcCH_2OH

or 10 mM $\text{Ru}(\text{NH}_3)_6^{3+}$ with 0.1 M KCl as the supporting electrolyte were prepared in deionized water (18 M Ω .cm, MilliQ water, Etobicoke, ON). The Pt IAME was purchased from ABTECH Scientific, Inc. (IAME 0504-Pt, Richmond, VA). The IAME has 4 alternating independently addressable Pt and glass microbands, each 5 μm in width. The 10 nm Formvar and 1 nm carbon-coated 400 mesh Ni TEM grids were obtained from Electron Microscopy Sciences (Hatfield, PA).

6.2.2 Electrode Fabrication

The electrodes were fabricated in-house using a procedure adapted from the Mauzeroll Group³⁶ on a P-2000 laser-based micropipette puller system (Sutter Instrument, Novato, CA). The two modifications from their established procedure include:³⁶ two single line heat settings were used in place of their single line setting. The first of the two is a partial quartz seal program using a line setting of Heat: 580, Filament: 003, Velocity: 140, Delay: 060, Pull: 000, followed by the complete quartz seal at Heat: 580, Filament: 002, Velocity: 140, Delay: 060, Pull: 000. These line settings were found to improve the integrity of the Pt wire for our experimental configuration.

Freshly pulled Pt NEs were first checked optically (under a microscope) for obvious breakage(s) in Pt wire, followed by extension of the internal electrical connections. Following successful visual inspection, these electrodes were tested for electrical connection and Pt size through the use of cyclic voltammetry (CV). Pt NEs were tested using 10 mM $\text{Ru}(\text{NH}_3)_6^{3+}$ with 0.1 M KCl and used as pulled (unpolished) or polished. FIB-milling and scanning electron microscopy (SEM) images were conducted using a LEO Zeiss 1540 XB (Zeiss, Oberkochen, Germany). For NEs that were manually polished, the tip of the NEs were removed by polishing of the tip surface on a homemade polishing wheel attached with abrasive alumina-coated polishing pads (3.0, 0.3, and 0.05 μm , Buehler, Whitby, ON). Due to its size, the 4.4 μm Pt UME was optically characterize for its Pt tip diameter and geometry (RG 3). UMEs were electrochemically tested using 0.9 mM FcCH_2OH with 0.1 M KCl in deionized water (CV).

6.2.3 Electrochemical Measurements

Electrochemical experiments were performed using an electrochemical analyzer (CHI 800B, CH Instruments, Austin, TX) with a CHI 200 Picoamp Booster to reduce noise (CH Instruments), which was recorded by the Alpha-SNOM instrument (WITec, Ulm, Germany).^{19, 37} For this Chapter, the Pt NEs or UME were used as the SECM probe (working electrode) and a Ag/AgCl electrode was used as a combined auxiliary/reference electrode. The details of this SECM instrumentation and operation procedure have been described elsewhere in great detail.^{20, 37-39}

6.2.4 SECM Experiments

The details of this SECM instrumentation and operation procedure has been described elsewhere in great detail^{20, 37-39} and is described in Chapter 2. Briefly, SECM measurements were performed on the TEM grid or IAME adhered with 3M double-sided tape (conductive side exposed) onto a glass bottom petri dish (P35G-0-20C, MatTek Corporation, Ashland, MA). The petri dish was mounted onto the scanning stage (P-517K064, Polytec PI, Germany) of the microscope. Utilizing the Alpha-SNOM positioning system along with an inverted objective lens (Nikon objective, 50x lens, N.A.: 0.55, Japan), the electrode's approach to the sample was made. The biased electrodes (0.300 V for FcCH₂OH or -0.350 V for Ru(NH₃)₆³⁺) approached the samples using the confocal mode setting within the WITec software, resulting in the generation of 2D SECM images (current vs. probe coordinates).

For the 250 nm Pt NE SECM experiments, the constant height images includes 512 x 512 pixels, a scan width and height of 20 μm each, and an integration time of 0.01 s on each pixel. The depth scan image comprised of 512 x 200 pixels, a scan width and depth of 20 μm and 10 μm , respectively and an integration time of 0.01 s for each pixel. SECM depth scan images with the 4.4 μm Pt UME were obtained with an image resolution of 256 x 256 pixels, a scan scale of 60 μm in width and 30 μm of depth, as well as an integration time of 0.05 s on each pixel. The constant height SECM images have the same parameters as the depth scan images with the following exceptions: the scan width and height were set to 60 μm each. These experiments were all carried out at ambient lab conditions (23 ± 1 °C).

6.3 Theory and Simulation

6.3.1 Simulation geometry

The simulation model was designed in full 3D geometry in COMSOL Multiphysics v.5.2 (COMSOL, Boston, MA) to represent the system under study (Figures 6.1A and B). For example, the UME was configured to have a Pt tip size of $4.4\ \mu\text{m}$ (diameter) and an RG of 3. The IAME substrate consisted of 4 sets of alternating Pt and glass microbands, $5\ \mu\text{m}$ in width each, on a glass plane (Figure 6.1C). The IAME model was simplified to idealized flat microbands to reduce the complexity of the simulation model. A plane was designed to intersect the solution domain, allowing the tilting of the IAME sample, with the axis of rotation positioned at the center of the IAME parallel to the microbands (Figures 6.1A and B).

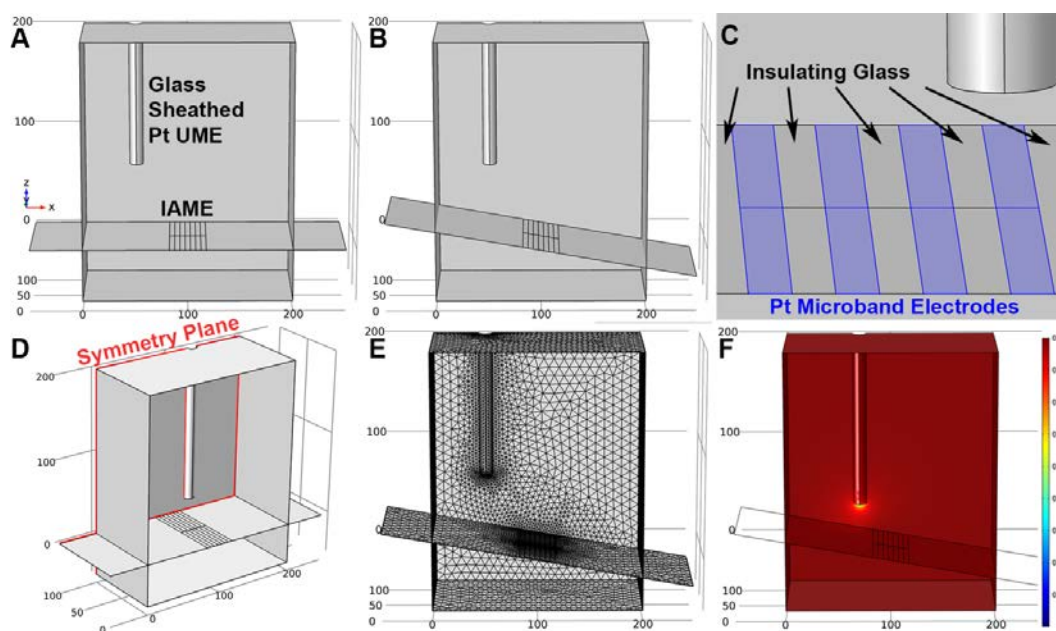


Figure 6.1. The model geometries of the SECM analysis of an IAME sample (A) parallel to the UME tip and (B) at a 10° tilt relative to the electrode. (C) A zoomed in and labelled model of the Pt and glass microband electrodes of the IAME. (D) The 3D perspective view illustrating the symmetry plane in the simulation model. (E) The tetrahedrally-meshed simulation model with further refinement at the electrode tip and the IAME microbands to improve the accuracy of the simulation. (F) An example of a simulated concentration map of the IAME with the SECM probe positioned in bulk solution.

A symmetry plane exists in the 3D model through the electrode center, perpendicular to the Pt microbands of the IAME sample (Figure 6.1D). As a result, it was possible to reduce the size of the model geometry by half and employ a symmetric physics boundary. This allows for the flux of the solution across the symmetry boundary into the symmetrical region opposite the boundary (Figure 6.1D).

The IAME sample was configured as a thin impermeable boundary, effectively separating the solution in the upper region of the domain from the lower region (Figures 6.1A and B). The conductive Pt microbands on the IAME were set to regenerate the initial bulk solution concentration of FcCH₂OH, behaving as an ideal conductive boundary. The lower region of the model geometry was created to facilitate the impermeable tilting substrate that has no interaction with the upper region under study (Figure 6.1B).

The initial solution concentration of FcCH₂OH was set at 0.9 mM to match the stock solution concentration used in the physical experiment. The diffusion coefficient for FcCH₂OH was set to $7.6 \times 10^{-10} \text{ m}^2/\text{s}$.^{1, 22, 40} At the UME biased at 0.300 V, the one-electron oxidation of FcCH₂OH to Fc⁺CH₂OH is a diffusion-controlled process that follows Fick's second law of diffusion (eqn 6.1):

$$\frac{\partial C_B}{\partial t} = D_B \left(\frac{\partial^2 C_B}{\partial x^2} + \frac{\partial^2 C_B}{\partial y^2} + \frac{\partial^2 C_B}{\partial z^2} \right) \quad [6.1]$$

The boundaries interfacing with the bulk solution were set to match the initial concentration of FcCH₂OH to simulate a relatively infinite solution containing 0.9 mM FcCH₂OH. The glass microbands, glass slide and SECM probe sheathing (quartz) were set as no flux boundaries to simulate the insulating characteristics of these substrates. The Pt disk of the SECM tip was set to remove FcCH₂OH from solution, generating a concentration of 0 M at the disk surface.

A tetrahedral mesh was utilized to mesh the 3D simulation model (Figure 6.1E). An element scale size of 0.2x was set at the UME tip, while the Pt microbands were set to 0.4x. Further refinement in the mesh at the areas of greatest concentration variations was completed. A maximum element growth rate of 1.2x was set to ensure a fine mesh in

proximity to these areas, up to a maximum element size of 10 μm from a minimum of 0.05 μm .

For the 250 nm Pt NE-IAME simulations, the geometry of the electrode was modified to represent a Pt tip diameter of 250 nm with an RG of 10 and the IAME dimensions remained the same. The RG of the 250 nm Pt NE was simplified from 30 to 10 due to minimal effects on feedback current at RG values greater than 10.⁴¹ The concentration and diffusion coefficient were changed from FcCH₂OH to Ru(NH₃)₆³⁺, 10 mM and 6.7 x 10⁻¹⁰ m/s,⁴² respectively which was used in these experiments.

6.3.2 Simulation Methodology

The electrode's x and z positions, as well as the substrate angle were set as parameterized variables in the creation of the model geometry. This allows the automated movement of these parameters over the course of numerous simulations. All simulations specified in the parametric sweeps were performed sequentially, generating large sets of data rapidly. By nesting the parametric sweeps of these parameters, simulations with combinations of all three parameters can be obtained simultaneously. Concentration maps of FcCH₂OH were generated for all combinations of parameters specified.

A post processing surface integration is performed on the resulting simulated concentration data (Figure 6.1F) to calculate the electrochemical current feedback obtained at the circular electrode tip surface. Due to the symmetry plane, the integration of the semicircular electrode tip boundary has to be doubled to obtain the total electrode tip current. The surface integration follows eqn 6.2:

$$i = 2\pi nFD \int_0^a r \left[\frac{\partial c(r,z)}{\partial z} \right] dr \quad [6.2]$$

In this formula, a is the radius of the Pt disk, n is the number of electrons transferred in the redox reaction (1), F is the Faraday constant (96,485 C/mol), and D is the diffusion coefficient of the redox mediator. The resulting tip current for all electrode tip locations were normalized with respect to the tip current at a distance far away from the substrate, i_∞ , yielding:

$$I(x, z) = \frac{i(x, z)}{i_{\infty}} \quad [6.3]$$

I in this case represents the normalized current. PACs were obtained by plotting the normalized tip current (eqn 6.3) versus the normalized distance, L (eqn 6.4):

$$L = \frac{\text{tip-to-sample distance, } d}{\text{electrode radius, } a} \quad [6.4]$$

6.4 Results and Discussion

6.4.1 Laser-pulled Pt Nanoelectrodes

NEs are extremely advantageous in SECM since the image resolution is directly dependent on the probe size. With the larger UMEs, nanometer-sized surface features can be overlooked or averaged out due to the loss in resolution. Utilizing a laser micropipette puller to heat seal and pull a Pt wire sheathed in a quartz capillary, the diameter of the Pt wire can be greatly reduced.³⁶ Taking advantage of this fabrication method, we were able to pull 25 μm Pt wire to nm-sized Pt electrodes and test them for immediate electrochemical use after extension of the internal electrical connections.

6.4.1.1 Unpolished Laser-pulled Nanoelectrodes

Here, the Pt tips of the NEs were immediately exposed as a result of the electrode fabrication process. The 2 electrode set-up (Pt NE and a Ag/AgCl reference electrode) was immersed in 10 mM $\text{Ru}(\text{NH}_3)_6^{3+}$ with 0.1 M KCl (supporting electrolyte) in ultrapure deionized water. For these CVs, the potential was cathodically scanned to -0.40 V (vs. Ag/AgCl), achieving a steady state current (~ 20 pA) for the reduction of $\text{Ru}(\text{NH}_3)_6^{3+}$ to $\text{Ru}(\text{NH}_3)_6^{2+}$ at applied potentials greater than -0.30 V (Figure 6.2A).

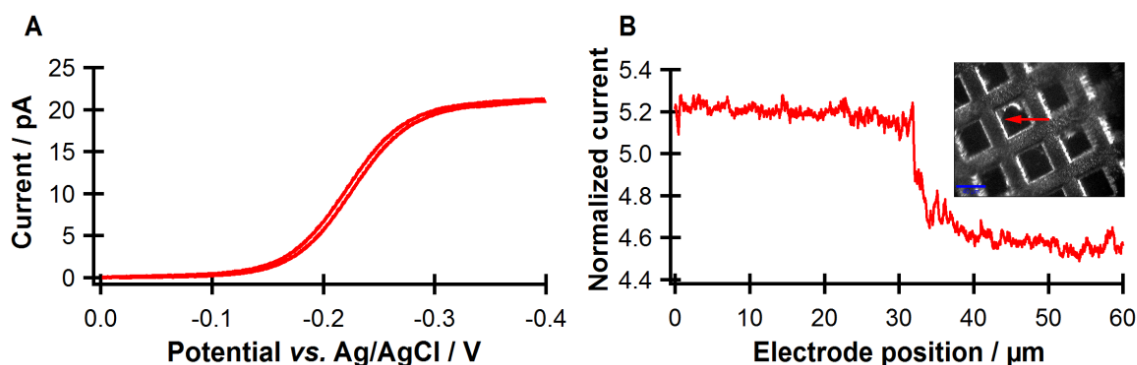


Figure 6.2. (A) The CV obtained in 10 mM $\text{Ru}(\text{NH}_3)_6^{3+}$ and 0.1 M KCl as the supporting electrolyte in ultrapure deionized water testing for electrode conductivity. (B) A horizontal line scan obtained across 1 grid square, where the first 30 μm is over the Ni portion of the grid and the second half of the scan (30-60 μm) is over the “hole” portion of the grid. The inset is an optical image of the TEM grid with the scan path of the SECM probe identified in red arrow. The blue scale bar in the image represents 40 μm .

Assuming the NE has an $\text{RG} > 10$, the equivalent Pt disk diameter can be estimated based on the measured reductive steady state (bulk) current, using the following equation:⁴¹

$$i_{\infty} = 4nFDac \quad [6.5]$$

where i_{∞} is the steady state current, n is the number of electrons reduced in the reaction (1), D is the diffusion coefficient for $\text{Ru}(\text{NH}_3)_6^{3+}$ (6.7×10^{-10} m/s).⁴² From eqn 6.5 and Figure 6.2A, this Pt NE has a Pt diameter of approximately 15 nm. Repetitive CV testing of the Pt NEs did not show a significant change in faradaic current (high reproducibility), leading us to conclude this electrode has good stability in solution.

Utilizing a Formvar and carbon-coated square Ni-mesh TEM grid as a sample, a horizontal line scan was taken over part of the Ni grid and hole (red arrow, inset in Figure 6.2B) using the above NE. For the first 30 μm of the scan, higher feedback current was detected over the grid portion of the sample ($I = 5.2$), followed by lower feedback current over the hole ($I = 4.6$, electrode position 30-60 μm). Over the conductive grid, higher feedback current was detected since this substrate is capable of accepting an electron from the reduced $\text{Ru}(\text{NH}_3)_6^{2+}$ species, regenerating the reactant $\text{Ru}(\text{NH}_3)_6^{3+}$ required to drive the

electrochemical reaction at the biased electrode tip forward. The reduced conductivity observed over the hole, results in a decrease in feedback current. In addition, due to the height variation provided by the Ni mesh, stronger electrochemical feedback will be seen over the grid since lower tip-to-sample distances will be reached (Figure 6.2B). Variations in sample topography can become more problematic as the electrode tip size is reduced, since smaller tip-to-sample distances are required for NEs to detect changes in electrochemical feedback ($L < 2$). The fragility of the NE tip can lead to higher degrees of tip damage if collision is made.

6.4.1.2 Polished Nanoelectrodes

SEM imaging of the laser-pulled Pt NEs confirmed a significant reduction in the Pt diameter occurred as a result of this particular fabrication method (1000 times less, Figure 6.3A). SEM also revealed these laser-pulled Pt NEs have the reduced Pt wire receded within the quartz capillary tip. This indicates that an additional step is required to expose the Pt surface. If these laser-pulled electrodes are fabricated with a recessed Pt tip, it is possible the tip diameter of the NE used to report the SECM current feedback of the TEM grid (Figure 6.2) is underestimated using eqn 6.5.

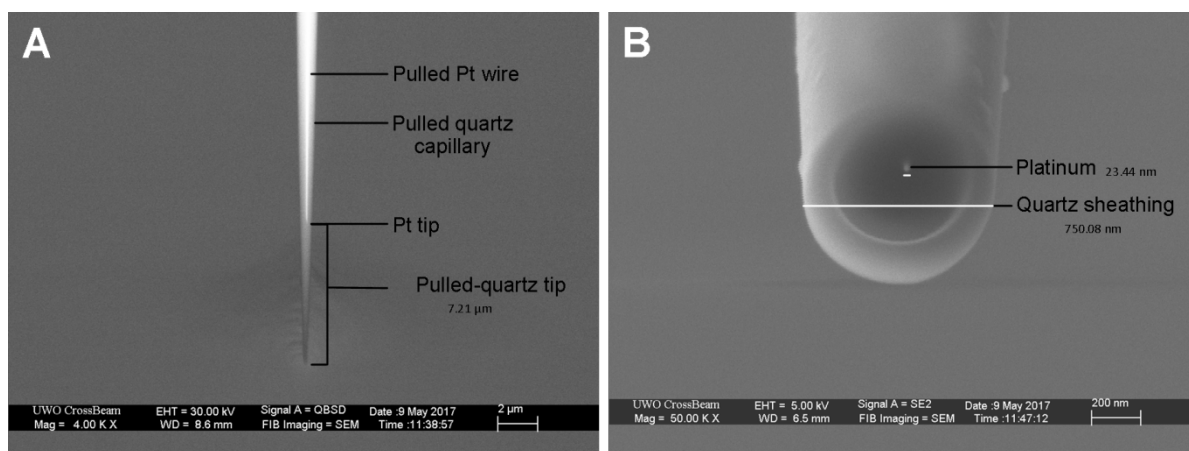


Figure 6.3. (A) An SEM image of a freshly pulled NE. The 25 nm diameter Pt wire can be seen to be recessed 7 μm within the pulled quartz capillary tip. (B) A SEM image of a FIB-milled laser-pulled Pt NE with Pt tip exposed by FIB-milling. The indicated area in (B) provides an estimate of ~25 nm for the diameter of the Pt wire with an $RG > 30$.

One method to expose the Pt tips is to use FIB-milling in conjunction with SEM imaging to remove the excess quartz capillary (Figure 6.3). This produced NEs with Pt tip diameters of 25 nm (or greater), while having RG ratios greater than 25 (Figure 6.3B). In these cases ($RG \geq 10$), eqn 6.5 provides a good estimation of the steady state current for the NEs.² Therefore, when coupled with CV, eqn 6.5 can be used to estimate the radius of the Pt disk of the laser-pulled and FIB-milled electrodes. In addition, the modeling of these NEs in finite elemental analysis simulations can be simplified to an RG of 10 (when $RG > 10$).^{2, 41}

The above method of using SEM and FIB-milling to expose the Pt tip of the NEs is an effective means of preparing probes with small electrode diameters. However, there are a few limitations that must be considered when preparing these NEs. If the SECM instrument does not provide sufficiently small stepping in the x and z directions, the resolution advantage of these NEs becomes lost. For example, the SECM instrument used throughout this dissertation is equipped with a z piezo actuator that is limited to 50 nm step sizes, which is too large for these FIB-milled NEs (strongest feedback current detected at $L < 2$). As NEs are considerably fragile, the likelihood of damaging the tips also increases when approaching the sample at these distances. When the cost of fabricating the FIB-milled NEs is also considered, an alternative approach to the fabrication and implementation of the NEs must be used. In addition, FIB-milling of the NEs does not reduce the size of the glass sheathing surrounding the exposed Pt tip, yielding NEs with overall dimensions in the high nanometer to low micron range.

6.4.2 SECM Imaging of an IAME by a 250 nm Diameter Pt NE (RG30)

To prepare a greater number of NEs in a more cost-effective manner, it was necessary to use alternative techniques to FIB-milling. Manual polishing of the nanoelectrodes becomes a viable alternative as it can expose the Pt tips similar to the UME fabrication method. While manual polishing may result in larger Pt tip diameters than through FIB-milling, it is still significantly smaller than the commercially obtained Pt wires used in the fabrications of UMEs (Chapters 2-4).

As a demonstration of the effectiveness of this fabrication method, a manually polished 250 nm diameter Pt NE (RG30) was used as an SECM probe to electrochemically image 2 pairs of alternating 5 μm glass and Pt microbands of an IAME sample. Figure 6.4A shows the 2D (x,y) current map of the microbands, where the Pt microbands are represented in the bright white-yellow to orange-red colors and the glass microbands by the dark blue-black colors, when the Pt NE is scanned at a constant height in the z plane above the sample. A 3D representation of the 2D image is shown in Figure 6.4B for better visualization of the alternating natures of the microbands (insulating and conductive).

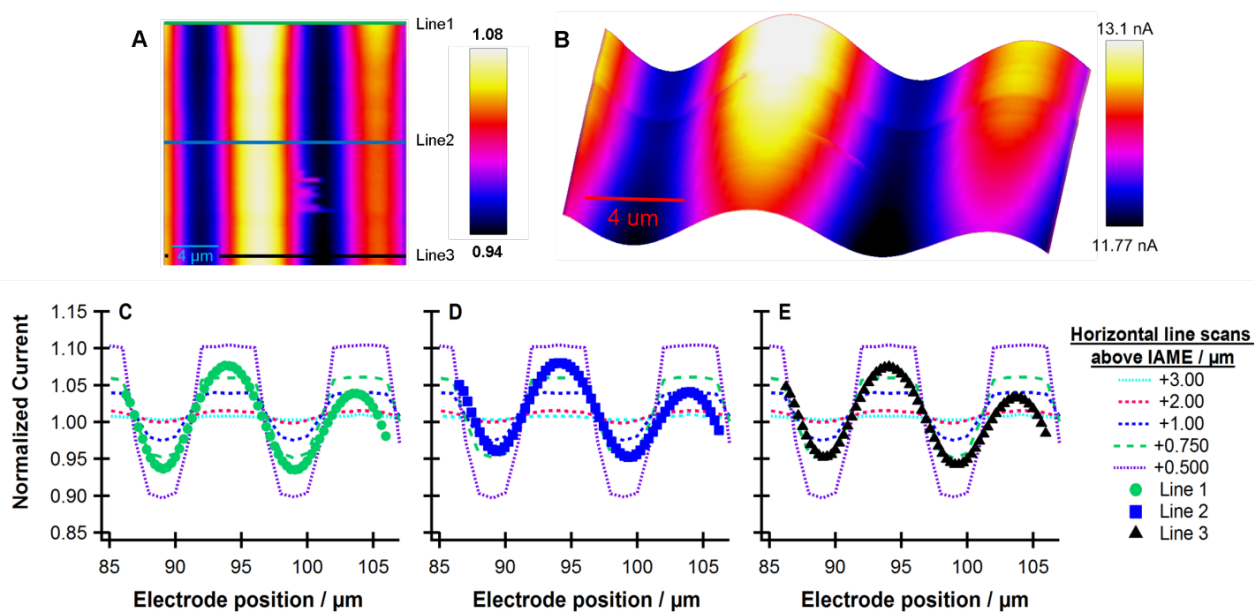


Figure 6.4. (A) and (B) are the constant height SECM images of two alternating pairs of Pt and glass microbands collected in 10 mM $\text{Ru}(\text{NH}_3)_6^{3+}$ solution with 0.1 M KCl as the supporting electrolyte by a 250 nm diameter Pt NE with RG 30. (A) is the 2D current map view and (B) is a 3D view of (A), providing stronger visualization of the electrochemical behavior of the Pt and glass microbands. The scale bars in the images represent 4 μm and the current scale bar in (A) is been normalized against the steady state current. (C)-(E) are the horizontal line scans taken at the locations specified in (A), that are overlaid over simulated curves generated at 0.50, 0.75, 1.00, 2.00 and 3.00 μm above the sample. From successful overlays, the 250 nm Pt NE was scanned approximately 0.75 μm above the sample. The simulation geometry of the working electrode was simplified to a 250 nm Pt NE with an RG of 10.

From this constant height image, one can see that the feedback response of the first Pt microband is slightly wider than its surrounding glass microbands. This is observed despite the physical dimensions of the IAME as specified by the manufacturer, which dictated that the Pt and glass microbands are equal in widths (5 μm). The increase in feedback is a cumulative effect of the increased signal strength of conductive substrates over insulators, the electrochemical cycling between the probe and adjacent Pt microbands, and the height difference between the Pt microbands and interdigit glass space (110 nm). Therefore, a broader band of electrochemical feedback will be detected as the 250 nm Pt NE scans over the Pt microbands (smaller tip-to-sample distance achieved). The simulation of the IAME accounts for relative signal intensities of the two substrates and the diffusion-limited cycling of the mediator and species to the defined geometry. The simulation model however, does not account for the height differences between the Pt and glass microbands. This corresponds to a tip-to-glass distance which has to be offset by an additional 0.110 μm . Higher feedback current was also observed as the 250 nm Pt NE is scanned over the first (left) Pt microband as opposed to the second Pt microband. This signifies that the second Pt microband had a larger tip-to-sample distance as the scan progressed, indicating the IAME sample or electrode is likely tilted relative to each other (Figures 6.4A and B).

Horizontal line scans extracted in three locations (start, middle and end of the image in Figure 6.4A) were overlaid onto simulated horizontal sweep curves to quantify the tip-to-sample distances (Figures 6.4C, D and E, respectively). For these curves, the tip current was normalized against the steady state current in the bulk solution (eqn. 6.3). At the start of the image (line 1 (green), Figure 6.4A), the 250 nm Pt NE scans over the first glass microband of 5 μm width, which shows its insulating properties through a decrease in normalized tip current ($I = 0.90$ (negative feedback), green circles, Figure 6.4C). Following this glass microband, the NE scans over the first of the two Pt microbands, where the normalized tip current increased to 1.08 (positive feedback). As the NE continues its horizontal scan, the adjacent insulating glass microband causes another decrease in electrochemical feedback ($I = 0.94$), followed by increased electrochemical feedback at the second Pt microband ($I = 1.04$). However, the feedback current from the second Pt microband is less than that of

the first Pt microband (1.04 vs 1.08), which reinforces the conclusion that either the sample or electrode is tilted.

This tilt can be confirmed through the successful overlay of the experimental horizontal curve onto the simulated curves (Figure 6.4C). A tip-to-sample distance of approximately 0.60 μm was reached over the first Pt and glass microbands, while the scan over the second Pt microband revealed a tip-to-sample distance of 1 micron. This indicates there is a 1.53° tilt across the sample, without considering the tilting of the other plane, which is significant relative to the size of this NE. Horizontal line scans taken midway (line 2, blue) and at the end of the SECM constant height image (line 3, black) also confirms that sample or electrode tilt occurs (Figure 6.4A). Therefore, for the collection of this constant height image, the 250 nm Pt NE was scanned approximately 0.75 μm above the IAME sample.

Following the constant height image collection, the NE was raised by the z piezo actuator to perform SECM depth scan imaging of the microbands, where the final horizontal scan of the depth scan image mirrored the tip-to-sample distance maintained in the constant height scan (Figure 6.5). From the SECM depth scan, the electrochemical influence from the Pt and glass microbands can be seen as the NE approaches the IAME from above. Specifically, the strong feedback current from the conductive Pt microbands onto the NE is observed (minimal insulating or negative feedback from the glass microbands). As previously mentioned, this is partially due to the height difference between the Pt and glass microbands (110 nm, equivalent to $L = 0.88$).

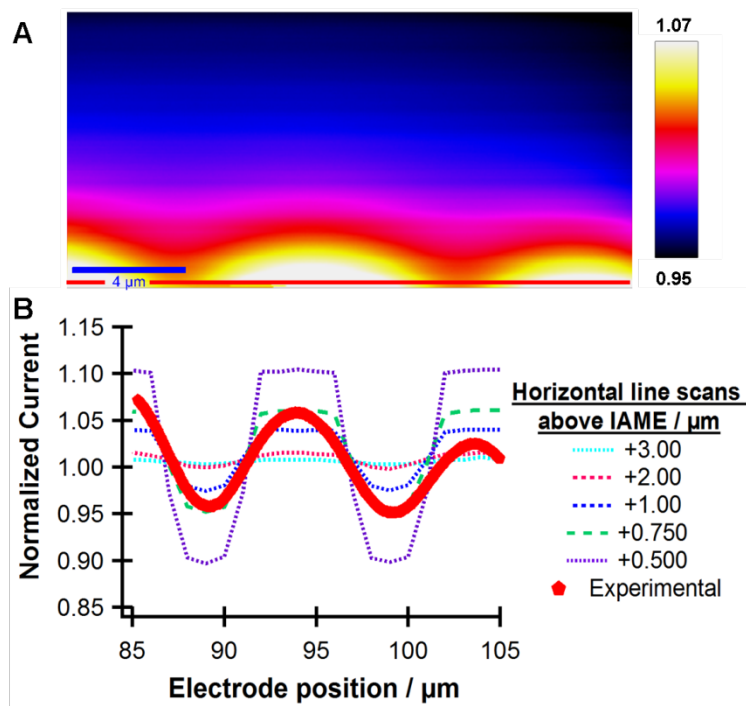


Figure 6.5. (A) SECM depth scan image towards the glass and Pt microbands of the IAME with a 250 nm Pt probe (RG30). A horizontal line scan (red pentagons) is extracted near the end of the scan. (B) The experimental horizontal scan is overlaid onto theoretical curves to quantify tip-to-sample distance.

A horizontal line scan extracted near the bottom of the SECM depth scan image (red line, Figure 6.5A) reveals a tip-to-sample distance of 0.75 μm when overlaid onto the simulated horizontal curves (Figure 6.5B). This tip-to-sample distance is comparable to the tip-to-sample distance maintained in the collection of the constant height image. The immediate horizontal line scan extracted below this red line indicates that the NE tip collided with the microbands (Figure 6.5A). Since the RG of this NE is quite large (30), the diameter of the glass sheathing prevents the exposed Pt tip from approaching the bands closer.

While achieving tip-to-sample distances of approximately 0.75 μm may be ideal for larger UMEs, for an electrode with an effective Pt diameter of 250 nm, this would equate to normalized distances greater than 6 for the Pt bands and 7 for the glass microbands (accounting the height differences between the microbands). At these normalized distances, the fitting of experimental PACs onto simulated curves would not hold much accuracy. However, the normalized feedback currents from the SECM depth scan can be used to

determine their tip-to-sample distances using the simulated PACs to the center of the glass and Pt microbands (Figure 6.6).^{1, 16} For example, from the SECM depth scan (Figure 6.5A), the highest normalized current towards a Pt microband was identified as 1.07. From Figure 6.6, the corresponding normalized distance can be identified as 5.10. Similarly, the lowest normalized current towards a glass microband was identified as 0.95 (Figure 6.5A) and its corresponding normalized distance was identified as 6.10. The difference between these normalized distances is therefore 1.00 or 125 nm unnormalized (eqn 6.4). This height discrepancy is in close agreement with manufacturer specification of 110 nm Pt microbands. This also gives a tilt angle of 1.43° across the x plane of the SECM depth scan, which was similar to the tilt angle of the constant height scan (1.53°).

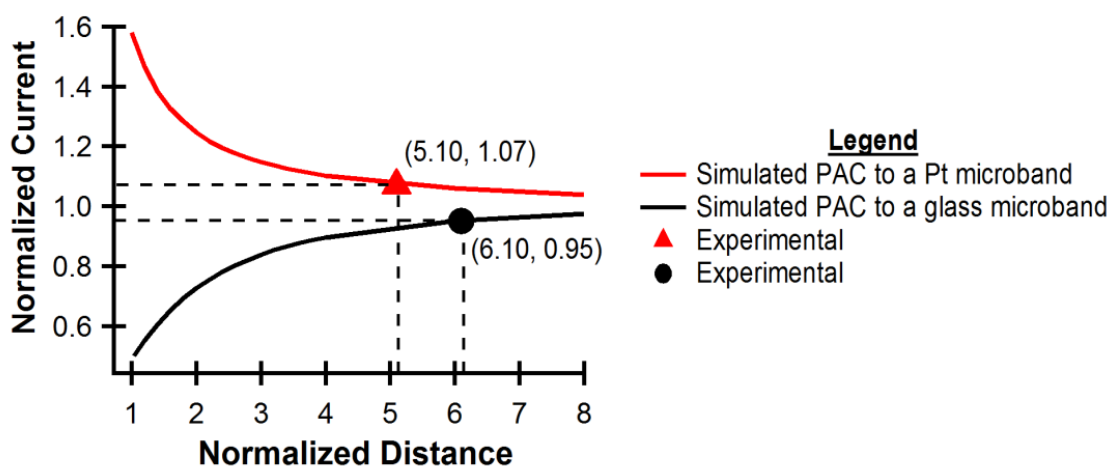


Figure 6.6. Theoretical PACs of a 250 nm Pt NE's approach to the Pt and glass microbands (red and black) of the IAME.

While NEs may provide higher SECM image resolution, the exact tip geometry of these probes are unknown without the use of high resolution microscopy. Researchers have demonstrated the effects of the tip sheathing (relative to the electrode size) on the faradaic current, especially in SECM⁴³⁻⁴⁴ and we have confirmed these effects through simulations as well.²¹ In order to simulate the theoretical curves, the exact geometry of the probe is needed, as recessed, conical or disk shape will affect the PACs.^{1, 6, 17, 45-47} Therefore, to investigate the effects of redox cycling and sample tilt, a SECM probe closer in size to the individual microbands was used.

6.4.3 SECM Imaging of an IAME by a 4.4 μm Pt UME (RG3)

Firstly, the microbands of the IAME were located using the inverted objective lens of the Alpha-SNOM instrument (Figure 6.7A), followed by the SECM experiments (Figure 6.7B). In SECM images, each pixel embedded into the image represents both the probe's coordinates and its corresponding current. The experimental SECM (x,y) image obtained at a constant height illustrates the conductive and insulating nature of the Pt and glass microbands, respectively (Figure 6.7B). When the 4.4 μm Pt UME is above the Pt microbands, the current increases due to the cyclic regeneration of the FcCH_2OH species at the solid-liquid interface (darker current, Figure 6.7B). However, when the electrode is above any insulating glass surface, the current becomes reduced (yellow current, Figure 6.7B).

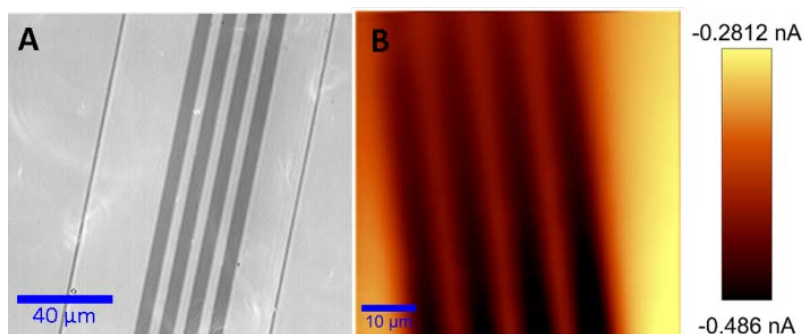


Figure 6.7. An optical micrograph of the (A) Pt and glass microbands of an IAME sample with a scale bar of 40 μm . (B) The corresponding SECM constant height image taken above the IAME collected using a 4.4 μm Pt UME (RG3) with FcCH_2OH as the redox mediator. The scale bar in the image represents 10 μm .

Note, our SECM instrument moves the electrode from right to left, resulting in an inverted SECM image (with respect to the optical micrograph).

While the alternating microbands are actually equal in width, the SECM image would suggest otherwise (Figure 6.7B), specifically when the SECM tip is over the insulating glass microbands. When the electrode is over these regions, diffusion of the reduced FcCH_2OH from the neighboring Pt microbands is still possible due to the size of the working electrode. This results in the Pt microbands appearing larger than their actual size (5 μm). In comparison, the SECM image of the glass and Pt microbands obtained by the smaller 250 nm

Pt NE reveals the microbands appear closer in size relative to one another (Figure 6.4A). This constant height image also shows stronger electrochemical feedback at the bottom of the SECM image (Figure 6.7) and it is evident the sample is tilted (angle $> 0^\circ$).

6.4.3.1 Depth scan mode

Experimental SECM depth scans towards the IAME were also performed using the $4.4\ \mu\text{m}$ Pt UME, as illustrated in Figure 6.8A. In this mode, when the SECM probe is far above the sample surface, a steady state current is detected ($L > 3$), as illustrated by the orange-brown current (Figure 6.8A). When the SECM probe is in close proximity to the IAME surface, its electrochemical influence is detected. Similar to the constant height image (Figure 6.7B), the darker, black current represents the conductive nature of the Pt microbands, while the insulating glass surface is represented as yellow current. Also, parallel to the constant height SECM image (Figure 6.7B), as the UME approaches the IAME the glass microbands appear thinner in width than their Pt microband counterparts, regardless of the Pt and glass microbands being physically identical in width ($5\ \mu\text{m}$).

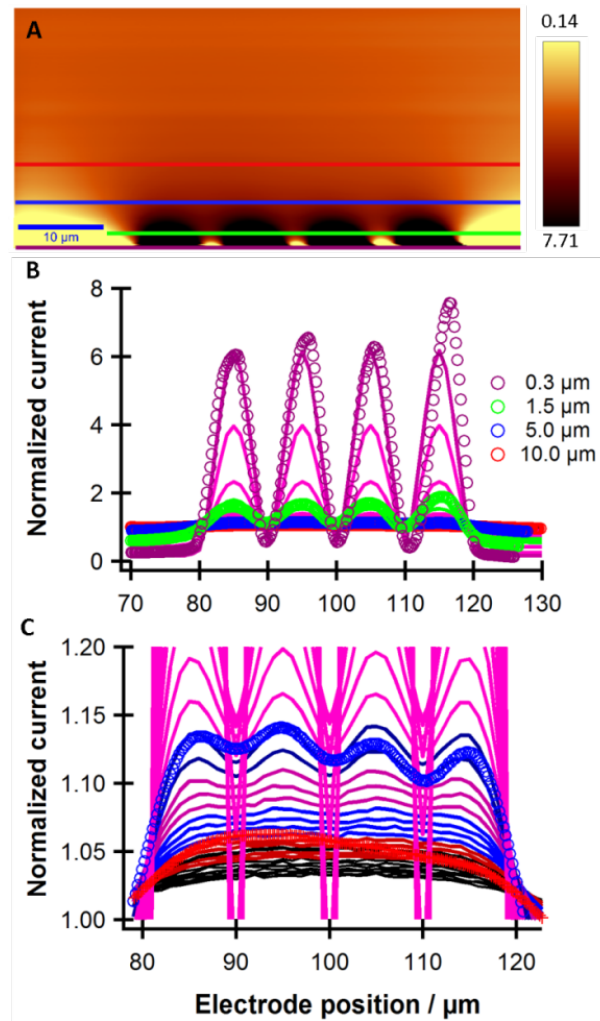


Figure 6.8. (A) A horizontally-labelled SECM depth scan image taken across the IAME surface using a 4.4 μm Pt UME (RG3). The purple line is taken at the edge of the image, while the green, blue, and red lines are taken 1.4, 5, and 10 μm above the purple line respectively. (B) and (C) are the simulated horizontal sweeps across the IAME with the experimental SECM data overlaid on top. (B) Displays a wide range of curves (0.5 to 30 μm) while the (C) is magnified from (B), focused on the normalized current range between 1.00 and 1.20 and the electrode position between 80 and 120 μm. From this plot, the purple and green experimental horizontal scans are removed for improved clarity.

6.4.3.2 Horizontal Cross Sections

After performing horizontal cross sections across the SECM depth scan image, we can determine the tip-to-sample distances by overlaying these experimental curves onto simulated ones generated by COMSOL (Figure 6.8B). However, the current must be first normalized against the steady state current ($L > 10$, eqn 6.3) to allow proper fitting. For example, a horizontal cross section obtained at the bottom of the SECM image (purple line, Figure 6.8A) overlaps the theoretical curve generated 0.3 μm above the IAME (purple circles, Figure 6.8B). This quantifies the closest distance the UME achieves in this particular SECM depth scan. In this experiment, the detected current is in close agreement to the simulated curve 0.3 μm above the sample when the electrode scans over the first three Pt microbands but deviates for the fourth microband (left to right in Figure 6.8A). Since stronger positive feedback is observed, this indicates that the probe reaches a smaller tip-to-sample distance than 0.3 μm .

When a horizontal cross section is taken 1.4 μm above the edge of the image (green line, Figure 6.8A), it can be seen to overlap closely with a generated horizontal scan 1.5 μm above the sample. Horizontal cross sections obtained 5 and 10 μm above the scan window (blue and red lines, Figure 6.8A) also yields successful overlay with their corresponding simulated curves at the same distances. It is evident based on the overlapping of these experimental curves, as the UME passes the first two Pt bands, the tip-to-sample distance is the smallest and in perfect agreement with the simulated curves. However, once the electrode crosses the third and fourth bands, the normalized current begins to deviate from the original theoretical curve and instead overlap with a curve further away from the IAME surface (5.5 for 5 μm and 11 μm for 10 μm).

The SECM probe begins to detect the feedback sooner for the first two Pt microbands (5 and 10 μm above the IAME), as opposed to the end of the scan where the fourth band appears to be closer. This indicates that prior to the completion of this scan, physical contact between the SECM probe and the IAME sample was made. As a result of this physical contact, two possible outcomes could occur: the IAME or petri dish was moved to compensate (possible tilting effect) or the electrode tip was damaged. However, since no physical damage was observed to our electrode tip (optical and CV characterization), this

would suggest either the sample or petri dish had sufficient clearance to compensate this contact resulting in the tilting of either of the two objects. This tilting effect will be addressed later in this Chapter.

6.4.3.3 PACs towards the IAME bands

Vertical PACs can also be extracted from the SECM depth scan image to provide further insight into the electrochemical functionality of the IAME sample. To confirm the simulation model, a PAC was first extracted to the center of the Pt microband which yielded a PAC in close agreement to an approach towards an ideal conductor (positive feedback). The same holds true when a PAC is extracted to the glass substrate 10 μm away from the microbands (Figure S6.1 in Appendix VI).

Experimental PACs were then obtained to the center of the Pt and glass microbands, as well as the transition boundary between the glass and Pt microbands were taken (blue, purple and green, respectively, Figure 6.9A). The experimental PAC towards the center of the Pt microband agrees successfully with the theoretical curve, up to a L value of 0.15 (blue, Figure 6.9B). Whereas when a PAC is extracted over the center of the glass microband (purple, Figure 6.9B), the UME achieves a lower tip-to-sample distance ($L < 0.11$), suggesting that the sample is once again tilted. The experimental PAC extracted towards the Pt-glass transition boundary deviates as the UME gets in close proximity to the sample surface ($L < 0.25$, green, Figure 6.9B). This is possibly due to UME detecting stronger electrochemical influence from the neighboring Pt microbands as tip-to-sample distance is minimized (increased redox cycling effect).

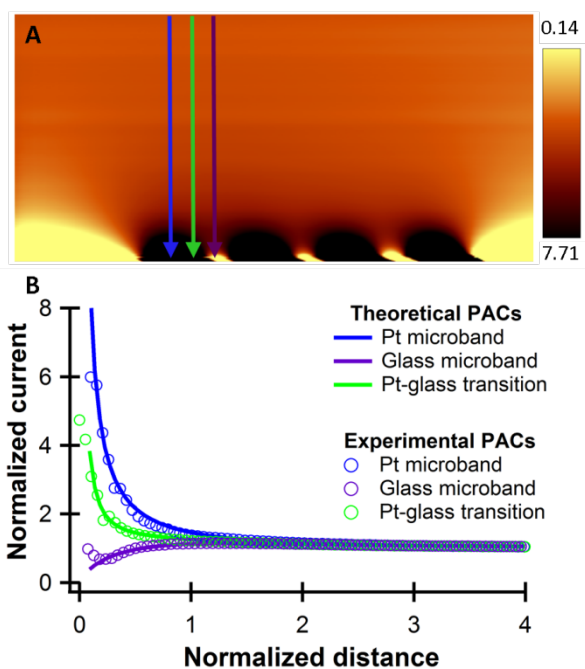


Figure 6.9. (A) A SECM depth scan image taken across the microbands of the IAME using a 4.4 μm Pt UME with a RG value of 3, with the vertical cross-sectional lines identified. The blue and purple cross-sections represents a PAC extracted to the center of a Pt and glass microband respectively, while the green cross-section represents a PAC extracted to the transition region between the two microbands

6.4.4 Redox Cycling Effect

Redox cycling can be extremely beneficial to improve the electrochemical detection of a reversible redox active species.^{31, 48-49} This is possible when the two electrodes are placed in close proximity to one another. Traditionally, redox cycling consist of at least two working electrodes that are biased at the opposing cathodic and anodic potentials required to reduce and oxidize the redox mediator, respectively.⁴⁸ The working electrodes, being in close proximity to one another, allow the products of the reduction and oxidation reactions to diffuse from one electrode to the other, supplying the opposing electrode the reactant it requires to drive its electrochemical reaction forward.

In our previous study of the electrochemical functionalization of an interdigitated array of electrodes, minor redox cycling was believed to be observed.³⁹ The PACs to the center of a 20 μm glass band were found to deviate from a true insulator (5 μm Pt UME with RG2).³⁹ However, the large band to electrode size made it difficult to assess if redox cycling is truly present. Here, to confirm the contribution of redox cycling we utilized a biased SECM probe close in size to the microbands of the IAME (4.4 vs. 5 μm). In this scenario, at narrow tip-to-sample distances, the SECM probe will act as the generator electrode while the Pt microbands can act as the collector electrodes. As the biased SECM probe completes a horizontal line scan across the IAME surface, it is in close proximity to several microbands of the IAME at any given position. This allows the $\text{Fc}^+\text{CH}_2\text{OH}$ formed at the electrode tip to quickly diffuse to one of the Pt microbands to regenerate FcCH_2OH , thus allowing redox cycling to occur.

From the SECM images, the Pt microbands appear much larger than their glass microband counterparts. Not surprisingly, it can be seen that any PAC extracted in the region above any portion of the Pt microbands, very little electrochemical influence from the neighboring glass microbands is detected (Figure 6.10A).

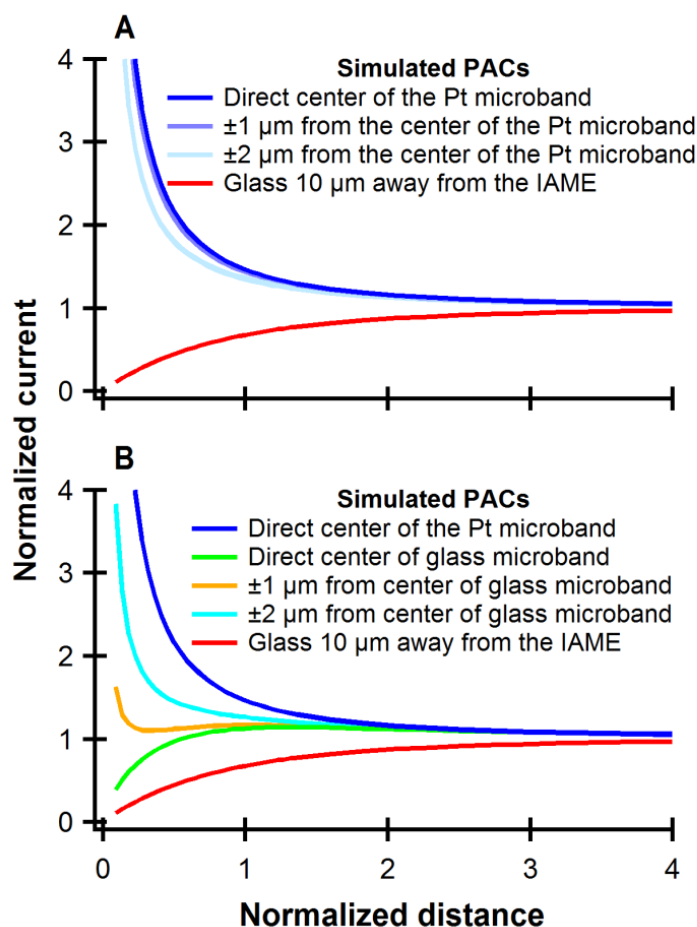


Figure 6.10. The comparison of the experimental PACs extracted to the (A) Pt and (B) glass microbands. In each of these figures, a PAC to the glass neighboring the IAME is also included (pure insulator).

However, for the PACs extracted towards the direct center of a glass microband, significant deviation from the ideal insulator is seen (green vs. red curves in Figure 6.10B). When the SECM probe is at the exact center of a glass microband, each side of the Pt disk of the UME is within $0.3 \mu\text{m}$ of the neighboring Pt microbands. This means that the regenerated mediator requires less distance and therefore time to diffuse from the Pt microband back to the UME (and the oxidized species from the UME tip to the Pt microbands, Figure 6.10A). However, in this scenario, the electrochemical contribution of the insulating glass to the electrode is dominating feature in the resulting PAC. The effects of redox cycling from the Pt microbands remains strongly detectable as indicated by the theoretical PAC deviating from displaying purely insulating characteristics (negative feedback).

Not surprisingly, as the PAC extraction moves towards the Pt microbands, the detected current displays increasingly positive feedback-like behavior (orange, light blue and dark blue curves in Figure 6.10B). When the electrode is positioned within 1 μm from the direct center of the glass microband, there is an increase in positive feedback as the L approaches 0 (orange curve, Figure 6.10B). When the electrode is positioned 2 μm from the center of the glass microbands, the PACs become more conductive-like (light blue curve, Figure 6.10B). The strong redox cycling effects from the Pt microbands cause them to appear larger than their physical dimensions in the SECM images ($<5 \mu\text{m}$, schematic shown in Figure 6.11A). The effects of redox cycling can be visualized through the simulated concentration maps (Figures 6.11B and C). Figure 6.11B shows the concentration profile as the biased UME is positioned over the center of a Pt microband. Here, as a result of the oxidation of FcCH_2OH at the UME tip, the concentration profile can diffuse to three microbands of the IAME. This is further evidence of the influence that the Pt microbands have on their neighboring glass microbands. Whereas, when the UME is positioned over the center of a glass microband and at smaller tip-to-sample distance (Figure 6.11C), its influence on the neighboring Pt microband is minimal.

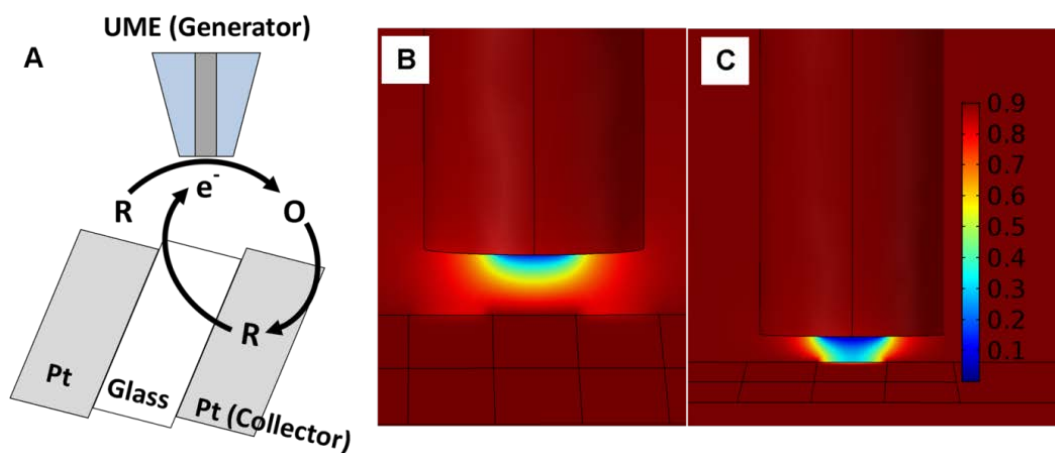


Figure 6.11. (A) A schematic illustration of the redox cycling occurring at the IAME when the SECM probe is over the insulating glass microband. The Pt UME acts as the electron generator while the Pt microband acts as an electron collector. (B) and (C) are the concentration maps of the UME over the direct center of a Pt and glass microband, respectively.

The presence of redox cycling should be further amplified if these individually addressable microband electrodes were biased at varying potentials in conjunction with the biased working electrode.^{31, 48-49} Upon biasing the microband electrodes (individually or collectively), redox cycling is expected to amplify significantly, leading to multiple-fold increases in faradaic current. To minimize the redox cycling effects, larger glass microbands are required (while maintaining the same electrode size) or smaller SECM probes can be used (while maintaining the same interdigit glass width), as demonstrated by the 250 nm Pt NE (Figure 6.5). The simulated and experimental horizontal line scans show an oscillation pattern between the insulating and conductive bands that are more uniform in widths across the glass and Pt microbands (Figure 6.5C). This was unlike the horizontal sweep curves generated using a UME similar in size to the microbands where the electrochemical feedback of the Pt microbands dominated over the glass microbands.

In the constant height SECM scans, the effects of redox cycling can also be minimized with sample tilt. If the probe is maintaining a constant z position over an uneven sample, the tip-to-sample distance is likely to vary. When the tip-to-sample distance is greater, the oxidized species will likely diffuse away from the electrode tip into solution, thereby minimizing redox cycling.

6.4.5 Determining the sample tilt

The orientation of a sample in SECM is extremely important: a tilted or uneven sample topography can result in the SECM probe making physical contact, resulting in damage to the probe itself or causing detrimental or physical changes to the sample. Without instrumental sample tilt compensation, tilted samples can still be studied and characterized by SECM in conjunction with finite elemental analysis simulations. Sample tilt can be characterized by several methods: the traditional PAC comparison approach and the analysis of horizontal line scans with 3D simulated horizontal sweeps.

6.4.5.1 PAC extractions

Experimental PACs extracted to the glass surrounding the microbands show close agreement with the simulated curves at the same location relative to the IAME (Figure 6.12A). From these PACs (Figure 6.12B and C), the tip-to-sample distance to the left and

right of the IAME were determined to be 0.55 and -0.22 μm respectively (Eqn 6.4). This negative distance indicates that the sample was tilted and the electrode physically made contact with the IAME sample. Assuming the petri dish to be fixed and flat (0°), the distance between the two extracted PACs is 56.72 μm . The height difference across the sample was found to be 0.77 μm . From here, the tilt angle can be found using trigonometry, which is 0.78° .

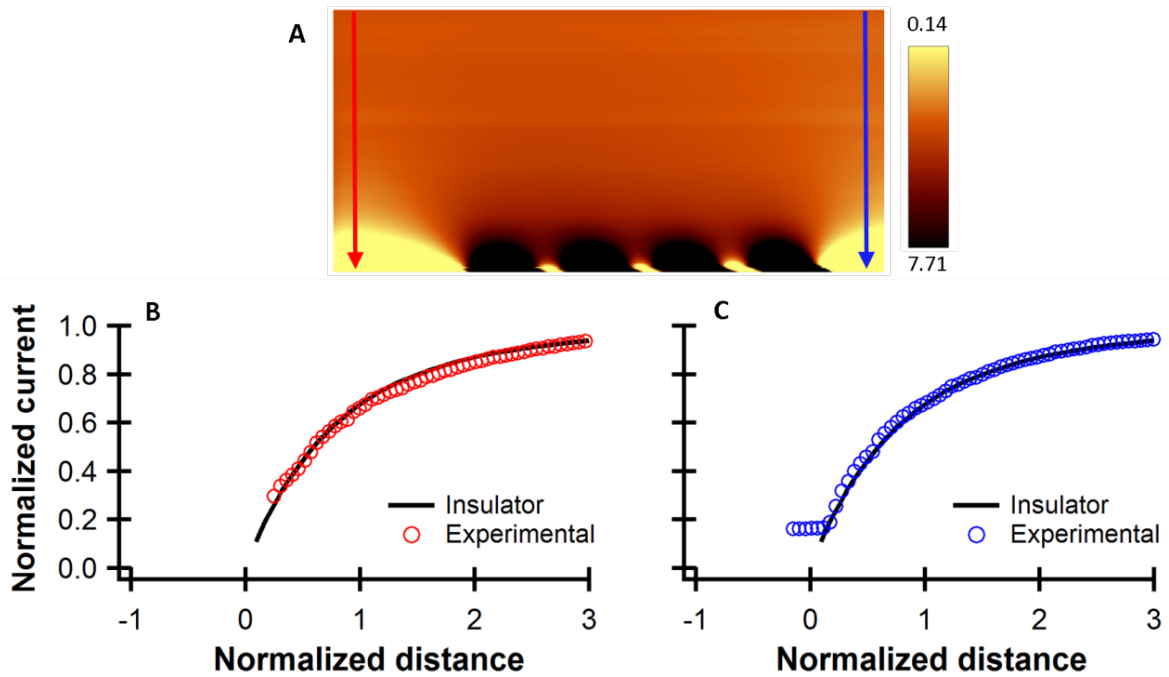


Figure 6.12. (A) The SECM depth scan image of the IAME with the two vertical cross-sections labelled as detected by a 4.4 μm Pt UME (RG3). The PACs illustrated in (B) and (C) corresponds to the vertical cross-sections taken beside the microbands (red and blue respectively in (A)) overlaid onto theoretical curves generated at the same distances relative to the microbands.

Figure 6.12C once again confirms the UME made physical contact with the IAME on the right side of the scan ($L < 0.17$), since the current remains constant when the electrode is still being lowered by the piezo actuator of the Alpha-SNOM instrument. This crash also confirms the horizontal fitting which was previously shown in Figure 6.8B, where the fourth band was found to have a tip-to-sample distance of less than 0.3 μm .

6.4.5.2 Simulated depth scan of an UME approach to the IAME

The 3D current map of an UME's approach towards the IAME sample was also simulated using COMSOL (Figure 6.13).

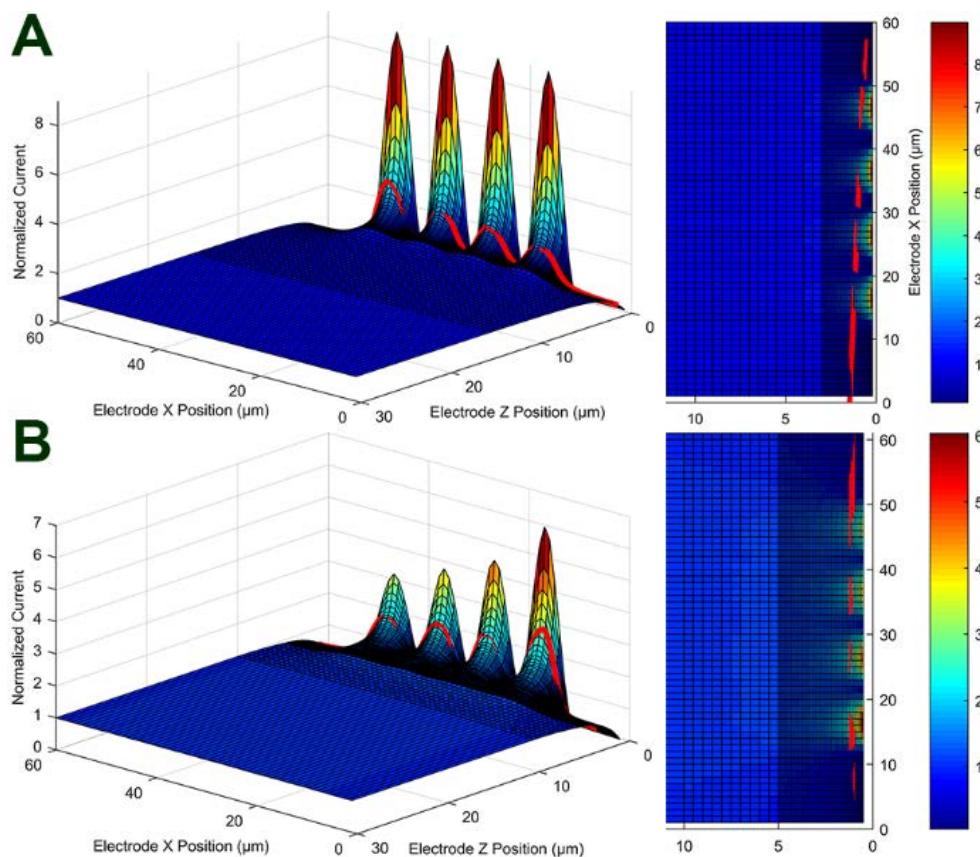


Figure 6.13. (A) The simulated 3D current maps of a 4.4 μm UME approach towards a fixed IAME sample with the experimental horizontal sweep tilted at 0.76° overlaid directly on top (red curve). (B) The 3D mapping of a tilted IAME sample (0.75°) with the experimental horizontal sweep overlaid directly on top (red curve).

The simulated depth scan is reflective of the SECM depth scan experiments: the electrochemical influence of the microbands is strongest when the UME is in close proximity. For these simulations, the IAME sample was assumed to be perfectly flat (0°). From here, the tilt angle of the experiment can be determined from the overlay of an experimentally obtained horizontal cross section. From Figure 6.13A, it can be seen that in order for the experimental scan (red curve) to be fitted successfully, it must be positioned on a tilt. When the tilted horizontal line scan is plotted against the theoretical depth scan, the

initial electrode position was found to fit at $0.55\ \mu\text{m}$ ($L = 0.25$). However, the final electrode position successfully overlaid at $-0.20\ \mu\text{m}$ ($L = -0.09$). This separation in the tip-to-sample distances across the horizontal line scan ($0.75\ \mu\text{m}$) confirms a sample tilt of 0.76° .

6.4.5.3 Angle tilted simulations

A series of additional simulations were performed where the center of the IAME sample was fixed and the entire substrate was tilted by varying degrees ranging between 0° and 5° . Here, the experimental horizontal sweep is overlaid directly onto the simulated horizontal sweep. From Figure 6.13B we can confirm when the simulated IAME is tilted 0.75° , the experimental sweep is in excellent alignment with the theoretical curve. As the electrode sweeps across the Pt microbands, the electrochemical feedback become stronger as seen in the oscillation amplitude of the faradaic current becomes stronger. As the tilt angle increases (5°), the SECM probe detects very weak electrochemical influence from the furthest band (see Figure S6.2 in Appendix VI).

6.4.5.4 Comparison of sample tilts

While a sample may appear perfectly flat to the human eye, it is still possible that the sample is tilted. The tilt angle can be characterized by using any of the aforementioned methods for quantification by SECM. The tilt angle of the IAME sample was found to be in close agreement regardless of the methodology used ($\sim 0.76^\circ$). While the tilt angle of the IAME sample was extremely small, it was still able to affect the UME's approach such that physical collision of the electrode and sample was made. This action can lead to the destruction of the electrode tip or damage to the sample topography to occur. Even minor sample tilt can become significant over large scans across the surface of a sample. In this experiment, the early collision of the SECM probe to the IAME sample led to the sample or dish compensation, changing the tilt angle throughout the depth scan experiment. In the case of a tilted substrate, redox cycling will be amplified if the tip-to-sample distance becomes minimized (constant height mode) or minimized if the tip-to-sample distance becomes larger. In our case, the effects of redox cycling would be greatest when the UME is in close proximity to the third and fourth Pt bands of the IAME.

6.5 Conclusions

Here, we report the successful fabrication of laser-pulled quartz sealed Pt NEs to improve lateral resolution of the SECM. As a result of this fabrication method, the Pt tips were exposed within the pulled quartz capillary and were tested without the additional polishing step. The estimated Pt disk-equivalent diameter of the NE was determined from its steady state reductive current of $\text{Ru}(\text{NH}_3)_6^{3+}$ to $\text{Ru}(\text{NH}_3)_6^{2+}$ (found by CV) to be approximately 15 nm in diameter (assuming $\text{RG} > 10$). Utilizing a Formvar/carbon-coated Ni TEM grid, a horizontal line scan was achieved illustrating higher conductivity over the Ni grid and lower feedback over the hole of the grid. SEM of these unpolished, laser-pulled Pt NEs confirmed a significant reduction in the diameter of the Pt wire: from 25 μm to 25 nm (1000 times reduction). However, SEM also revealed the Pt wires of these NEs to be recessed within the pulled quartz capillary. As a result of the recessed Pt tip, the calculated disk size was revealed to be underestimated (than its true tip size).

Using SEM and FIB-milling, the Pt tips of the NE were exposed, however the RG of these NEs are greater than 25. To prepare a greater number of NEs in a more cost-effective manner, manual polishing of the NEs became a viable alternative. While manual polishing of the NEs often result in larger exposed Pt diameter tips (than FIB-milling), it is still significantly smaller than the commercially obtained Pt wires. A manually polished 250 nm Pt NE (RG30) was used to characterize 2 pairs of Pt and glass microbands of an IAME sample. Even with the high RG value, the NE was still SECM compatible as the constant height image indicated weak redox cycling between the microbands. In conjunction with theoretical simulations completed in COMSOL Multiphysics v.5.2, the tip-to-sample distances could be determined through fitting of the experimental horizontal line scans. This indicated that the 250 nm Pt NE was scanned approximately 0.75 μm above the IAME sample. In addition, the presence of either sample or electrode tilt of 1.53° was identified in the electrodes imaging of the IAME.

The SECM depth scan image obtained over the IAME sample demonstrated strong electrochemical feedback upon the electrode's approach to the conductive Pt microbands due to smaller normalized distance achieved relative to the glass microbands. The final

horizontal line scan in the SECM depth scan was performed at the equivalent tip-to-sample distance maintained in the collection of the constant height image. Expectedly, this horizontal line scan revealed a tip-to-sample distance that was in close agreement to that of the probe's z position during the collection constant height image. Due to the large tip-to-sample distance, experimental PACs could not be used to accurately determine tip-to-sample distance. Instead, the normalized currents of the SECM depth scan were used to determine their corresponding normalized distances using the theoretical conductive and insulating PACs. This revealed a height variation of 125 nm between the Pt and glass microbands, which is similar to manufacturer's specifications (110 nm). The scan of the 250 nm Pt NE in the x plane of the depth scan image was determined to have a tilt angle of 1.43° , which is similar to that determined in the constant height scan (1.53°).

Utilizing a Pt UME of known geometry, the constant height and depth scan modes of SECM were used to characterize the electrochemical functionality of the IAME sample. The electrode's size allowed the tip-to-sample distances, as well as the tilt angle of the IAME sample to be determined from the simulated curves. The first method used to determine the sample tilt was through the more traditional approach, comparing PACs to different locations on the IAME. The second and third approach required more intensive 3D simulations, where the first method assumed a fixed (0°) orientation of the simulated IAME sample, requiring the adjustment of the experimental curves onto theoretical; while the second method varied the tilt angle of the simulated IAME sample while maintaining the experimental horizontal cross section. This tilt angle was found to be $\sim 0.76^\circ$ across the IAME using the three different approaches, all within close agreement.

The use of an UME that is similar in size to the Pt and glass microbands of the IAME (4.4 and 5 μm , respectively), the effects of redox cycling from the Pt microbands is strongly felt by any location within the insulating glass microbands. This results in the Pt microbands appearing much larger than their glass counterparts in the SECM images. To maximize the effects of redox cycling, a potential bias to the IAME sample is required in order to greatly amplify the tip current. To minimize the effects of redox cycling, larger interdigit space or smaller SECM probes are required, which was demonstrated by the use of a 250 nm Pt NE. A sample that is tilted can greatly affect the contribution of redox cycling since the tip-to-

sample distance will vary depending on the electrode's position and the tilt angle. Sample or electrode tilt can also lead to physical damage of either object, which risks become greater as the electrode diameter decreases.

6.6 References

1. Bard, A. J.; Faulkner, L. R., *Electrochemical Methods: Fundamentals and Applications, 2nd Edition*, 2 ed.; John Wiley & Sons, Inc., 2001.
2. Bard, A. J.; Mirkin, M. V., *Scanning Electrochemical Microscopy*, 2 ed.; CRC Press, 2012.
3. Zoski, C. G., Review - Advances in Scanning Electrochemical Microscopy (SECM). *J. Electrochem. Soc.* **2015**, *163*, H3088-H3100.
4. Amemiya, S.; Bard, A. J.; Fan, F.-R. F.; Mirkin, M. V.; Unwin, P. R., Scanning Electrochemical Microscopy. *Annu. Rev. Anal. Chem.* **2008**, *1*, 95-131.
5. Bergner, S.; Vatsyayan, P.; Matysik, F.-M., Recent Advances in High Resolution Scanning Electrochemical Microscopy of Living Cells – A Review. *Anal. Chim. Acta* **2013**, *775*, 1-13.
6. Fulian, Q.; Fisher, A. C.; Denuault, G., Applications of the Boundary Element Method in Electrochemistry: Scanning Electrochemical Microscopy. *J. Phys. Chem. B* **1999**, *103*, 4387-4392.
7. Eifert, A.; Mizaikoff, B.; Kranz, C., Advanced Fabrication Process for Combined Atomic Force-Scanning Electrochemical Microscopy (AFM-SECM) Probes. *Micron* **2015**, *68*, 27-35.
8. Ufheil, J.; Hess, C.; Borgwarth, K.; Heinze, J., Nanostructuring and Nanoanalysis by Scanning Electrochemical Microscopy (SECM). *Phys. Chem. Chem. Phys.* **2005**, *7*, 3185-3190.
9. Barker, A. L.; Macpherson, J. V.; Slevin, C. J.; Unwin, P. R., Scanning Electrochemical Microscopy (SECM) as a Probe of Transfer Processes in Two-Phase Systems: Theory and Experimental Applications of SECM-Induced Transfer with Arbitrary Partition Coefficients, Diffusion Coefficients, and Interfacial Kinetics. *J. Phys. Chem. B* **1998**, *102*, 1586-1598.
10. Nioradze, N.; Kim, J.; Amemiya, S., Quasi-Steady-State Voltammetry of Rapid Electron Transfer Reactions at the Macroscopic Substrate of the Scanning Electrochemical Microscope. *Anal. Chem.* **2011**, *83*, 828-835.

11. Li, M. S. M.; Filice, F. P.; Henderson, J. D.; Ding, Z. F., Probing Cd²⁺-Stressed Live Cell Membrane Permeability with Various Redox Mediators in Scanning Electrochemical Microscopy. *J. Phys. Chem. C* **2016**, *120*, 6094-6103.
12. Bard, A. J.; Li, X.; Zhan, W., Chemically Imaging Living Cells by Scanning Electrochemical Microscopy. *Biosens. Bioelectron.* **2006**, *22*, 461-472.
13. Wittstock, G.; Burchardt, M.; Pust, S. E.; Shen, Y.; Zhao, C., Scanning Electrochemical Microscopy for Direct Imaging of Reaction Rates. *Angew. Chem. Int. Ed.* **2007**, *46*, 1584-1617.
14. Liu, B.; Cheng, W.; Rotenberg, S. A.; Mirkin, M. V., Scanning Electrochemical Microscopy of Living Cells: Part 2. Imaging Redox and Acid/Basic Reactivities. *J. Electroanal. Chem.* **2001**, *500*, 590-597.
15. Li, X.; Bard, A. J., Scanning Electrochemical Microscopy of HeLa Cells – Effects of Ferrocene Methanol and Silver Ion. *J. Electroanal. Chem.* **2009**, *628*, 35-42.
16. Bard, A.; Fan, F.; Kwak, J.; Lev, O., Scanning Electrochemical Microscopy. Introduction and Principles. *Anal. Chem.* **1989**, *61*, 132-138.
17. Zoski, C. G., In *Handbook of Electrochemistry*, Elsevier: Amsterdam, 2007.
18. Nebel, M.; Eckhard, K.; Erichsen, T.; Schulte, A.; Schuhmann, W., 4D Shearforce-Based Constant-Distance Mode Scanning Electrochemical Microscopy. *Anal. Chem.* **2010**, *82*, 7842-7848.
19. Zhang, M. M. N.; Long, Y.-T.; Ding, Z., Cisplatin Effects on Evolution of Reactive Oxygen Species from Single Human Bladder Cancer Cells Investigated by Scanning Electrochemical Microscopy. *J. Inorg. Biochem.* **2012**, *108*, 115-122.
20. Li, M. S. M.; Filice, F. P.; Ding, Z., A Time Course Study of Cadmium Effect on Membrane Permeability of Single Human Bladder Cancer Cells Using Scanning Electrochemical Microscopy. *J. Inorg. Biochem.* **2014**, *136*, 177-183.
21. Filice, F. P.; Li, M. S. M.; Henderson, J. D.; Ding, Z., Mapping Cd²⁺-Induced Membrane Permeability Changes of Single Live Cells by Means of Scanning Electrochemical Microscopy. *Anal. Chim. Acta* **2016**, *908*, 85-94.
22. Guo, J.; Amemiya, S., Permeability of the Nuclear Envelope at Isolated Xenopus Oocyte Nuclei Studied by Scanning Electrochemical Microscopy. *Anal. Chem.* **2005**, *77*, 2147-2156.
23. Kranz, C., Recent Advancements in Nanoelectrodes and Nanopipettes Used in Combined Scanning Electrochemical Microscopy Techniques. *Analyst* **2014**, *139*, 336-352.

24. Katemann, B. B.; Schuhmann, W., Fabrication and Characterization of Needle-Type. *Electroanalysis* **2002**, *14*, 22-28.
25. Mezour, M. A.; Morin, M.; Mauzeroll, J., Fabrication and Characterization of Laser Pulled Platinum Microelectrodes with Controlled Geometry. *Anal. Chem.* **2011**, *83*, 2378-2382.
26. Danis, L.; Gateman, S. M.; Snowden, M. E.; Halalay, I. C.; Howe, J. Y.; Mauzeroll, J., Anodic Stripping Voltammetry at Nanoelectrodes: Trapping of Mn^{2+} by Crown Ethers. *Electrochim. Acta* **2015**, *162*, 169-175.
27. Kim, B. M.; Murray, T.; Bau, H. H., The Fabrication of Integrated Carbon Pipes with Sub-Micron Diameters. *Nanotechnology* **2005**, *16*, 1317-1320.
28. Rees, H. R.; Anderson, S. E.; Privman, E.; Bau, H. H.; Venton, B. J., Carbon Nanopipette Electrodes for Dopamine Detection in Drosophila. *Anal. Chem.* **2015**, *87*, 3849-3855.
29. Chen, R.; Hu, K.; Yu, Y.; Mirkin, M. V.; Amemiya, S., Focused-Ion-Beam-Milled Carbon Nanoelectrodes for Scanning Electrochemical Microscopy. *J. Electrochem. Soc.* **2016**, *163*, H3032-H3037.
30. Neugebauer, S.; Zimdars, A.; Liepold, P.; Gębala, M.; Schuhmann, W.; Hartwich, G., Optimization of an Electrochemical DNA Assay by Using a 48-Electrode Array and Redox Amplification Studies by Means of Scanning Electrochemical Microscopy. *ChemBioChem* **2009**, *10*, 1193-1199.
31. Odijk, M.; Olthuis, W.; Dam, V. A. T.; van den Berg, A., Simulation of Redox-Cycling Phenomena at Interdigitated Array (IDA) Electrodes: Amplification and Selectivity. *Electroanalysis* **2008**, *20*, 463-468.
32. Wittstock, G., Sensor Arrays and Array Sensors. *Anal. Bioanal. Chem.* **2002**, *372*, 16-17.
33. Lesch, A.; Chen, P.-C.; Roelfs, F.; Dosche, C.; Momotenko, D.; Cortés-Salazar, F.; Girault, H. H.; Wittstock, G., Finger Probe Array for Topography-Tolerant Scanning Electrochemical Microscopy of Extended Samples. *Anal. Chem.* **2014**, *86*, 713-720.
34. Zoski, C. G.; Simjee, N.; Guenat, O.; Koudelka-Hep, M., Addressable Microelectrode Arrays: Characterization by Imaging with Scanning Electrochemical Microscopy. *Anal. Chem.* **2004**, *76*, 62-72.
35. Zoski, C. G.; Yang, N.; He, P.; Berdondini, L.; Koudelka-Hep, M., Addressable Nanoelectrode Membrane Arrays: Fabrication and Steady-State Behavior. *Anal. Chem.* **2007**, *79*, 1474-1484.

36. Danis, L.; Snowden, M. E.; Tefashe, U. M.; Heinemann, C. N.; Mauzeroll, J., Development of Nano-Disc Electrodes for Application as Shear Force Sensitive Electrochemical Probes. *Electrochim. Acta* **2014**, *136*, 121-129.
37. Zhang, M. M.; Long, Y. T.; Ding, Z., Filming a Live Cell by Scanning Electrochemical Microscopy: Label-Free Imaging of the Dynamic Morphology in Real Time. *Chem. Cent. J.* **2012**, *6*, 20.
38. Zhang, M.-N.; Ding, Z.; Long, Y.-T., Sensing Cisplatin-Induced Permeation of Single Live Human Bladder Cancer Cells by Scanning Electrochemical Microscopy. *Analyst* **2015**, *140*, 6054-6060.
39. Filice, F. P.; Li, M. S. M.; Henderson, J. D.; Ding, Z., Three-Dimensional Electrochemical Functionality of an Interdigitated Array Electrode by Scanning Electrochemical Microscopy. *J. Phys. Chem. C* **2015**, *119*, 21473-21482.
40. Miao, W.; Ding, Z.; Bard, A. J., Solution Viscosity Effects on the Heterogeneous Electron Transfer Kinetics of Ferrocenemethanol in Dimethyl Sulfoxide-Water Mixtures. *J. Phys. Chem. B* **2002**, *106*, 1392-1398.
41. Bard, A. J.; Mirkin, M. V., *Scanning Electrochemical Microscopy*; Marcel Dekker: New York, 2001.
42. Mauzeroll, J.; Hueske, E. A.; Bard, A. J., Scanning Electrochemical Microscopy. 48. Hg/Pt Hemispherical Ultramicroelectrodes: Fabrication and Characterization. *Anal. Chem.* **2003**, *75*, 3880-3889.
43. Kwak, J.; Bard, A., Scanning Electrochemical Microscopy. Theory of the Feedback Mode. *Anal. Chem.* **1989**, *61*, 1221-1227.
44. Amphlett, J. L.; Denuault, G., Scanning Electrochemical Microscopy (SECM): An Investigation of the Effects of Tip Geometry on Amperometric Tip Response. *J. Phys. Chem. B* **1998**, *102*, 9946-9951.
45. Zoski, C. G.; Liu, B.; Bard, A. J., Scanning Electrochemical Microscopy: Theory and Characterization of Electrodes of Finite Conical Geometry. *Anal. Chem.* **2004**, *76*, 3646-3654.
46. Sun, P.; Mirkin, M. V., Scanning Electrochemical Microscopy with Slightly Recessed Nanotips. *Anal. Chem.* **2007**, *79*, 5809-5816.
47. Danis, L.; Polcari, D.; Kwan, A.; Gateman, S. M.; Mauzeroll, J., Fabrication of Carbon, Gold, Platinum, Silver, and Mercury Ultramicroelectrodes with Controlled Geometry. *Anal. Chem.* **2015**, *87*, 2565-2569.
48. Goluch, E. D.; Wolfrum, B.; Singh, P. S.; Zevenbergen, M. A. G.; Lemay, S. G., Redox Cycling in Nanofluidic Channels Using Interdigitated Electrodes. *Anal. Bioanal. Chem.* **2009**, *394*, 447-456.

49. Bustin, D.; Mesároš, Š.; Tomčík, P.; Rievaj, M.; Tvarožek, V., Application of Redox Cycling Enhanced Current at an Interdigitated Array Electrode for Iron-Trace Determination in Ultrapure Spectral Carbon. *Anal. Chim. Acta* **1995**, *305*, 121-125.

Chapter 7

7 Concluding Remarks and Future Work

7.1 Concluding Remarks

As highlighted in this dissertation, scanning electrochemical microscopy (SECM) is an electroanalytical technique of the scanning probe microscopy family that has gained applications in a variety of scientific disciplines. The research presented in this dissertation is primarily focused on the use of SECM to non-invasively study single live cells under an *in vitro* experimental environment. Specifically, SECM membrane permeability studies were used to investigate the membrane responses of human bladder cancer (T24) cells after their exposure to heavy metal ions at various concentrations and time durations.

Firstly, Chapter 2 focused on the use of SECM to investigate the cellular topography in T24 cells in the absence of any heavy metal treatment. Using the membrane-impermeable redox mediator, ferrocenecarboxylate (FcCOO^-), the cellular geometry and topography was confirmed through three approaches. The first method is the more traditional approach, where cellular height was determined from the comparison of two different probe approach curves (PACs); one to the center of the cell and another to the (neighboring) petri dish, while the second approach relied on the direct fitting of a PAC extracted to the center of the cell onto simulated curves of varying cellular heights. A 3D simulation model was also used to confirm the cellular topography across the cell (elliptical) based on its electrochemical reactivity with the redox mediator. The development and success of these 3D simulations now allow for characterization of asymmetric samples and PACs to be taken over any vertical cross section obtained from a SECM depth scan image, which was previously limited to a single PAC extracted to the center of a cell.

Chapters 3, 4, and 5 focused on the effects of heavy metals, Cd and Zn, on membrane permeability in single live cancer cells. Since toxic heavy metals do not have essential biological roles, their introduction into living organisms can lead to lifelong health complications, such as diseases, cancers and death. Toxic heavy metals are known to displace the essential metals in many key cellular processes, as well as structurally in

proteins and enzymes, which can lead to their dysfunction. In humans and test animals, one well documented effect of toxic heavy metal exposure is increased generation of reactive oxygen species which can lead to a variety of detrimental consequences. For example, the overwhelming of the antioxidant defense system by increased intracellular oxidative stress can lead to lipid peroxidation of the cell membranes, followed by membrane integrity loss and increased permeation to chemical agents. Therefore, to successfully investigate the effects of toxic heavy metals *in vitro* and non-invasively by SECM poses great insight in the biological responses of single live cells without any ethical risks.

In Chapter 3, it was shown that SECM can detect the immediate membrane permeability changes in T24 cells after their exposure to acute concentrations of Cd^{2+} (0-10 mM). The membrane permeability coefficient to the membrane-permeable redox mediator, ferrocenemethanol (FcCH_2OH), was quantified through SECM depth scan experiments. In control T24 cells, the membrane permeability coefficient was found to be 4.3×10^{-5} m/s. After exposure to low, but acute, Cd^{2+} (1-2.5 mM), T24 cells were able to resist membrane permeability changes throughout these exposure durations (45 min). However, upon the introduction of significant Cd^{2+} (7.5-10.0 mM), the membrane permeability coefficient to FcCH_2OH increased to 3.5×10^{-4} m/s. After high Cd^{2+} exposure, T24 cells appeared to decrease in their cellular heights, required lowering of the SECM probe, while increasing their occupied surface areas on the petri dish. It is possible that these observed morphological changes and increased membrane permeability to FcCH_2OH were indicative that Cd^{2+} -induced cell death in T24 cells had begun.

Expanding on the findings of Chapter 3, both low (25 μM , $t \leq 6$ hrs) and acute (1-5 mM, $t = 1$ hr) Cd^{2+} exposure on T24 cells was investigated in Chapter 4. It is well known that increased membrane permeability to impermeable chemical agents is an indicator of membrane integrity loss. Therefore, membrane integrity loss in Cd^{2+} -treated T24 cells can be confirmed by SECM through the permeation of hydrophilic and charged redox mediators, FcCOO^- , 1,1'-ferrocene dicarboxylate ($\text{Fc}(\text{COO})_2^{2-}$) and hexaamineruthenium(III) ($\text{Ru}(\text{NH}_3)_6^{3+}$). Upon low Cd^{2+} treatment, T24 cells displayed a gradual increase in their permeation to these redox mediators across the cell membrane ($t \geq 2$ hrs), from 0 m/s (impermeable) to approximately 7×10^{-5} m/s (permeable). After confirmation of membrane

integrity loss by SECM, it was demonstrated through the MTT cell proliferation assay, that 25 μM Cd^{2+} had minimal effect on cellular viability during these exposure periods. However, after exposure to acute Cd^{2+} concentrations, permeation of these redox mediators occurred at Cd^{2+} concentrations greater than 2.5 mM, such that their membrane permeability coefficients increased from 0 m/s to approximately 2×10^{-4} m/s. This membrane integrity loss correlated well with a decrease in cellular viability (MTT cell proliferation assay). The findings in this Chapter confirmed the relationship between cellular viability and SECM membrane permeability.

In Chapter 5, SECM was used to monitor the physiological changes in Zn^{2+} -treated T24 cells. Using FcCH_2OH and $\text{Ru}(\text{NH}_3)_6^{3+}$ as the SECM redox mediators, the membrane changes induced by Zn^{2+} exposure were quantified. In the case of low Zn^{2+} -treatment for 24 hours (10-75 μM), T24 cells resisted significant membrane permeability change (5.0×10^{-5} to 1.3×10^{-4} m/s for FcCH_2OH and 0 m/s for $\text{Ru}(\text{NH}_3)_6^{3+}$), while displaying no adverse effects to Zn^{2+} . However, after T24 cells were exposed to high Zn^{2+} concentrations (100-400 μM), the membrane permeability coefficients to these redox mediators increased from 2.3×10^{-4} to 5.9×10^{-4} m/s for FcCH_2OH and 0 to 2.5×10^{-5} m/s for $\text{Ru}(\text{NH}_3)_6^{3+}$. The increase in passive diffusion of the redox mediators across the cell membrane suggested that the membrane integrity of the Zn^{2+} -treated T24 cells has weakened. It is possible this is due to lipid peroxidation, formation of pores, or structural collapse within the cell membrane. This correlated with the appearance of unhealthy T24 cells and a decrease in cellular viability as Zn^{2+} concentration increased. Since the membrane integrity and cellular viability were maintained during low Zn^{2+} -treatment, it was predicted that T24 cells treated with high Zn^{2+} concentrations underwent apoptotic cell death. This was confirmed through several techniques, such as flow cytometry and immunofluorescence. The presence of externalized phosphatidylserine residues on the outer leaflet of the cell membrane confirmed early apoptosis, as well as the increased expression of caspase-3/7 as Zn^{2+} concentration increased. Necrosis was excluded as the primary cell death mechanism through the confirmation of intact cell membranes in Zn^{2+} -treated T24 cells, since 7-aminoactinomycin and propidium iodide were mostly excluded by the cells.

Lastly, Chapter 6 focused on the fabrication of nanometer-sized SECM probes to improve the resolution of the SECM in the Ding Lab. Laser-pulled, quartz-sealed Pt nanoelectrodes (NEs) decreased the Pt tip diameter from 25 μm to 25 nm (thousand times reduction), improving the spatial resolution of SECM. Successful electrochemical and SECM characterization of a transmission electron microscopy grid and independently addressable microband electrodes (IAMEs) were obtained using these laser-pulled probes. When the SECM probe was much smaller in size relative to these microbands (250 nm vs 5 μm), the effects of redox cycling was minor in SECM, however sample tilt posed a larger issue (risk of tip damage) due to the size of the probe. Using a larger laser-pulled Pt SECM probe that closer in size to the microbands (4.4 μm vs. 5 μm), the effects of redox cycling and sample tilt were easily observed. 3D finite elemental analysis simulations allowed in depth analyses of the 2D data set obtained by the SECM depth scan method. Advancements in this Chapter will be applied towards improvements in spatial resolution studies, targeting smaller sample features. Concurrently, finite elemental analysis will no longer be restricted to symmetric samples.

7.2 Future Works

The successful reduction of SECM probes from 25 μm to 25 nm in Pt diameter was developed for this dissertation; however, the ratio of the glass sheathing to the Pt wire was quite high ($RG > 25$). Currently being explored in the Ding Lab is the further optimization of the laser-pulled nanoelectrode fabrication procedure in order to reduce this value. Doing so can show the benefit of nanoscale electrodes since the probes are less affected by electrode tilt. The fabrication of these nanoelectrodes using other conductive materials, such as PtIr, Ag, Au or C, may also allow for their production to be readily prepared with smaller tip diameters and optimal RG values, which would improve the spatial resolution of SECM. This is of particular interest for the SECM studies on single live cells. While biological cells may be on the micron scale overall, they are comprised of many complex organelles within a membrane-enclosed cytoplasm that are on the sub-micron scale. Therefore, if one wishes to probe these regions, the electrode tip must be the same size or smaller than these features.

Using SECM, significant membrane permeability to membrane-impermeable redox mediators was induced after treatment to the heavy metals, Cd^{2+} and Zn^{2+} . While weakening of the membrane integrity was confirmed, one hypothesis for increased membrane permeation is through pore formation or structural collapse of the cell membrane. With improved spatial resolution, it is possible that nanometer-sized SECM probes may be able to identify these changes and are worth exploring. It is also possible that if these changes are organelle specific, e.g. the cell nucleus may have different effects on membrane permeability, the improved resolution offered by these nanoprobe may become advantageous in identifying these areas of localization. In addition, should these organelles affect membrane permeability differently; asymmetric models can now be successfully simulated in 3D finite elemental analysis to quantify their membrane permeability coefficients.

For this dissertation, SECM was shown to be a powerful analytical technique that can be used to investigate the membrane responses in single live T24 cells after their exposure to toxic heavy metal treatment. Other biological changes, such as extracellular reactive oxygen species or ion release (or uptake) can also be monitored by SECM. It is therefore, not surprising, that SECM may have great potential as an analytical tool in biomedical research. In addition, SECM biological studies are not restricted to singular cells, but cell monolayers and tissue samples can also be analyzed. The size of the SECM probes may allow higher throughput in testing of pharmaceutical or chemical agents. Specifically, multiple locations (spot sizes) can be tested with these agents, increasing the number of testing conditions that can be examined.

In addition, combining SECM with other analytical techniques, such as confocal laser scanning and/or Raman microscopy, may become advantageous. For example, using Raman microscopy, mapping the distribution of a particular receptor over the cell's surface may lead to a predetermination of a drug's effectiveness, while the membrane permeability changes can be monitored by SECM. Simultaneous analysis is expected to provide additional insight in the biological changes cells have after stimulation. SECM is a technique that can be used for wide range of applications, not just limited to strictly biological studies. The non-invasive nature of this scanning probe microscopy technique, in addition to its high spatial

and temporal resolution, offers promise in studying the local properties, reactivity and electrocatalytic activities of samples.

Appendices

Appendix I. Chapter 1: Introduction

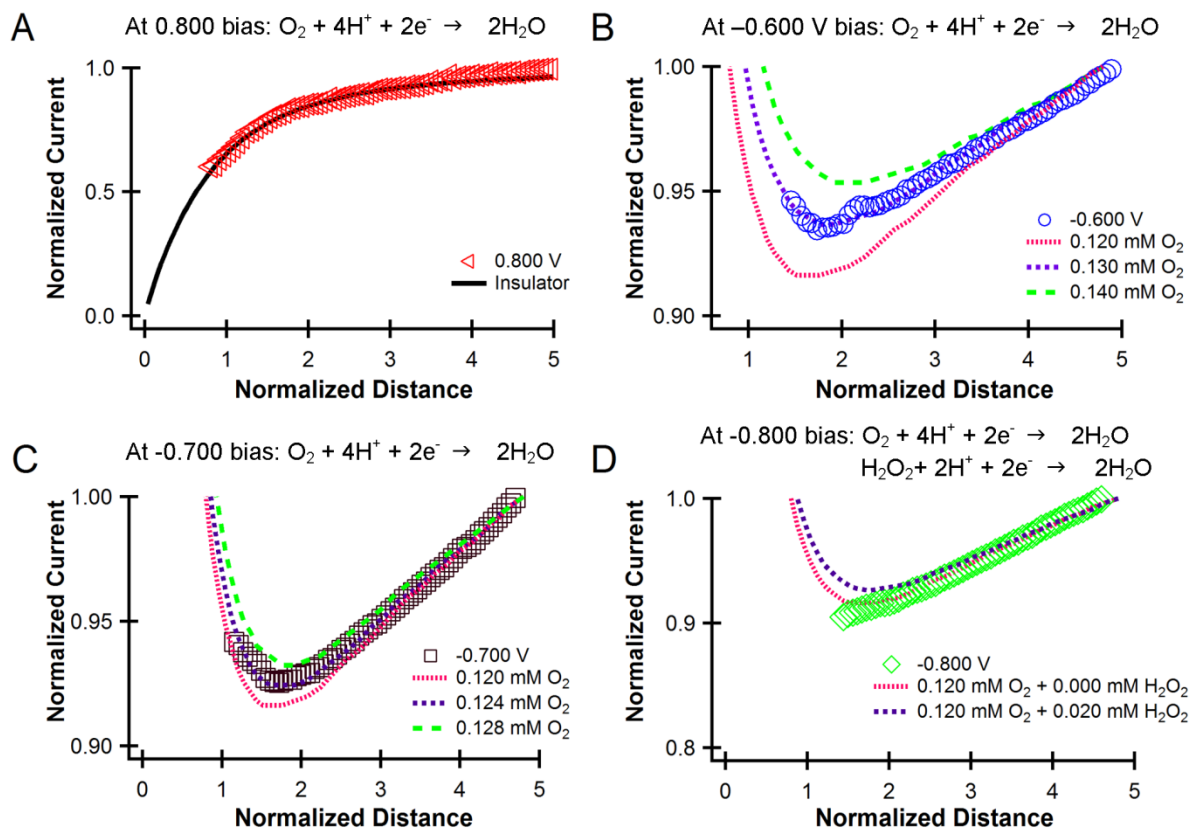


Figure S1.1. Using extracellular ROS release from T24 cells as a non-labelled SECM redox mediator. Quantification of H₂O₂ concentration can be determined (A) directly from on its oxidative bias (+0.800 V) and (B-D) indirectly from the reductive bias (-0.800 V), which reduces both O₂ and H₂O₂. This requires the determination of O₂ concentration (-0.600 V) from prior to H₂O₂ (D).

Appendix II. Chapter 2: Determining Live Cell Topography by Scanning Electrochemical Microscopy

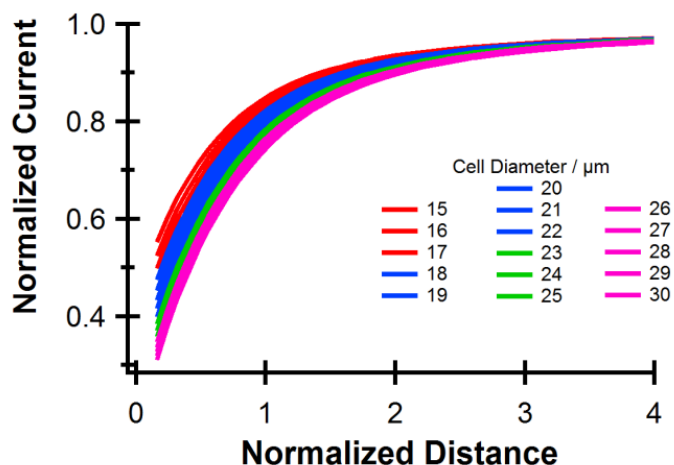


Figure S2.1. The PACs extracted over the center of an ellipsoid cell with a fixed height of 8 μm , varying cell diameters using a 5 μm Pt UME with RG 3. The blue PAC represents 3D model geometry and the purple diamond PAC represents 2D-axially symmetric model geometry.

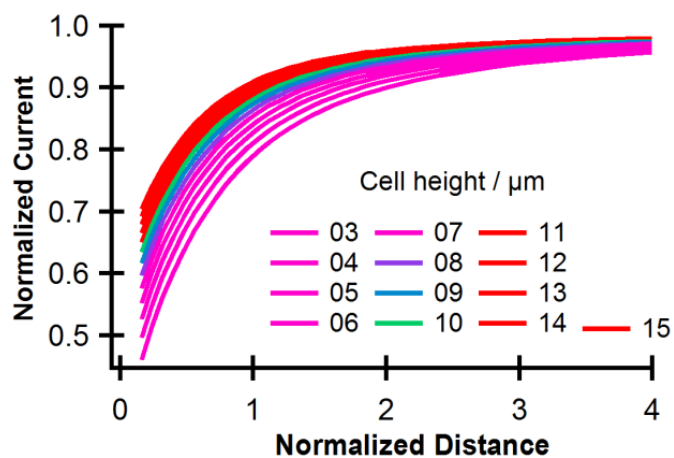


Figure S2.2 The PACs extracted over the center of an ellipsoid cell with a fixed diameter of 20 μm , varying cell heights using a 5 μm Pt UME with RG 3. The blue PAC represents 3D model geometry and the purple diamond PAC represents 2D-axially symmetric model geometry.

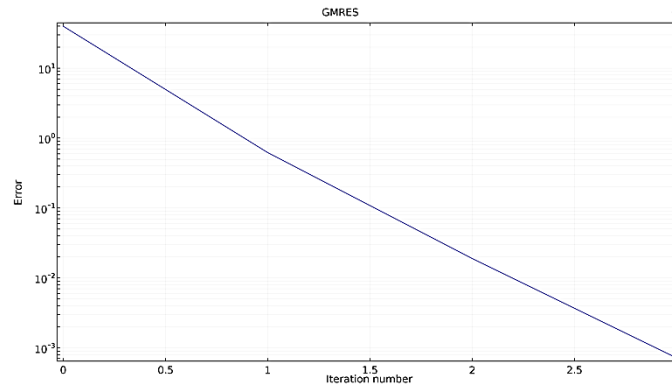


Figure S2.3. A meshing convergence plot of a single data point simulated using the 3D geometric model. An error of less than 10^{-3} is observed with the mesh (previously defined in text) applied to the model. For more information regarding simulation mesh, please see COMSOL export.

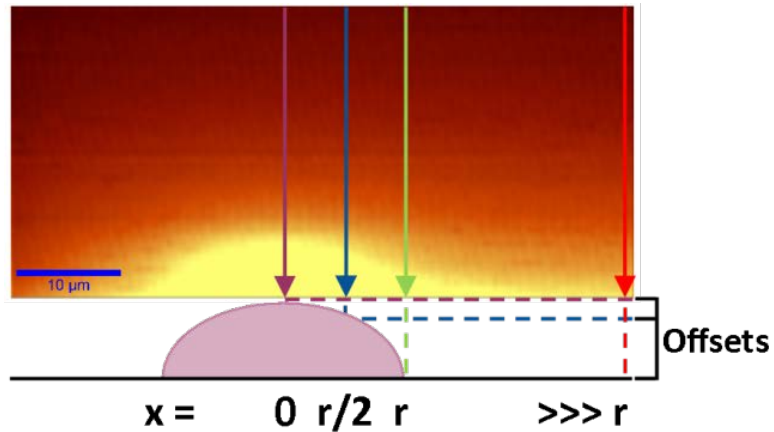


Figure S2.4. An SECM depth scan image collected over all illustrative T24 cell. The offsets due to the height changes across the cell. At $x = 0$ (cell center), the UME tip is directly on top of the cell, therefore no offset is needed. At a distance of $r/2$ away from the cell center, the offset of the tip-to-cell distance is governed by the equation of an ellipse. When $x = r$ or $\gg r$, the tip-to-sample distance is governed directly by the height of the cell.

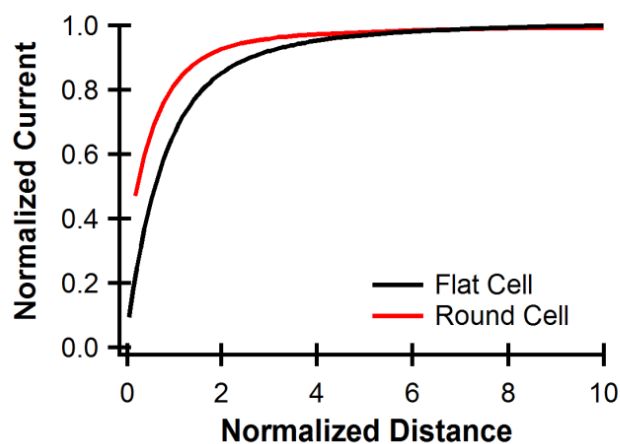


Figure S2.5. Theoretical PACs of a 5 μm Pt UME towards a flat and elliptical cell of 8 μm height by 20 μm diameter. The curvature of the flat cell is more pronounced as the UME approaches the cell.

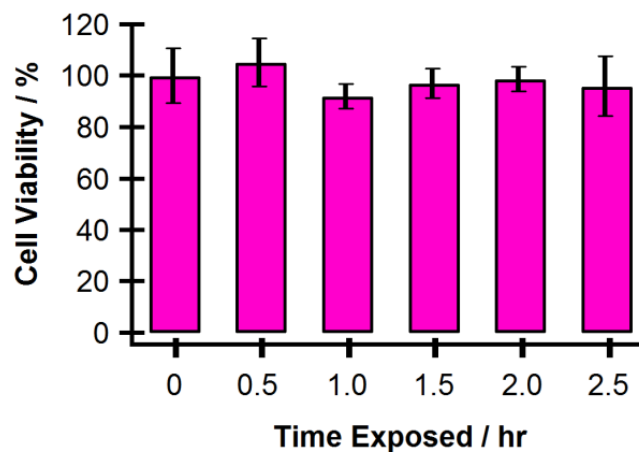


Figure S2.6. Cell viability of T24 cells treated with 0.5 mM FcCOO^- was measured by the MTT assay. The mean \pm RSD of 4 experiments (8 replicates of each condition/experiment) is shown. The viability remains constant over the experiment time.

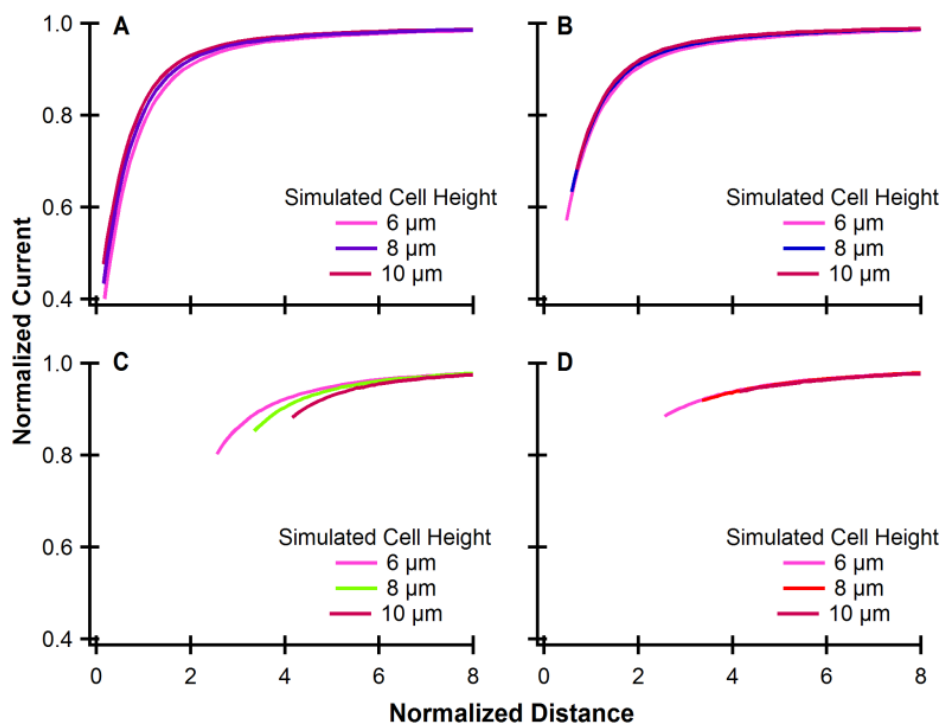


Figure S2.7. The theoretical PACs generated at $x =$ (A) 0, (B) $r/2$, and (C) r and (D) $\gg r$ for a cell height of 6, 8 and 10 μm .

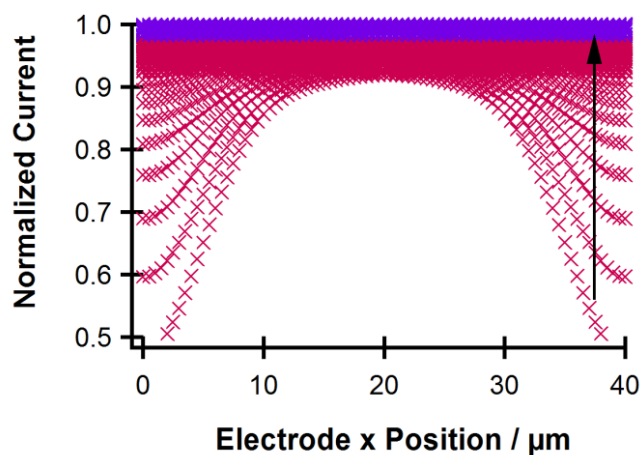


Figure S2.8. The 3D horizontal sweeps of a UME over the petri dish and cell with a height of 8 μm by 20 μm diameter using a 5 μm Pt UME with RG 3. The bottommost sweep corresponds to 0.5 to 10.0 μm above the cell (0.5 μm incremental steps, pink), followed by 15 to 60 μm (5 μm incremental steps, purple) as the curves go upwards.

COMSOL Report

A detailed COMSOL report on a 3D simulation model has been included below. This model is representative of the 3D models used to complete various sets of theoretical data for this work. The model includes a 5 μm electrode with an RG of 3 approaching an elliptical cell with a height of 8 μm and a radius of 10 μm . In this model, the electrode position is swept in the z and x axis through the nesting of parametric sweeps. The electrode is swept through a range of z coordinates from a tip to cell distance of 5 μm to 0.5 μm with 0.5 μm steps. Within each z sweep, a range of x coordinates is also investigated. The x coordinates in this model range from 0 μm (centered over the cell) to 40 μm in an interval of 0.5 μm .

5.1SECM3D SymmetricalXZ v4

Report date	Jan 2, 2016 11:50:52 PM
-------------	-------------------------

Contents

1.	Global Definitions	174
1.1.	Parameters 1	174
2.	Component 1	175
2.1.	Definitions	175
2.2.	Geometry 1	175
2.3.	Transport of Diluted Species	178
2.4.	Mesh	1186
3.	Study 1	189
3.1.	Parametric Sweep	189
3.2.	Stationary	189
3.3.	Solver Configurations	189
4.	Results	190
4.1.	Data Sets	190
4.2.	Derived Values	190
4.3.	Tables	Error! Bookmark not defined.
4.4.	Plot Groups	191

1 Global Definitions

Date	Dec 17, 2015 6:02:20 PM
------	-------------------------

Global settings

Name	5.1SECM3D SymmetricalXZ v4.mph
Path	/home/fraser/Desktop/toBeSorted/5.1SECM3D_SymmetricalXZ_v4.mph
COMSOL version	COMSOL 5.1 (Build: 180)
Unit system	SI

Used products

COMSOL Multiphysics

1.1 Parameters 1

Parameters

Name	Expression	Value	Description
elecPt	2.5[um]	2.5E-6 m	Electrode disk radius
RG	3	3	Electrode RG
elecGlass	elecPt*RG	7.5E-6 m	Electrode Glass Radius
solnSize	100*elecPt	2.5E-4 m	
cellZ	8[um]	8E-6 m	Cell Z Dimension
cellX	10[um]	1E-5 m	Cell X Dimension
cellY	10[um]	1E-5 m	Cell Y Dimension
elecZ	60[um]	6E-5 m	Electrode Z Position
elecX	0[um]	0 m	Electrode X Position
initC	0.5[mmol/L]	0.5 mol/m ³	Initial concentration FcCOOH
D	5.7e-10[m ² /s]	5.7E-10 m ² /s	diffusion coefficient for FcCOOH
n	1	1	Number of Electrons Transferred
F	96485[C/mol]	96485 C/mol	Faraday's Constant

2 Component 1

Date	Dec 7, 2015 11:12:38 PM
------	-------------------------

Component settings

Unit system	SI
Geometry shape order	automatic

2.1 Definitions

2.1.1 Coordinate Systems

7.2.1.1 Boundary System 1

Coordinate system type	Boundary system
Tag	sys1

Coordinate names

First (t1)	Second (t2)	Third (n)
t1	t2	n

Settings

Description	Value
Create first tangent direction from	Global Cartesian

2.2 Geometry 1

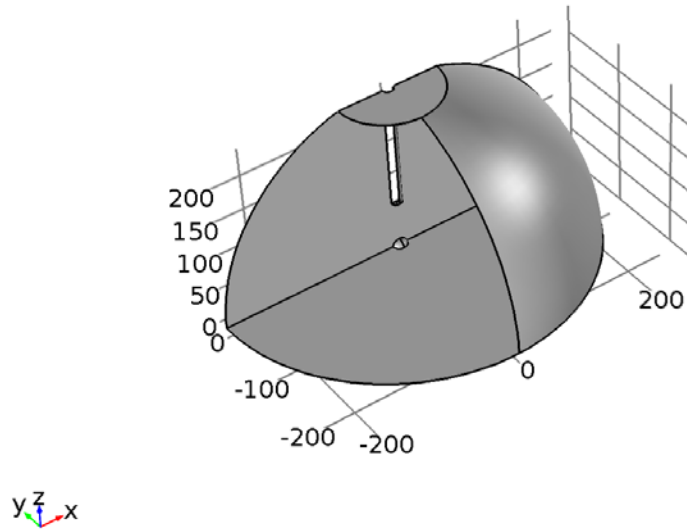


Figure 1. Geometry 1

Units

Length unit	μm
Angular unit	deg

Geometry statistics

Description	Value
Space dimension	3
Number of domains	1
Number of boundaries	11

Description	Value
Number of edges	28
Number of vertices	19

2.2.1 soln (cyl1)

Position

Description	Value
Position	{0, 0, 0}

Axis

Description	Value
Axis type	z - axis
Layers	

Size and shape

Description	Value
Radius	solnSize
Height	solnSize

2.2.2 soln_inner (cyl3)

Position

Description	Value
Position	{0, 0, 0}

Axis

Description	Value
Axis type	z - axis
Layers	

Size and shape

Description	Value
Radius	100
Height	100

2.2.3 soln_sph (sph1)

Position

Description	Value
Position	{0, 0, 0}

Axis

Description	Value
Axis type	z - axis
Layers	

Size

Description	Value
Radius	solnSize

2.2.4 solninner_sph (sph2)

Position

Description	Value
Position	{0, 0, 0}

Axis

Description	Value
Axis type	z - axis
Layers	

Size

Description	Value
Radius	200

2.2.5 solninner_sph 1 (sph3)

Position

Description	Value
Position	{0, 0, 0}

Axis

Description	Value
Axis type	z - axis
Layers	

Size

Description	Value
Radius	200

2.2.6 base (blk2)

Position

Description	Value
Position	{-solnSize, -solnSize, -solnSize}

Axis

Description	Value
Axis type	z - axis

Size and shape

Description	Value
Width	2*solnSize
Depth	2*solnSize
Height	solnSize

Layers

Description	Value
Layers	

2.2.7 top (blk3)

Position

Description	Value
Position	{-solnSize, -solnSize, solnSize-10}

Axis

Description	Value
Axis type	z - axis

Size and shape

Description	Value
Width	solnSize*2
Depth	solnSize*2
Height	20

Layers

Description	Value
Layers	

2.2.8 elecGlass (cyl2)**Position**

Description	Value
Position	{elecX, 0, elecZ + cellZ}

Axis

Description	Value
Axis type	z - axis
Layers	

Size and shape

Description	Value
Radius	elecGlass
Height	solnSize-(elecZ + cellZ)

2.2.9 cell (elp1)**Position**

Description	Value
Position	{0, 0, 0}

Description	Value
Axis type	z - axis
Layers	

Description	Value
a-semiaxis	cellX
b-semiaxis	cellY
c-semiaxis	cellZ

Axis**Size**

Description	Value

2.2.10 Work Plane 1 (wp1)**Unite objects**

Description	Value
Unite objects	On

7.2.1.2 Plane Geometry (wp1)**7.2.1.2.1 elecPt (c1)****Position**

Description	Value
Position	{elecX, 0}
Layers	

Size and shape

Description	Value
Radius	elecPt

2.2.11 Block 1 (blk1)**Position**

Description	Value
Position	{-solnSize, 0, 0}

Axis

Description	Value
Axis type	z - axis

Size and shape

Description	Value
Width	solnSize*2
Depth	solnSize
Height	solnSize

Layers

Description	Value
Layers	

2.3 Transport of Diluted Species

Used products

COMSOL Multiphysics

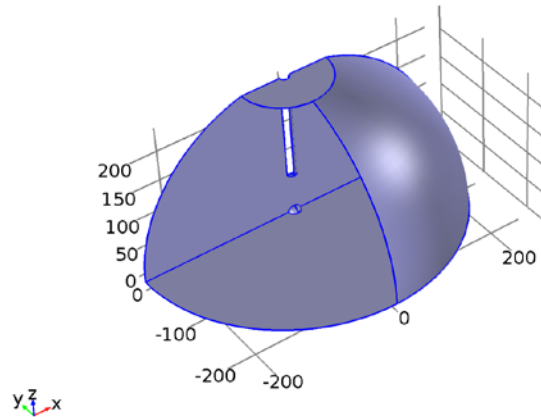


Figure 2.

Figure 3. Transport of Diluted Species

Selection

Geometric entity level	Domain
Selection	Domain 1

Equations

$$\nabla \cdot (-D_i \nabla C_i) + \mathbf{u} \cdot \nabla C_i = R_i$$

$$\mathbf{N}_i = -D_i \nabla C_i + \mathbf{u} C_i$$

Settings

Description	Value
Concentration	Linear
Compute boundary fluxes	On
Apply smoothing to boundary fluxes	On
Value type when using splitting of complex variables	Real
Adsorption in porous media	Off
Dispersion in porous media	Off
Volatilization in partially saturated porous media	Off
Convection	On
Migration in electric field	Off
Streamline diffusion	On
Crosswind diffusion	On
Crosswind diffusion type for free flow	Do Carmo and Galeão
Equation residual	Approximate residual
Isotropic diffusion	Off
Convective term	Non - conservative form

Variables

Name	Expression	Unit	Description	Selection
domflux.FcMeOHx	tds.dflux_FcMeOHx	mol/(m ² *s)	Domain flux, x component	Domain 1
domflux.FcMeOHy	tds.dflux_FcMeOHy	mol/(m ² *s)	Domain flux, y component	Domain 1
domflux.FcMeOHz	tds.dflux_FcMeOHz	mol/(m ² *s)	Domain flux, z component	Domain 1
tds.R_FcMeOH	0	mol/(m ³ *s)	Total rate expression	Domain 1
tds.epsilon_p	1	1	Porosity	Domain 1
tds.theta	tds.epsilon_p	1	Liquid volume fraction	Domain 1
tds.av	0	1	Gas volume fraction	Domain 1
tds.nx	dnx	1	Normal vector, x component	Boundaries 1–11
tds.ny	dny	1	Normal vector, y component	Boundaries 1–11
tds.nz	dnz	1	Normal vector, z component	Boundaries 1–11
tds.nxmesh	root.dnxmesh	1	Normal vector (mesh), x component	Boundaries 1–11
tds.nymesh	root.dnymesh	1	Normal vector (mesh), y component	Boundaries 1–11
tds.nzmesh	root.dnzmesh	1	Normal vector (mesh), z component	Boundaries 1–11
tds.nxc	root.nxc/sqrt(root.nxc ² +root.nyc ² +root.nzc ² +eps)	1	Normal vector, x component	Boundaries 1–11
tds.nyc	root.nyc/sqrt(root.nxc ² +root.nyc ² +root.nzc ² +eps)	1	Normal vector, y component	Boundaries 1–11
tds.nzc	root.nzc/sqrt(root.nxc ² +root.nyc ² +root.nzc ² +eps)	1	Normal vector, z component	Boundaries 1–11
tds.ndflux_FcMeOH	tds.bndFlux_FcMeOH	mol/(m ² *s)	Normal diffusive flux	Boundaries 1–11
tds.ncflux_FcMeOH	tds.cflux_FcMeOHx*tds.nxc+tds.cflux_FcMeOHy*tds.nyc+tds.cflux_FcMeOHz*tds.nzc	mol/(m ² *s)	Normal convective flux	Boundaries 1–11
tds.ntflux_FcMeOH	tds.bndFlux_FcMeOH+tds.cflux_FcMeOHx*tds.nxc+tds.cflux_FcMeOHy*tds.nyc+tds.cflux_FcMeOHz*tds.nzc	mol/(m ² *s)	Normal total flux	Boundaries 1–11
tds.bndFlux_FcMeOH	-dflux_spatial(FcMeOH)	mol/(m ² *s)	Boundary flux	Boundaries 1–11

2.3.1 Transport Properties 1

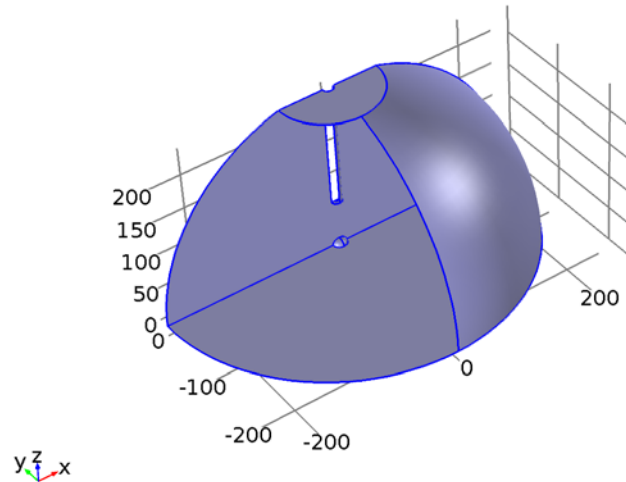


Figure 4. Transport Properties 1

Selection

Geometric entity level	Domain
Selection	Domain 1

Equations

$$\nabla \cdot (-D_i \nabla c_i) + \mathbf{u} \cdot \nabla c_i = R_i$$

$$\mathbf{N}_i = -D_i \nabla c_i + \mathbf{u} c_i$$

Settings

Description	Value
Velocity field	User defined
Velocity field	{0, 0, 0}
Material	None
Diffusion coefficient	User defined
Diffusion coefficient	{{D, 0, 0}, {0, D, 0}, {0, 0, D}}

7.2.1.3 Variables

Name	Expression	Unit	Description	Selection
tds.cbf_FcMeOH	0	mol/(m ² *s)	Convective boundary flux	Boundaries 1–11
tds.D_FcMeOHx x	D	m ² /s	Diffusion coefficient, xx component	Domain 1
tds.D_FcMeOHx y	0	m ² /s	Diffusion coefficient, yx component	Domain 1
tds.D_FcMeOHx z	0	m ² /s	Diffusion coefficient, zx component	Domain 1
tds.D_FcMeOHx y	0	m ² /s	Diffusion coefficient, xy	Domain 1

Name	Expression	Unit	Description	Selection
			component	
tds.D_FcMeOHyy	D	m ² /s	Diffusion coefficient, yy component	Domain 1
tds.D_FcMeOHzy	0	m ² /s	Diffusion coefficient, zy component	Domain 1
tds.D_FcMeOHxz	0	m ² /s	Diffusion coefficient, xz component	Domain 1
tds.D_FcMeOHyz	0	m ² /s	Diffusion coefficient, yz component	Domain 1
tds.D_FcMeOHzz	D	m ² /s	Diffusion coefficient, zz component	Domain 1
tds.Dav_FcMeOH	(tds.D_FcMeOHxx+tds.D_FcMeOHyy+tds.D_FcMeOHzz)/3	m ² /s	Average diffusion coefficient	Domain 1
tds.tflux_FcMeOHx	tds.dflux_FcMeOHx+tds.cflux_FcMeOHx	mol/(m ² *s)	Total flux, x component	Domain 1
tds.tflux_FcMeOHy	tds.dflux_FcMeOHy+tds.cflux_FcMeOHy	mol/(m ² *s)	Total flux, y component	Domain 1
tds.tflux_FcMeOHz	tds.dflux_FcMeOHz+tds.cflux_FcMeOHz	mol/(m ² *s)	Total flux, z component	Domain 1
tds.dfluxMag_FcMeOH	sqrt(tds.dflux_FcMeOHx ² +tds.dflux_FcMeOHy ² +tds.dflux_FcMeOHz ²)	mol/(m ² *s)	Diffusive flux magnitude	Domain 1
tds.tfluxMag_FcMeOH	sqrt(tds.tflux_FcMeOHx ² +tds.tflux_FcMeOHy ² +tds.tflux_FcMeOHz ²)	mol/(m ² *s)	Total flux magnitude	Domain 1
tds.dflux_FcMeOHx	-tds.D_FcMeOHxx*FcMeOHx-tds.D_FcMeOHxy*FcMeOHy-tds.D_FcMeOHxz*FcMeOHz	mol/(m ² *s)	Diffusive flux, x component	Domain 1
tds.dflux_FcMeOHy	-tds.D_FcMeOHyx*FcMeOHx-tds.D_FcMeOHyy*FcMeOHy-tds.D_FcMeOHyz*FcMeOHz	mol/(m ² *s)	Diffusive flux, y component	Domain 1
tds.dflux_FcMeOHz	-tds.D_FcMeOHzx*FcMeOHx-tds.D_FcMeOHzy*FcMeOHy-tds.D_FcMeOHzz*FcMeOHz	mol/(m ² *s)	Diffusive flux, z component	Domain 1
tds.grad_FcMeOHx	FcMeOHx	mol/m ⁴	Concentration gradient, x component	Domain 1
tds.grad_FcMeOHy	FcMeOHy	mol/m ⁴	Concentration gradient, y component	Domain 1
tds.grad_FcMeOHz	FcMeOHz	mol/m ⁴	Concentration gradient, z component	Domain 1
tds.u	model.input.u1	m/s	Velocity field, x component	Domain 1
tds.v	model.input.u2	m/s	Velocity field, y component	Domain 1

Name	Expression	Unit	Description	Selection
			component	
tds.w	model.input.u3	m/s	Velocity field, z component	Domain 1
tds.cflux_FcMeOHx	FcMeOH*model.input.u1	mol/(m ² *s)	Convective flux, x component	Domain 1
tds.cflux_FcMeOHy	FcMeOH*model.input.u2	mol/(m ² *s)	Convective flux, y component	Domain 1
tds.cflux_FcMeOHz	FcMeOH*model.input.u3	mol/(m ² *s)	Convective flux, z component	Domain 1
tds.cfluxMag_FcMeOH	sqrt(tds.cflux_FcMeOHx ² +tds.cflux_FcMeOHy ² +tds.cflux_FcMeOHz ²)	mol/(m ² *s)	Convective flux magnitude	Domain 1
tds.Res_FcMeOH	tds.u*FcMeOHx+tds.v*FcMeOHy+tds.w*FcMeOHz-tds.R_FcMeOH	mol/(m ³ *s)	Equation residual	Domain 1

7.2.1.4 Shape functions

Name	Shape function	Unit	Description	Shape frame	Selection
FcMeOH	Lagrange (Linear)	mol/m ³	Concentration	Material	Domain 1

7.2.1.5 Weak expressions

Weak expression	Integration frame	Selection
- FcMeOHt*test(FcMeOH)+tds.dflux_FcMeOHx*test(FcMeOHx)+tds.dflux_FcMeOHy*test(FcMeOHy)+tds.dflux_FcMeOHz*test(FcMeOHz)	Material	Domain 1
- (tds.u*FcMeOHx+tds.v*FcMeOHy+tds.w*FcMeOHz)*test(FcMeOH)*(isScalingSystemDomain==0)	Material	Domain 1
tds.cbf_FcMeOH*test(FcMeOH)	Material	Boundaries 1–11
tds.streamline*(isScalingSystemDomain==0)	Material	Domain 1
tds.crosswind*(isScalingSystemDomain==0)	Material	Domain 1

2.3.2 No Flux 1

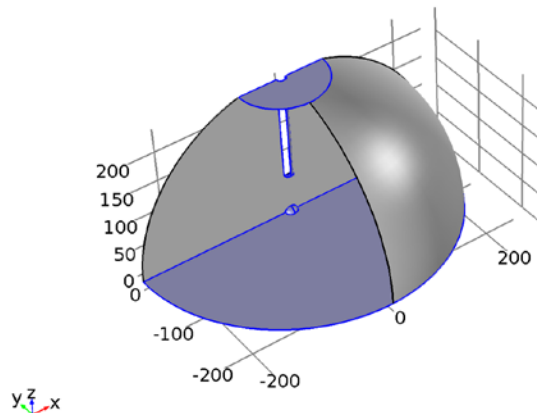


Figure 5. No Flux 1

Selection

Geometric entity level	Boundary
Selection	Boundaries 3–7, 10–11

Equations

$$-\mathbf{n} \cdot \mathbf{N}_i = 0$$

7.2.1.6 Variables

Name	Expression	Unit	Description	Selection
tds.cbf_Fc MeOH	$Fc_{\text{MeOH}} * (t_{\text{ds}}.u * t_{\text{ds}}.n_{\text{xmesh}} + t_{\text{ds}}.v * t_{\text{ds}}.n_{\text{ymesh}} + t_{\text{ds}}.w * t_{\text{ds}}.n_{\text{zmesh}})$	mol/(m ² *s)	Convective boundary flux	Boundaries 3–7, 10–11

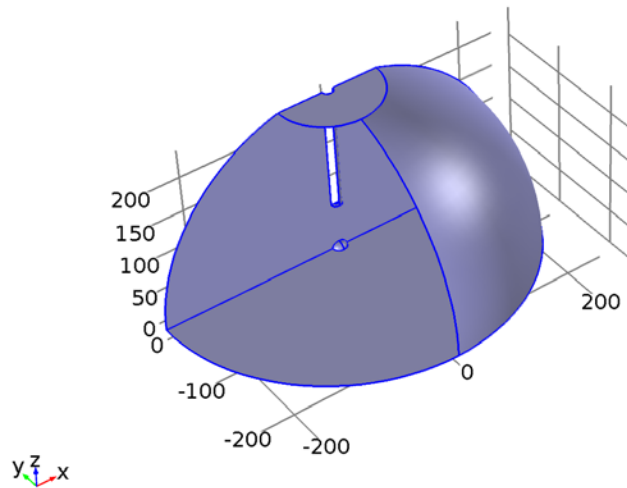
2.3.3 Initial Values 1

Figure 6. Initial Values 1

Selection

Geometric entity level	Domain
Selection	Domain 1

Settings

Description	Value
Concentration	initC

2.3.4 Symmetry 1

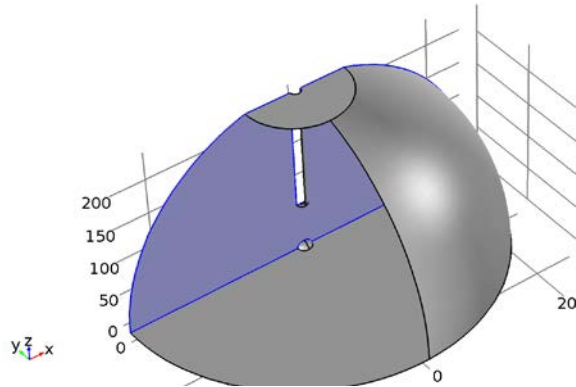


Figure 7. Symmetry 1

Selection

Geometric entity level	Boundary
Selection	Boundary 1

Equations

$$-n \cdot N_i = 0$$

7.2.1.7 Variables

Name	Expression	Unit	Description	Selection
tds.cbf_Fc MeOH	FcMeOH*(tds.u*tds.nxmesh+tds.v*tds.ny ymesh+tds.w*tds.nzmesh)	mol/(m ² *s)	Convective boundary flux	Boundary 1

2.3.5 Concentration 1

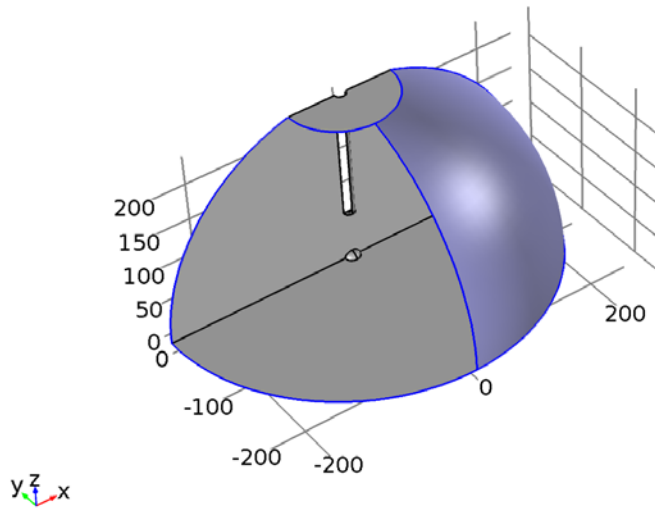


Figure 8. Concentration 1

Selection

Geometric entity level	Boundary
Selection	Boundaries 2, 9

Equations

$$c_i = c_{0,i}$$

Settings

Description	Value
Species FcMeOH	On
Concentration	initC
Apply reaction terms on	All physics (symmetric)
Use weak constraints	Off
Constraint method	Elemental

7.2.1.8 Variables

Name	Expression	Unit	Description	Selection
tds.c0_FcMeOH	initC	mol/m ³	Concentration	Boundaries 2, 9

7.2.1.9 Shape functions

Constraint	Constraint force	Shape function	Selection
-FcMeOH+tds.c0_FcMeOH	test(-FcMeOH+tds.c0_FcMeOH)	Lagrange (Linear)	Boundaries 2, 9

2.3.6 Concentration 2

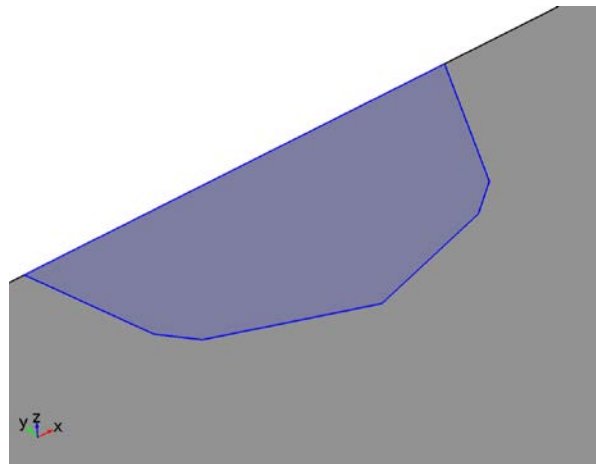


Figure 9. Concentration 2

Selection

Geometric entity level	Boundary
Selection	Boundary 8

Equations

$$c_i = c_{0,i}$$

Settings

Description	Value
Species FcMeOH	On
Concentration	0
Apply reaction terms on	All physics (symmetric)
Use weak constraints	Off
Constraint method	Elemental

7.2.1.10 Variables

Name	Expression	Unit	Description	Selection
tds.c0_FcMeOH	0	mol/m ³	Concentration	Boundary 8

7.2.1.11 Shape functions

Constraint	Constraint force	Shape function	Selection
-FcMeOH+tds.c0_FcMeOH	test(- FcMeOH+tds.c0_FcMeOH)	Lagrange (Linear)	Boundary 8

2.4 Mesh 1

Mesh statistics

Description	Value
Minimum element quality	0.1468
Average element quality	0.7626
Tetrahedral elements	227013
Triangular elements	14106
Edge elements	625
Vertex elements	19

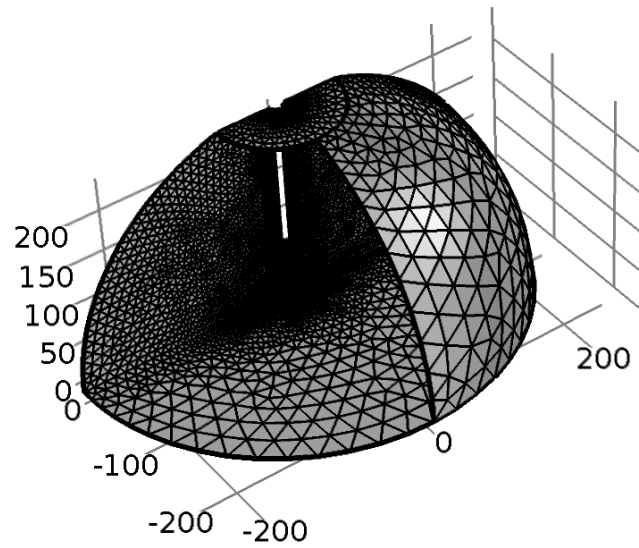


Figure 10. Mesh 1

2.4.1 Size (size)

Settings

Description	Value
Maximum element size	50
Curvature factor	0.4
Resolution of narrow regions	0.4
Maximum element growth rate	1.15
Custom element size	Custom

2.4.2 Scale 1 (sca1)

Selection

Geometric entity level	Boundary
Selection	Boundary 8

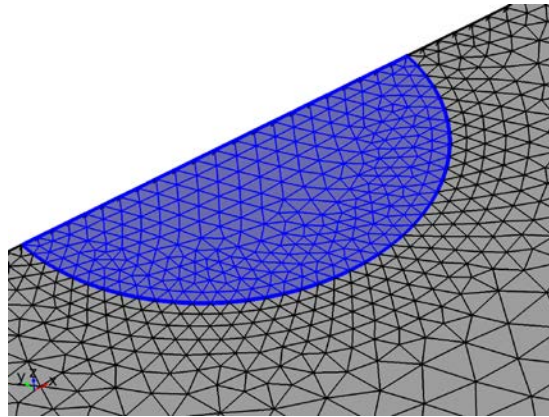


Figure 11.

Figure 12. Scale 1

Settings

Description	Value
Element size scale	0.2

Scale 2 (sca2)**Selection**

Geometric entity level	Boundary
Selection	Boundaries 5, 10

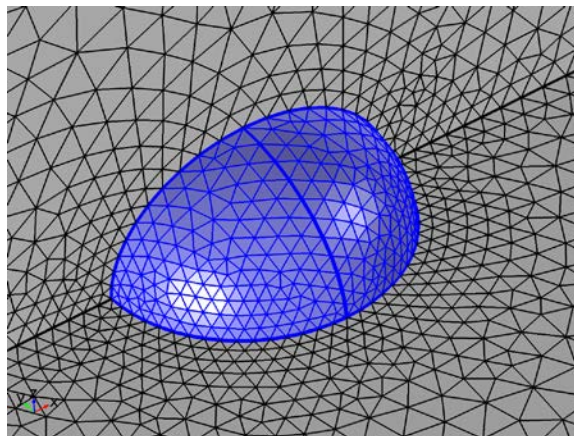


Figure 13. Scale 2

Settings

Description	Value
Element size scale	0.4

2.4.3 Free Tetrahedral 2 (ftet2)**Selection**

Geometric entity level	Domain
Selection	Remaining

3 Study 1

3.1 Parametric Sweep

Parameter name	Parameter value list
elecZ	range(5,-0.5,0.5)
elecX	range(0,0.5,40)

3.2 Stationary

Study settings

Description	Value
Include geometric nonlinearity	Off

Physics and variables selection

Physics interface	Discretization
Transport of Diluted Species (tds)	physics

Mesh selection

Geometry	Mesh
Geometry 1 (geom1)	mesh1

3.3 Solver Configurations

3.3.1 Solution 1

7.2.1.12 Compile Equations: Stationary (st1)

Study and step

Description	Value
Use study	Study 1
Use study step	Stationary

7.2.1.13 Dependent Variables 1 (v1)

General

Description	Value
Defined by study step	Stationary

Initial values of variables solved for

Description	Value
Solution	Zero

Values of variables not solved for

Description	Value
Solution	Zero

7.2.1.13.1 Concentration (comp1.FcMeOH) (comp1_FcMeOH)

General

Description	Value
Field components	comp1.FcMeOH

7.2.1.14 Stationary Solver 1 (s1)

General

Description	Value
Defined by study step	Stationary

Results while solving

Description	Value
Probes	None

4 Results

4.1 Data Sets

4.1.1 Study 1/Solution 1

Solution

Description	Value
Solution	Solution 1
Component	Save Point Geometry 1

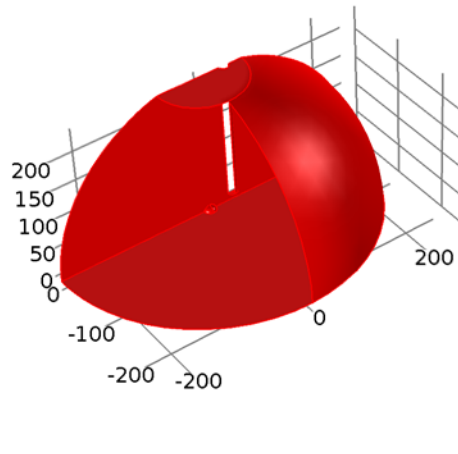


Figure 14. Data set: Study 1/Solution 1

4.1.2 Study 1/Parametric Solutions 1

Solution

Description	Value
Solution	Parametric Solutions 1
Component	Save Point Geometry 1

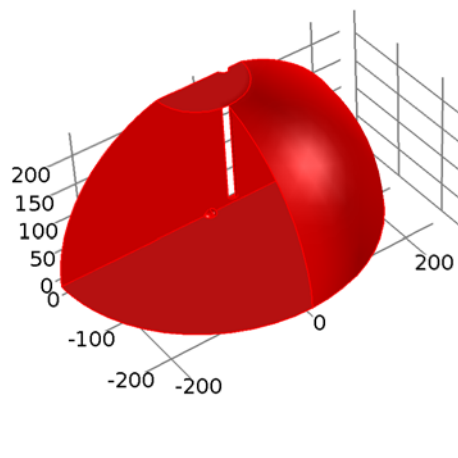


Figure 15. Data set: Study 1/Parametric Solutions 1

4.2 Derived Values

Surface Integration 1

Selection

Geometric entity level	Boundary
Selection	Boundary 10

Data

Description	Value
Data set	Study 1/Parametric Solutions 1

Expression

Description	Value
Expression	$\text{tds.ndflux_FcMeOH} \cdot F \cdot n \cdot 2$
Unit	A
Description	$\text{tds.ndflux_FcMeOH} \cdot F \cdot n \cdot 2$

4.3 Plot Groups

4.3.1 Concentration (tds)

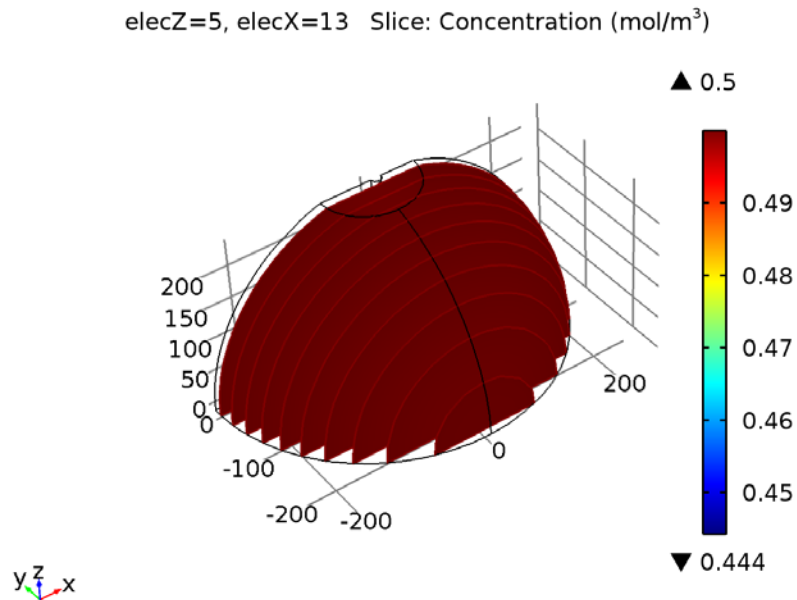


Figure 16. elecZ=5, elecX=13 Slice: Concentration (mol/m³)

4.3.2 Concentration (tds) 1

elecZ=5, elecX=13 Surface: Concentration (mol/m³)

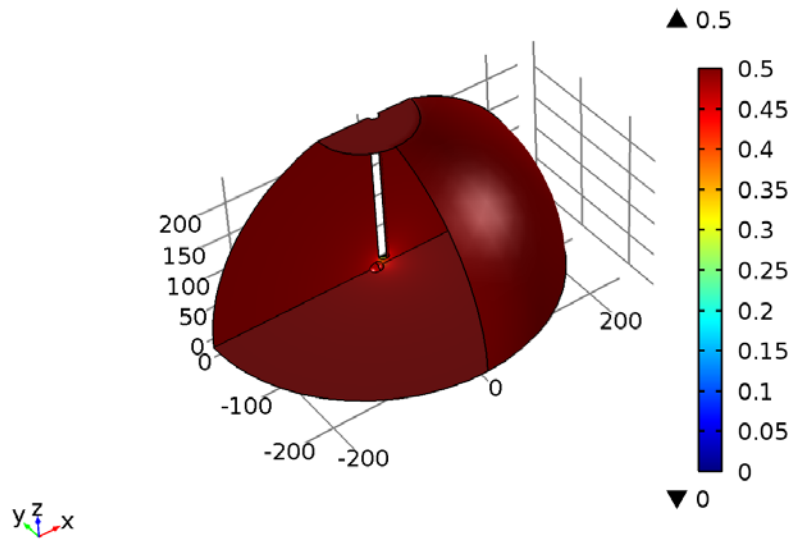


Figure 17. elecZ=5, elecX=13 Surface: Concentration (mol/m³)

Figure 18.

4.3.3 Concentration (tds) 2

Slice: Concentration (mol/m³)

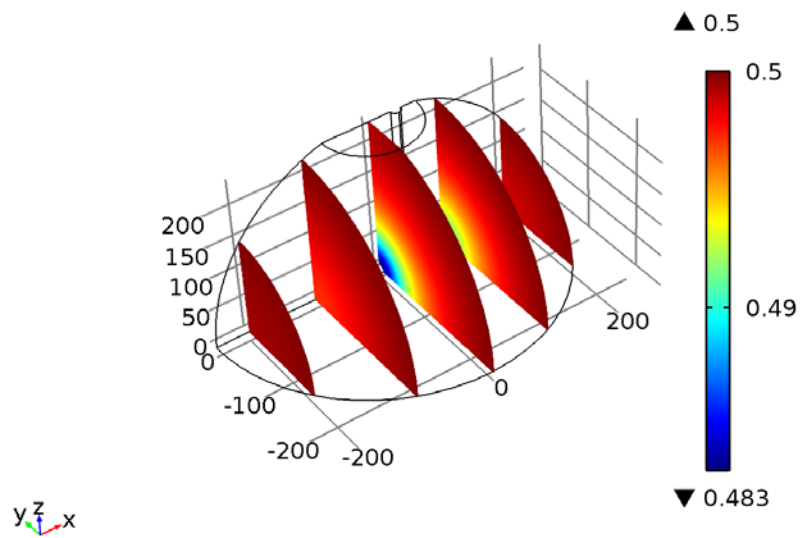
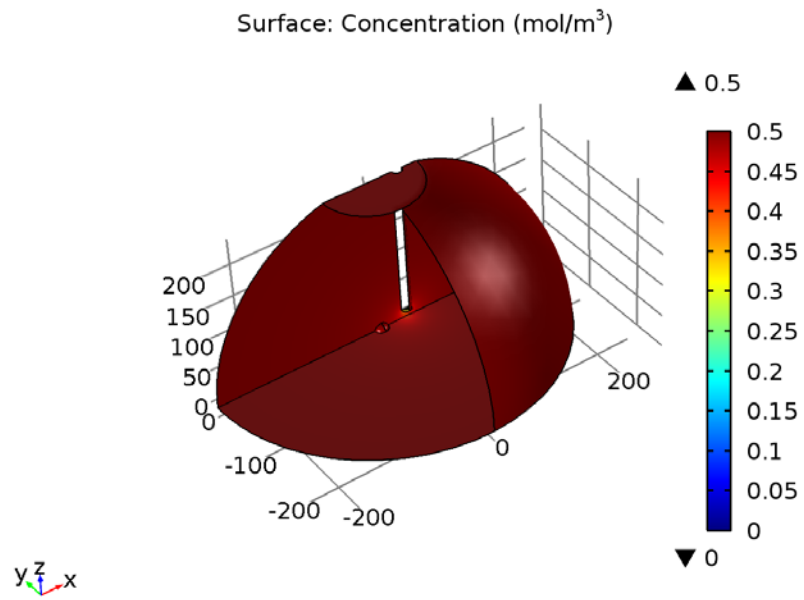


Figure 19. Slice: Concentration (mol/m³)

4.3.4 Concentration (tds) 3

Figure 20. Surface: Concentration (mol/m³)

6/28/2017

RightsLink Printable License

**ELSEVIER LICENSE
TERMS AND CONDITIONS**

Jun 28, 2017

This Agreement between Michelle Li ("You") and Elsevier ("Elsevier") consists of your license details and the terms and conditions provided by Elsevier and Copyright Clearance Center.

License Number	4137811075631
License date	Jun 28, 2017
Licensed Content Publisher	Elsevier
Licensed Content Publication	Journal of Electroanalytical Chemistry
Licensed Content Title	Determining live cell topography by scanning electrochemical microscopy
Licensed Content Author	Michelle S.M. Li, Fraser P. Filice, Zhifeng Ding
Licensed Content Date	Oct 15, 2016
Licensed Content Volume	779
Licensed Content Issue	n/a
Licensed Content Pages	11
Start Page	176
End Page	186
Type of Use	reuse in a thesis/dissertation
Intended publisher of new work	other
Portion	full article
Format	both print and electronic
Are you the author of this Elsevier article?	Yes
Will you be translating?	No
Order reference number	
Title of your thesis/dissertation	Scanning Electrochemical Microscopy of Single Live Human Bladder Cancer Cells
Expected completion date	Sep 2017
Estimated size (number of pages)	200
Elsevier VAT number	GB 494 6272 12
Requestor Location	Michelle Li Western University 1151 Richmond Street Department of Chemistry London, ON N6A5B7 Canada Attn: Michelle Li
Total	0.00 USD
Terms and Conditions	

<https://s100.copyright.com/AppDispatchServlet>

1/6

INTRODUCTION

1. The publisher for this copyrighted material is Elsevier. By clicking "accept" in connection with completing this licensing transaction, you agree that the following terms and conditions apply to this transaction (along with the Billing and Payment terms and conditions established by Copyright Clearance Center, Inc. ("CCC"), at the time that you opened your Rightslink account and that are available at any time at <http://myaccount.copyright.com>).

GENERAL TERMS

2. Elsevier hereby grants you permission to reproduce the aforementioned material subject to the terms and conditions indicated.

3. Acknowledgement: If any part of the material to be used (for example, figures) has appeared in our publication with credit or acknowledgement to another source, permission must also be sought from that source. If such permission is not obtained then that material may not be included in your publication/copies. Suitable acknowledgement to the source must be made, either as a footnote or in a reference list at the end of your publication, as follows:

"Reprinted from Publication title, Vol /edition number, Author(s), Title of article / title of chapter, Pages No., Copyright (Year), with permission from Elsevier [OR APPLICABLE SOCIETY COPYRIGHT OWNER]." Also Lancet special credit - "Reprinted from The Lancet, Vol. number, Author(s), Title of article, Pages No., Copyright (Year), with permission from Elsevier."

4. Reproduction of this material is confined to the purpose and/or media for which permission is hereby given.

5. Altering/Modifying Material: Not Permitted. However figures and illustrations may be altered/adapted minimally to serve your work. Any other abbreviations, additions, deletions and/or any other alterations shall be made only with prior written authorization of Elsevier Ltd. (Please contact Elsevier at permissions@elsevier.com). No modifications can be made to any Lancet figures/tables and they must be reproduced in full.

6. If the permission fee for the requested use of our material is waived in this instance, please be advised that your future requests for Elsevier materials may attract a fee.

7. Reservation of Rights: Publisher reserves all rights not specifically granted in the combination of (i) the license details provided by you and accepted in the course of this licensing transaction, (ii) these terms and conditions and (iii) CCC's Billing and Payment terms and conditions.

8. License Contingent Upon Payment: While you may exercise the rights licensed immediately upon issuance of the license at the end of the licensing process for the transaction, provided that you have disclosed complete and accurate details of your proposed use, no license is finally effective unless and until full payment is received from you (either by publisher or by CCC) as provided in CCC's Billing and Payment terms and conditions. If full payment is not received on a timely basis, then any license preliminarily granted shall be deemed automatically revoked and shall be void as if never granted. Further, in the event that you breach any of these terms and conditions or any of CCC's Billing and Payment terms and conditions, the license is automatically revoked and shall be void as if never granted. Use of materials as described in a revoked license, as well as any use of the materials beyond the scope of an unrevoked license, may constitute copyright infringement and publisher reserves the right to take any and all action to protect its copyright in the materials.

9. Warranties: Publisher makes no representations or warranties with respect to the licensed material.

10. Indemnity: You hereby indemnify and agree to hold harmless publisher and CCC, and their respective officers, directors, employees and agents, from and against any and all claims arising out of your use of the licensed material other than as specifically authorized pursuant to this license.

11. No Transfer of License: This license is personal to you and may not be sublicensed, assigned, or transferred by you to any other person without publisher's written permission.

12. **No Amendment Except in Writing:** This license may not be amended except in a writing signed by both parties (or, in the case of publisher, by CCC on publisher's behalf).

13. **Objection to Contrary Terms:** Publisher hereby objects to any terms contained in any purchase order, acknowledgment, check endorsement or other writing prepared by you, which terms are inconsistent with these terms and conditions or CCC's Billing and Payment terms and conditions. These terms and conditions, together with CCC's Billing and Payment terms and conditions (which are incorporated herein), comprise the entire agreement between you and publisher (and CCC) concerning this licensing transaction. In the event of any conflict between your obligations established by these terms and conditions and those established by CCC's Billing and Payment terms and conditions, these terms and conditions shall control.

14. **Revocation:** Elsevier or Copyright Clearance Center may deny the permissions described in this License at their sole discretion, for any reason or no reason, with a full refund payable to you. Notice of such denial will be made using the contact information provided by you. Failure to receive such notice will not alter or invalidate the denial. In no event will Elsevier or Copyright Clearance Center be responsible or liable for any costs, expenses or damage incurred by you as a result of a denial of your permission request, other than a refund of the amount(s) paid by you to Elsevier and/or Copyright Clearance Center for denied permissions.

LIMITED LICENSE

The following terms and conditions apply only to specific license types:

15. **Translation:** This permission is granted for non-exclusive world **English** rights only unless your license was granted for translation rights. If you licensed translation rights you may only translate this content into the languages you requested. A professional translator must perform all translations and reproduce the content word for word preserving the integrity of the article.

16. **Posting licensed content on any Website:** The following terms and conditions apply as follows: Licensing material from an Elsevier journal: All content posted to the web site must maintain the copyright information line on the bottom of each image; A hyper-text must be included to the Homepage of the journal from which you are licensing at <http://www.sciencedirect.com/science/journal/xxxx> or the Elsevier homepage for books at <http://www.elsevier.com>; Central Storage: This license does not include permission for a scanned version of the material to be stored in a central repository such as that provided by Heron/XanEdu.

Licensing material from an Elsevier book: A hyper-text link must be included to the Elsevier homepage at <http://www.elsevier.com>. All content posted to the web site must maintain the copyright information line on the bottom of each image.

Posting licensed content on Electronic reserve: In addition to the above the following clauses are applicable: The web site must be password-protected and made available only to bona fide students registered on a relevant course. This permission is granted for 1 year only. You may obtain a new license for future website posting.

17. **For journal authors:** the following clauses are applicable in addition to the above:

Preprints:

A preprint is an author's own write-up of research results and analysis, it has not been peer-reviewed, nor has it had any other value added to it by a publisher (such as formatting, copyright, technical enhancement etc.).

Authors can share their preprints anywhere at any time. Preprints should not be added to or enhanced in any way in order to appear more like, or to substitute for, the final versions of articles however authors can update their preprints on arXiv or RePEc with their Accepted Author Manuscript (see below).

If accepted for publication, we encourage authors to link from the preprint to their formal publication via its DOI. Millions of researchers have access to the formal publications on ScienceDirect, and so links will help users to find, access, cite and use the best available

version. Please note that Cell Press, The Lancet and some society-owned have different preprint policies. Information on these policies is available on the journal homepage.

Accepted Author Manuscripts: An accepted author manuscript is the manuscript of an article that has been accepted for publication and which typically includes author-incorporated changes suggested during submission, peer review and editor-author communications.

Authors can share their accepted author manuscript:

- immediately
 - via their non-commercial person homepage or blog
 - by updating a preprint in arXiv or RePEc with the accepted manuscript
 - via their research institute or institutional repository for internal institutional uses or as part of an invitation-only research collaboration work-group
 - directly by providing copies to their students or to research collaborators for their personal use
 - for private scholarly sharing as part of an invitation-only work group on commercial sites with which Elsevier has an agreement
- After the embargo period
 - via non-commercial hosting platforms such as their institutional repository
 - via commercial sites with which Elsevier has an agreement

In all cases accepted manuscripts should:

- link to the formal publication via its DOI
- bear a CC-BY-NC-ND license - this is easy to do
- if aggregated with other manuscripts, for example in a repository or other site, be shared in alignment with our hosting policy not be added to or enhanced in any way to appear more like, or to substitute for, the published journal article.

Published journal article (JPA): A published journal article (PJA) is the definitive final record of published research that appears or will appear in the journal and embodies all value-adding publishing activities including peer review co-ordination, copy-editing, formatting, (if relevant) pagination and online enrichment.

Policies for sharing publishing journal articles differ for subscription and gold open access articles:

Subscription Articles: If you are an author, please share a link to your article rather than the full-text. Millions of researchers have access to the formal publications on ScienceDirect, and so links will help your users to find, access, cite, and use the best available version. Theses and dissertations which contain embedded PJAs as part of the formal submission can be posted publicly by the awarding institution with DOI links back to the formal publications on ScienceDirect.

If you are affiliated with a library that subscribes to ScienceDirect you have additional private sharing rights for others' research accessed under that agreement. This includes use for classroom teaching and internal training at the institution (including use in course packs and courseware programs), and inclusion of the article for grant funding purposes.

Gold Open Access Articles: May be shared according to the author-selected end-user license and should contain a [CrossMark logo](#), the end user license, and a DOI link to the formal publication on ScienceDirect.

Please refer to Elsevier's [posting policy](#) for further information.

18. **For book authors** the following clauses are applicable in addition to the above:

Authors are permitted to place a brief summary of their work online only. You are not allowed to download and post the published electronic version of your chapter, nor may you scan the printed edition to create an electronic version. **Posting to a repository:** Authors are permitted to post a summary of their chapter only in their institution's repository.

19. Thesis/Dissertation: If your license is for use in a thesis/dissertation your thesis may be submitted to your institution in either print or electronic form. Should your thesis be published commercially, please reapply for permission. These requirements include permission for the Library and Archives of Canada to supply single copies, on demand, of the complete thesis and include permission for Proquest/UMI to supply single copies, on demand, of the complete thesis. Should your thesis be published commercially, please reapply for permission. Theses and dissertations which contain embedded PJAs as part of the formal submission can be posted publicly by the awarding institution with DOI links back to the formal publications on ScienceDirect.

Elsevier Open Access Terms and Conditions

You can publish open access with Elsevier in hundreds of open access journals or in nearly 2000 established subscription journals that support open access publishing. Permitted third party re-use of these open access articles is defined by the author's choice of Creative Commons user license. See our [open access license policy](#) for more information.

Terms & Conditions applicable to all Open Access articles published with Elsevier:

Any reuse of the article must not represent the author as endorsing the adaptation of the article nor should the article be modified in such a way as to damage the author's honour or reputation. If any changes have been made, such changes must be clearly indicated.

The author(s) must be appropriately credited and we ask that you include the end user license and a DOI link to the formal publication on ScienceDirect.

If any part of the material to be used (for example, figures) has appeared in our publication with credit or acknowledgement to another source it is the responsibility of the user to ensure their reuse complies with the terms and conditions determined by the rights holder.

Additional Terms & Conditions applicable to each Creative Commons user license:

CC BY: The CC-BY license allows users to copy, to create extracts, abstracts and new works from the Article, to alter and revise the Article and to make commercial use of the Article (including reuse and/or resale of the Article by commercial entities), provided the user gives appropriate credit (with a link to the formal publication through the relevant DOI), provides a link to the license, indicates if changes were made and the licensor is not represented as endorsing the use made of the work. The full details of the license are available at <http://creativecommons.org/licenses/by/4.0>.

CC BY NC SA: The CC BY-NC-SA license allows users to copy, to create extracts, abstracts and new works from the Article, to alter and revise the Article, provided this is not done for commercial purposes, and that the user gives appropriate credit (with a link to the formal publication through the relevant DOI), provides a link to the license, indicates if changes were made and the licensor is not represented as endorsing the use made of the work. Further, any new works must be made available on the same conditions. The full details of the license are available at <http://creativecommons.org/licenses/by-nc-sa/4.0>.

CC BY NC ND: The CC BY-NC-ND license allows users to copy and distribute the Article, provided this is not done for commercial purposes and further does not permit distribution of the Article if it is changed or edited in any way, and provided the user gives appropriate credit (with a link to the formal publication through the relevant DOI), provides a link to the license, and that the licensor is not represented as endorsing the use made of the work. The full details of the license are available at <http://creativecommons.org/licenses/by-nc-nd/4.0>. Any commercial reuse of Open Access articles published with a CC BY NC SA or CC BY NC ND license requires permission from Elsevier and will be subject to a fee.

Commercial reuse includes:

- Associating advertising with the full text of the Article
- Charging fees for document delivery or access
- Article aggregation
- Systematic distribution via e-mail lists or share buttons

6/28/2017

RightsLink Printable License

Posting or linking by commercial companies for use by customers of those companies.

20. Other Conditions:

v1.9

Questions? customercare@copyright.com or +1-855-239-3415 (toll free in the US) or +1-978-646-2777.



Appendix III. Chapter 3: A Time Course Study of Cadmium Effect on Membrane Permeability of Single Human Bladder Cancer Cells Using Scanning Electrochemical Microscopy

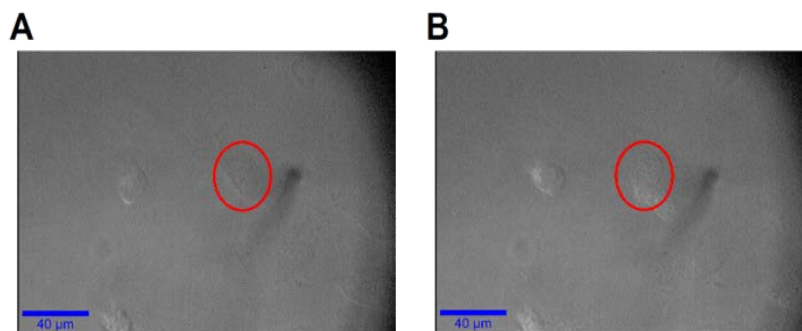
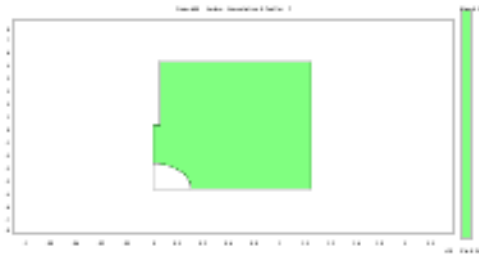


Figure S3.1. Optical micrographs of T24 cells (A) unexposed to Cd^{2+} and (B) exposed to 10 mM Cd^{2+} for 45 min. The nucleus of the studied T24 cell is more easily observable optically after Cd^{2+} treatment (circled).

Membrane Permeability Simulations - COMSOL Model Report



1. Table of Contents

- Title - COMSOL Model Report
- Table of Contents
- Model Properties
- Constants
- Geometry
- Geom1
- Solver Settings
- Postprocessing
- Variables

2. Model Properties

Property	Value
Model name	
Author	
Company	
Department	
Reference	
URL	
Saved date	Sep 29, 2013 9:20:26 PM
Creation date	Sep 26, 2013 4:37:34 PM
COMSOL version	COMSOL 3.5.0.494

File name: G:\SECM P1en4\SECM Eins P1en4 D12.mph

Application modes and modules used in this model:

- Geom1 (Axial symmetry (2D))
 - Diffusion (Chemical Engineering Module)
 - Diffusion (Chemical Engineering Module)

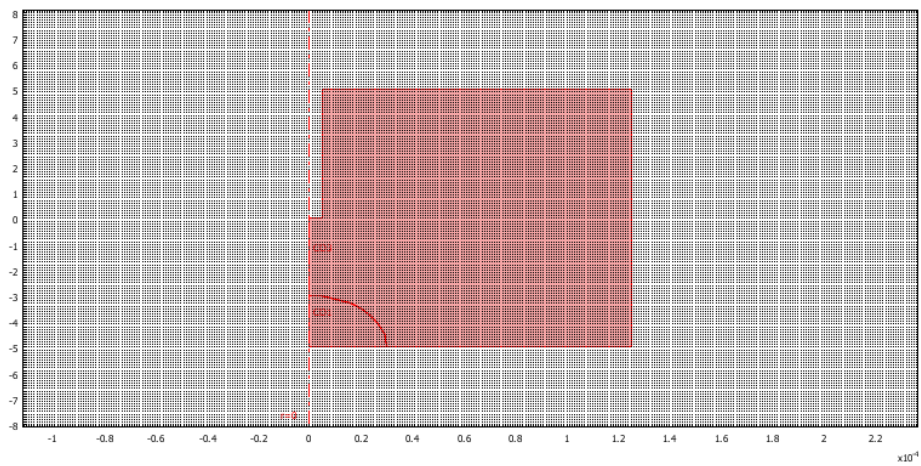
3. Constants

Name	Expression	Value	Description
n	1	1	Number of electrons
F	96485	96485	Faraday's constant
D	7.6e-10	7.6e-10	Diffusion coefficient of FcCH ₂ OH
P	1e-4	1e-4	Cell membrane permeability

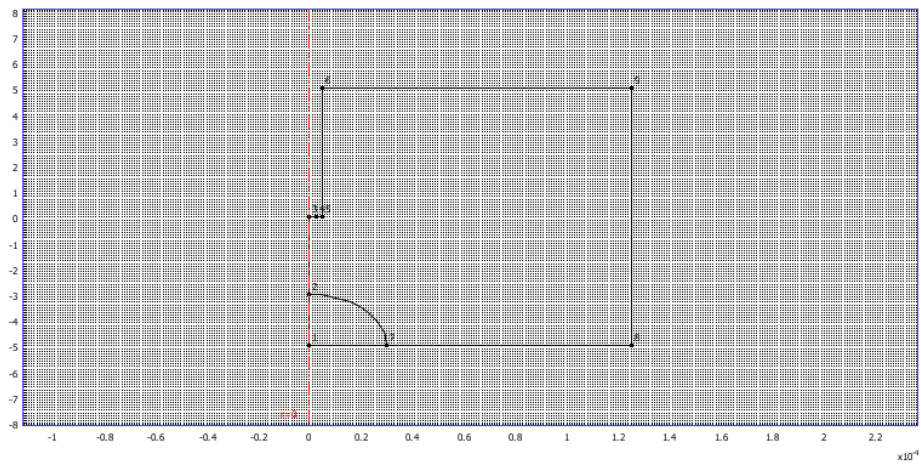
4. Geometry

Number of geometries: 1

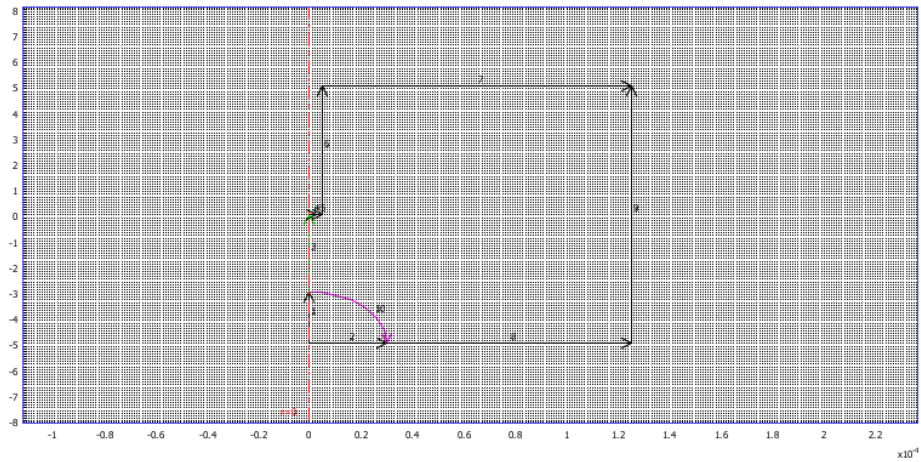
4.1. Geom1



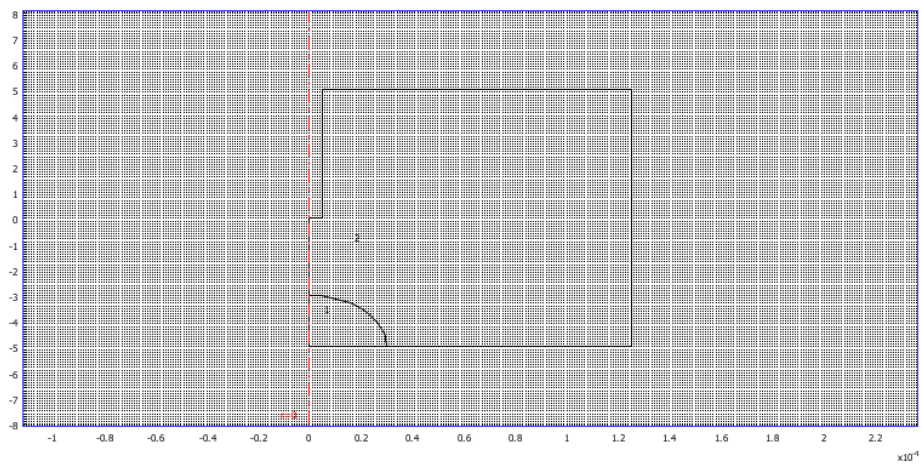
4.1.1. Point mode



4.1.2. Boundary mode



4.1.3. Subdomain mode



5. Geom1

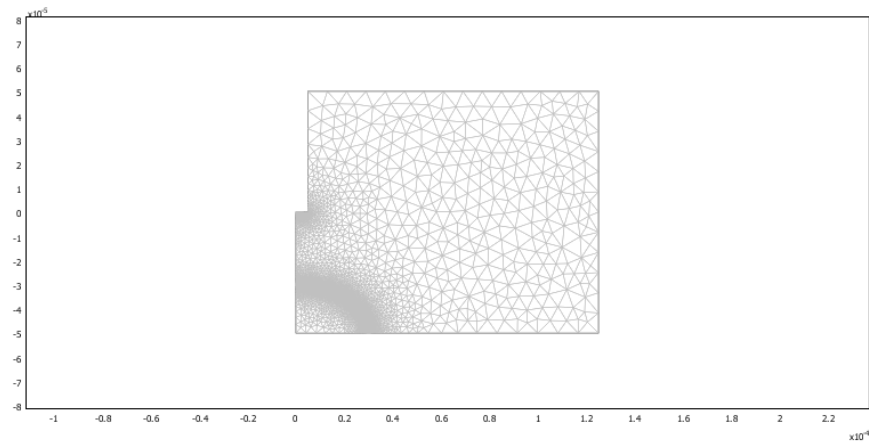
Space dimensions: Axial symmetry (2D)

Independent variables: r , ϕ , z

5.1. Mesh

5.1.1. Mesh Statistics

Number of degrees of freedom	343041
Number of mesh points	83896
Number of elements	167315
Triangular	167315
Quadrilateral	0
Number of boundary elements	4442
Number of vertex elements	9
Minimum element quality	0.668
Element area ratio	0



5.2. Application Mode: Diffusion (chdi)

Application mode type: Diffusion (Chemical Engineering Module)

Application mode name: chdi

5.2.1. Application Mode Properties

Property	Value
Default element type	Lagrange - Quadratic
Analysis type	Transient
Equilibrium assumption	Off
Frame	Frame (ref)
Weak constraints	Off
Constraint type	Ideal

5.2.2. Variables

Dependent variables: R

Shape functions: shlag(2,'R')

Interior boundaries not active

5.2.3. Boundary Settings

Boundary		3	4-6, 8	7, 9
Type		Axial symmetry	Insulation/Symmetry	Concentration
Mass transfer coefficient (kc)	m/s	0	0	0
Bulk concentration (cb)	mol/m ³	0	0	0
Concentration (c0)	mol/m ³	0	0	0.45
Boundary		10		
Type		Flux		
Mass transfer coefficient (kc)	m/s	P		
Bulk concentration (cb)	mol/m ³	R1		
Concentration (c0)	mol/m ³	0		

5.2.4. Subdomain Settings

Subdomain		2
-----------	--	---

Diffusion coefficient (D)	m ² /s	D
Subdomain initial value		2
Concentration, R (R)	mol/m ³	0.45

5.3. Application Mode: Diffusion (chdi2)

Application mode type: Diffusion (Chemical Engineering Module)

Application mode name: chdi2

5.3.1. Application Mode Properties

Property	Value
Default element type	Lagrange - Quadratic
Analysis type	Transient
Equilibrium assumption	Off
Frame	Frame (ref)
Weak constraints	Off
Constraint type	Ideal

5.3.2. Variables

Dependent variables: R1

Shape functions: shlag(2,'R1')

Interior boundaries not active

5.3.3. Boundary Settings

Boundary		1	2	10
Type		Axial symmetry	Insulation/Symmetry	Flux
Mass transfer coefficient (kc)	m/s	0	0	P
Bulk concentration (cb)	mol/m ³	0	0	R

5.3.4. Subdomain Settings

Subdomain		1
Diffusion coefficient (D)	m ² /s	D

6. Solver Settings

Solve using a script: off

Analysis type	Transient
Auto select solver	On
Solver	Time dependent
Solution form	Automatic
Symmetric	auto
Adaptive mesh refinement	Off
Optimization/Sensitivity	Off
Plot while solving	Off

6.1. Direct (UMFPACK)

Solver type: Linear system solver

Parameter	Value
-----------	-------

Pivot threshold	0.1
Memory allocation factor	0.7

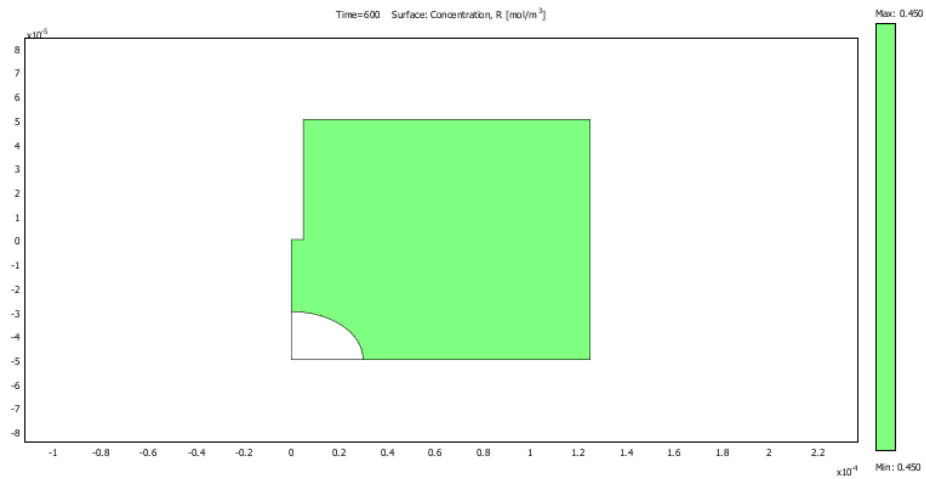
6.2. Time Stepping

Parameter	Value
Times	0:1:600
Relative tolerance	1e-9
Absolute tolerance	1e-10
Times to store in output	Specified times
Time steps taken by solver	Free
Maximum BDF order	5
Singular mass matrix	Maybe
Consistent initialization of DAE systems	Backward Euler
Error estimation strategy	Include algebraic
Allow complex numbers	Off

6.3. Advanced

Parameter	Value
Constraint handling method	Elimination
Null-space function	Automatic
Automatic assembly block size	On
Assembly block size	1000
Use Hermitian transpose of constraint matrix and in symmetry detection	Off
Use complex functions with real input	Off
Stop if error due to undefined operation	On
Store solution on file	Off
Type of scaling	Automatic
Manual scaling	
Row equilibration	On
Manual control of reassembly	Off
Load constant	On
Constraint constant	On
Mass constant	On
Damping (mass) constant	On
Jacobian constant	On
Constraint Jacobian constant	On

7. Postprocessing



8. Variables

8.1. Boundary

8.1.1. Boundary 1-2

Name	Description	Unit	Expression
ndflux_R_chdi	Normal diffusive flux, R	mol/(m ² *s)	
ndflux_R1_chdi2	Normal diffusive flux, R1	mol/(m ² *s)	nr_chdi2 * dflux_R1_r_chdi2+nz_chdi2 * dflux_R1_z_chdi2

8.1.2. Boundary 3-9

Name	Description	Unit	Expression
ndflux_R_chdi	Normal diffusive flux, R	mol/(m ² *s)	nr_chdi * dflux_R_r_chdi+nz_chdi * dflux_R_z_chdi
ndflux_R1_chdi2	Normal diffusive flux, R1	mol/(m ² *s)	

8.1.3. Boundary 10

Name	Description	Unit	Expression
ndflux_R_chdi	Normal diffusive flux, R	mol/(m ² *s)	nr_chdi * dflux_R_r_chdi+nz_chdi * dflux_R_z_chdi
ndflux_R1_chdi2	Normal diffusive flux, R1	mol/(m ² *s)	nr_chdi2 * dflux_R1_r_chdi2+nz_chdi2 * dflux_R1_z_chdi2

8.2. Subdomain

8.2.1. Subdomain 1

Name	Description	Unit	Expression
grad_R_r_chdi	Concentration gradient, R, r component	mol/m ⁴	
dflux_R_r_chdi	Diffusive flux, R, r component	mol/(m ² *s)	
grad_R_z_chdi	Concentration gradient, R, z component	mol/m ⁴	
dflux_R_z_chdi	Diffusive flux, R, z component	mol/(m ² *s)	
grad_R_chdi	Concentration gradient, R	mol/m ⁴	
dflux_R_chdi	Diffusive flux, R	mol/(m ² *s)	
grad_R1_r_chdi2	Concentration gradient, R1, r component	mol/m ⁴	R1r
dflux_R1_r_chdi2	Diffusive flux, R1, r component	mol/(m ² *s)	-Drr_R1_chdi2 * R1r-Drz_R1_chdi2 * R1z
grad_R1_z_chdi2	Concentration gradient, R1, z component	mol/m ⁴	R1z
dflux_R1_z_chdi2	Diffusive flux, R1, z component	mol/(m ² *s)	-Dzr_R1_chdi2 * R1r-Dzz_R1_chdi2 * R1z
grad_R1_chdi2	Concentration gradient, R1	mol/m ⁴	sqrt(grad_R1_r_chdi2 ² +grad_R1_z_chdi2 ²)
dflux_R1_chdi2	Diffusive flux, R1	mol/(m ² *s)	sqrt(dflux_R1_r_chdi2 ² +dflux_R1_z_chdi2 ²)

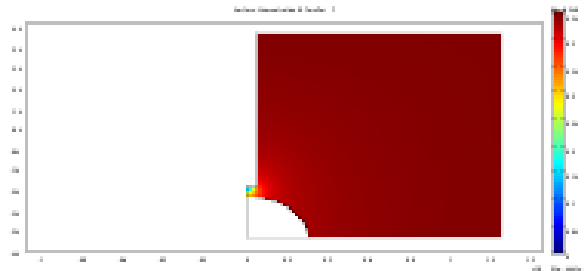
8.2.2. Subdomain 2

Name	Description	Unit	Expression
grad_R_r_chdi	Concentration gradient, R, r component	mol/m ⁴	Rr
dflux_R_r_chdi	Diffusive flux, R, r component	mol/(m ² *s)	-Drr_R_chdi * Rr-Drz_R_chdi * Rz
grad_R_z_chdi	Concentration gradient, R, z component	mol/m ⁴	Rz
dflux_R_z_chdi	Diffusive flux, R, z component	mol/(m ² *s)	-Dzr_R_chdi * Rr-Dzz_R_chdi * Rz
grad_R_chdi	Concentration gradient, R	mol/m ⁴	sqrt(grad_R_r_chdi ² +grad_R_z_chdi ²)
dflux_R_chdi	Diffusive flux, R	mol/(m ² *s)	sqrt(dflux_R_r_chdi ² +dflux_R_z_chdi ²)
grad_R1_r_chdi2	Concentration gradient, R1, r component	mol/m ⁴	
dflux_R1_r_chdi2	Diffusive flux, R1, r component	mol/(m ² *s)	
grad_R1_z_chdi2	Concentration gradient, R1, z component	mol/m ⁴	
dflux_R1_z_chdi2	Diffusive flux, R1, z component	mol/(m ² *s)	
grad_R1_chdi2	Concentration gradient, R1	mol/m ⁴	
dflux_R1_chdi2	Diffusive flux, R1	mol/(m ² *s)	

This Supplementary Material contains the COMSOL Model Report, as generated internally by the software, for the electrode approach to the surface of the cell described in the main text.



COMSOL Model Report



1. Table of Contents

- Title - COMSOL Model Report
- Table of Contents
- Model Properties
- Constants
- Geometry
- Geom1
- Solver Settings
- Postprocessing
- Variables

2. Model Properties

Property	Value
Model name	
Author	
Company	
Department	
Reference	
URL	
Saved date	Jan 8, 2014 2:17:48 PM
Creation date	Sep 26, 2013 4:37:34 PM
COMSOL version	COMSOL 3.5.0.603

File name: D:\2013-2014 School Year\Chem4491\Comsol\Michelle Paper\SECM Pcond\SECM Eon Pcond D2.mph

Application modes and modules used in this model:

- Geom1 (Axial symmetry (2D))
 - Diffusion (Chemical Engineering Module)
 - Diffusion (Chemical Engineering Module)

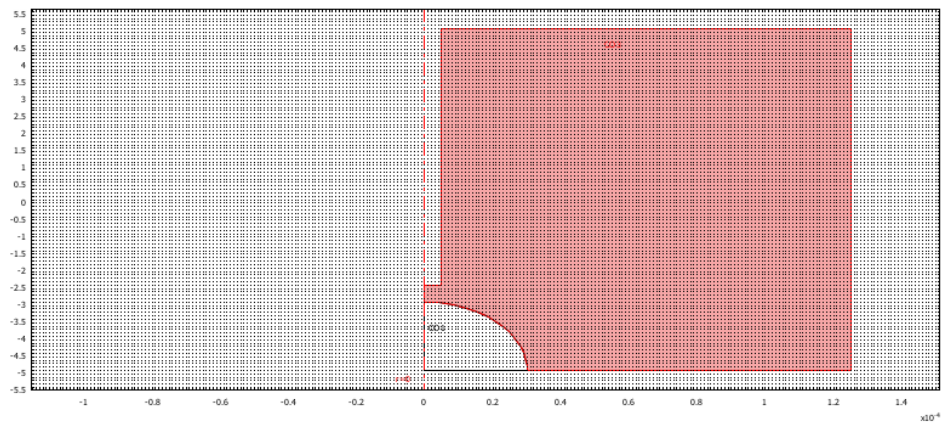
3. Constants

Name	Expression	Value	Description
n	1	1	Number of electrons
F	96485	96485	Faraday's constant
D	7.6e-10	7.6e-10	Diffusion coefficient of FcCH_2OH
P	1e-4	1e-4	Cell membrane permeability

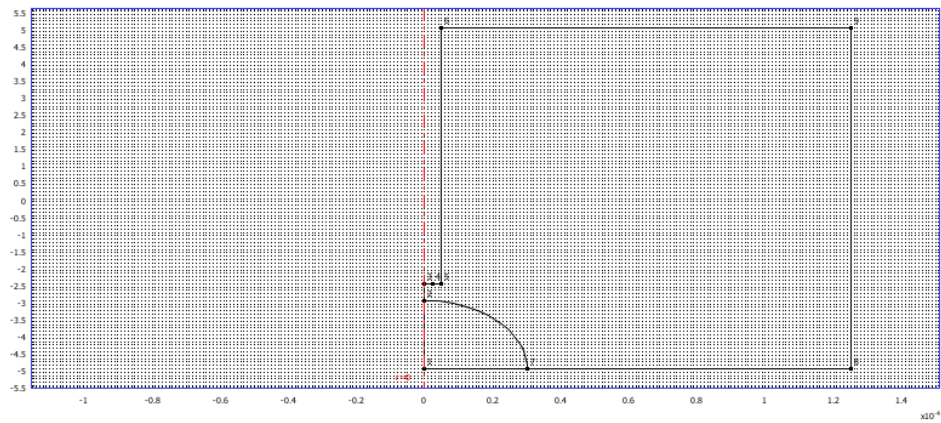
4. Geometry

Number of geometries: 1

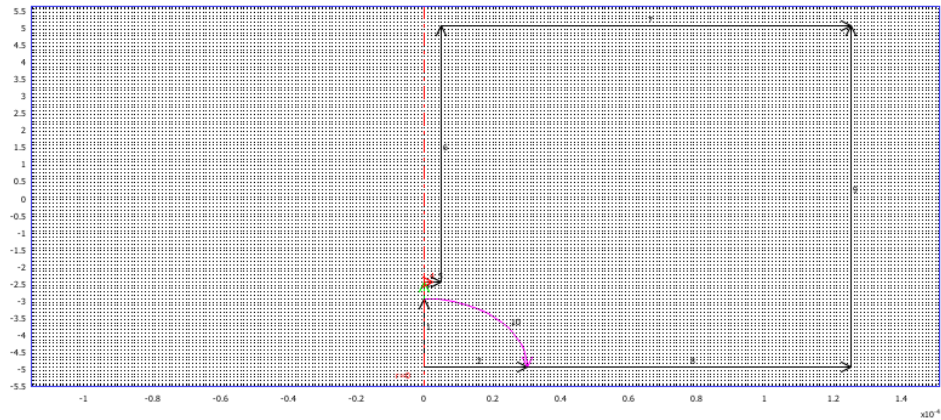
4.1. Geom1



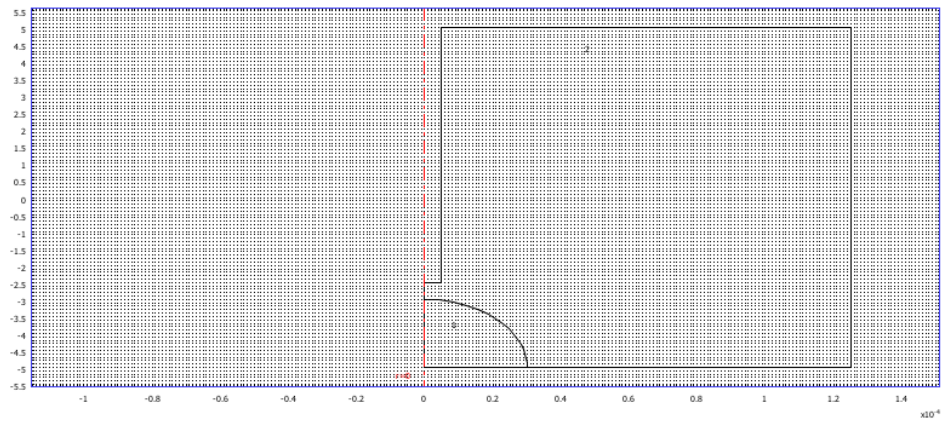
4.1.1. Point mode



4.1.2. Boundary mode



4.1.3. Subdomain mode



5. Geom1

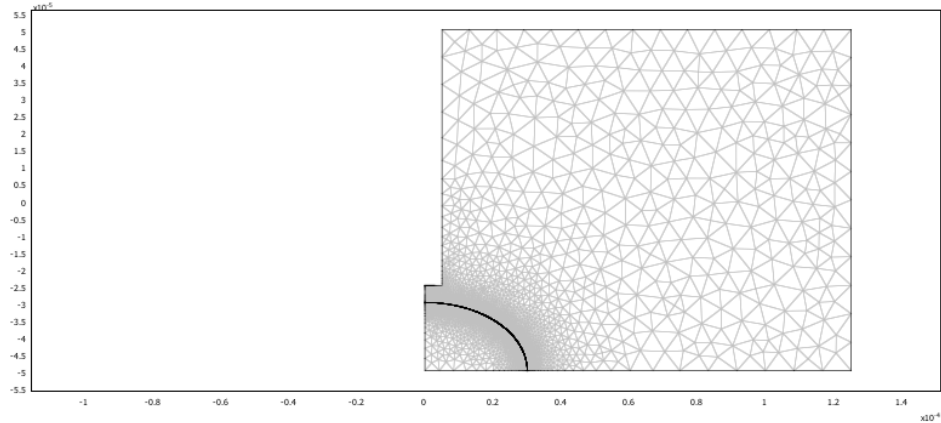
Space dimensions: Axial symmetry (2D)

Independent variables: r , ϕ , z

5.1. Mesh

5.1.1. Mesh Statistics

Number of degrees of freedom	341427
Number of mesh points	83489
Number of elements	166515
Triangular	166515
Quadrilateral	0
Number of boundary elements	4428
Number of vertex elements	9
Minimum element quality	0.668
Element area ratio	0



5.2. Application Mode: Diffusion (chdi)

Application mode type: Diffusion (Chemical Engineering Module)

Application mode name: chdi

5.2.1. Application Mode Properties

Property	Value
Default element type	Lagrange - Quadratic
Analysis type	Stationary
Equilibrium assumption	Off
Frame	Frame (ref)
Weak constraints	Off
Constraint type	Ideal

5.2.2. Variables

Dependent variables: R

Shape functions: shlag(2,'R')

Interior boundaries not active

5.2.3. Boundary Settings

Boundary		3	5-6, 8	7, 9
Type		Axial symmetry	Insulation/Symmetry	Concentration
Mass transfer coefficient (kc)	m/s	0	0	0
Bulk concentration (cb)	mol/m ³	0	0	0
Concentration (c0)	mol/m ³	0	0	0.45
Boundary		10	4	
Type		Flux	Concentration	
Mass transfer coefficient (kc)	m/s	P	0	
Bulk concentration (cb)	mol/m ³	R1	0	
Concentration (c0)	mol/m ³	0	0	

5.2.4. Subdomain Settings

Subdomain		2
Shape functions (shape)		shlag(2,'R')
Integration order (gporder)		4
Constraint order (cporder)		2
Diffusion coefficient (D)	m ² /s	D
Subdomain initial value		2
Concentration, R (R)	mol/m ³	0.45

5.3. Application Mode: Diffusion (chdi2)

Application mode type: Diffusion (Chemical Engineering Module)

Application mode name: chdi2

5.3.1. Application Mode Properties

Property	Value
Default element type	Lagrange - Quadratic
Analysis type	Stationary
Equilibrium assumption	Off
Frame	Frame (ref)
Weak constraints	Off
Constraint type	Ideal

5.3.2. Variables

Dependent variables: R1

Shape functions: shlag(2,'R1')

Interior boundaries not active

5.3.3. Boundary Settings

Boundary		1	2	10
Type		Axial symmetry	Insulation/Symmetry	Flux
Mass transfer coefficient (kc)	m/s	0	0	P
Bulk concentration (cb)	mol/m ³	0	0	R

5.3.4. Subdomain Settings

Subdomain		1
Shape functions (shape)		shlag(2,'R1')
Integration order (gporder)		4
Constraint order (cporder)		2
Diffusion coefficient (D)	m ² /s	D

6. Solver Settings

Solve using a script: off

Analysis type	Stationary
Auto select solver	On
Solver	Stationary
Solution form	Automatic
Symmetric	auto
Adaptive mesh refinement	Off
Optimization/Sensitivity	Off
Plot while solving	Off

6.1. Direct (UMFPACK)

Solver type: Linear system solver

Parameter	Value
Pivot threshold	0.1
Memory allocation factor	0.7

6.2. Stationary

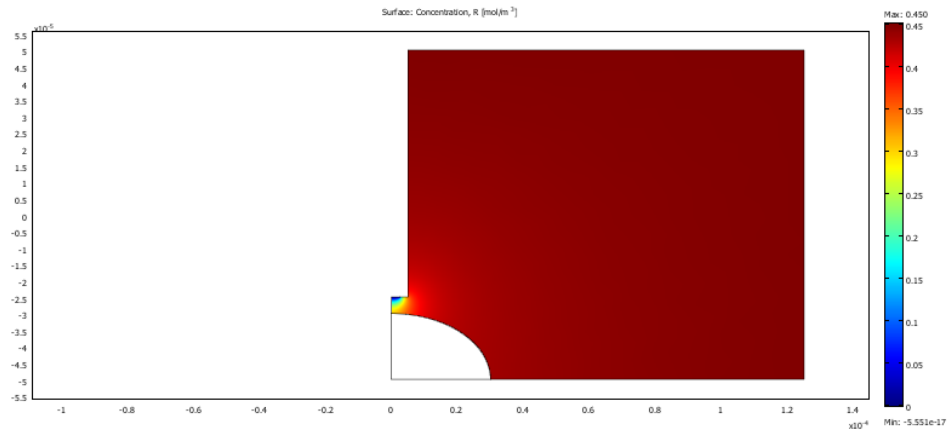
Parameter	Value
Linearity	Automatic
Relative tolerance	1.0E-6
Maximum number of iterations	25
Manual tuning of damping parameters	Off
Highly nonlinear problem	Off
Initial damping factor	1.0
Minimum damping factor	1.0E-4
Restriction for step size update	10.0

6.3. Advanced

Parameter	Value
Constraint handling method	Elimination
Null-space function	Automatic
Automatic assembly block size	On
Assembly block size	1000
Use Hermitian transpose of constraint matrix and in symmetry detection	Off
Use complex functions with real input	Off
Stop if error due to undefined operation	On
Store solution on file	Off
Type of scaling	Automatic
Manual scaling	
Row equilibration	On
Manual control of reassembly	Off
Load constant	On
Constraint constant	On

Mass constant	On
Damping (mass) constant	On
Jacobian constant	On
Constraint Jacobian constant	On

7. Postprocessing



8. Variables

8.1. Boundary

8.1.1. Boundary 1-2

Name	Description	Unit	Expression
ndflux_R_chdi	Normal diffusive flux, R	mol/(m ² *s)	
ndflux_R1_chdi2	Normal diffusive flux, R1	mol/(m ² *s)	nr_chdi2 * dflux_R1_r_chdi2+nz_chdi2 * dflux_R1_z_chdi2

8.1.2. Boundary 3-9

Name	Description	Unit	Expression
ndflux_R_chdi	Normal diffusive flux, R	mol/(m ² *s)	nr_chdi * dflux_R_r_chdi+nz_chdi * dflux_R_z_chdi
ndflux_R1_chdi2	Normal diffusive flux, R1	mol/(m ² *s)	

8.1.3. Boundary 10

Name	Description	Unit	Expression
ndflux_R_chdi	Normal diffusive flux, R	mol/(m ² *s)	nr_chdi * dflux_R_r_chdi+nz_chdi * dflux_R_z_chdi
ndflux_R1_chdi2	Normal diffusive flux, R1	mol/(m ² *s)	nr_chdi2 * dflux_R1_r_chdi2+nz_chdi2 * dflux_R1_z_chdi2

8.2. Subdomain

8.2.1. Subdomain 1

Name	Description	Unit	Expression
grad_R_r_chdi	Concentration gradient, R, r	mol/m ⁴	

	component		
dflux_R_r_chdi	Diffusive flux, R, r component	mol/(m ² *s)	
grad_R_z_chdi	Concentration gradient, R, z component	mol/m ⁴	
dflux_R_z_chdi	Diffusive flux, R, z component	mol/(m ² *s)	
grad_R_chdi	Concentration gradient, R	mol/m ⁴	
dflux_R_chdi	Diffusive flux, R	mol/(m ² *s)	
grad_R1_r_chdi2	Concentration gradient, R1, r component	mol/m ⁴	R1r
dflux_R1_r_chdi2	Diffusive flux, R1, r component	mol/(m ² *s)	-Drr_R1_chdi2 * R1r-Drz_R1_chdi2 * R1z
grad_R1_z_chdi2	Concentration gradient, R1, z component	mol/m ⁴	R1z
dflux_R1_z_chdi2	Diffusive flux, R1, z component	mol/(m ² *s)	-Dzr_R1_chdi2 * R1r-Dzz_R1_chdi2 * R1z
grad_R1_chdi2	Concentration gradient, R1	mol/m ⁴	sqrt(grad_R1_r_chdi2 ² +grad_R1_z_chdi2 ²)
dflux_R1_chdi2	Diffusive flux, R1	mol/(m ² *s)	sqrt(dflux_R1_r_chdi2 ² +dflux_R1_z_chdi2 ²)

8.2.2. Subdomain 2

Name	Description	Unit	Expression
grad_R_r_chdi	Concentration gradient, R, r component	mol/m ⁴	Rr
dflux_R_r_chdi	Diffusive flux, R, r component	mol/(m ² *s)	-Drr_R_chdi * Rr-Drz_R_chdi * Rz
grad_R_z_chdi	Concentration gradient, R, z component	mol/m ⁴	Rz
dflux_R_z_chdi	Diffusive flux, R, z component	mol/(m ² *s)	-Dzr_R_chdi * Rr-Dzz_R_chdi * Rz
grad_R_chdi	Concentration gradient, R	mol/m ⁴	sqrt(grad_R_r_chdi ² +grad_R_z_chdi ²)
dflux_R_chdi	Diffusive flux, R	mol/(m ² *s)	sqrt(dflux_R_r_chdi ² +dflux_R_z_chdi ²)
grad_R1_r_chdi2	Concentration gradient, R1, r component	mol/m ⁴	
dflux_R1_r_chdi2	Diffusive flux, R1, r component	mol/(m ² *s)	
grad_R1_z_chdi2	Concentration gradient, R1, z component	mol/m ⁴	
dflux_R1_z_chdi2	Diffusive flux, R1, z component	mol/(m ² *s)	
grad_R1_chdi2	Concentration gradient, R1	mol/m ⁴	
dflux_R1_chdi2	Diffusive flux, R1	mol/(m ² *s)	

6/28/2017

RightsLink Printable License

**ELSEVIER LICENSE
TERMS AND CONDITIONS**

Jun 28, 2017

This Agreement between Michelle Li ("You") and Elsevier ("Elsevier") consists of your license details and the terms and conditions provided by Elsevier and Copyright Clearance Center.

License Number	4137810685306
License date	Jun 28, 2017
Licensed Content Publisher	Elsevier
Licensed Content Publication	Journal of Inorganic Biochemistry
Licensed Content Title	A time course study of cadmium effect on membrane permeability of single human bladder cancer cells using scanning electrochemical microscopy
Licensed Content Author	Michelle S.M. Li, Fraser P. Filice, Zhifeng Ding
Licensed Content Date	Jul 1, 2014
Licensed Content Volume	136
Licensed Content Issue	n/a
Licensed Content Pages	7
Start Page	177
End Page	183
Type of Use	reuse in a thesis/dissertation
Portion	full article
Format	both print and electronic
Are you the author of this Elsevier article?	Yes
Will you be translating?	No
Order reference number	
Title of your thesis/dissertation	Scanning Electrochemical Microscopy of Single Live Human Bladder Cancer Cells
Expected completion date	Sep 2017
Estimated size (number of pages)	200
Elsevier VAT number	GB 494 6272 12
Requestor Location	Michelle Li Western University 1151 Richmond Street Department of Chemistry London, ON N6A5B7 Canada Attn: Michelle Li
Total	0.00 USD
Terms and Conditions	

INTRODUCTION

1. The publisher for this copyrighted material is Elsevier. By clicking "accept" in connection with completing this licensing transaction, you agree that the following terms and conditions apply to this transaction (along with the Billing and Payment terms and conditions established by Copyright Clearance Center, Inc. ("CCC"), at the time that you opened your Rightslink account and that are available at any time at <http://myaccount.copyright.com>).

GENERAL TERMS

2. Elsevier hereby grants you permission to reproduce the aforementioned material subject to the terms and conditions indicated.

3. Acknowledgement: If any part of the material to be used (for example, figures) has appeared in our publication with credit or acknowledgement to another source, permission must also be sought from that source. If such permission is not obtained then that material may not be included in your publication/copies. Suitable acknowledgement to the source must be made, either as a footnote or in a reference list at the end of your publication, as follows:

"Reprinted from Publication title, Vol /edition number, Author(s), Title of article / title of chapter, Pages No., Copyright (Year), with permission from Elsevier [OR APPLICABLE SOCIETY COPYRIGHT OWNER]." Also Lancet special credit - "Reprinted from The Lancet, Vol. number, Author(s), Title of article, Pages No., Copyright (Year), with permission from Elsevier."

4. Reproduction of this material is confined to the purpose and/or media for which permission is hereby given.

5. Altering/Modifying Material: Not Permitted. However figures and illustrations may be altered/adapted minimally to serve your work. Any other abbreviations, additions, deletions and/or any other alterations shall be made only with prior written authorization of Elsevier Ltd. (Please contact Elsevier at permissions@elsevier.com). No modifications can be made to any Lancet figures/tables and they must be reproduced in full.

6. If the permission fee for the requested use of our material is waived in this instance, please be advised that your future requests for Elsevier materials may attract a fee.

7. Reservation of Rights: Publisher reserves all rights not specifically granted in the combination of (i) the license details provided by you and accepted in the course of this licensing transaction, (ii) these terms and conditions and (iii) CCC's Billing and Payment terms and conditions.

8. License Contingent Upon Payment: While you may exercise the rights licensed immediately upon issuance of the license at the end of the licensing process for the transaction, provided that you have disclosed complete and accurate details of your proposed use, no license is finally effective unless and until full payment is received from you (either by publisher or by CCC) as provided in CCC's Billing and Payment terms and conditions. If full payment is not received on a timely basis, then any license preliminarily granted shall be deemed automatically revoked and shall be void as if never granted. Further, in the event that you breach any of these terms and conditions or any of CCC's Billing and Payment terms and conditions, the license is automatically revoked and shall be void as if never granted. Use of materials as described in a revoked license, as well as any use of the materials beyond the scope of an unrevoked license, may constitute copyright infringement and publisher reserves the right to take any and all action to protect its copyright in the materials.

9. Warranties: Publisher makes no representations or warranties with respect to the licensed material.

10. Indemnity: You hereby indemnify and agree to hold harmless publisher and CCC, and their respective officers, directors, employees and agents, from and against any and all claims arising out of your use of the licensed material other than as specifically authorized pursuant to this license.

11. No Transfer of License: This license is personal to you and may not be sublicensed, assigned, or transferred by you to any other person without publisher's written permission.

12. **No Amendment Except in Writing:** This license may not be amended except in a writing signed by both parties (or, in the case of publisher, by CCC on publisher's behalf).

13. **Objection to Contrary Terms:** Publisher hereby objects to any terms contained in any purchase order, acknowledgment, check endorsement or other writing prepared by you, which terms are inconsistent with these terms and conditions or CCC's Billing and Payment terms and conditions. These terms and conditions, together with CCC's Billing and Payment terms and conditions (which are incorporated herein), comprise the entire agreement between you and publisher (and CCC) concerning this licensing transaction. In the event of any conflict between your obligations established by these terms and conditions and those established by CCC's Billing and Payment terms and conditions, these terms and conditions shall control.

14. **Revocation:** Elsevier or Copyright Clearance Center may deny the permissions described in this License at their sole discretion, for any reason or no reason, with a full refund payable to you. Notice of such denial will be made using the contact information provided by you. Failure to receive such notice will not alter or invalidate the denial. In no event will Elsevier or Copyright Clearance Center be responsible or liable for any costs, expenses or damage incurred by you as a result of a denial of your permission request, other than a refund of the amount(s) paid by you to Elsevier and/or Copyright Clearance Center for denied permissions.

LIMITED LICENSE

The following terms and conditions apply only to specific license types:

15. **Translation:** This permission is granted for non-exclusive world **English** rights only unless your license was granted for translation rights. If you licensed translation rights you may only translate this content into the languages you requested. A professional translator must perform all translations and reproduce the content word for word preserving the integrity of the article.

16. **Posting licensed content on any Website:** The following terms and conditions apply as follows: Licensing material from an Elsevier journal: All content posted to the web site must maintain the copyright information line on the bottom of each image; A hyper-text must be included to the Homepage of the journal from which you are licensing at <http://www.sciencedirect.com/science/journal/xxxx> or the Elsevier homepage for books at <http://www.elsevier.com>; Central Storage: This license does not include permission for a scanned version of the material to be stored in a central repository such as that provided by Heron/XanEdu.

Licensing material from an Elsevier book: A hyper-text link must be included to the Elsevier homepage at <http://www.elsevier.com>. All content posted to the web site must maintain the copyright information line on the bottom of each image.

Posting licensed content on Electronic reserve: In addition to the above the following clauses are applicable: The web site must be password-protected and made available only to bona fide students registered on a relevant course. This permission is granted for 1 year only. You may obtain a new license for future website posting.

17. **For journal authors:** the following clauses are applicable in addition to the above:

Preprints:

A preprint is an author's own write-up of research results and analysis, it has not been peer-reviewed, nor has it had any other value added to it by a publisher (such as formatting, copyright, technical enhancement etc.).

Authors can share their preprints anywhere at any time. Preprints should not be added to or enhanced in any way in order to appear more like, or to substitute for, the final versions of articles however authors can update their preprints on arXiv or RePEc with their Accepted Author Manuscript (see below).

If accepted for publication, we encourage authors to link from the preprint to their formal publication via its DOI. Millions of researchers have access to the formal publications on ScienceDirect, and so links will help users to find, access, cite and use the best available

version. Please note that Cell Press, The Lancet and some society-owned have different preprint policies. Information on these policies is available on the journal homepage.

Accepted Author Manuscripts: An accepted author manuscript is the manuscript of an article that has been accepted for publication and which typically includes author-incorporated changes suggested during submission, peer review and editor-author communications.

Authors can share their accepted author manuscript:

- immediately
 - via their non-commercial person homepage or blog
 - by updating a preprint in arXiv or RePEc with the accepted manuscript
 - via their research institute or institutional repository for internal institutional uses or as part of an invitation-only research collaboration work-group
 - directly by providing copies to their students or to research collaborators for their personal use
 - for private scholarly sharing as part of an invitation-only work group on commercial sites with which Elsevier has an agreement
- After the embargo period
 - via non-commercial hosting platforms such as their institutional repository
 - via commercial sites with which Elsevier has an agreement

In all cases accepted manuscripts should:

- link to the formal publication via its DOI
- bear a CC-BY-NC-ND license - this is easy to do
- if aggregated with other manuscripts, for example in a repository or other site, be shared in alignment with our hosting policy not be added to or enhanced in any way to appear more like, or to substitute for, the published journal article.

Published journal article (JPA): A published journal article (PJA) is the definitive final record of published research that appears or will appear in the journal and embodies all value-adding publishing activities including peer review co-ordination, copy-editing, formatting, (if relevant) pagination and online enrichment.

Policies for sharing publishing journal articles differ for subscription and gold open access articles:

Subscription Articles: If you are an author, please share a link to your article rather than the full-text. Millions of researchers have access to the formal publications on ScienceDirect, and so links will help your users to find, access, cite, and use the best available version. Theses and dissertations which contain embedded PJAs as part of the formal submission can be posted publicly by the awarding institution with DOI links back to the formal publications on ScienceDirect.

If you are affiliated with a library that subscribes to ScienceDirect you have additional private sharing rights for others' research accessed under that agreement. This includes use for classroom teaching and internal training at the institution (including use in course packs and courseware programs), and inclusion of the article for grant funding purposes.

Gold Open Access Articles: May be shared according to the author-selected end-user license and should contain a [CrossMark logo](#), the end user license, and a DOI link to the formal publication on ScienceDirect.

Please refer to Elsevier's [posting policy](#) for further information.

18. **For book authors** the following clauses are applicable in addition to the above:

Authors are permitted to place a brief summary of their work online only. You are not allowed to download and post the published electronic version of your chapter, nor may you scan the printed edition to create an electronic version. **Posting to a repository:** Authors are permitted to post a summary of their chapter only in their institution's repository.

19. Thesis/Dissertation: If your license is for use in a thesis/dissertation your thesis may be submitted to your institution in either print or electronic form. Should your thesis be published commercially, please reapply for permission. These requirements include permission for the Library and Archives of Canada to supply single copies, on demand, of the complete thesis and include permission for Proquest/UMI to supply single copies, on demand, of the complete thesis. Should your thesis be published commercially, please reapply for permission. Theses and dissertations which contain embedded PJAs as part of the formal submission can be posted publicly by the awarding institution with DOI links back to the formal publications on ScienceDirect.

Elsevier Open Access Terms and Conditions

You can publish open access with Elsevier in hundreds of open access journals or in nearly 2000 established subscription journals that support open access publishing. Permitted third party re-use of these open access articles is defined by the author's choice of Creative Commons user license. See our [open access license policy](#) for more information.

Terms & Conditions applicable to all Open Access articles published with Elsevier:

Any reuse of the article must not represent the author as endorsing the adaptation of the article nor should the article be modified in such a way as to damage the author's honour or reputation. If any changes have been made, such changes must be clearly indicated.

The author(s) must be appropriately credited and we ask that you include the end user license and a DOI link to the formal publication on ScienceDirect.

If any part of the material to be used (for example, figures) has appeared in our publication with credit or acknowledgement to another source it is the responsibility of the user to ensure their reuse complies with the terms and conditions determined by the rights holder.

Additional Terms & Conditions applicable to each Creative Commons user license:

CC BY: The CC-BY license allows users to copy, to create extracts, abstracts and new works from the Article, to alter and revise the Article and to make commercial use of the Article (including reuse and/or resale of the Article by commercial entities), provided the user gives appropriate credit (with a link to the formal publication through the relevant DOI), provides a link to the license, indicates if changes were made and the licensor is not represented as endorsing the use made of the work. The full details of the license are available at <http://creativecommons.org/licenses/by/4.0>.

CC BY NC SA: The CC BY-NC-SA license allows users to copy, to create extracts, abstracts and new works from the Article, to alter and revise the Article, provided this is not done for commercial purposes, and that the user gives appropriate credit (with a link to the formal publication through the relevant DOI), provides a link to the license, indicates if changes were made and the licensor is not represented as endorsing the use made of the work. Further, any new works must be made available on the same conditions. The full details of the license are available at <http://creativecommons.org/licenses/by-nc-sa/4.0>.

CC BY NC ND: The CC BY-NC-ND license allows users to copy and distribute the Article, provided this is not done for commercial purposes and further does not permit distribution of the Article if it is changed or edited in any way, and provided the user gives appropriate credit (with a link to the formal publication through the relevant DOI), provides a link to the license, and that the licensor is not represented as endorsing the use made of the work. The full details of the license are available at <http://creativecommons.org/licenses/by-nc-nd/4.0>. Any commercial reuse of Open Access articles published with a CC BY NC SA or CC BY NC ND license requires permission from Elsevier and will be subject to a fee.

Commercial reuse includes:

- Associating advertising with the full text of the Article
- Charging fees for document delivery or access
- Article aggregation
- Systematic distribution via e-mail lists or share buttons

6/28/2017

RightsLink Printable License

Posting or linking by commercial companies for use by customers of those companies.

20. Other Conditions:

v1.9

Questions? customercare@copyright.com or +1-855-239-3415 (toll free in the US) or +1-978-646-2777.



Appendix IV. Chapter 4: Probing Cd²⁺-Stressed Live Cell Membrane Permeability with Various Redox Mediators in Scanning Electrochemical Microscopy

To find the diffusion coefficient of Fc(COOH)₂, we utilized the steady state voltammogram (Figure S4.1).

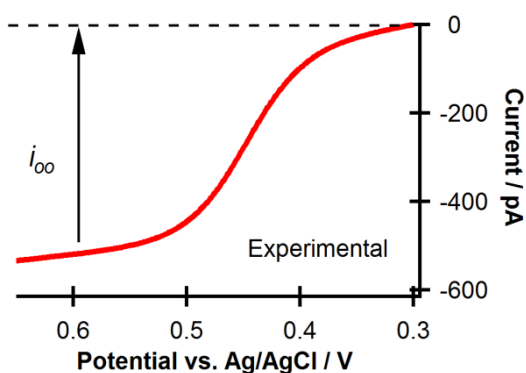


Figure S4.1. Typical CV of 0.5 mM Fc(COO)₂²⁻ in 0.1 M KCl (supporting electrolyte) using a 10 μm Pt UME, at a scan rate of 0.02 V/s and sensitivity of 1 x 10⁻¹⁰ A/V. The steady state current (*i*_∞) is identified in the CV.

The steady state current (*i*_∞) was determined among 5 CVs to have an average current of 507.4 pA (Table S4.1).

Table S4.1. The *i*_∞ obtained from 5 CV's of 0.5 mM Fc(COO)₂²⁻ in 0.1 M KCl

Trial	<i>i</i> _∞ [pA]
1	483.6
2	499.1
3	524.9
4	512.7
5	516.5
Average	507.4
Standard deviation	±16.2

To determine the diffusion coefficient, the average steady state current was placed into the following equation,

$$i_{\infty} = 4nFDac \quad (\text{S4.1})$$

where, n is the number of electrons transferred in the oxidation reaction of $\text{Fc}(\text{COO})_2^{2-}$ to $\text{Fc}(\text{COO})_2^{\cdot -}$ (1), F is Faraday's constant (96,485 C/mol), D is the diffusion coefficient, a is the electrode radius, and c is the concentration of redox mediator in solution. This gave an average diffusion coefficient \pm standard deviation of $(5.3 \pm 1.7) \times 10^{-10} \text{ m}^2/\text{s}$.

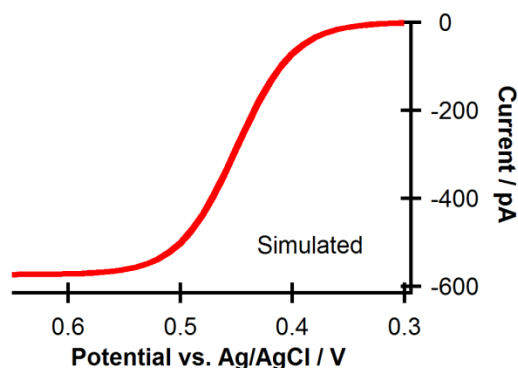


Figure S4.2. Simulated CV of 0.5 mM $\text{Fc}(\text{COO})_2^{2-}$ in 0.1 M KCl (supporting electrolyte) using a 10 μm Pt UME, a scan rate of 0.02 V/s and D of $5.3 \times 10^{-10} \text{ m}^2/\text{s}$. The simulated CV had a steady state oxidative current as 571 pA, while the experimental CVs had an average steady state current of 507 pA.

Theory and Simulation

Simulation Geometry. The electrodes modelled in the simulation reflect the fabricated UME used in these experiments (**Figure S4.3**): a 5 or 10 μm diameter Pt wire surrounded by a glass sheathing of either 15 or 30 μm diameter respectively (RG 3). The T24 cell was represented as a nominal semi-oblate ellipsoid with 9 μm in height and 10 μm in radius – a model of the average cell geometry experimentally observed (see **Figure S4.4 & S4.5**).

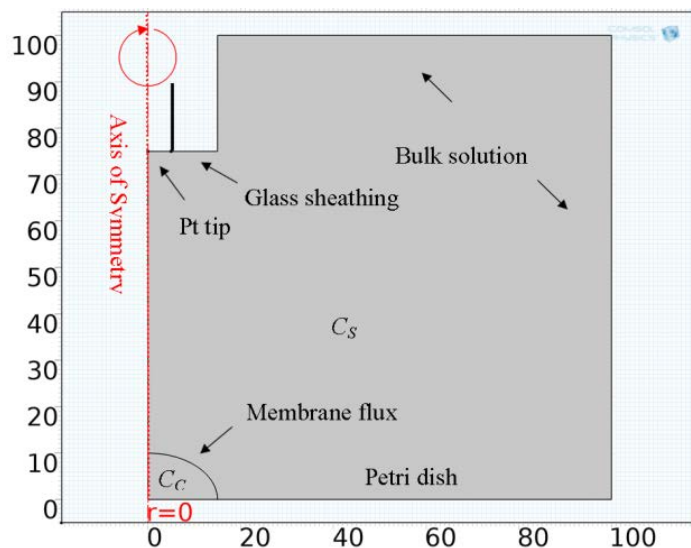


Figure S4.3. An illustration of the 2D axial geometry simulated for a T24 cell in COMSOL Multiphysics 4.4. c_s and c_c are the bulk concentrations outside and inside the cell, respectively. At the cell membrane, the membrane flux, f , is defined as: $f_{\text{in}} = P_m (c_s - c_c)$ and $f_{\text{out}} = P_m (c_c - c_s)$.

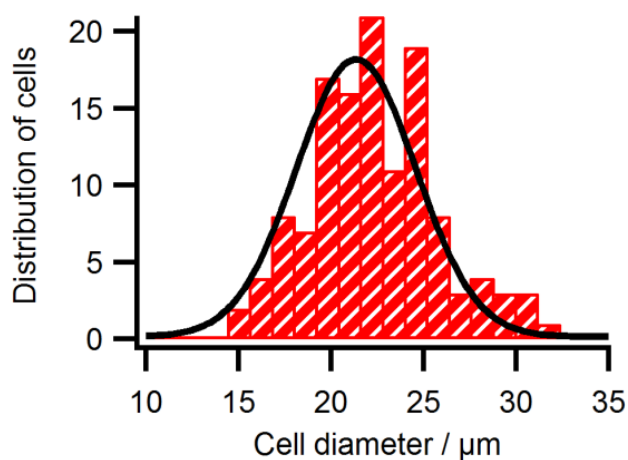


Figure S4.4. Distribution of cell diameters among T24 cells in this SECM study. The average cell diameter of T24 cells was determined through optical micrographs to be $21.7 \pm 3.5 \mu\text{m}$ for $N = 127$ cells.

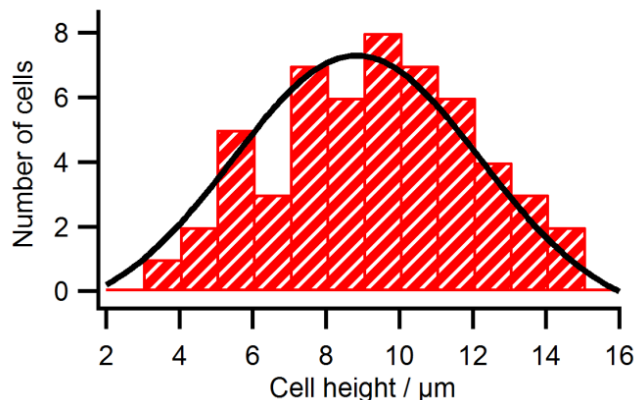


Figure S4.5. Distribution of cellular heights among control T24 cells. The average cell height of T24 cells was determined to be $8.68 \pm 2.69 \mu\text{m}$ ($N = 54$ cells) through PAC comparison of T24 cells using the hydrophilic sensing agents.

Simulation Methodology. The interior of the cell and the solution are defined as two separate domains with their own physics and initial concentrations. The two domains interact with each other through a shared flux boundary. The diffusion coefficient, D , of the redox mediators were assumed to be the same both inside and outside of the cell (**Table 4.1**).

The diffusion of the mediator in both domains followed Fick's Second Law, eqns S4.2 and S4.3:

$$\frac{\partial c_s(r,z)}{\partial t} = D \left(\frac{\partial^2 c_s(r,z)}{\partial r^2} + \frac{1}{r} \left(\frac{\partial c_s(r,z)}{\partial r} \right) + \frac{\partial^2 c_s(r,z)}{\partial z^2} \right) \quad (\text{S4.2})$$

$$\frac{\partial c_c(r,z)}{\partial t} = D \left(\frac{\partial^2 c_c(r,z)}{\partial r^2} + \frac{1}{r} \left(\frac{\partial c_c(r,z)}{\partial r} \right) + \frac{\partial^2 c_c(r,z)}{\partial z^2} \right) \quad (\text{S4.3})$$

where c_s and c_c represent the mediator's concentration in the solution and cell respectively, r and z are the cylindrical coordinates used in 2D axially symmetric modelling, and t , time.

The concentration of the redox mediators in bulk were defined to match the experimental conditions (**Table 4.1**), while the cell interior is initially defined as 0 mM. The two domains are both subjected to a two-step simulation process, similar to those previously demonstrated by Koley and Bard, and then our group.^{5a, 20a} The first study step was a time-dependent fixed geometry simulation. The cell was soaked for 600 s to allow the exterior and interior

mediator concentrations to equilibrate. During this step, the electrode was kept in an off state (no potential bias applied), where it behaves as a no flux boundary and current flow is assumed to be 0 A. The solution of this first study step is then stored by COMSOL to be used as the initial concentration for the second study step. The second study step consisted of a stationary phase (steady state) simulation. The electrode tip boundary is then turned on, consuming the mediator at the tip, generating a concentration of 0 M.

The bulk solution boundaries (**Figure S4.3**) were set to generate the initial bulk solution concentration. Since the glass electrode sheathing and petri dish have insulating characteristics, they were set as no flux boundaries. Biasing the electrode at its oxidizing (ferrocene-based compounds) or reducing ($\text{Ru}(\text{NH}_3)_6^{3+}$) potentials results in a one electron transfer (diffusion controlled) at the UME surface (**Table 4.1**).

The boundary between the cell interior and the solution domains were set as a flux boundary, which was controlled by the permeability coefficient parameter, P_m , eqns S4.4 and S4.5:

$$f_{\text{in}} = P_m (c_s - c_c) \quad (\text{S4.4})$$

$$f_{\text{out}} = P_m (c_c - c_s) \quad (\text{S4.5})$$

The entire model geometry (**Figure S4.2**) is then finely meshed (**Figure S4.6A**) prior to computation, with further refinement at the regions of interest (electrode tip and cell membrane boundary) to provide greater accuracy and precision.

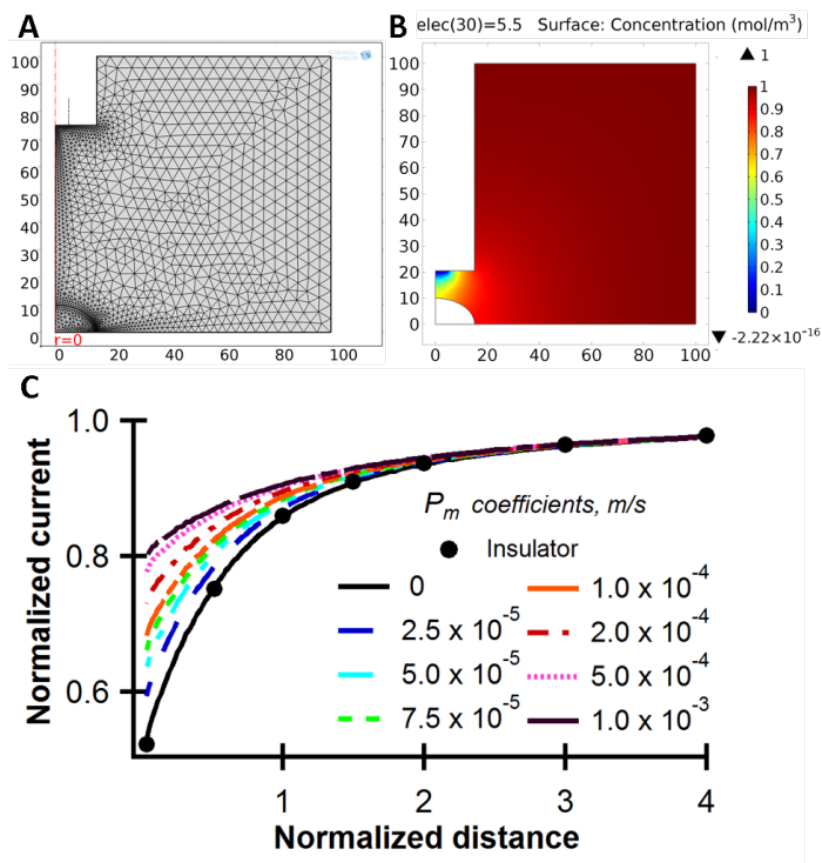


Figure S4.6. (A) A typical meshed 2D SECM model, with finer meshing located in the areas of interest (Pt tip and cell membrane). (B) A simulated concentration map of the SECM probe positioned 5 μm above the T24 cell with a fixed membrane permeability coefficient, P_m , of 0 m/s, and (C) a full set of simulated curves for $\text{Fc}(\text{COO})_2^{2-}$ with P_m values ranged from 0 to 1.0×10^{-3} m/s.

As described elsewhere,^{5a} a post-processing surface integration is performed on the resulting simulation concentration distribution map (**Figure S4.6B**) to calculate the current over the Pt disk surface, eqn S4.6:

$$i = nDF \int_0^a r \left[\frac{\partial c_s(r,z)}{\partial z} \right] dr \quad (\text{S4.6})$$

Where n is the number of electrons transferred in the oxidation or reduction reaction ($n=1$ for all redox mediators used in this project) and F is Faraday's constant.

To generate the full set of (unnormalized) theoretical PACs, the UME's z position and membrane permeability coefficients were parameterized and varied using the COMSOL parametric sweep function. The tip-to-cell distance was varied between 0.2 and 60 μm , and the permeability coefficient was varied between 0 and 1.0×10^{-3} m/s. The parameterized electrode z -positions allow for the automated movement of the electrode tip, while the parameterized membrane permeability coefficient allows for the automated configuration of membrane permeability. Note that as a result of parametric sweeps, numerous PACs can be generated from a single simulation.

To normalize the PACs, the resulting tip currents were normalized against the faradaic current in bulk solution and the distance was normalized against the electrode size. A sample set of normalized theoretical PACs is simulated and illustrated in **Figure S4.6C**, using the redox mediator, $\text{Fc}(\text{COO})_2^{2-}$. As the permeability coefficient increases from 0 m/s (insulating), the curvature of the PACs display less negative feedback characteristics in nature.

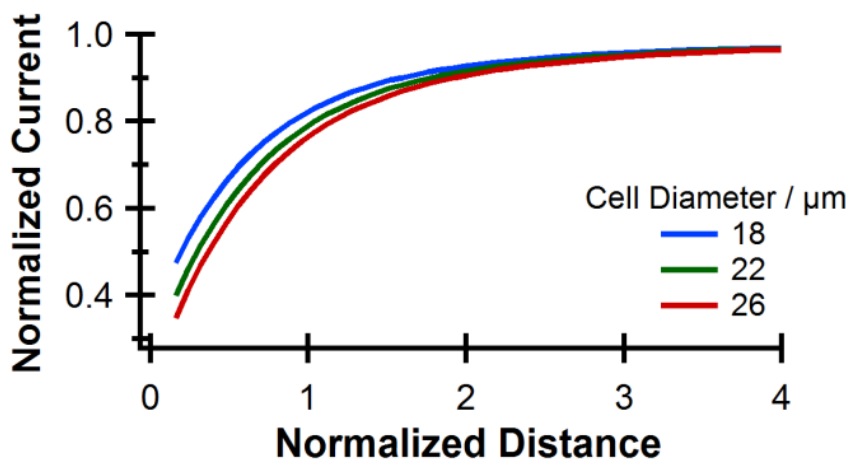


Figure S4.7 Simulated PACs towards a cell of fixed height with varying diameters around the average diameter \pm standard deviation ($21.7 \pm 3.5 \mu\text{m}$): minimal effect on PACs is observed. The greatest effect occurs when the diameter is much smaller.

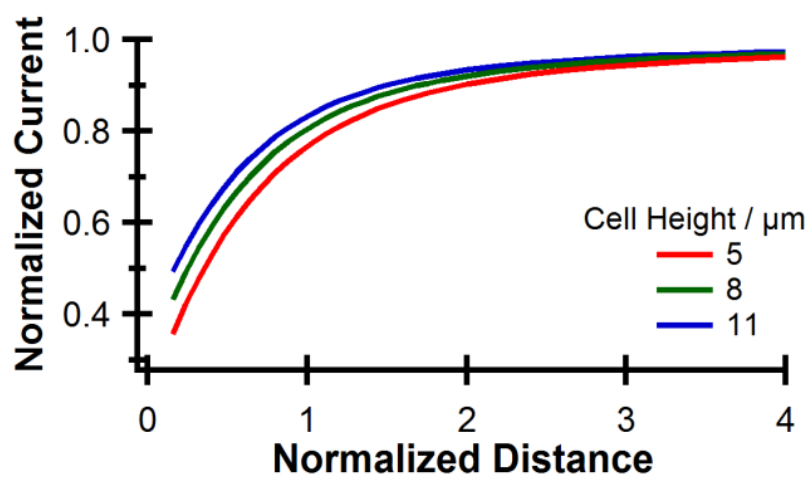


Figure S4.8. Simulated PACs towards a cell of fixed diameter with varying heights around the average height \pm standard deviation ($8.68 \pm 2.69 \mu\text{m}$): minimal effect on PACs is observed.

6/28/2017

Rightslink® by Copyright Clearance Center



RightsLink®

Home

Account
Info

Help

ACS Publications
Most Trusted. Most Cited. Most Read.

Title: Probing Cd²⁺-Stressed Live Cell Membrane Permeability with Various Redox Mediators in Scanning Electrochemical Microscopy

Logged in as:
Michelle Li

LOGOUT

Author: Michelle S. M. Li, Fraser P. Filice, Jeffrey D. Henderson, et al

Publication: The Journal of Physical Chemistry C

Publisher: American Chemical Society

Date: Mar 1, 2016

Copyright © 2016, American Chemical Society

PERMISSION/LICENSE IS GRANTED FOR YOUR ORDER AT NO CHARGE

This type of permission/license, instead of the standard Terms & Conditions, is sent to you because no fee is being charged for your order. Please note the following:

- Permission is granted for your request in both print and electronic formats, and translations.
- If figures and/or tables were requested, they may be adapted or used in part.
- Please print this page for your records and send a copy of it to your publisher/graduate school.
- Appropriate credit for the requested material should be given as follows: "Reprinted (adapted) with permission from (COMPLETE REFERENCE CITATION). Copyright (YEAR) American Chemical Society." Insert appropriate information in place of the capitalized words.
- One-time permission is granted only for the use specified in your request. No additional uses are granted (such as derivative works or other editions). For any other uses, please submit a new request.

BACK

CLOSE WINDOW

Copyright © 2017 Copyright Clearance Center, Inc. All Rights Reserved. [Privacy statement](#), [Terms and Conditions](#).
Comments? We would like to hear from you. E-mail us at customer.care@copyright.com

Appendix V. Chapter 5: Zn²⁺-Induced Apoptosis in Single Human Bladder Cancer Cells Interrogated by Scanning Electrochemical Microscopy

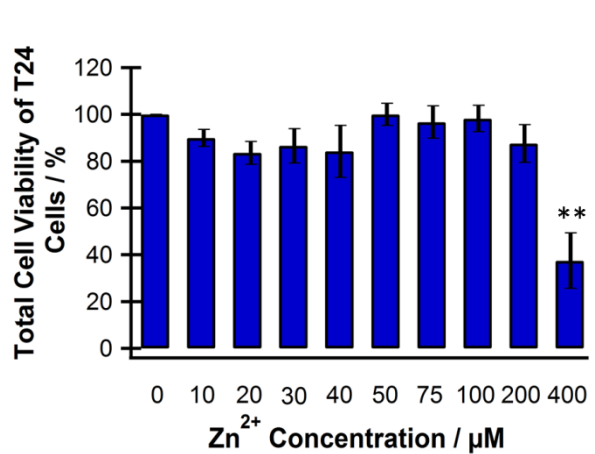


Figure S5.1. Cellular viability of Zn²⁺-treated T24 cells using the MTT proliferation assay. The MTT assays were replicated in four sets of experiments, each containing 8 replicates per trial. Student t-test, **p < 0.0001.

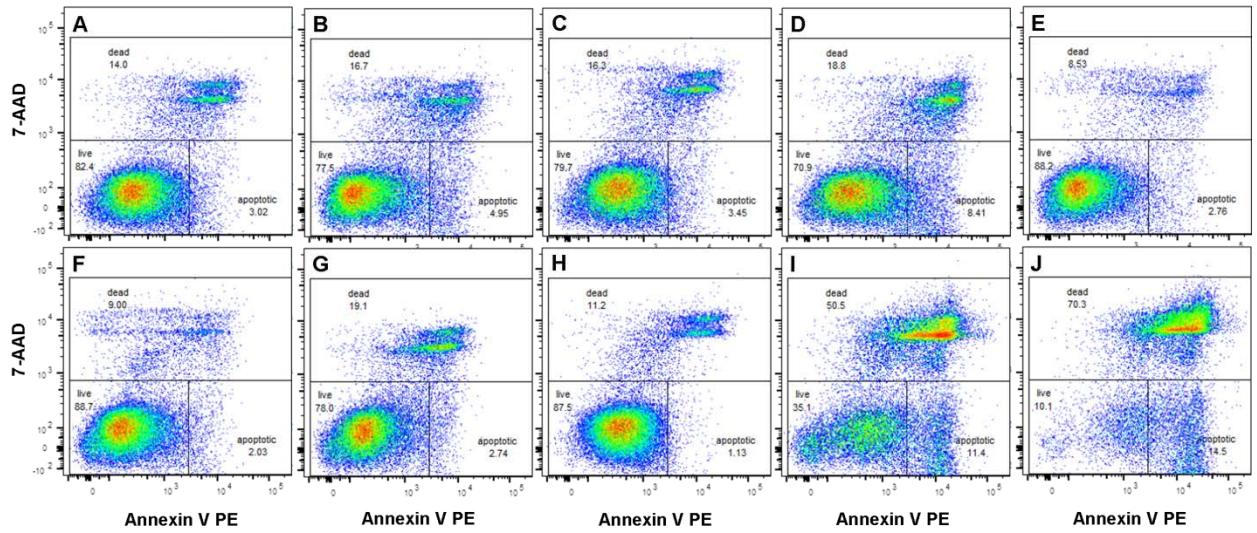


Figure S5.2. Statistical validation of T24 cells treated with (A) 0 (control), (B) 10, (C) 20, (D) 30, (E) 40, (F) 50, (G) 75, (H) 100, (I) 200, and (J) 400 $\mu\text{M Zn}^{2+}$ for 24 hours undergoing apoptosis-induced cellular death. 50,000 Zn^{2+} -treated T24 cells (0-100 μM) were analyzed 7-AAD and Annexin V PE expression, while 35,908 and 30,823 cells were analyzed after 200 and 400 $\mu\text{M Zn}^{2+}$ -treatment, respectively. Higher seeding density (8x) were used in the higher Zn^{2+} -treatments to accommodate for cellular loss due to Zn^{2+} overburden.

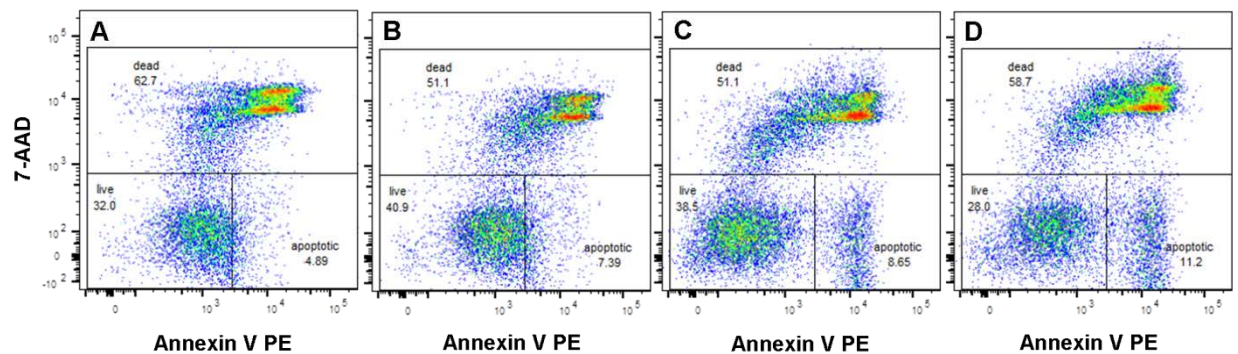


Figure S5.3. Statistical validation of T24 cells treated with (A) 0 (control), (B) 100, (C) 200, and (D) 400 $\mu\text{M Zn}^{2+}$ for 12 hours undergoing apoptosis-induced cellular death. 20,000 Zn^{2+} -treated T24 cells were analyzed for 7-AAD and Annexin V PE expression.

Appendix VI. Chapter 6: Scanning Electrochemical Microscopy with Laser-Pulled Submicron Pt Probes

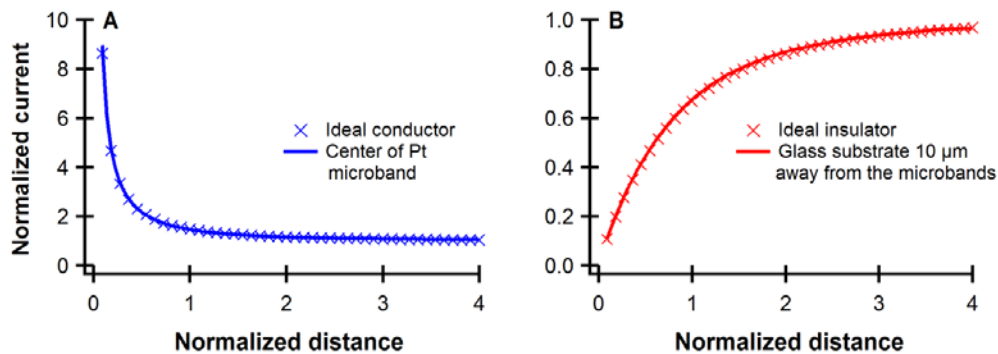


Figure S6.1. A comparison of the PACs extracted to (A) an ideal conductor and the center of a Pt microband from the IAME, and (B) an ideal insulator and the glass substrate, 10 μm away from the IAME.

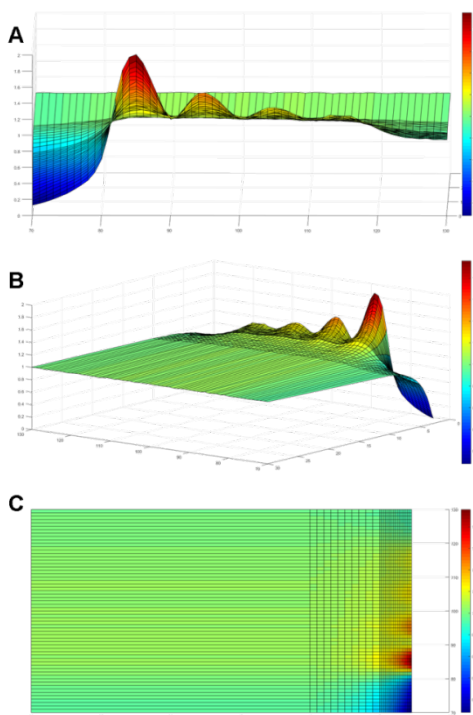


Figure S6.2. Simulated 5° tilt SECM depth scans as viewed from (A) closest approach, (B) three-quarter angle and (C) top perspective views.

6/28/2017

RightsLink Printable License

**ELSEVIER LICENSE
TERMS AND CONDITIONS**

Jun 28, 2017

This Agreement between Michelle Li ("You") and Elsevier ("Elsevier") consists of your license details and the terms and conditions provided by Elsevier and Copyright Clearance Center.

License Number	4137810965012
License date	Jun 28, 2017
Licensed Content Publisher	Elsevier
Licensed Content Publication	Journal of Electroanalytical Chemistry
Licensed Content Title	Scanning electrochemical microscopy imaging with laser-pulled probes
Licensed Content Author	Michelle S.M. Li, Fraser P. Filice, Zhifeng Ding
Licensed Content Date	Nov 15, 2016
Licensed Content Volume	781
Licensed Content Issue	n/a
Licensed Content Pages	10
Start Page	126
End Page	135
Type of Use	reuse in a thesis/dissertation
Intended publisher of new work	other
Portion	full article
Format	both print and electronic
Are you the author of this Elsevier article?	Yes
Will you be translating?	No
Order reference number	
Title of your thesis/dissertation	Scanning Electrochemical Microscopy of Single Live Human Bladder Cancer Cells
Expected completion date	Sep 2017
Estimated size (number of pages)	200
Elsevier VAT number	GB 494 6272 12
Requestor Location	Michelle Li Western University 1151 Richmond Street Department of Chemistry London, ON N6A5B7 Canada Attn: Michelle Li
Total	0.00 USD
Terms and Conditions	

<https://s100.copyright.com/AppDispatchServlet>

1/6

INTRODUCTION

1. The publisher for this copyrighted material is Elsevier. By clicking "accept" in connection with completing this licensing transaction, you agree that the following terms and conditions apply to this transaction (along with the Billing and Payment terms and conditions established by Copyright Clearance Center, Inc. ("CCC"), at the time that you opened your Rightslink account and that are available at any time at <http://myaccount.copyright.com>).

GENERAL TERMS

2. Elsevier hereby grants you permission to reproduce the aforementioned material subject to the terms and conditions indicated.

3. Acknowledgement: If any part of the material to be used (for example, figures) has appeared in our publication with credit or acknowledgement to another source, permission must also be sought from that source. If such permission is not obtained then that material may not be included in your publication/copies. Suitable acknowledgement to the source must be made, either as a footnote or in a reference list at the end of your publication, as follows:

"Reprinted from Publication title, Vol /edition number, Author(s), Title of article / title of chapter, Pages No., Copyright (Year), with permission from Elsevier [OR APPLICABLE SOCIETY COPYRIGHT OWNER]." Also Lancet special credit - "Reprinted from The Lancet, Vol. number, Author(s), Title of article, Pages No., Copyright (Year), with permission from Elsevier."

4. Reproduction of this material is confined to the purpose and/or media for which permission is hereby given.

5. Altering/Modifying Material: Not Permitted. However figures and illustrations may be altered/adapted minimally to serve your work. Any other abbreviations, additions, deletions and/or any other alterations shall be made only with prior written authorization of Elsevier Ltd. (Please contact Elsevier at permissions@elsevier.com). No modifications can be made to any Lancet figures/tables and they must be reproduced in full.

6. If the permission fee for the requested use of our material is waived in this instance, please be advised that your future requests for Elsevier materials may attract a fee.

7. Reservation of Rights: Publisher reserves all rights not specifically granted in the combination of (i) the license details provided by you and accepted in the course of this licensing transaction, (ii) these terms and conditions and (iii) CCC's Billing and Payment terms and conditions.

8. License Contingent Upon Payment: While you may exercise the rights licensed immediately upon issuance of the license at the end of the licensing process for the transaction, provided that you have disclosed complete and accurate details of your proposed use, no license is finally effective unless and until full payment is received from you (either by publisher or by CCC) as provided in CCC's Billing and Payment terms and conditions. If full payment is not received on a timely basis, then any license preliminarily granted shall be deemed automatically revoked and shall be void as if never granted. Further, in the event that you breach any of these terms and conditions or any of CCC's Billing and Payment terms and conditions, the license is automatically revoked and shall be void as if never granted. Use of materials as described in a revoked license, as well as any use of the materials beyond the scope of an unrevoked license, may constitute copyright infringement and publisher reserves the right to take any and all action to protect its copyright in the materials.

9. Warranties: Publisher makes no representations or warranties with respect to the licensed material.

10. Indemnity: You hereby indemnify and agree to hold harmless publisher and CCC, and their respective officers, directors, employees and agents, from and against any and all claims arising out of your use of the licensed material other than as specifically authorized pursuant to this license.

11. No Transfer of License: This license is personal to you and may not be sublicensed, assigned, or transferred by you to any other person without publisher's written permission.

12. **No Amendment Except in Writing:** This license may not be amended except in a writing signed by both parties (or, in the case of publisher, by CCC on publisher's behalf).

13. **Objection to Contrary Terms:** Publisher hereby objects to any terms contained in any purchase order, acknowledgment, check endorsement or other writing prepared by you, which terms are inconsistent with these terms and conditions or CCC's Billing and Payment terms and conditions. These terms and conditions, together with CCC's Billing and Payment terms and conditions (which are incorporated herein), comprise the entire agreement between you and publisher (and CCC) concerning this licensing transaction. In the event of any conflict between your obligations established by these terms and conditions and those established by CCC's Billing and Payment terms and conditions, these terms and conditions shall control.

14. **Revocation:** Elsevier or Copyright Clearance Center may deny the permissions described in this License at their sole discretion, for any reason or no reason, with a full refund payable to you. Notice of such denial will be made using the contact information provided by you. Failure to receive such notice will not alter or invalidate the denial. In no event will Elsevier or Copyright Clearance Center be responsible or liable for any costs, expenses or damage incurred by you as a result of a denial of your permission request, other than a refund of the amount(s) paid by you to Elsevier and/or Copyright Clearance Center for denied permissions.

LIMITED LICENSE

The following terms and conditions apply only to specific license types:

15. **Translation:** This permission is granted for non-exclusive world **English** rights only unless your license was granted for translation rights. If you licensed translation rights you may only translate this content into the languages you requested. A professional translator must perform all translations and reproduce the content word for word preserving the integrity of the article.

16. **Posting licensed content on any Website:** The following terms and conditions apply as follows: Licensing material from an Elsevier journal: All content posted to the web site must maintain the copyright information line on the bottom of each image; A hyper-text must be included to the Homepage of the journal from which you are licensing at <http://www.sciencedirect.com/science/journal/xxxx> or the Elsevier homepage for books at <http://www.elsevier.com>; Central Storage: This license does not include permission for a scanned version of the material to be stored in a central repository such as that provided by Heron/XanEdu.

Licensing material from an Elsevier book: A hyper-text link must be included to the Elsevier homepage at <http://www.elsevier.com>. All content posted to the web site must maintain the copyright information line on the bottom of each image.

Posting licensed content on Electronic reserve: In addition to the above the following clauses are applicable: The web site must be password-protected and made available only to bona fide students registered on a relevant course. This permission is granted for 1 year only. You may obtain a new license for future website posting.

17. **For journal authors:** the following clauses are applicable in addition to the above:

Preprints:

A preprint is an author's own write-up of research results and analysis, it has not been peer-reviewed, nor has it had any other value added to it by a publisher (such as formatting, copyright, technical enhancement etc.).

Authors can share their preprints anywhere at any time. Preprints should not be added to or enhanced in any way in order to appear more like, or to substitute for, the final versions of articles however authors can update their preprints on arXiv or RePEc with their Accepted Author Manuscript (see below).

If accepted for publication, we encourage authors to link from the preprint to their formal publication via its DOI. Millions of researchers have access to the formal publications on ScienceDirect, and so links will help users to find, access, cite and use the best available

version. Please note that Cell Press, The Lancet and some society-owned have different preprint policies. Information on these policies is available on the journal homepage.

Accepted Author Manuscripts: An accepted author manuscript is the manuscript of an article that has been accepted for publication and which typically includes author-incorporated changes suggested during submission, peer review and editor-author communications.

Authors can share their accepted author manuscript:

- immediately
 - via their non-commercial person homepage or blog
 - by updating a preprint in arXiv or RePEc with the accepted manuscript
 - via their research institute or institutional repository for internal institutional uses or as part of an invitation-only research collaboration work-group
 - directly by providing copies to their students or to research collaborators for their personal use
 - for private scholarly sharing as part of an invitation-only work group on commercial sites with which Elsevier has an agreement
- After the embargo period
 - via non-commercial hosting platforms such as their institutional repository
 - via commercial sites with which Elsevier has an agreement

In all cases accepted manuscripts should:

- link to the formal publication via its DOI
- bear a CC-BY-NC-ND license - this is easy to do
- if aggregated with other manuscripts, for example in a repository or other site, be shared in alignment with our hosting policy not be added to or enhanced in any way to appear more like, or to substitute for, the published journal article.

Published journal article (JPA): A published journal article (PJA) is the definitive final record of published research that appears or will appear in the journal and embodies all value-adding publishing activities including peer review co-ordination, copy-editing, formatting, (if relevant) pagination and online enrichment.

Policies for sharing publishing journal articles differ for subscription and gold open access articles:

Subscription Articles: If you are an author, please share a link to your article rather than the full-text. Millions of researchers have access to the formal publications on ScienceDirect, and so links will help your users to find, access, cite, and use the best available version. Theses and dissertations which contain embedded PJAs as part of the formal submission can be posted publicly by the awarding institution with DOI links back to the formal publications on ScienceDirect.

If you are affiliated with a library that subscribes to ScienceDirect you have additional private sharing rights for others' research accessed under that agreement. This includes use for classroom teaching and internal training at the institution (including use in course packs and courseware programs), and inclusion of the article for grant funding purposes.

Gold Open Access Articles: May be shared according to the author-selected end-user license and should contain a [CrossMark logo](#), the end user license, and a DOI link to the formal publication on ScienceDirect.

Please refer to Elsevier's [posting policy](#) for further information.

18. **For book authors** the following clauses are applicable in addition to the above:

Authors are permitted to place a brief summary of their work online only. You are not allowed to download and post the published electronic version of your chapter, nor may you scan the printed edition to create an electronic version. **Posting to a repository:** Authors are permitted to post a summary of their chapter only in their institution's repository.

19. Thesis/Dissertation: If your license is for use in a thesis/dissertation your thesis may be submitted to your institution in either print or electronic form. Should your thesis be published commercially, please reapply for permission. These requirements include permission for the Library and Archives of Canada to supply single copies, on demand, of the complete thesis and include permission for Proquest/UMI to supply single copies, on demand, of the complete thesis. Should your thesis be published commercially, please reapply for permission. Theses and dissertations which contain embedded PJAs as part of the formal submission can be posted publicly by the awarding institution with DOI links back to the formal publications on ScienceDirect.

Elsevier Open Access Terms and Conditions

You can publish open access with Elsevier in hundreds of open access journals or in nearly 2000 established subscription journals that support open access publishing. Permitted third party re-use of these open access articles is defined by the author's choice of Creative Commons user license. See our [open access license policy](#) for more information.

Terms & Conditions applicable to all Open Access articles published with Elsevier:

Any reuse of the article must not represent the author as endorsing the adaptation of the article nor should the article be modified in such a way as to damage the author's honour or reputation. If any changes have been made, such changes must be clearly indicated.

The author(s) must be appropriately credited and we ask that you include the end user license and a DOI link to the formal publication on ScienceDirect.

If any part of the material to be used (for example, figures) has appeared in our publication with credit or acknowledgement to another source it is the responsibility of the user to ensure their reuse complies with the terms and conditions determined by the rights holder.

Additional Terms & Conditions applicable to each Creative Commons user license:

CC BY: The CC-BY license allows users to copy, to create extracts, abstracts and new works from the Article, to alter and revise the Article and to make commercial use of the Article (including reuse and/or resale of the Article by commercial entities), provided the user gives appropriate credit (with a link to the formal publication through the relevant DOI), provides a link to the license, indicates if changes were made and the licensor is not represented as endorsing the use made of the work. The full details of the license are available at <http://creativecommons.org/licenses/by/4.0>.

CC BY NC SA: The CC BY-NC-SA license allows users to copy, to create extracts, abstracts and new works from the Article, to alter and revise the Article, provided this is not done for commercial purposes, and that the user gives appropriate credit (with a link to the formal publication through the relevant DOI), provides a link to the license, indicates if changes were made and the licensor is not represented as endorsing the use made of the work. Further, any new works must be made available on the same conditions. The full details of the license are available at <http://creativecommons.org/licenses/by-nc-sa/4.0>.

CC BY NC ND: The CC BY-NC-ND license allows users to copy and distribute the Article, provided this is not done for commercial purposes and further does not permit distribution of the Article if it is changed or edited in any way, and provided the user gives appropriate credit (with a link to the formal publication through the relevant DOI), provides a link to the license, and that the licensor is not represented as endorsing the use made of the work. The full details of the license are available at <http://creativecommons.org/licenses/by-nc-nd/4.0>. Any commercial reuse of Open Access articles published with a CC BY NC SA or CC BY NC ND license requires permission from Elsevier and will be subject to a fee.

Commercial reuse includes:

- Associating advertising with the full text of the Article
- Charging fees for document delivery or access
- Article aggregation
- Systematic distribution via e-mail lists or share buttons

6/28/2017

RightsLink Printable License

Posting or linking by commercial companies for use by customers of those companies.

20. Other Conditions:

v1.9

Questions? customercare@copyright.com or +1-855-239-3415 (toll free in the US) or +1-978-646-2777.



Curriculum Vitae

Name: Michelle S. M. Li

Post-secondary Education and Degrees: *The University of Western Ontario*
London, Ontario, Canada
2005-2009 B.Sc. (honors)

University of Saskatchewan
Saskatoon, Saskatchewan, Canada
2010-2012 M.Sc.

The University of Western Ontario
London, Ontario, Canada
2013-2017 Ph.D.

Honours and Awards: University of Saskatchewan Travel Grant
2011

Western Graduate Research Scholarship (WGRS)
2013-2016

Queen Elizabeth II Graduate Scholarship in Science & Technology
2015-2017

PSAC 610 Academic Achievement Scholarship
Ph.D. Student in the Biological Sciences
2017

Related Work Experience Teaching Assistant
Saskatoon, Saskatchewan, Canada
2010-2012

Research Assistant
The University of Western Ontario
2008-2009, 2013

Teaching Assistant
The University of Western Ontario
2013-2017

Publications:

1. **M.S.M. Li**, F.P. Filice, and Z. Ding. A Time Course Study of Cadmium Effect on Membrane Permeability of Single Human Bladder Cancer Cells Using Scanning Electrochemical Microscopy. *Journal of Inorganic Biochemistry*, **2014**, *136*, 177-183.
2. F.P. Filice, **M.S.M. Li**, J.D. Henderson, and Z. Ding. Three-Dimensional Electrochemical Functionality of an Interdigitated Array Electrode by Scanning Electrochemical Microscopy. *Journal of Physical Chemistry C*, **2015**, *119*, 21473-21482.
3. J.D. Henderson, F.P. Filice, **M.S.M. Li**, and Z. Ding, Tracking Live Cell Response to Cadmium(II) Concentrations by Scanning Electrochemical Microscopy, *Journal of Inorganic Biochemistry*, **2016**, *158*, 92-98.
4. F.P. Filice, **M.S.M. Li**, J.D. Henderson, and Z. Ding, Mapping Cd²⁺-Induced Membrane Permeability Changes of Single Live Cells by Means of Scanning Electrochemical Microscopy, *Analytica Chimica Acta*, **2016**, *908*, 85-94.
5. **M.S.M. Li**, F.P. Filice, J.D. Henderson, and Z. Ding, Probing Cd²⁺-Stressed Live Cell Membrane Permeability Using Various Redox Mediators in Scanning Electrochemical Microscopy, *Journal of Physical Chemistry C*, **2016**, *120*, 6094-6103.
6. **M.S.M. Li**, F.P. Filice, and Z. Ding, Determining Cellular Topography by Scanning Electrochemical Microscopy, *Journal of Electroanalytical Chemistry*, **2016**, *779*, 176-186.
7. **M.S.M. Li**, F.P. Filice, and Z. Ding, Scanning Electrochemical Microscopy Imaging with Laser-Pulled Probes, *Journal of Electroanalytical Chemistry*, **2016**, *781*, 126-135.
8. **M.S.M. Li***, K. Chu*, J.T. Price, N.D. Jones, and Z. Ding, Analyzing Electrochemiluminescence Mechanisms of Thiophene-Triazole-Thiophene Luminophores with In-situ Spectroscopy, *ChemElectroChem*, **2016**, *3*, 2170-2178.
9. J.T. Price*, **M.S.M. Li***, A.L. Brazeau, D. Tao, G. Xiang, Y. Chen, R. McDonald, N.D. Jones, and Z. Ding, Structural Insight into Electrogenerated Chemiluminescence of Para-Substituted Aryl-Triazole-Thienyl Compounds, *Journal of Physical Chemistry C*, **2016**, *120*, 21778-21789.
10. J.D. Henderson*, F.P. Filice*, **M.S.M. Li**, and Z. Ding, Tracking Live Cell Response to Hexavalent Chromium by Scanning Electrochemical Microscopy, *ChemElectroChem*, **2017**, *4*, 856-863.
11. G. Xiang, X. Wang, **M.S.M. Li**, K. Lac, S. Wang, and Z. Ding. Probing Excimers of Pt(II) Compounds with a Phenyl-1,2,3-Triazolyl and Pyridyl-1,2,4-Triazolyl Chelate Ligands by Means of Electrochemiluminescence, *ChemElectroChem*, **2017**, *4*, 1757-1762.

12. **M.S.M. Li**, F.P. Filice, Z. Ding. Zn²⁺-Induced Apoptosis in Single Human Bladder Cancer Cells Interrogated by Scanning Electrochemical Microscopy, **2017**. *Upon Submission.*)
13. **M.S.M. Li**, F.P. Filice, Z. Ding. Electrochemical Functionality of Microband Electrodes Imaged by Scanning Electrochemical Microscopy with Submicron Probes, **2017**. *Upon Submission.*)

Conference Presentations:

Oral:

1. "Cytotoxic Effects of Cadmium on Human Bladder Cancer Cells Studied by Scanning Electrochemical Microscopy." **M.S.M. Li**, F.P. Filice, and Z. Ding. 97th Canadian Chemistry Conference and Exhibition (CSC). Vancouver, BC, Canada. June 4, **2014**.
2. "The Effects of Cd²⁺ on the Membrane Permeability of T24 Cells Investigated via SECM." **M.S.M. Li**, F.P. Filice, and Z. Ding. 5th Georgian Bay International Conference on Bioinorganic Chemistry (CanBIC-5). Parry Sound, ON, Canada. May 21, **2015**.
3. "Insights into the Effects of Heavy Metal Exposure on Single Human Bladder Cancer Cells." **M.S.M. Li**, F.P. Filice, and Z. Ding. 6th Georgian Bay International Conference on Bioinorganic Chemistry (CanBIC-6). Parry Sound, ON, Canada. May 25, **2017**.
4. "Electrochemical Investigation of Heavy Metal Exposure on Human Bladder Cancer Cells." **M.S.M. Li**, F. P. Filice, and Z. Ding. 100th Canadian Chemistry Conference and Exhibition (CSC). Toronto, ON, Canada. May 30, **2017**.

Poster:

1. "Development of a Spectroelectrochemical Method for the Study of Biological Cells Grown on Gold Surfaces." **M.S.M. Li**, I.J. Burgess, D.J. Schreyer, and T. Berry. 94th Canadian Chemistry Conference and Exhibition (CSC). Montreal, QC, Canada. June 8, **2011**.
2. "The Effect of Cadmium on Membrane Permeability to Ferrocenemethanol of Human Bladder Cancer Cells as Detected by Scanning Electrochemical Microscopy." **M.S.M. Li**, F.P. Filice, and Z. Ding. Centre for Advanced Materials and Biomaterials Research Day. London, ON, Canada. November 1, **2013**.
3. "A Scanning Electrochemical Microscopy Study on the Effects of Cadmium on the Membrane Permeability to Ferrocenemethanol in Human Bladder Cancer Cells." **M.S.M. Li**, F.P. Filice, and Z. Ding. ECS Canada Section Meeting, Fall 2013. Montreal, QC, Canada. November 23, **2013**.

4. “A SECM Study on the Effects of Cadmium on Membrane Permeability in Human Bladder Cancer Cells.” **M.S.M. Li**, J.D. Henderson, F.P. Filice, and Z. Ding. Centre for Advanced Materials and Biomaterials Research Day. London, ON, Canada. April 27, **2015**.
5. “Induction of Membrane Permeability of T24 Cells through Cd²⁺ Stimulation Using Scanning Electrochemical Microscopy.” **M.S.M. Li**, F.P. Filice, J.D. Henderson, and Z. Ding, Gordon Research Conference (Cell Biology of Metals), Mount Snow, VT, USA. July 30, **2015**.

